UFU Universidade Federal de Uberlândia

Université de Lille

Universidade Federal de Uberlândia
Université de Lille

Doctoral Schools **Programa de Pós-Graduação em Engenharia Mecânica (Brazil) and ED Régionale SPI 72 (France)**

University Departments **Laboratório de Mecânica dos Fluidos and Unité Mécanique de Lille - Joseph Boussinesq - EA 7512**

Thesis defended by **João Rodrigo Andrade**

Defended on **27th March, 2019**

In order to become Doctor from Universidade Federal de Uberlândia and from Université de Lille

Academic Field **Mechanics, Energetics, Materials**

Speciality **Fluid Mechanics**

Thesis Title

Spectral analysis of the turbulent energy cascade and the development of a novel nonlinear subgrid-scale model for large eddy simulation

Thesis supervised by	Aristeu da Silveira Neto	Supervisor
	Gilmar Mompean	Supervisor
	Roney Leon Thompson	Co-Supervisor

Committee members

Referees	Rémi Manceau	CNRS - Univ. de Pau et des pays de l'Adour	
	Angela Ourivio Nieckele	Pontifícia Univ. Católica do Rio de Janeiro	Committee President
Guests	Francisco José de Souza	Univ. Federal de Uberlândia	
	Taygoara F. de Oliveira	Univ. de Brasília	
Supervisors	Aristeu da Silveira Neto	Univ. Federal de Uberlândia	
	Gilmar Mompean	Univ. de Lille	
	Roney Leon Thompson	Univ. Federal do Rio de Janeiro	

UFU Universidade Federal de Uberlândia

Université de Lille

Universidade Federal de Uberlândia
Université de Lille

Doctoral Schools **Programa de Pós-Graduação em Engenharia Mecânica (Brazil) and ED Régionale SPI 72 (France)**

University Departments **Laboratório de Mecânica dos Fluidos and Unité Mécanique de Lille - Joseph Boussinesq - EA 7512**

Thesis defended by **João Rodrigo Andrade**

Defended on **27th March, 2019**

In order to become Doctor from Universidade Federal de Uberlândia and from Université de Lille

Academic Field **Mechanics, Energetics, Materials**

Speciality **Fluid Mechanics**

Thesis Title

Spectral analysis of the turbulent energy cascade and the development of a novel nonlinear subgrid-scale model for large eddy simulation

Thesis supervised by	Aristeu da Silveira Neto	Supervisor
	Gilmar Mompean	Supervisor
	Roney Leon Thompson	Co-Supervisor

Committee members

Referees	Rémi Manceau	CNRS - Univ. de Pau et des pays de l'Adour	
	Angela Ourivio Nieckele	Pontifícia Univ. Católica do Rio de Janeiro	Committee President
Guests	Francisco José de Souza	Univ. Federal de Uberlândia	
	Taygoara F. de Oliveira	Univ. de Brasília	
Supervisors	Aristeu da Silveira Neto	Univ. Federal de Uberlândia	
	Gilmar Mompean	Univ. de Lille	
	Roney Leon Thompson	Univ. Federal do Rio de Janeiro	

Universidade Federal de Uberlândia
Université de Lille

Écoles doctorales **Programa de Pós-Graduação em Engenharia Mecânica (Brazil) and ED Régionale SPI 72 (France)**

Unités de recherche **Laboratório de Mecânica dos Fluidos and Unité Mécanique de Lille - Joseph Boussinesq - EA 7512**

Thèse présentée par **João Rodrigo Andrade**

Soutenue le **27 mars 2019**

En vue de l'obtention du grade de docteur de l'Universidade Federal de Uberlândia et de l'Université de Lille

Discipline **Mécanique, Énergétique, Matériaux**

Spécialité **Mécanique des Fluides**

Titre de la thèse

Analyse spectrale de la cascade d'énergie turbulente et développement d'un nouveau modèle non-linéaire sous-maille pour la simulation de grandes échelles

Thèse dirigée par

Aristeu da Silveira Neto	directeur
Gilmar Mompean	directeur
Roney Leon Thompson	co-directeur

Composition du jury

Rapporteurs	Rémi Manceau	CNRS - Univ. de Pau et des pays de l'Adour	
	Angela Ourivio Nieckele	Pontifícia Univ. Católica do Rio de Janeiro	Présidente du jury
Invités	Francisco José de Souza	Univ. Federal de Uberlândia	
	Taygoara F. de Oliveira	Univ. de Brasília	
Directeurs de thèse	Aristeu da Silveira Neto	Univ. Federal de Uberlândia	
	Gilmar Mompean	Univ. de Lille	
	Roney Leon Thompson	Univ. Federal do Rio de Janeiro	

The Universidade Federal de Uberlândia and the Université de Lille neither endorse nor censure authors' opinions expressed in the theses: these opinions must be considered to be those of their authors.

Keywords: turbulent wall-bounded flows, energy cascade, turbulent kinetic energy budget, inhomogeneity, anisotropy, turbulent channel flow, turbulence, direct numerical simulation, large eddy simulation, subgrid-scale model, nonlinear subgrid-scale model

Mots clés : écoulements turbulentes de parois, cascade d'énergie, équation différentielle de l'énergie cinétique turbulent, inhomogénéité, anisotropie, écoulement turbulent en canal plan, turbulence, simulation numérique directe, simulation des grandes échelles, modèle sous maille, modèle sous maille non linéaire

This thesis has been prepared at the following research units.

Laboratório de Mecânica dos Fluidos (MFLab)
Av. João Naves de Ávila, 2121
Bairro Santa Mônica
38400-902 Uberlândia
Brasil

☎ (55)(34) 32 39 40 40
Web Site http://www.mflab.mecanica.ufu.br

Unité de Mécanique de Lille - Joseph Boussinesq (UML) – EA 7512
Boulevard Paul Langevin
Cité Scientifique
59650 Villeneuve d'Ascq Cedex
France

☎ (33)(0)3 20 33 61 30
Web Site http://uml.univ-lille.fr

To my parents, João and Ana Maria, and my wife, Paula.

Acknowledgements

Firstly, I would like to express my sincere gratitude to my Supervisors Professors Aristeu da Silveira Neto, Roney Leon Thompson and Gilmar Mompean. For the continuous support of my Ph.D. study and related research, for their patience, motivation, and immense knowledge. Their guidance helped me all the time of research and writing of this thesis.

This work would not be possible without constant help of Ramon Silva Martins, Rafael Romão and Pedro Ricardo, who were always willing to kindly help in my Fortran programming related problems.

Financial support for this work was provided by FEMEC, CNPq, CAPES, FAPEMIG, PETROBRAS and the Brazilian scholarship program Ciências sem Fronteiras. This support is gratefully acknowledged.

Huge thanks for the professors, secretaries and all staff from Université de Lille and Universidade Federal de Uberlândia for their help. Many thanks to Luismar for his administrative assistance.

I thank my fellow labmates from MFLab and LML for the stimulating discussions, for the new ideas, for all the coffee we have drunk together, and for all the fun we had during my thesis.

I would like to thank Martin and Kristine Leurent for welcome me into their home during the period I lived in France, their sympathy and patience helped me a lot to face this year, even being thousands of kilometers away from my family. It was a great experience.

I must express my very profound gratitude to my parents, João and Ana Maria, my sisters, Ana Paula and Juliana, and to my wife, Paula, for providing me with unfailing support and continuous encouragement throughout my years of study and through the process of researching and writing this thesis. This accomplishment would not have been possible without them. Thank you. A special thanks to Paula, my lovely wife, I must acknowledge my partner and best friend, without whose love, encouragement and patience, I would not have finished this thesis. I am also grateful to my friends who have supported me along the way, especially Ramon Silva Martins, Carlos Antônio Ribeiro Duarte, Bruno Tadeu Pereira Jacob, Dário Oliveira Canossi and Geovana Pereira Drumond.

Finally, I thank all the people who contributed, even unintentionally, to my life to be more pleasant during these last four years.

Spectral analysis of the turbulent energy cascade and the development of a novel nonlinear subgrid-scale model for large eddy simulation

Abstract

The purpose of the present work is to analyze and to provide an enhancement of the knowledge about the subgrid-scale behavior and to propose novel nonlinear subgrid-scale models for large eddy simulations of turbulent fluid flows. In this way, the present thesis is subdivided into three main parts. The first topic is an analysis of the statistical uncertainties associated with direct numerical simulation data for turbulent channel flow, showing a novel physically-based quantification of these errors. In this analysis, the mean velocity error is estimated by considering the Reynolds stress tensor, and using the balance of mean force equation. This analysis is performed in order to verify the quality of the statistical data coming from the direct numerical simulation applied in the present work. Secondly, seeking to understand the contained physics in the whole wavenumber spectrum of turbulent flows, an analysis of the spectral turbulent kinetic energy budget in fully developed turbulent plane channel flow is performed. The analysis is focused on the influence of the Reynolds number on the spectral cascade of energy and the corresponding energy cascade in physical space in the presence of inhomogeneity and anisotropy. Finally, a novel nonlinear subgrid-scale model for large eddy simulation based on a set of objective tensors is presented. In the proposed closure model, the modeled subgrid-scale stress tensor is a function of the resolved rate-of-strain tensor and the resolved non-persistence-of-straining tensor, where both are local and objective kinematic entities. The non-persistence-of-straining tensor represents the local ability of the fluid to avoid being persistently stretched. To check the consistency of the proposed model, *a priori* and *a posteriori* tests are performed by simulating different wall-bounded turbulent flows. Comparisons with the exact subgrid-scale stress tensor and experimental data revealed that the inclusion of nonlinear terms on the subgrid-scale model can significantly increase the accuracy of the results, showing the great potential of the proposed tensorial base.

Keywords: turbulent wall-bounded flows, energy cascade, turbulent kinetic energy budget, inhomogeneity, anisotropy, turbulent channel flow, turbulence, direct numerical simulation, large eddy simulation, subgrid-scale model, nonlinear subgrid-scale model

Laboratório de Mecânica dos Fluidos (MFLab)
Av. João Naves de Ávila, 2121 – Bairro Santa Mônica – 38400-902 Uberlândia – Brasil

Analyse spectrale de la cascade d'énergie turbulente et développement d'un nouveau modèle non-linéaire sous-maille pour la simulation de grandes échelles

Résumé

L'objectif de cette thèse est d'analyser et d'acquérir de nouvelles connaissances sur le comportement de la dynamique de petites échelles des écoulements turbulents et de proposer un nouveau modèle sous-maille non linéaire pour la simulation des grandes échelles de la turbulence. De cette façon, la présente thèse est subdivisée en trois parties principales. Le premier sujet concerne l'analyse des incertitudes statistiques associées aux données de simulation numérique directe pour des écoulements turbulents en canal plan, fournissant une nouvelle quantification physique de ces erreurs. Dans cette analyse, l'erreur de vitesse moyenne est estimée en prenant en compte le tenseur de contrainte de Reynolds et en utilisant l'équation de forces moyennes. Cette analyse est effectuée afin de vérifier la qualité des données statistiques provenant de la simulation numérique directe appliquée dans le présent travail. Deuxièmement, pour comprendre la physique contenue dans l'ensemble du spectre de nombre d'ondes des écoulements turbulents, une analyse du bilan d'énergie cinétique turbulente dans un écoulement de canal plan turbulent complètement développé est réalisée. L'analyse est centrée sur l'influence du nombre de Reynolds sur la cascade spectrale d'énergie et la cascade d'énergie correspondante dans l'espace physique en présence d'inhomogénéité et d'anisotropie. Finalement, nous présentons un nouveau modèle sous-maille non linéaire, conçu pour la simulation des grandes échelles de la turbulence, basé sur un ensemble de tenseurs objectifs. Dans le modèle de fermeture proposé, le tenseur de contrainte à l'échelle sous-maille est fonction du tenseur de la vitesse de déformation et du tenseur de non-persistance de contraintes, où les deux sont des entités cinématiques locales et objectives. Le tenseur non-persistance de contraintes représente la capacité locale du fluide à ne pas être constamment étiré. Pour vérifier la cohérence du modèle proposé, de tests *a priori* et *a posteriori* sont effectués en simulant différents écoulements turbulents délimités par de parois. Des comparaisons avec le tenseur de contrainte exact à l'échelle de sous-maille et de données expérimentales ont révélé que l'inclusion de termes non linéaires dans le modèle sous-maille peut conduire à de meilleurs résultats, montrant le potentiel important de la base tensorielle proposée.

Mots clés : écoulements turbulentes de parois, cascade d'énergie, équation différentielle de l'énergie cinétique turbulent, inhomogénéité, anisotropie, écoulement turbulent en canal plan, turbulence, simulation numérique directe, simulation des grandes échelles, modèle sous maille, modèle sous maille non linéaire

Acronyms

Numbers | B | C | D | E | H | L | R | S | T

Numbers

3D three dimensional.

B

BMFE balance of mean forces.
BMME mean momentum equation.

C

CDS central difference scheme.
CFL Courant-Friedrichs-Lewy.
CUBISTA convergent and universally bounded interpolation scheme for the treatment of advection.

D

DNS Direct Numerical Simulation.

E

EVM eddy viscosity model.

H

HIT homogeneous isotropic turbulence.
HR-DNS high-resolution direct numerical simulation.
HST homogeneous sheared turbulence.

L

LES large eddy simulation.

R

RANS Reynolds averaged Navier-Stokes.
RHS right-hand side.
RMS root mean square.

S

SGS subgrid-scale.

T

TCF turbulent channel flow.
TKE turbulent kinetic energy.

Symbols

A | B | C | D | E | F | G | H | I | K | L | M | N | O | P | Q | R | S | T | U | V | W | X | Y | Z

A

a box filtering parameter.
$\boldsymbol{A}$ generic second order tensor.

B

b box filtering parameter.
β_k subgrid-scale model coefficients.

C

C_k plane averaged model coefficients.
C_S Smagorinsky model coefficient.

D

d channel gap or pipe diameter.
D characteristic length.
Δ characteristic grid width.
Δx_i grid spacing in the i-direction.
$\mathcal{D}_p$ diffusion by pressure fluctuations.
$\mathcal{D}_\nu$ viscous diffusion.
$\delta(\ )$ Dirac function.

E

$E_{ij}^{\mathcal{L}}$ components of the Leonard local error tensor.
E_{ij}^{τ} components of the subgrid-scale local error tensor.
ε_{in} in-plane turbulent energy dissipation rate.
ε_{out} inter-plane turbulent energy dissipation rate.
$||E_R||$ norm of the residual error related to the Reynolds shear stress.
$||E_U||$ norm of the residual error related to the mean velocity.
e_k^S normalized eigenvectors of the filtered rate-of-strain tensor.
E_R residual error related to the Reynolds shear stress in direct numerical simulations.
$\dot{e}_k^S$ time derivatives of the normalized eigenvectors of the filtered rate-of-strain tensor.
$\varepsilon_{tot,t}^+$ total dissipation spectral density normalized in wall units.
ε turbulent kinetic energy dissipation rate.
E turbulent kinetic energy spectral density.
E^+ turbulent kinetic energy spectral density normalized in wall units.

F

$\overline{\phi}$ mean value of a generic quantity.
$\mathbf{\Phi}_{ij}$ components of the spectrum tensor.
ϕ' fluctuating part of a generic quantity.

G

$\widetilde{G}(\,)$ grid filter.
$G(\,)$ kernel function.
$G_{\Delta}(\,)$ spatial low-pass filter.
$\widehat{G}$ test filter.

H

h channel half-gap.
H domain size in the y-direction.
h step height.

I

$\boldsymbol{I}$ identity tensor.
ι imaginary unit.

K

k_i wavevector components.
K_m turbulent kinetic energy contribution from the spectral band associated with bin-m.
K^+ mean kinetic energy normalized in wall units.
K turbulent kinetic energy.
$\bar{\kappa}_m$ average wavenumber contained within bin-m.
κ^+ dimensionless wavenumber normalized in wall units.

L

L domain size in the x-direction.
L_x domain length in x-direction.
L_z domain length in z-direction.
λ_i wavelength components.
$\mathcal{L}_{ij}$ components of the Leonard tensor.
$\mathcal{L}^*_{ij}$ components of the deviatoric part of the Leonard tensor.
$L_{x,min}$ length in x-direction of the domain size containing the minimal flow unit in the logarithmic layer.
$L_{z,min}$ length in z-direction of the domain size containing the minimal flow unit in the logarithmic layer.

M

m bin number.
$\left\{\boldsymbol{M}^{(1)}, \boldsymbol{M}^{(2)}, ..., \boldsymbol{M}^{(6)}\right\}$ generic second order tensors.

N

η Kolmogorov length scales.
N_x number of discretized cells in the x-direction.
N_y number of discretized cells in the y-direction.
N_z number of discretized cells in the z-direction.
ν kinematic viscosity.
ν_{SGS} turbulent eddy viscosity.

O

ω_i components of the vorticity first order tensor.
ω_i' components of the fluctuating part of the vorticity first order tensor.

P

p' fluctuating part of the pressure.
Ψ_n generic n order tensor.
$\overline{p}$ mean pressure.
$\widetilde{\boldsymbol{P}}$ filtered non-persistence-of-straining tensor.
$\mathcal{P}_r$ energy transfer between the filtered and subgrid scales.
ϕ instantaneous generic quantity.
p pressure.
$\mathcal{P}$ turbulent production by mean shear.
$\mathcal{P}_t^+$ production spectral density normalized in wall units.

Q

$\mathcal{Q}^{\mathcal{L}}$ Leonard quadratic error function.
$\mathcal{Q}^{\tau}$ subgrid-scale quadratic error function.

R

R^2 correlation coefficient.
r radial distance in a pipe.
R^+ Kármán number normalized in wall units.
R_M normalized parameter to measure correlation between two tensors.
R pipe radius.
Re Reynolds number.
Re_h Reynolds number based on the channel half-gap.
$\mathcal{R}e[\ ]$ represents the real part of a complex number.
Re_τ frictional Reynolds number.
ρ specific mass.
R_{yx} component xy of the Reynolds shear stress.
$\hat{R}_{yx}$ component xy of the Reynolds shear stress provided by the DNS data.

S

$\widetilde{\boldsymbol{S}}$ Filtered rate-of-strain tensor.
s_{ij}' components of the fluctuating part of the rate-of-strain tensor.
$\widetilde{\boldsymbol{S}}$ filtered rate-of-strain tensor.
$\widetilde{S}_{ij}$ components of the filtered rate-of-strain tensor.
$\left|\widetilde{\boldsymbol{S}}\right|$ magnitude of the rate-of-strain tensor.

T

T averaging time.
$\mathcal{T}_{in}$ in-plane turbulent transport by the velocity fluctuation.
$\mathcal{T}_{out}$ inter-plane turbulent transport.
t_η Kolmogorov time scales.
$\boldsymbol{\tau}^M$ modeled subgrid-scale stress tensor.
T^* non-dimensional averaging time.
$\boldsymbol{\tau}$ subgrid-scale stress tensor.
τ_w wall shear stress.
θ angle in a cylindrical coordinate.
θ generic variable.
T_{ij} components of the subtest stress tensor.
T_{ij}^M components of the modeled subtest stress tensor.
t time.
$\boldsymbol{T}^M$ modeled subtest stress tensor.
τ total shear stress.
$\mathcal{T}_{tot}^+$ total turbulent transport normalized in wall units.

U

U_b bulk streamwise velocity.
U_c centerline velocity.
U characteristic velocity.
u_i' components of the fluctuating part of the velocity.
$\overline{u}_i$ components of the mean velocity.
$\widetilde{u_i}$ components of the filtered velocity vector.
u_x' fluctuating part of the velocity in the x direction.
u_y' fluctuating part of the velocity in the y direction.
$\hat{u}_i$ components of the velocity first order tensor in Fourier domain.
u_i components of the fluid velocity first order tensor.
(u_r, u_θ, u_x) velocity components in cylindrical coordinates.
$\hat{u}_i^*$ velocity complex conjugate.
$\hat{U}$ mean velocity provided by the DNS data.
u_τ friction velocity.

V

v_η Kolmogorov velocity scales.

W

W domain size in the z-direction.
$\widetilde{\boldsymbol{W}}^*$ relative-rate-of-rotation tensor.

X

x streamwise direction.
x_1 streamwise direction.
x_2 normal-wall direction.
x_3 spamwise direction.

X_i step size in the x-direction.
ξ^+ enstrophy normalized in wall units.
X spatial position first order tensor.
x_i component of the spatial coordinates.

Y

y normal-wall direction.
y^+ distance from the wall normalized in wall units.
y^+_{max} y^+ maximun for each region, i.e., at the viscous sublayer, at the buffer layer, and in the log-law region.
y^+_{min} y^+ minimum for each region, i.e., at the viscous sublayer, at the buffer layer, and in the log-law region.

Z

z spamwise direction.

Contents

List of Tables

List of Figures

Chapter 1

Introduction

1.1 Turbulence

Turbulence in fluids is a complex and nonlinear phenomenon involving vortex stretching, and is characterized by an apparently random and chaotic fluid motion. It presents highly irregular behavior and diffusivity with great mixing potential [23, 127]. Figure 1.1 shows some characteristic structures present in turbulent flows. The snapshots of instantaneous isosurfaces of the Q-criterion field in a turbulent channel flow at different friction Reynolds number (Re_τ) are shown (i.e. $Re_\tau = 180$, $Re_\tau = 590$ and $Re_\tau = 1000$). The friction Reynolds number is based on the friction velocity and the channel half-gap in a channel flow. Turbulent structures containing several scales can be observed. Significant differences between each flow at a different Reynolds number can also be noticed, where the higher the Reynolds number, the more structures arise in the flow with a wider range of scales. Briefly, Q-criterion represents the local balance between shear strain rate and vorticity magnitude, defining vortices as areas where the vorticity magnitude is greater than the magnitude of rate-of-strain [63]. For more in-depth discussions on the Q-criterion, see Hunt et al. [63].

In order to quantify the relationship and interaction between the various scales of turbulent flows, it is important to understand the energy transfer mechanism to the residual motions, and to thermal energy. The energy cascade concept of Richardson [131] was proposed as one of the basic ideas in turbulence which discusses and explain, in a simple way, this dynamic relationship between the various scales. It states that turbulent flows can be imagined to consist of eddies of different sizes. The large eddies which contains most of the energy are unstable and break down, transferring energy into smaller eddies. This process goes on until the smallest eddies, where the energy is transformed into heat by viscous effects in a irreversible way. This idea is stated in Richardson's famous poem:

Big whorls have little whorls

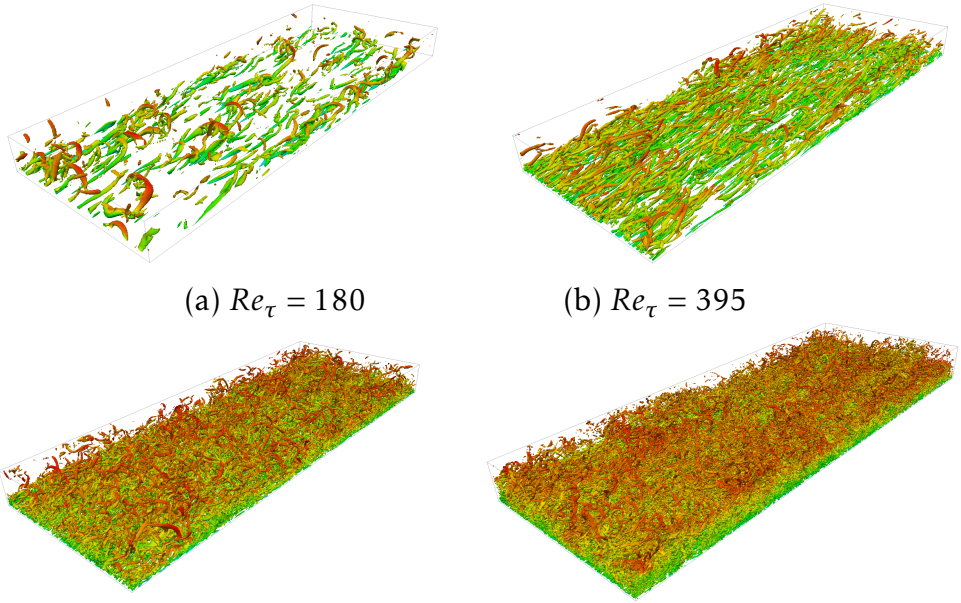

(a) $Re_\tau = 180$ (b) $Re_\tau = 395$

(c) $Re_\tau = 590$ (d) $Re_\tau = 1000$

Figure 1.1 – Contour plots of instantaneous isosurfaces of the Q-criterion ($Q = 1$) field of channel flow colored by the velocity magnitude at (a) $Re_\tau = 180$, (b) $Re_\tau = 395$, (c) $Re_\tau = 590$ and (d) $Re_\tau = 1000$.

That feed on their velocity
And little whorls have lesser whorls
And so on to viscosity (in the molecular sense).

The concept idealized by Richardson received several criticisms regarding its total truthfulness, and needs additional considerations. It is known that the energy transport through the scales does not occur in only one direction, this assertion is based on the triadic interactions [82] between different wavelengths found in the momentum balance equations in the spectral domain. The energy transfer mechanisms among the different turbulent scales does not occur in a simple and linearly manner with only one direction of energy flow. Actually, it occurs in both directions, the so-called backscatter and forward scatter [124]. Conflicting situations with the Richardson cascade have already been observed, such as, for example, the net transfer of turbulent kinetic energy from the smallest to the largest scales, the so-called inverse energy cascade phenomenon, regularly evinced in laboratory and numerical experiments [3].

According to Tennekes and Lumley [145], and as it will be shown in the following chapters, the turbulence is generally produced in the largest scales and these scales are typically set by the flow domain, e.g. the channel height in a plane channel flow. Following Kolmogorov [78], the size and time scales of the smallest eddies can be deduced analytically. It was stated that, at sufficiently high Reynolds number, the statistics of the small scales are universal and are determined solely by the kinematic viscosity, ν, and turbulent kinetic energy dissipation rate, ε. Then, the Kolmogorov

length (η), time (t_η) and velocity (v_η) scales are given by

$$\eta = \left(\frac{\nu^3}{\varepsilon}\right)^{1/4}, \tag{1.1}$$

$$t_\eta = \left(\frac{\nu}{\varepsilon}\right)^{1/2}, \tag{1.2}$$

$$v_\eta = (\nu\varepsilon)^{1/4}. \tag{1.3}$$

Since the simulation of a turbulent flow with the computation of the whole eddy sizes, including the smallest ones (Kolmogorov scale), demands a high computational cost, Smagorinsky [141] formulated the large eddy simulation (LES) method to overcome this problem and still maintain the fidelity of the large spatial and temporal scales. The Smagorinsk model is derived based on the Boussinesq approximation for Reynolds averaged Navier-Stokes (RANS) equation. The LES approach is better discussed in next section.

1.2 Energy transfer in turbulence

In the classical homogeneous isotropic turbulence (HIT), it is known that the energy transport occurs only in the spectral space. This type of flow has been exhaustively studied in the last decades [140, 78, 131, 49, 31, 145, 127]. Following Richardson [131] and Kolmogorov [78], by characterizing the HIT, it was shown that the continuous energy density spectrum can be divided into three main spectral ranges: large production scales, inertial energy transfer scales, and small dissipative scales.

If the turbulent flow is bounded by one or more solid surface, in contrast to the HIT, the velocity field properties are altered and the flow field becomes more complex. Due to this complexity added to the velocity field, inhomogeneity and anisotropy arise in the flow and generate a mean energy transfer in the physical spatial domain. The energy sources and sinks will behave in different ways depending on the distances from the wall. In this context, for a turbulent channel flow (TCF), the flow domain also presents well-defined regions where there are different contributions to the balance of the turbulent kinetic energy, i.e., the viscous sub-layer, where viscosity dominates, the buffer layer, where production has its peak, the logarithmic layer, where production is in equilibrium with dissipation and the outer layer region, where turbulence is energized by the spatial flux of turbulent kinetic energy generated within the buffer layer [127].

In the channel flow, the turbulent kinetic energy is produced through the interaction of the turbulent shear stress and mean shear with the maximum occurring in a buffer region at scales above the shear scale. This generated energy then cascades (forward

and reverse) through a broad range of scales associated with both the viscous sub-layer and the outer bulk region of the flow. Since the energy generated at the intermediate scales feed larger motions farther away from the wall [28], a local energetic equilibrium (energy production balances dissipation rate) can exist in a logarithmic region. This Kolmogorov hypothesis [78] on the locality of the energy transfer [41] and interacting scales [176, 177] has been validated by numerical simulations whenever channel flow simulations have been performed.

This energetic transfer behavior in wall-bounded turbulent flows is an important characteristic and gives rise to a reverse energy cascade from the smaller to the larger scales, the so-called energy backscatter [123, 66].

Marati et al. [102] were the first to utilize simulation data of channel flow within the structure function framework to analyze the energetic fluxes and scale energy budgets. They analyzed a direct numerical simulation (DNS) data set of a low Reynolds number turbulent channel flow and examined the transference of energy associated with a specific scale of motion through the spectrum of scales and, simultaneously, how the same scale of motion exchanges energy with a properly defined spatial flux. The second order structure function was considered to develop the kinetic energy density scale-by-scale analysis.

Dunn and Morrison [44] analyzed the evolution equation for the kinetic energy density by means of the wavelet transform, which offers a relation between a spatial and a spectral description to investigate the spatial and scale–to–scale flux of turbulence kinetic energy in turbulent channel flow at $Re_\tau = 300$.

Cimarelli et al. [28] studied the behavior of the energy fluxes in the spectral and physical spaces in wall-bounded turbulent flows by means of the balance equation for the second-order structure function. It has been shown [27] that an inverse cascade energy flux mechanism acts when the turbulence is firstly generated in a near-to-wall region in an intermediate range of small scales. From these small scales sources, turbulent energy spreads towards larger structures in regions farthest from the wall. Then, the largest turbulent structures are converted to the smallest scales of motion and are dissipated. The authors identified two main dynamical processes as driving mechanisms for the fluxes. One, stronger, is located in the near-wall region and a second one further away from the wall. This forward and reverse cascade of the energy flux has a direct influence on the modeling of the subgrid scale stresses in large-eddy simulations.

In a recent work, Mollicone et al. [114] have an important contribution investigating the energy cascade in physical space using a generalised Kolmogorov equation. They extended the comprehension of the production and transfer of the turbulent kinetic energy (TKE) in the combined positions/scales spaces for a more complex geometry, a separation bubble generated by a bulge at a turbulent plane channel flow. The

generalised Kolmogorov equation was proven to be appropriate for the understanding of such a kind of complex flow.

Bolotnov et al. [17] analyzed a direct numerical simulation of turbulent channel flow at $Re_\tau = 178.12$ to understand the spectral turbulent kinetic energy distribution and the terms which determine the energy distribution in physical and wavenumber spaces by using DNS data from Trofimova et al. [155].

In short, the description in spectral space alone is insufficient to capture the real dynamics of TCF, which differs from the HIT by the existence of two forms of mean energy transfer, in the wavenumber and in the physical spaces. Such processes are strongly scale and position dependent. In conclusion, a necessary task to describe in more details the real dynamics, in presence of the spatial fluxes induced by inhomogeneity, is to study the spatial and the spectral behaviors of a turbulent plane channel flow and the impact of the Reynolds number.

1.3 Large eddy simulation

Due to the complex relationship and interaction between the various scales of the turbulent phenomenon in fluids, even the smallest turbulent structures (Kolmogorov scale) affect the flow as a whole. Therefore, in order to compute the exact prediction of the velocity field, these small structures must be considered, demanding a high computational cost. To overcome this hardware restriction and still maintain a good mathematical representation of the large spatial and temporal scales, Smagorinsky [141] formulated the large eddy simulation (LES) method. This method was proposed based on the fact that in the small scales in high Reynolds number flows, the turbulent structures present a more universal behavior [23, 126]. Another physical aspect of the Smagorinsky model is that it is based on the equilibrium hypothesis which, according to Blazek [16], leads to a complete and instantaneous energy transference from the large scales to the small ones, and finally to thermal energy. The LES was firstly developed for meteorological applications and its first complex application was proceeded by Silveira-Neto et al. [139]. Since then, there have been many reviews on the prescription of the Smagorinsky model coefficient and its behavior [108].

In general, the LES intends to compute the more energized scales (large-scales) and to model the energetic effects of the nonlinear interaction between the largest and the unresolved smallest scales. Generally, the separation of the turbulent structures into the resolved and unresolved scales is done by the discretization grid. According to Meneveau [106], a necessary condition to correctly predict the mean flow statistics in LES is the reasonably correct amount of viscous transformation rate in a filtered sense provided by the subgrid-scale (SGS) model. This formulation is based on the filtering process of the Navier-Stokes equations and explores the fact that the large-scale

motions are more sensitive to the boundary conditions then the smaller scales and are responsible for most of the energy transferred in the flow. This process is made by modeling the SGS stress tensor, $\boldsymbol{\tau}$. In the Smagorinsky's formulation, this modeling is considered by the hypothesis of a proportionality between the SGS modeled stress tensor, $\boldsymbol{\tau}^M$, and the filtered rate-of-strain tensor. The Smagorinsky's model can be considered as the precursor of all SGS stress models.

Reasonable results using the Smagorinsky's model were achieved with the simulation of homogeneous isotropic turbulence (HIT), where it is known that the energy transport occurs in the spectral space solely. However, when the turbulent flow is bounded by one or more solid surface, such as the turbulent channel flow (TCF), the form of the velocity field is altered and the flow field becomes more complex. Due to this complexity added to the velocity field, the flow presents inhomogeneity and anisotropy that are responsible for the generation of an energy transfer in the physical space, where the energy sources will behave differently depending on the distance from the wall [102, 44, 17, 28, 27, 114, 4].

Since the Smagorinsky's SGS model imposes an alignment of the eigenvectors and a proportionality of the eigenvalues of the modeled SGS stress, $\boldsymbol{\tau}^M$, and filtered rate-of-strain tensor, it is considered as a linear SGS model for which inconsistencies in its assumptions are inherent to the modeling approach. Hence, special treatments are needed [29, 95], especially in regions close to walls, e.g., Deardorff [35] proposed a wall-function to channel flow and Moin and Kim [110] applied a van Driest damping function to reduce the near-wall turbulent viscosity. This imposed alignment was proved to be inaccurate for the exact subgrid-scale tensor, $\boldsymbol{\tau}$, by several authors by analyzing filtered data coming from DNS, e.g. [19, 144, 167, 61, 129]. It means that the eddy viscosity models based on the direct relationship between the modeled subgrid Reynolds stress tensor and rate-of-strain tensor is poor and cannot predict correctly the exchange of turbulent kinetic energy between the resolved scales and the small scales. According to Meneveau and Katz [107], even by considering an exact turbulent viscosity field in the Smagorinsky closure model, $\boldsymbol{\tau}^M$ still could not be well predicted. Another consequence of the linear closure model is the poor prediction of the SGS anisotropy, which is particularly high at close-to-wall regions, and, therefore, cannot be correctly represented for coarse resolution mesh [54]. In addition, the energetic transfer dynamics in wall-bounded turbulent flows can lead to a reverse energy cascade from the smaller to the larger scales, the so-called energy backscatter [66, 123], which can not be well predicted by linear SGS models.

1.3.1 Filtering in large eddy simulation

Only the largest scales of turbulence are calculated in the large eddy simulation approach, while the energetic effects of the smaller scales are modeled. Consequently, statistical amounts computed from a large eddy simulation must be interpreted as statistics of the large scales. According to Jiménez and Moser [67], it can be stated that for some quantities, such as the mean velocity and the statistics of multi-point velocity differences (for large spatial separation), there is no small-scale contribution, and LES is able to predict those well. Nevertheless, for others quantities, e.g. the single-point moments of order higher than one, a small-scale contribution must be taken into account, and the large-scale values computed through LES will differ from those measured in an experiment or computed in a DNS. In this manner, to properly contrast a LES and a DNS (or experiment), it is important to extract the large scale statistics.

The large scales in LES are characterized by means of a spatial low-pass filter which, for a single homogeneous spatial direction, is defined through an suitable kernel function, $G(\ )$. According to the suggestion of Leonard [90], the appropriate averaging process for LES should be a local spatial filter, given by

$$\widetilde{\Psi}_n(\mathbf{X}) = \int \Psi_n(\mathbf{X}')\, G(\mathbf{X}-\mathbf{X}')\, dx', \tag{1.4}$$

where the filtered (or resolved, or large-scale) variable is denoted by an overtilde $\widetilde{(\ )}$, Ψ_n is a generic n order tensor. For instance, in a three-dimensional flow, the filtered velocity field is formally defined as

$$\widetilde{u_i}(x,y,z) = \int_{-\infty}^{\infty}\int_{-\infty}^{\infty}\int_{-\infty}^{\infty} u_i(x',y',z') G_\Delta(x-x',y-y',z-z')dx'dy'dz', \tag{1.5}$$

where $G_\Delta(\ )$ is a spatial low-pass filter with characteristic width Δ.

Several sensible choices for the functional form of $G(\mathbf{X})$ can be found in literature, where $\mathbf{X}$ is the spatial position vector. One of the most common is the Fourier truncation, which corresponds to

$$G_\Delta(x) = \frac{sin(2\pi x/\Delta)}{\pi x}, \tag{1.6}$$

and which is mostly used in spectral numerical codes. Its only parameter is the filter width Δ.

The Gaussian filter is given by

$$G_\Delta(x) = \sqrt{\frac{6}{\pi\Delta^2}} e^{\left(-6x^2/\Delta^2\right)}. \tag{1.7}$$

Another popular choice is the box filter, also by by top-hat filter, given by

$$G_\Delta(x) = (1/2)\Delta \quad \text{if} \quad |x| < \Delta, \quad G_\Delta(x) = 0, \quad \text{otherwise}, \tag{1.8}$$

which is easier to apply to computations or measurements in physical, rather than spectral, space.

For instance, if the box filter is applied in a homogeneous grid with sides of length $\Delta_a = (a/b)\Delta$ where Δ is the mesh spacing in the current node of the coarse grid and $a > b$. The filtered velocity $\widetilde{u_i}(i,j,k)$, where i,j,k are the coordinates of the point on the fine grid, is:

$$\widetilde{u_i}(i,j,k) = \frac{1}{a^3} \sum_{i'=i-b}^{i+b} \sum_{j'=j-b}^{j+b} \sum_{k'=k-b}^{k+b} u_i(i',j',k'). \tag{1.9}$$

A deeper discussion about filtering in LES can be found in Vreman et al. [165], Meneveau and Katz [107], Pope [127], and Sagaut [133].

1.3.2 Mathematical formulation and the closure problem

The filtered Navier-Stokes equations, that are being solved in LES, are written as

$$\frac{\partial \widetilde{u_i}}{\partial t} + \frac{\partial \left(\widetilde{u_i u_j}\right)}{\partial x_j} = -\frac{\partial \widetilde{p}}{\partial x_i} + \frac{\partial}{\partial x_j}\left[\frac{1}{Re}\left(\frac{\partial \widetilde{u_i}}{\partial x_j} + \frac{\partial \widetilde{u_j}}{\partial x_i}\right)\right], \tag{1.10}$$

and the continuity equation, assuming incompressible fluid, is given by

$$\frac{\partial \widetilde{u_i}}{\partial x_i} = 0, \tag{1.11}$$

where tilde refers to the implicit grid filter, u_i are components of the fluid velocity, t is the time, x_i are spatial coordinates, p is the pressure and Re is the Reynolds number, which is given by

$$Re = \frac{UD}{\nu}, \tag{1.12}$$

where U and D are the characteristic velocity and length, respectively, and ν is the kinematic viscosity.

Hence, the nonlinear term can be written as

$$\frac{\partial \left(\widetilde{u_i u_j}\right)}{\partial x_j} = \frac{\partial \widetilde{u_i}\widetilde{u_j}}{\partial x_j} + \frac{\partial \left(\widetilde{u_i u_j} - \widetilde{u_i}\widetilde{u_j}\right)}{\partial x_j}, \tag{1.13}$$

and then, the filtered Navier-Stokes equation becomes

$$\frac{\partial \widetilde{u_i}}{\partial t} + \frac{\partial \left(\widetilde{u_i}\widetilde{u_j}\right)}{\partial x_j} = -\frac{\partial \widetilde{p}}{\partial x_i} + \frac{\partial}{\partial x_j}\left[\frac{1}{Re}\left(\frac{\partial \widetilde{u_i}}{\partial x_j} + \frac{\partial \widetilde{u_j}}{\partial x_i}\right)\right] - \alpha_i. \tag{1.14}$$

where α_i is the second term on the right side of Eq. 1.13, $\alpha_i = \partial\left(\widetilde{u_i u_j} - \widetilde{u_i}\widetilde{u_j}\right)/\partial x_j$.

In this formulation, the first-order tensor α_i is the divergence of the SGS stress and involves the $\boldsymbol{\tau}$ terms that requires modeling. Then, by knowing the exact velocity field, one can obtain the exact SGS tensor.

$$\tau_{ij} = \widetilde{u_i u_j} - \widetilde{u_i}\widetilde{u_j}. \tag{1.15}$$

For incompressible flows, the spherical (isotropic) part of the SGS tensor does not influence the dynamics of the filtered flow and then is usually lumped into the pressure term, therefore only the deviatoric part of the SGS stress tensor, $D = \tau_{ij} - \tau_{kk}\delta_{ij}/3$, is modeled (see, e.g. Winckelmans et al. [169]).

Hence, the term $\boldsymbol{\tau}$ imposes a closure problem to the filtered linear momentum balance equation (Eq. 1.14) and needs to be modeled. Since the scales larger than the grid filter are directly computed in LES, the energetic influence of $\boldsymbol{\tau}$ can be modeled depending only on resolved quantities. The most common model to estimate the influence of $\boldsymbol{\tau}$ is the eddy viscosity Smagorinsky's model. The Smagorinsky model is also based on the equilibrium hypothesis, which, according to Blazek [16], suggests that the small scales transfer completely and instantaneously all the energy they receive from the large scale to thermal energy. According to Baggett et al. [9], in LES of wall-bounded flows close to the walls, the number of anisotropic non Kolmogorov-type of modes, i.e. those that depend on more parameters than just the energy dissipation and viscosity, will be of the order of Re_τ^2.

The hypothesis of eigenvectors alignment between $\boldsymbol{\tau}$ and filtered rate-of-strain tensor ($\widetilde{\boldsymbol{S}}$) is only possible to estimate a correctly general mean drain of energy from the resolved scales if the grid is sufficiently fine to resolve the anisotropy in the velocity field. At coarse resolutions, by the attribute of its isotropic formulation and the anisotropy of the SGS the model gives poor predictions [129]. In other words, the consequences listed above implies that isotropic SGS models cannot provide accurate and reliable predictions unless those anisotropic scales are resolved by the grid, which involves considerably computational cost.

More complex subgrid-scale models have been developed to improve the prediction of the modeled $\boldsymbol{\tau}$ and resolve the SGS anisotropy and are presented in Sec. 1.3.5. A new nonlinear model introduced in the Sec. 2.4 is developed and tested and is the subject of investigation in the present thesis.

1.3.3 The Smagorinsky turbulence model

The Smagorinsky model or eddy viscosity model (EVM) is often used to model the deviatoric part of the SGS stress tensor. It is expressed as

$$\tau_{ij}^{M} - \frac{1}{3}\tau_{kk}^{M}\delta_{ij} = -2\nu_{SGS}\widetilde{S}_{ij}, \tag{1.16}$$

where τ_{ij}^{M} are the components of the modeled subgrid-scale tensor, the superscript M stands for "modeled", ν_{SGS} is the turbulent eddy viscosity and $\widetilde{S}_{ij}$ are the components of the filtered rate-of-strain tensor, given, respectively, by

$$\nu_{SGS} = (C_S\Delta)^2\left|\widetilde{\boldsymbol{S}}\right|, \tag{1.17}$$

and

$$\widetilde{S}_{ij} = \frac{1}{2}\left(\frac{\partial\widetilde{u_i}}{\partial x_j} + \frac{\partial\widetilde{u_j}}{\partial x_i}\right), \tag{1.18}$$

$\left|\widetilde{\boldsymbol{S}}\right|$ is the rate-of-strain magnitude (e.g. the square root of its second invariant), C_S is the model coefficient and Δ is the grid scale, generally given by $(\Delta x_1\Delta x_2\Delta x_3)^{1/3}$, where Δx_i is the grid spacing in the i-direction. The EVM is an adaptation of the corresponding Boussinesq hypothesis for RANS.

The Smagorinsky model is also based on the equilibrium hypothesis, which, according to Blazek [16], suggests that the small scales dissipate completely and instantaneously all the energy they receive from the large scale:

$$-\tau_{ij}\bar{S}_{ij} = \varepsilon_v. \tag{1.19}$$

1.3.4 Germano identity and the dynamic procedure

Since the need for a constant coefficient in Smagorinsk model gives rise to a poor prediction of statistics in some turbulent flows simulation, an important development in LES modelling was the introduction of the dynamic procedure proposed by Germano et al. [51]. The dynamic methodology allowed the calculation of the Smagorinsky coefficient during the simulations rather than an *a priori* solution and gives a correct asymptotic close-to-wall behavior of the computed eddy viscosity. The Germano identity that is utilized in the dynamic procedure is largely applied in different domains of LES, see Meneveau [105].

In a dynamic eddy viscosity model, two filter operators are defined to obtain the large-scale quantities. One is the grid filter $\widetilde{G}(\ )$, the other one is the test filter $\widehat{G}$ with a filter width larger than $\widetilde{G}(\ )$, let $\widehat{\widetilde{G}} = \widetilde{G}\widehat{G}$. Applying the filters $\widetilde{G}(\ )$ and $\widehat{\widetilde{G}}$ to the

incompressible Navier-Stokes equations one obtains subgrid and subtest stresses:

$$\tau_{ij} = \widetilde{u_i u_j} - \widetilde{u}_i \widetilde{u}_j, \tag{1.20}$$

$$T_{ij} = \widehat{\widetilde{u_i u_j}} - \widehat{\widetilde{u}}_i \widehat{\widetilde{u}}_j. \tag{1.21}$$

The resolved stress is defined as

$$\mathcal{L}_{ij} = \widehat{\widetilde{u_i}\widetilde{u_j}} - \widehat{\widetilde{u}}_i \widehat{\widetilde{u}}_j. \tag{1.22}$$

As shown by Germano et al. [51], T_{ij}, τ_{ij}, $\mathcal{L}_{ij}$ are related by

$$\mathcal{L}_{ij} = T_{ij} - \widehat{\tau}_{ij}. \tag{1.23}$$

The tensor $\mathcal{L}_{ij}$ is called “the resolved stress tensor" (or Leonard stress) and $\boldsymbol{T}$ corresponds to the $\boldsymbol{\tau}$ arising at a scale that corresponds to the combined hat and tilde filters. This relationship is correct and holds at each point in the flow and at every time, for all tensor components.

Since the Smagorinsky model is invariant to the filtering process, both subgrid-scale stress and subtest-scale stress are expressed in the Smagorinsky model as

$$\tau_{ij}^M - \frac{1}{3}\delta_{ij}\tau_{kk}^M = -2c^2\widetilde{\Delta}^2 \left|\widetilde{\mathbf{S}}\right| \widetilde{S}_{ij}, \tag{1.24}$$

$$T_{ij}^M - \frac{1}{3}\delta_{ij}T_{kk}^M = -2c^2\widehat{\Delta}^2 \left|\widehat{\widetilde{\mathbf{S}}}\right| \widehat{\widetilde{S}}_{ij}, \tag{1.25}$$

where $\widetilde{\Delta}$ and $\widehat{\Delta}$ are the filter widths associated with $\widetilde{G}(\ )$ and $\widehat{\widetilde{G}}$ respectively. In Eqs. 1.24 and 1.25, c is locally invariant to the filtering process. By substituting Eqs. 1.24 and 1.25 into Eq. 1.23 and assuming c is constant in the test filter, one obtains:

$$\mathcal{L}_{ij}^* = c^2 M_{ij}, \tag{1.26}$$

where

$$M_{ij} = -2\left(\widehat{\Delta}^2 \left|\widehat{\widetilde{\mathbf{S}}}\right| \widehat{\widetilde{S}}_{ij} - \widetilde{\Delta}^2 \widetilde{\left|\widetilde{\mathbf{S}}\right| \widetilde{S}_{ij}}\right). \tag{1.27}$$

and $\mathcal{L}_{ij}^*$ is the deviatoric part of the Leonard tensor, given by:

$$\mathcal{L}_{ij}^* = \mathcal{L}_{ij} - \frac{1}{3}\delta_{ij}\mathcal{L}_{kk} \tag{1.28}$$

Equation 1.26 is used to determine the coefficient c dynamically. In order to avoid possible divisions by zero, Lilly [93] proposed a least-squares approach to minimize the

error locally, from this approach c is calculated by:

$$c^2 = \frac{\left\langle \mathcal{L}^*_{ij} M_{ij} \right\rangle}{\left\langle M_{ij} M_{ij} \right\rangle}. \tag{1.29}$$

1.3.5 Nonlinear subgrid-scale stress models

Since Smagorinsky [141] proposed the turbulent viscosity model, the development of closure models to characterize the influence of the $\boldsymbol{\tau}$ has been a subject of intense research. The inconsistencies found in linear SGS models somehow imply that the Eq. 1.16 cannot correctly predict the individual SGS stresses in some flow situation, e.g. complex turbulent flows involving recirculations, turbulent jets, flows over curved surfaces or behind bluff bodies, wall-bounded flow, etc. Due to these inconsistencies (e.g. the fact that the SGS stress tensor is not aligned with the resolved rate-of-strain tensor and the poorly prediction of the SGS anisotropy), a significant number of more complex closure schemes have been proposed to improve the prediction of $\boldsymbol{\tau}$.

In the work of Cimarelli and De Angelis [27] it was shown how the modeling of subgrid stresses in large-eddy simulations can be improved from a physical insight on the energy transfer phenomenon in wall turbulent flows. In their work, a mixed subgrid-scale model was proposed where the backward energy transfer effects in near-wall region is captured for very large filter lengths.

Gualtieri et al. [55] performed an LES of homogeneous sheared turbulence (HST) using an approximate deconvolution method (rather than a functional model). They found that when the energy producing scales are well resolved and the lower-order statistics well captured, higher-order statistics did not exhibit significant deterioration in accuracy. Nevertheless, even in this case an enhanced knowledge of the detailed energetic spectral transfer could lead to further insights into reasons behind such surprising behavior.

The scale similarity model from Bardina et al. [11] has been proven to attain a high correlation with the real SGS stress (as high as 0.8). Other important nonlinear models that provided a better description of turbulent effects when compared to linear models can be found in the literature, as, for example, the nonlinear model proposed by Lund and Novikov [99], the dynamic nonlinear model of Wong [170], the simplified nonlinear SGS model of Kosovic [80], the dynamic nonlinear SGS model of Wang and Bergstrom [167], the explicit algebraic subgrid-scale stress model of Marstorp et al. [103] and the mixed models [175]. See also Bardina et al. [11], Cimarelli and De Angelis [27] and Zang, Street, and Koseff [175].

On the side of RANS equations, several nonlinear closure model were proposed, e.g. Rivlin [132], Lumley [98], Pope [126], Speziale [142], and Gatski and Speziale [48] and Thompson et al. [152]. The first attempt of using a nonlinear tensorial polynomial

closure model was made by Rivlin [132] for turbulent non-Newtonian flows.

1.4 Direct numerical simulation

1.4.1 General aspects

Direct numerical simulations (DNS) and experiments are extremely useful tools to understand turbulence. The increasing capacity of the new computers and clusters that act in parallel, together with new techniques and devices used to capture and determine statistical informations of turbulent flows are becoming responsible for important contributions that are expanding our comprehension of turbulence phenomenon. In addition, these approaches are useful to built closure turbulent models, what in turns enables us to solve practical engineering problems involving turbulent flows. Since these two tools are the most powerful methods to enlarge our knowledge in this field, a crucial aspect that needs to be addressed is how reliable are the results provided by DNS and experiments.

Due to the complexity of turbulence it is usual to employ statistical analysis in order to provide suitable quantities that can capture the physics of this kind of chaotic motion. The procedure proposed by Reynolds in his seminal paper Reynolds [130] that decomposes an instantaneous generic quantity, ϕ, into two additive parts: a mean, $\overline{\phi}$ and a fluctuating part, ϕ', has become a common practice in turbulence. A key concept is what is meant by *the mean of a quantity*. In the original paper, Reynolds [130] associates the mean quantity with an average “for a certain period of time" and he admits that “there still remains the question as to ....what intervals of time?". Needless to say, this procedure leads to the RANS equations and the conception of the Reynolds stress tensor. This entity is expected to be part of the set of outputs provided by DNS or experiment of turbulent flows. Since the Reynolds stress tensor is a statistical quantity, it seems natural to include this quantity on statistical error computation.

1.4.2 Statistical uncertainties and convergence in DNS

On the side of DNS, very few works are dedicated to discuss convergence criteria and uncertainties associated to the simulation. Recently, however, the works of Oliver et al. [118], Vreman and Kuerten [162], Thompson et al. [153], and Vinuesa et al. [159] were dedicated to the subject. The investigation conducted by Oliver et al. [118] is one of the first works that places the statistical convergence of DNS as a central concern. They analyze the problem from the perspective of the traditional approach of Richardson extrapolation and came to the conclusion that a modified approach should be used, since the traditional one is not able to address sampling errors. Vreman and Kuerten

[162] compared DNS databases to assess the accuracy and reproducibility of turbulence statistics of incompressible plane channel flow, they used relative deviations of mean profile of different cases in relation to the case that has probably a much lower statistical error, according to them. In Thompson et al. [153], the balance of the mean momentum equation (BMME) is integrated to obtain the balance of mean forces (BMFE) that is used to construct two kinds of statistical residual errors associated to plane channel flows: the residual error associated to shear Reynolds stress component and the residual error associated to mean streamwise velocity. The description given next shows that these two quantities can be seen as dual ones. Each residual error is defined as the difference between a calculated quantity and the same quantity provided by the DNS data. The calculated quantity is obtained from the BMFE by considering the DNS data of the dual quantity. One important conclusion is that a great number of databases available in the literature exhibit quite low errors associated to the Reynolds shear stress R_{yx}, but quite large mean velocity errors. In other words, the mean velocity calculated from the BMFE, $\tilde{U}$, considering the shear Reynolds stress component provided by the DNS data, $\hat{R}_{yx}$ can be significantly discrepant from the mean velocity associated to the DNS data, $\hat{U}$.

A noticeable exception is the high-resolution direct numerical simulation (HR-DNS) methodology employed by Vreman and Kuerten [162, 163], whose data led to small corresponding residual errors. In a similar approach, Vinuesa et al. [159] established a convergence indicator based on the root mean square (RMS) norm of the deviation between the total shear stress and a linear profile for turbulent channel and duct flows. They evaluated the residual error of several databases available in literature and studied the influence of the time for which the statistics begins to be computed and the averaging times necessary to obtain sufficiently converged statistics. The averaging time stands for the time interval in which the statistics are taken starting from a fully developed turbulent field. An interesting rationale developed by Vinuesa et al. [159] is to consider the computational box size to correct the *eddy turnover time*, what seems to be important to make a fair comparison among different databases. It is worth noticing that Vineusa et al. (2016) have used the integrated form (BMFE) for the analysis of channel flows while the original form (BMME) was used to analyze duct flows.

Despite the particularities of these papers, they share the common impression that convergence criteria and uncertainties in the measurements need further investigation and, therefore, it would be of interest to the turbulence community if more attention was dedicated to this matter.

Another factor affecting the quality of the statistics is the averaging time used to compute them. This interval is frequently chosen to be large enough to ensure a certain level of accuracy for the measured variable. As far as the averaging time is concerned, the ergodic hypothesis is usually assumed. Therefore, a technique which is widely used is an estimate based on the concept of *integral scale* [50, 127, 145], which is a measure of

the time necessary for a variable to become uncorrelated with itself. The averaging time is usually presented in terms of convective time scales [77, 119] or large eddy turnover time [137]. According to Antonia, Satyaprakash, and Hussain [5], the averaging time has been shown to vary not only with the variable itself, but also with some parameters of the flow (e.g., the Reynolds number or the distance from the wall) and with the statistical moment desired (average, variance, skewness, kurtosis, etc.).

It is important to note that there is no consensus with respect to the averaging time, even for the same geometry. In fact, they can vary by one order of magnitude. In this regard, a different dimensionless averaging time $2TU_c/d$ (where T is the averaging time, U_c is the centerline velocity, and d is the channel gap or the pipe diameter) to obtain the turbulent statistics with respect to the turbulent flow can be found. For example, investigating turbulent channel flows, Blackwelder and Eckelmann [14] used $2TU_c/d = 3440$ for $Re_h = 3850$, while Kastrinakis and Eckelmann [72] used $2TU_c/d = 2670$ for $Re_h = 12\ 000$, where Re_h is the Reynolds number based on the channel half-gap, h. In the case of turbulent pipe flows, Hogenes and Hanratty [60] used $2TU_c/d = 540$ at $Re_h = 18\ 040$. More recently, Kim and Adrian [76] and Monty [116] studied the fully developed turbulent pipe flow over a range of Reynolds numbers.

1.5 Objective

The numerical computation of turbulent flow of Newtonian fluids is still a field in which numerous questions remain open due to the complexity of this phenomenon. Among the open questions, in the present work, we shall address important question concerning turbulent flows and simulation.

In the classical prediction of Kolmogorov [78], at a sufficiently large Reynolds number, every turbulent flow is expected to approach a universal state at small scales [115, 102]. In order to analyze this effect, in the present work it is shown the behavior of the energy transfer variation for a higher Reynolds number. The influence of the Reynolds number in the turbulent kinetic energy (TKE) is evaluated by examining in detail how the energy is transferred through the wavenumber domain and the exchange of energy in physical spatial domain.

A characterizing feature of previous studies (Marati, Cimarelli and Mollicone) is the utilization of the structure function partitioning originally exploited by Kolmogorov [78] and recently formalized and generalized by Hill [58, 59]. These structure function are closely linked to the two-point correlation function in physical space. In the more general inhomogeneous case, account must be taken of the separation distance between two points as well as the location in the flow field itself (in the homogeneous case only separation distance is needed). In the study reported here, the analysis is restricted to a single-point formulation in physical space coupled with a spectral representation of the

instantaneous turbulent flow field. Within this context, the turbulent flow is assumed partitioned into locally homogeneous turbulence in planes parallel to the bounding channel walls with effects of inhomogeneous mean shear dependent on distance from the channel walls. Such an approach attempts to simplify a generally complex system of energetic dynamics into a within-plane and an out-of-plane energy exchange system.

In this context, the present thesis analyzes the energy flux in the complete physical space and spectral domain, allowing the direct correlation between different wall-parallel planes, and helps to unveil new important details of the energy transfer processes. We aim to enrich this study with further analysis of the influence of the turbulent Reynolds number, helping to provide more insight into the physics of turbulent Newtonian fluid flows. The effect of the Reynolds number on the turbulent kinetic energy (TKE) transfer of Newtonian fluids at $Re_\tau = 180$ and $Re_\tau = 1000$ by means of the Fourier transform was never done before and is evaluated in detail in the present work. Various energy fluxes were analyzed for wall bounded turbulence due to both spectral and spatial energy variations.

Direct numerical simulation is of great importance to analyze the phenomenon of turbulence in fluids. In this way, ensuring the quality of its statistical data is an unpredictable task for any numerical analysis involving this type of simulation. In the case of a plane channel, or a pipe, it is clear the interest for solving the fully developed, statistically steady case. The statistically steady state generally requires a long elapsed time in order to take an average that will not vary if a different interval of the same amount is used. Assuming statistically steady-state and fully developed flow, the BMME takes a simplified form and only the shear Reynolds stress component associated to the turbulent flow is accounted for in the equation. Therefore, its integration is simple.

Here, we significantly extend the prior study conducted in Thompson et al. [153] by creating a novel database at $Re_\tau = 180$ and 590 to characterize and estimate the convergence of uncertainties with respect to the averaging time and to evaluate the unbalance of mean forces in turbulent wall-bounded flows depending on Reynolds number and distance from the wall. The main objective of the present thesis is to evaluate the convergence rate of uncertainties of turbulent plane channel and pipe flow and to apply a novel tool to check it quantitatively for both DNS and experimental studies. Highly converged turbulent quantities are provided in the present work. The convergence rate is also evaluated for the turbulence kinetic energy (TKE) and the enstrophy at several averaging time with respect to a previous averaged field.

By understanding the physics of turbulent flow through the analysis of the source terms of the turbulent kinetic energy balance equation and by guaranteeing the quality of the data obtained by means of direct numerical simulation in a turbulent flat channel, we are able to move forward to the evaluation of the performance of a new subgrid-scale model for the large eddy simulations based on a set of objective tensors. This approach

incorporates more physics, by given a higher number of degrees of freedom to the SGS model, but is computationally more expensive and complicated than the simpler approaches. The proposed models seek to capture the anisotropy of the turbulence phenomenon by applying a closure model that showed good correlations when tested in previous work, employing RANS modeling [152]. In this way, the main objective of this thesis work is to utilize this modeling approach also for large eddy simulations by means of *a priori* and *a posteriori* tests.

Not long after the firsts works on LES, simulations employing different subgrid-scales models, experimental data and DNS results sets have been extensively employed to test SGS models. The use of noble data source to test LES modeling was introduced by Piomelli et al. [122] and was called as "*a priori* test". In the literature, many authors applied the *a priori* test in several situations, e.g. DNS tests with data from low-to-moderate Reynolds number of isotropic turbulence, turbulent channel flow or mixing layer simulations, see Clark et al. [29], Bardina et al. [11], Piomelli et al. [124], Domaradzki et al. [40], Härtel et al. [57], Salvetti and Banerjee [134], Salvetti and Beux [135], Lu, Rutland, and Smith [97], Jordan [69], Vreman, Geurts, and Kuerten [164], Labourasse et al. [85], and Keating et al. [73] and De Stefano et al. [34].

In this context, by means of the use of DNS data sets to test SGS models, the so-called *a priori* test [122], and by employing the proposed nonlinear SGS model for wall bounded turbulent flow simulations by means of the *a posteriori* test, the present work proposes, analyzes and evaluates a novel nonlinear subgrid-scale closure model based on the filtered field of the rate-of-strain and the non-persistence-of-straining tensor, a set of objective tensors. The modeled SGS stress $\boldsymbol{\tau}^M$ must be evaluated based solely on the velocity field, $\widetilde{u_i}$, sampled on the coarse grid (of mesh size $\widetilde{\Delta}$) used in the filtering process. Due to this fact, firstly is needed to separate the velocity field into resolved and SGS components by calculating $\widetilde{u_i}$ and $\widetilde{u_i u_j}$ where the tilde $\widetilde{()}$ is a filter at scale $\widetilde{\Delta}$.

In short, this work presents an analysis of the effects of the SGS component. We present the development of a nonlinear SGS model and demonstrate its performance in wall bounded turbulent cases. The nonlinear SGS model represents an attempt to address both the effects of anisotropy due to the shear and the role of backscatter of energy in under-resolved flow regions.

Chapter 2

Methodology

2.1 Applied algorithms

In the present work, several cases using the LES and DNS methodology were simulated in order to establish the validations and comparisons accomplished. However, the simulations employed in these two forms of turbulence modeling were performed by using two different codes, in this section we provide the description of both algorithms. For DNS, the turbulent plane channel flow case was simulated. For LES, a lid-driven cubic cavity flow and a backward step simulation flow were considered in the analysis.

2.1.1 The direct numerical simulation cases

Here we present the characteristics of the code used to calculate all direct numerical simulation cases. This algorithm is called “NNEWT". New direct numerical simulations were conducted to provide the data used for the spectral analysis. The Navier-Stokes equations for a divergent-free velocity field were solved on an hybrid spatial scheme that includes Fourier spectral accuracy in two directions (x and z) and sixth-order compact finite differences for first and second-order wall-normal derivatives (y). Spatial averaging is taken in the two homogeneous channel direction (x, z) and an initial turbulent field was used as initial condition.

The time steps used were $10^{-3}s$ and $7.5 \times 10^{-4}s$ for $Re_\tau = 180$ and 590, respectively, which give a mean Courant-Friedrichs-Lewy (CFL) factor of 0.064 for the $Re_\tau = 180$ case and 0.199 at $Re_\tau = 590$. The simulations were initiated from a fully turbulent field that come from previous simulations. In this way, the flow is already turbulent from the beginning of the calculation. In any case the averaging starts after a simulation time of 10 s, so we guarantee that only the fully turbulent regime is being taken into account. The full description of the employed algorithm can be found in Thais et al. [148].

In the present work, the direct numerical simulation of fully developed turbulent flow is analyzed at $Re_\tau = 180$, 590 and 1000, where Re_τ is the friction Reynolds number,

based on the friction velocity, $u_\tau \equiv \sqrt{\tau_w/\rho}$, ρ is the specific mass, τ_w is the wall shear stress and the channel half-gap, h, and is defined as

$$Re_\tau = \frac{\rho u_\tau h}{\mu}\,, \tag{2.1}$$

The database parameters of the numerical simulations for the different Reynolds numbers are given by Tab. 2.1. The presented parameters are: Reynolds number, domain size, number of grid points and mesh resolution.

Re_τ	$L_1/h \times L_3/h$	$N_{x_1} \times N_{x_2} \times N_{x_3}$	$\delta {x_1}^+$	$\delta {x_2}^+_{max}$, $\delta {x_2}^+_w$	$\delta {x_3}^+$
590	$8\pi \times 3\pi/2$	$512 \times 129 \times 128$	8.80	7.10, 0.200	6.60
180	$8\pi \times 3\pi/2$	$512 \times 129 \times 128$	8.80	7.10, 0.200	6.60
1000	$6\pi \times 3\pi/2$	$1536 \times 513 \times 768$	12.30	8.40, 0.500	6.10

Table 2.1 – Overview of DNS databases.

2.1.2 The large eddy simulation cases

In this section, the numerical characteristics of the code used to analyze the nonlinear SGS models are presented. In the present thesis, this in-house developed code is referred as “AMR3D". In general terms, the numerical method chosen for solving the momentum and Poisson equations for pressure correction is based on a three-dimensional, staggered, finite-volume discretization. The central difference scheme (CDS) is applied to express the diffusive contributions of the transport equations. For the advective terms, the discretization was done through the convergent and universally bounded interpolation scheme for the treatment of advection (CUBISTA) method [2]. The Fraction Step method, proposed by Chorin [25], is used. This method is composed by two steps: a predictor, where velocity is estimated, and a corrector, where velocity is corrected based on the pressure increment. Regarding time integration, the Semi-Backward Difference temporal time discretization is chosen in all cases, with a variable size of time step.

Space is discretized using the structured adaptive mesh refinement, which is based on the hierarchical grid structure proposed by Berger and Colella [12]. In this scheme, regions of the flow bearing special interest are covered by block-structured grids, defined as a hierarchical sequence of nested, progressively finer levels (composite grids). Each level is formed by a set of disjoint rectangular grids and the refinement ratio between two successive refinement levels are constant and equal to two. Ghost cells are employed around each grid, for all the levels, and underneath fine grid patches to formally prevent the finite difference operators from being redefined at grid borders and at interior regions which are covered by finer levels. Values defined in these cells

are obtained from interpolation schemes, usually with second or third order accuracy, and not from solving the equations of the problem. A staggered composite grid is used. The discretizations of the Laplacian, gradient and divergence differential operators are performed by standard, cell-centered second order stencils. Multilevel-multigrid methods are employed to solve for both the provisional vector field and the pressure increment.

The presence of the solid body in the fluid flow is considered by using the immersed boundary method. In this method, there is a momentum source term in the Navier-Stokes equations that accounts for the presence of the rigid body. The source term is evaluated by direct forcing methodology, proposed by Uhlmann [156]. The main characteristic of this method is that it is not necessary to use *ad-hoc* constants and it allows for the non-slip condition modeling along the immersed interface.

2.2 A new parameter to analyze the statistical data in turbulent flows

In this section we present the theoretical development of a new parameter to analyze the statistical uncertainties and convergence for turbulent plane channel flows. Following Pope [127], in steady-state fully-developed channel flow, the axial mean-momentum equation is given by

$$0 = \nu \frac{d^2U}{dy^2} - \frac{d}{dy}(\overline{u_x' u_y'}) - \frac{1}{\rho}\frac{\partial P}{\partial x}, \tag{2.2}$$

where U is the mean velocity in the streamwise x-direction, y is the normal-wall direction, $\overline{p}$ is the mean pressure, and u_x' and u_y' are the fluctuating parts of the velocity in the x and y directions, respectively. By assuming the pressure gradient to be uniform across the flow, from the lateral mean-momentum equation the total shear stress τ can be related to the mean pressure gradient as

$$\frac{d\tau}{dy} = \frac{dP}{dx}. \tag{2.3}$$

It is also known that τ is constrained by the boundary conditions $\tau = \tau_w$ at the wall ($y = 0$ or $r = R$) and $\tau = 0$ at the center of the geometry ($y = h$ or $r = 0$). Then, from Eqs. 2.2 and 2.3, τ is given by a linear function of the wall distance y or the pipe radius r and can be split into the sum of the molecular shear stress and the Reynolds shear stress $R_{xy} = -\overline{u_x' u_y'}$, hence,

$$\tau = \left(1 - \frac{y}{h}\right)\tau_w = \rho\nu\frac{dU}{dy} + \rho R_{yx}. \tag{2.4}$$

For the sake of simplification, we can consider the change of variables $r = R - y$ and $R = h$ and apply Eq. (2.4) to both turbulent channel and pipe flows.

Using $u_\tau = \sqrt{\tau_w/\rho}$ as the characteristic velocity and $\delta_\nu = \nu/u_\tau$ as the characteristic length, we can rewrite Eq. (2.4) as

$$\left(1 - \frac{y^+}{Re_\tau}\right) = \frac{dU^+}{dy^+}(y^+) + R^+_{yx}(y^+), \tag{2.5}$$

where the variables with a superscript + are expressed in wall units.

The two most obvious statistics provided in a plane channel and pipe flow experiments and DNS are the mean velocity field and the Reynolds stress tensor associated to the fully developed steady state. They are both determined by a hybrid averaging process: averaging is performed spatially in normal-to-wall plane slabs and in time, using as many flow snapshots as available. Therefore, both are subjected to discretization and sampling errors. In the case of numerical calculations, experience shows that the Reynolds shear stress, being a second-order statistical quantity, is much more difficult to achieve a converged value.

Here, we employ the method proposed by Thompson et al. [153], where Eq. (2.5) is used as a way to discuss the consequences of the numerical imbalance of the mean forces. We employ the symbol $\widehat{(\,)}$ to label any variable that is provided by the DNS or experimental hybrid space-time average. The symbol $\widetilde{(\,)}$ is used to label a variable that is computed from BMFE, such as Eq. (2.5). With this convention, we can write the following two equations:

$$\widetilde{R}^+_{yx}(y^+) = 1 - \frac{y^+}{Re_\tau} - \frac{d\widehat{U}^+}{dy^+}(y^+), \tag{2.6}$$

$$\widetilde{U}^+(y^+) = y^+ - \frac{{y^+}^2}{2Re_\tau} - \int_0^{y^+} \widehat{R}^+_{yx}(y')\,dy'. \tag{2.7}$$

Equation 2.6 expresses the yx-component of the Reynolds stress tensor that balances the mean forces equation in the x-direction using the axial mean velocity gradient provided by the input data. On the other hand, Eq. (2.7) expresses the mean velocity profile that would balance the mean forces equation using the yx-component of the Reynolds stress tensor available from the input data.

Equations 2.6 and 2.7 can be used to define two residual errors: $E_R(y^+) = \widetilde{R}^+_{yx}(y^+) - \widehat{R}^+_{yx}(y^+)$ and $E_U(y^+) = \widetilde{U}^+(y^+) - \widehat{U}^+(y^+)$. Using Eq. (2.6), $E_R(y^+)$ can be written as

$$E_R(y^+) = 1 - \frac{y^+}{Re_\tau} - \frac{d\widehat{U}^+}{dy^+}(y^+) - \widehat{R}^+_{yx}(y^+), \tag{2.8}$$

and can be interpreted as the residual of the balance of mean forces with respect to the

steady state fully developed channel flow. To guarantee a steady state fully developed flow, $E_R(y^+)$ computed from input data ought to be as small as possible across the channel width.

Using Eq. (2.7), the second residual error $E_U(y^+)$ can be written as

$$E_U(y^+) = \int_0^{y^+} E_R(y')\,dy', \tag{2.9}$$

i.e., $E_U(y^+)$ originates from the cumulative error estimate associated with the residual of the mean forces equation. Hence, introducing the mean residual error given by Eq. (2.10), we can rewrite Eq. (2.9) as Eq. (2.11).

$$\langle E_R\rangle(y^+) = (1/y^+)\int_0^{y^+} E_R(y')dy', \tag{2.10}$$

$$E_U(y^+) = y^+\left[\langle E_R\rangle(y^+)\right]. \tag{2.11}$$

The residual criteria E_U and E_R can also be seen as estimates of mean forces unbalances in the turbulent flow. Since they are based on physical parameters exclusively, comparisons between numerical and experimental results can be established.

To characterize the convergence of input statistics depending on the averaging time, a residual criterion, based on the RMS norm, independent of y^+ and varying with the non-dimensional averaging time (T^*), is considered. This last parameter was defined by Vinuesa et al. [159] as

$$T^* = \frac{T u_\tau}{h}\left(\frac{L_x L_z}{L_{x,min} L_{z,min}}\right), \tag{2.12}$$

where T is the averaging time, L_x and L_z are, respectively, the streamwise and spanwise box lengths, and $L_{x,min}= 6h$ and $L_{z,min}= 3h$ define the domain size containing the minimal flow unit in the logarithmic layer.

In the present thesis, the norms applied ($\|E_R\|$ and $\|E_U\|$) are given by Eqs. 2.13 and 2.14.

$$\|E_R\|(T^*) = \sqrt{\frac{1}{Re_\tau}\int_0^{Re_\tau}\left[E_R(y', T^*)\right]^2 dy'}, \tag{2.13}$$

$$\|E_U\|(T^*) = \sqrt{\frac{1}{Re_\tau}\int_0^{Re_\tau}\left[E_U(y', T^*)\right]^2 dy'}. \tag{2.14}$$

To ensure a statistically converged field, the residual errors $\|E_R\|$ and $\|E_U\|$ must asymptotically decay to zero with advancement of the averaging time and as converged state is approached.

In the present work, data at several averaging times for $Re_\tau = 180$ and 590 are generated and presented in Sec. 3.1.2. Details about the simulation parameters of the generated DNS for present study are presented in Tables A.2, A.3, A.7, and A.8. In this range, the behavior of the criterion given by Eqs. 2.8, 2.9, 2.13 and 2.14 is evaluated depending on space and time. Beyond this value ($Re_\tau > 590$), only spatial analyses are performed, and a comparison between the numerical results from DNS and the experimental results is established. The temporal evaluation of the residuals E_U and E_R is made for several values of T^*, which continuously increases throughout the simulation performed by applying high-order spatial discretization schemes.

2.3 Evaluation of spectral budget in DNS data of turbulent channel flow

Here we present the theoretical methodology developed to evaluate the spectral energy cascade in a turbulent plane channel flow in a hybrid space/spectral domain.

2.3.1 Momentum and turbulent energy equations

A fully developed channel flow of a Newtonian fluid is analyzed. The components of the total velocity, u_i, are given by $u_i = \overline{u}_i + u_i'$, where $\overline{u}_i$ and u_i' are the mean and fluctuating velocities, respectively. The pressure, p, field is given by $p = \overline{p} + p'$, similar to the velocity decomposition, $\overline{p}$ and p' are the mean and the fluctuating pressure fields, respectively. The fluctuation continuity and momentum equations are given by:

$$\frac{\partial u_j'}{\partial x_j} = 0 \,, \tag{2.15}$$

$$\frac{\partial u_i'}{\partial t} + u_j' \frac{\partial u_i'}{\partial x_j} + \overline{u}_j \frac{\partial u_i'}{\partial x_j} + u_j' \frac{\partial \overline{u}_i}{\partial x_j} = -\frac{\partial p'}{\partial x_i} + 2\nu \frac{\partial s_{ij}'}{\partial x_j} \,, \tag{2.16}$$

with $\partial p'/\partial x$ the nonzero streamwise pressure gradient driving the turbulent flow and s_{ij}' the components of the fluctuating rate-of-strain tensor.

2.3.2 Momentum equation in Fourier space

For a fully developed channel flow, a two-dimensional spatial Fourier transform pair is needed and defined here by:

$$\hat{u}_i(k_1, k_2, x_2, t) = \frac{1}{(2\pi)^3} \int e^{\imath(k_1 x_1 + k_3 x_3)} u_i'(x_1, x_2, x_3, t)\, \mathrm{d}x_1 \mathrm{d}x_3 \,, \tag{2.17}$$

$$u_i'(x_1,x_2,x_3,t) = \int e^{-\imath(k_1x_1+k_3x_3)}\hat{u}_i(k_1,k_2,x_2,t)\,\mathrm{d}k_1\mathrm{d}k_3\,, \tag{2.18}$$

where $\hat{u}_i$ are the velocity components in Fourier domain, the wavevector components are $k_i = 2\pi/\lambda_i$ with λ_i the wavelength components and $\imath$ is the imaginary unit. The transformed continuity equation is:

$$-\imath k_1\hat{u}_1 + \frac{\partial\hat{u}_2}{\partial x_2} - \imath k_3\hat{u}_3 = 0\,. \tag{2.19}$$

The transformed momentum equations are:

$$\begin{aligned}\partial_t\hat{u}_1 + \nu\kappa^2\hat{u}_1 - \nu\frac{\partial^2\hat{u}_1}{\partial x_2^2} =& \imath k_1\hat{p} + \imath k_1\hat{u}_1\overline{u}_1 - \hat{u}_2\frac{\partial\overline{u}_1}{\partial x_2}\\ &+ \imath k_1\hat{u}_1\star\hat{u}_1 + \imath k_3\hat{u}_3\star\hat{u}_1 - \frac{\partial(\hat{u}_2\star\hat{u}_1)}{\partial x_2}\,,\end{aligned} \tag{2.20}$$

$$\begin{aligned}\partial_t\hat{u}_2 + \nu\kappa^2\hat{u}_2 - \nu\frac{\partial^2\hat{u}_2}{\partial x_2^2} =& -\frac{\partial\hat{p}}{\partial x_2} + \imath k_1\hat{u}_2\overline{u}_1 + \imath k_j\hat{u}_j\star\hat{u}_2\\ &+ \imath k_1\hat{u}_1\star\hat{u}_2 + \imath k_3\hat{u}_3\star\hat{u}_2 - \frac{\partial(\hat{u}_2\star\hat{u}_2)}{\partial x_2}\,,\end{aligned} \tag{2.21}$$

$$\begin{aligned}\partial_t\hat{u}_3 + \nu\kappa^2\hat{u}_3 - \nu\frac{\partial^2\hat{u}_3}{\partial x_2^2} =& \imath k_3\hat{p} + \imath k_1\hat{u}_3\overline{u}_1 + \imath k_j\hat{u}_j\star\hat{u}_3\\ &+ \imath k_1\hat{u}_1\star\hat{u}_3 + \imath k_3\hat{u}_3\star\hat{u}_3 - \frac{\partial(\hat{u}_2\star\hat{u}_3)}{\partial x_2}\,,\end{aligned} \tag{2.22}$$

where $\kappa^2 = k_1^2 + k_3^2$ and $\star$ denotes the convolution operation It is worth noticing that the above equations were developed for a turbulent plane channel flow. Therefore the periodicity condition required for the Fourier transform is true only in the x_1 and x_3 directions. In this way, the derivative terms in the x_2 direction remain in the physical domain.

2.3.3 Turbulent kinetic energy budget in Fourier space

The spectrum tensor components $\mathbf{\Phi}_{ij}$ can be written as

$$\delta(\mathbf{k}-\mathbf{k}')\mathbf{\Phi}_{ij}(\mathbf{k}) = \frac{1}{2}\left[\overline{\hat{u}_i(\mathbf{k})\hat{u}_j^*(\mathbf{k}')} + \overline{\hat{u}_i^*(\mathbf{k})\hat{u}_j(\mathbf{k}')}\right] = \mathcal{R}e\left[\overline{\hat{u}_i(\mathbf{k})\hat{u}_j^*(\mathbf{k}')}\right]\,, \tag{2.23}$$

with the two wavenumbers vectors $\mathbf{k} = (k_1, k_3)$ and $\mathbf{k}' = (k_1', k_3')$, $\hat{u}_i^*$ is the velocity complex conjugate. The Dirac function is given by $\delta(\,)$ and $\mathcal{R}e[\,]$ represents the real part of a complex number. The trace of $\delta(\mathbf{k}-\mathbf{k}')\mathbf{\Phi}_{ij}(\mathbf{k})$ is given by

$$\delta(\mathbf{k}-\mathbf{k}')\mathbf{\Phi}_{ii}(\mathbf{k}) = \overline{\hat{u}_i(\mathbf{k})\hat{u}_i^*(\mathbf{k}')} = \mathcal{R}e\left[\overline{\hat{u}_i(\mathbf{k})\hat{u}_i^*(\mathbf{k}')}\right]\,. \tag{2.24}$$

The turbulent kinetic energy is obtained by multiplying the momentum equations (Eqs. 2.20, 2.21 and 2.22) by their respective complex conjugate, $\hat{u}_i^*$, adding the result to its complex conjugate and then averaging. Introduction of $\delta(\mathbf{k}-\mathbf{k}')\mathbf{\Phi}_{ii}(\mathbf{k})$ from Eq. 2.24 results each term being infinite due to the delta-function. This can be removed integrating over $\mathbf{k}'$. The integrate sum of the momentum equations in spectral domain can be decomposed into seven main mechanisms, yielding:

$$\frac{\partial E(\kappa,x_2)}{\partial t} = \mathcal{P} - \varepsilon_{in} - \varepsilon_{out} + \mathcal{T}_{in} + \mathcal{T}_{out} + \mathcal{D}_\nu + \mathcal{D}_p \,, \tag{2.25}$$

where E is the turbulent kinetic energy spectral density, $\mathcal{P}$ is the turbulent production by mean shear (shear turbulent production), ε_{in} is the in-plane turbulent energy dissipation rate, ε_{out} is the inter-plane turbulent energy dissipation rate, $\mathcal{T}_{in}$ is the in-plane turbulent transport by the velocity fluctuation, $\mathcal{T}_{out}$ the inter-plane turbulent transport, $\mathcal{D}_\nu$ is the viscous diffusion, $\mathcal{D}_p$ is the diffusion by pressure fluctuations and the energy spectral density is given by

$$E(\kappa,x_2) = \frac{1}{2}\int_0^{2\pi} \mathbf{\Phi}_{ii}(\kappa,x_2)d\kappa_\phi = \pi\mathbf{\Phi}_{ii}(\kappa,x_2)\kappa, \tag{2.26}$$

with polar coordinates used in the integral evaluation (κ,κ_ϕ). It follows that in the (k_1,k_3) spectral plane each budget term in Eq. 2.25 can be considered as only a function of $|\mathbf{k}|$ $(=\kappa)$ with $\kappa^2 = k_1^2 + k_3^2$. The seven terms on the right-hand side of Eq. 2.25 are functions only of $|\mathbf{k}|$ and x_2.

The nomenclature involved here is based on the work of Bolotnov et al. [17], where the terms with derivatives in the wall-normal direction $(\partial/\partial x_2)$ are named inter-plane terms and are represented by the subscript 'out' that means 'out-of-plane'. The terms with derivatives in the homogeneous x_1-x_3 plane ($\partial/\partial x_1$ and $\partial/\partial x_3$) are named in-plane terms and are represented by the subscript 'in'.

The turbulent production is given by

$$\mathcal{P}(\mathbf{k},x_2) = -\frac{1}{2}\frac{\partial \overline{u}_1}{\partial x_2}\left[\overline{\hat{u}_1^*(\mathbf{k})\,\hat{u}_2(\mathbf{k})} + \overline{\hat{u}_1(\mathbf{k})\,\hat{u}_2^*(\mathbf{k})}\right]. \tag{2.27}$$

The in-plane turbulent energy dissipation rate is

$$\varepsilon_{in}(\mathbf{k},x_2) = 2\nu\kappa^2 E(\kappa,x_2)\,. \tag{2.28}$$

The inter-plane turbulent energy dissipation rate is given by

$$\varepsilon_{out}(\mathbf{k},x_2) = \nu\left[\overline{\frac{\partial\hat{u}_i^*(\mathbf{k})}{\partial x_2}\frac{\partial\hat{u}_i(\mathbf{k})}{\partial x_2}}\right]. \tag{2.29}$$

The in-plane turbulent transfer is

$$\begin{aligned}\mathcal{T}_{in}(\mathbf{k},x_2) = &\frac{\imath k_1}{2}\left\{\overline{\hat{u}_m^*(\mathbf{k})\left[\hat{u}_1 \star \hat{u}_m\right]|_{\mathbf{k}}} - \overline{\hat{u}_m(\mathbf{k})\left[\hat{u}_1^* \star \hat{u}_m^*\right]|_{\mathbf{k}}}\right\} \\ &+ \frac{\imath k_3}{2}\left\{\overline{\hat{u}_m^*(\mathbf{k})\left[\hat{u}_3 \star \hat{u}_m\right]|_{\mathbf{k}}} - \overline{\hat{u}_m(\mathbf{k})\left[\hat{u}_3^* \star \hat{u}_m^*\right]|_{\mathbf{k}}}\right\}\end{aligned}. \tag{2.30}$$

The inter-plane turbulent transfer is

$$\mathcal{T}_{out}(\mathbf{k},x_2) = -\frac{1}{2}\left\{\overline{\hat{u}_m^*(\mathbf{k})\frac{\partial}{\partial x_2}\left[\hat{u}_2 \star \hat{u}_m\right]|_{\mathbf{k}}} + \overline{\hat{u}_m(\mathbf{k})\frac{\partial}{\partial x_2}\left[\hat{u}_2^* \star \hat{u}_m^*\right]|_{\mathbf{k}}}\right\}. \tag{2.31}$$

The viscous diffusion term is given by

$$\mathcal{D}_\nu(\mathbf{k},x_2) = \nu\frac{\partial^2 E(\kappa,x_2)}{\partial x_2^2}\,. \tag{2.32}$$

The pressure diffusion is

$$\mathcal{D}_p(\mathbf{k},x_2) = -\frac{1}{2}\frac{\partial}{\partial x_2}\left[\overline{\hat{u}_2^*\hat{p}} + \overline{\hat{u}_2\hat{p}^*}\right]. \tag{2.33}$$

In this two-dimensional shear flow, there is a planar homogeneity introduced in both the streamwise and spanwise directions. For the spectral function, $\mathbf{\Phi}_{ii}(\mathbf{k},x_2)$, the integration over the circumference in spectral space is given by

$$K(x_2) = \frac{1}{2}\int_{|\mathbf{k}|=\kappa}\mathbf{\Phi}_{ii}(\mathbf{k},x_2)d\mathbf{k} = \int_\kappa E(\kappa,x_2)d\kappa, \tag{2.34}$$

where K is the turbulent kinetic energy.

In part of the Bolotnov et al. [17] analysis, the spectrum was partitioned into wavenumber bands that were organized into $m(=24)$ bins. In the current study $m = 28$, and Eq. 2.35 can be written as

$$K_m(x_2) = \pi\int_{\kappa_{m-1}}^{\kappa_m}\mathbf{\Phi}_{ii}(\kappa,x_2)\kappa d\kappa \simeq \pi\mathbf{\Phi}_{ii}(\overline{\kappa}_m,x_2)\overline{\kappa}_m\Delta\kappa_m, \tag{2.35}$$

where $\bar{\kappa}_m = 0.5(\kappa_{m-1}+\kappa_m)$ is an average wavenumber contained within bin-m, $\Delta\kappa_m = \kappa_m - \kappa_{m-1}$ is the spectral width of bin-m, and K_m is the turbulent kinetic energy contribution from the spectral band associated with bin-m.

By integrating Eq. 2.25 over κ, the transport equation for the TKE in physical space is obtained

$$\frac{DK(x_2)}{Dt} = -\overline{u_i'u_j'}\frac{\partial\overline{u}_i}{\partial x_j} - \nu\overline{\frac{\partial u_i'}{\partial x_j}\frac{\partial u_i'}{\partial x_j}} - \frac{1}{\rho}\frac{\partial\overline{u_i'p'}}{\partial x_i} - \frac{1}{2}\frac{\partial\overline{u_j'u_j'u_i'}}{\partial x_i} + \nu\frac{\partial^2 K}{\partial x_j^2}\,, \tag{2.36}$$

where the five terms on the right, depending only on x_2, are the usual terms representing, respectively, production by mean shear, total energy dissipation rate, pressure diffusion, total turbulent transport, and viscous diffusion.

The spectral results presented in the current thesis were normalized with two different procedures, which are termed global and local normalization [17]. The global normalization is a common normalization of all terms on the right-hand of Eq. 2.25 and is based on the fluid viscosity and friction velocity of the flow:

$$\theta^+(\kappa, x_2) = \left(\frac{\nu}{u_\tau^4}\right)\theta(\kappa, x_2)\,, \tag{2.37}$$

where θ is a generic variable and can assume any of the source terms functions. The globally normalized source terms are marked with superscript " + ". The non-dimensional turbulent kinetic energy spectral density, E^+, is defined as:

$$E^+ = E/(u_\tau \nu)\ . \tag{2.38}$$

The local normalization expresses the spectral shape of the source based on its magnitude. In this normalization the variable is integrated over the whole wavenumber range at each x_2 location, and is given by

$$\hat{\theta} \equiv \frac{\theta^+}{\theta^*}\,, \tag{2.39}$$

where θ is a generic variable and can assume any source term, θ^* is given by:

$$\theta^*(x_2) = \int_{\kappa^+} \left|\theta^+(\kappa^+, x_2)\right| d\kappa^+\,, \tag{2.40}$$

where $\kappa^+ = (\nu/u_\tau)\kappa$ is the dimensionless wavenumber scaled by wall coordinates. The dimensionless distance from the wall in wall units (y^+) is given by

$$y^+ = \frac{x_2 u_\tau}{\nu}. \tag{2.41}$$

Similarly to Eq. 2.35, the source terms can be integrated over wavenumber bands (bins) and are given by

$$\theta_m^+ = \int_{\kappa_{m-1}^+}^{\kappa_m^+} \theta^+(\kappa^+) d\kappa^+\ . \tag{2.42}$$

In the present work, we have focused on the spatial/spectral analysis at a selection of homogeneous planes. Statistical data depending on spatial and spectral domain at $Re_\tau = 180$ and 1000 are generated and presented in Sec. 3.2.

2.4 A novel nonlinear subgrid-scale model

In this section we develop the whole mathematical formulation of the new nonlinear SGS model here proposed. Based on the idea developed for the closure model of the RANS by Thompson et al. [152], the present approach expresses the anisotropic part of $\boldsymbol{\tau}$ for LES as a function of the resolved rate-of-strain tensor $\widetilde{\boldsymbol{S}}$ and the resolved non-persistence-of-straining tensor $\widetilde{\boldsymbol{P}}$, where $\widetilde{\boldsymbol{P}}$ is given by.

$$\widetilde{\boldsymbol{P}} = \widetilde{\boldsymbol{S}} \cdot \widetilde{\boldsymbol{W}}^* - \widetilde{\boldsymbol{W}}^* \cdot \widetilde{\boldsymbol{S}}, \tag{2.43}$$

which includes $\widetilde{\boldsymbol{S}}$, and the relative-rate-of-rotation tensor $\widetilde{\boldsymbol{W}}^*$, given by:

$$\widetilde{\boldsymbol{W}}^* = \widetilde{\boldsymbol{W}} - \widetilde{\boldsymbol{\Omega}}^S, \tag{2.44}$$

where $\widetilde{\boldsymbol{W}}$ is the skew-symmetric part of the mean velocity gradient (the mean vorticity tensor). The starred $\widetilde{\boldsymbol{W}}$ indicates that this tensor is computed relative to $\widetilde{\boldsymbol{\Omega}}^S$, the rate of rotation of the eigenvectors of $\widetilde{\boldsymbol{S}}$, defined by

$$\widetilde{\boldsymbol{\Omega}}^S = \dot{e}_k^S e_k^S, \tag{2.45}$$

where e_k^S are the normalized eigenvectors of $\widetilde{\boldsymbol{S}}$, and $\dot{e}_k^S$ are their time derivatives.

Then, in the presented approach, the modeled deviatoric part of the SGS stress tensor is expressed as:

$$\boldsymbol{\tau}^M = f\left(\widetilde{\boldsymbol{S}}, \widetilde{\boldsymbol{P}}, \Delta\right). \tag{2.46}$$

From Eq. 2.46, a general form of the tensorial function can be obtained. It consists of a tensor polynomial with six elements and its coefficients. The most general model was obtained by Thompson et al. [152] using the representation theorems and is given by:

$$\tau_{ij}^M - \frac{1}{3}\tau_{kk}^M \delta_{ij} = \sum_{k=1}^{6} \beta_k T_{ij}^{(k)}, \tag{2.47}$$

where $T_{ij}^{(k)}$ are given by:

$$\begin{aligned} T_{ij}^{(1)} &= -\Delta^2 |\widetilde{\boldsymbol{S}}|^2 \delta_{ij} & T_{ij}^{(2)} &= \Delta^2 |\widetilde{\boldsymbol{S}}| \widetilde{S}_{ij} \\ T_{ij}^{(3)} &= \Delta^2 \widetilde{S}_{ik} \widetilde{S}_{kj} & T_{ij}^{(4)} &= \Delta^2 |\widetilde{\boldsymbol{P}}| \delta_{ij} \\ T_{ij}^{(5)} &= \Delta^2 \widetilde{P}_{ij} & T_{ij}^{(6)} &= \Delta^2 |\widetilde{\boldsymbol{P}}|^{-1} \widetilde{P}_{ik} \widetilde{P}_{kj}, \end{aligned} \tag{2.48}$$

and β_k are scalar coefficients, the tensor norms are given by $|\widetilde{\boldsymbol{S}}| = \sqrt{2tr(\boldsymbol{S}^2)}$ and $|\widetilde{\boldsymbol{P}}| =$

$\sqrt{2tr(\boldsymbol{P}^2)}$.

The non-persistence-of-straining was first introduced by Thompson and de Souza Mendes [150] as a kinematic criterion to classify flows. This kinematic criterion is local, frame-indifferent and is not restricted to particular classes of flows. The combination of this tensor with the rate-of-strain tensor was shown to be able to predict anisotropies presents in a turbulent plane channel and a square duct flows [152]. Besides the characteristics listed above, it is worth mentioning that the non-persistence-of-straining tensor is orthogonal to $\widetilde{\boldsymbol{S}}$. In other words, it means that $\widetilde{\boldsymbol{P}}$ can attain eigenvector regions that $\widetilde{\boldsymbol{S}}$ cannot.

The persistence-of-straining tensor captures the local ability of the flow to avoid being persistently stretched. In this sense, when this tensor vanishes the material filaments that are aligned with the eigenvectors of $\widetilde{\boldsymbol{S}}$ have the tendency to continue this alignment. However, a non-vanishing persistence-of-straining tensor indicates a stretch relieving in the sense that the material filaments aligned to the principal directions of $\widetilde{\boldsymbol{S}}$ tend to avoid this state. Therefore, as $\widetilde{\boldsymbol{S}}$ is increased, the local flow defies the directional tendency dictated by $\widetilde{\boldsymbol{S}}$. Additional insights for the persistence-of-straining tensor can be found in Thompson and de Souza Mendes [150] and Thompson [149]. Despite the use of a nonlinear tensor basis to represent $\boldsymbol{\tau}$ by several researchers, as far as the present authors are aware, however, there is no proposed model in literature involving the use of tensor $\widetilde{\boldsymbol{P}}$ to compose a tensor basis to model $\boldsymbol{\tau}$.

The most general tensor polynomial model for the modeled SGS tensor in the extended form becomes:

$$\begin{aligned}\tau_{ij}^M - \frac{1}{3}\tau_{kk}^M\delta_{ij} = & -\beta_1\Delta^2|\widetilde{\boldsymbol{S}}|^2\delta_{ij} + \beta_2\Delta^2|\widetilde{\boldsymbol{S}}|\widetilde{S}_{ij} + \beta_3\Delta^2\widetilde{S}_{ik}\widetilde{S}_{kj} \\ & + \beta_4\Delta^2|\widetilde{\boldsymbol{P}}|\delta_{ij} + \beta_5\Delta^2\widetilde{P}_{ij} + \beta_6\Delta^2|\widetilde{\boldsymbol{P}}|^{-1}\widetilde{P}_{ik}\widetilde{P}_{kj}.\end{aligned} \tag{2.49}$$

It is worth reminding that the whole tensorial basis is objective. In other words, is invariant under changes of reference frame. Since the influence of each tensor in the tensorial basis from Eq. 2.49 is not yet known, five simpler models derived from the general form (Eq. 2.47) can be proposed. The simplified models comes from the fact that, regarding RANS approach, the set of tensor basis composed by $\boldsymbol{S}$, $\boldsymbol{SS}$, $\boldsymbol{P}$ and $\boldsymbol{PP}$ is able to totally reproduce the anisotropic Reynolds stress [152].

- Model I

$$\tau_{ij}^M - \frac{1}{3}\tau_{kk}^M\delta_{ij} = -\beta_2\Delta^2|\widetilde{\boldsymbol{S}}|\widetilde{S}_{ij}, \tag{2.50}$$

  Model *I* become the Smagorinsky model (Eq. 1.16) by considering $\beta_2 = 2C_S^2$.

- Model II

$$\tau_{ij}^M - \frac{1}{3}\tau_{kk}^M\delta_{ij} = \beta_1\Delta^2|\widetilde{\boldsymbol{S}}|^2\delta_{ij} - \beta_2\Delta^2|\widetilde{\boldsymbol{S}}|\widetilde{S}_{ij} + \beta_3\Delta^2\widetilde{S}_{ik}\widetilde{S}_{kj}. \tag{2.51}$$

- Model III

$$\tau_{ij}^M - \frac{1}{3}\tau_{kk}^M\delta_{ij} = \beta_1\Delta^2|\widetilde{\boldsymbol{S}}|^2\delta_{ij} - \beta_2\Delta^2|\widetilde{\boldsymbol{S}}|\widetilde{S}_{ij} + \beta_3\Delta^2\widetilde{S}_{ik}\widetilde{S}_{kj} + \beta_5\Delta^2\widetilde{P}_{ij}. \tag{2.52}$$

- Model IV

$$\tau_{ij}^M - \frac{1}{3}\tau_{kk}^M\delta_{ij} = -\beta_2\Delta^2|\widetilde{\boldsymbol{S}}|\widetilde{S}_{ij} + \beta_5\Delta^2\widetilde{P}_{ij}. \tag{2.53}$$

- Model V

$$\tau_{ij}^M - \frac{1}{3}\tau_{kk}^M\delta_{ij} = -\beta_2\Delta^2|\widetilde{\boldsymbol{S}}|\widetilde{S}_{ij} + \beta_4\Delta^2|\widetilde{\boldsymbol{P}}|\delta_{ij} + \beta_5\Delta^2\widetilde{P}_{ij} + \beta_6\Delta^2|\widetilde{\boldsymbol{P}}|^{-1}\widetilde{P}_{ik}\widetilde{P}_{kj}. \tag{2.54}$$

In order to analyze and validate the present nonlinear SGS methods, and to understanding its characteristics and advantages, the present work presents the *a priori* and *a posteriori* evaluation methodologies for LES, both are explained next.

2.4.1 *A priori* test in turbulent plane channel flow

According to Jiménez and Moser [67], the large scales in LES are characterized by means of a spatial low-pass filter width. Following Leonard [90], the appropriate filtering process for LES should be a local spatial filter, given by

$$\widetilde{\Psi}_n(\mathbf{X}) = \int_\forall \Psi_n(\mathbf{X}')\,G(\mathbf{X}-\mathbf{X}') * dX', \tag{2.55}$$

where the filtered (or resolved, or large-scale) variable is denoted by an overtilde $\widetilde{(\,)}$, G is a spatial low-pass filter, Ψ_n is a generic n order tensor and $\mathbf{X}$ is the spatial position. For instance, in a tri-dimensional flow, the filtered velocity field is formally defined as:

$$\widetilde{u_i}(x,y,z) = \int_{-\infty}^{\infty}\int_{-\infty}^{\infty}\int_{-\infty}^{\infty} u_i(x',y',z')G_\Delta(x-x',y-y',z-z')dx'dy'dz', \tag{2.56}$$

where $G_\Delta(\,)$ is a spatial low-pass filter with characteristic width Δ.

Several sensible choices for the functional form of G can be found in literature; e.g., Vreman et al. [165], Meneveau and Katz [107], Pope [127], and Sagaut [133]. In the present work, the filtering operation is made by using the box filter in only the homogeneous (periodic) directions. The box filter is applied to a grid with sides of length $\widetilde{\Delta} = (a/b)\Delta$ where $\widetilde{\Delta}$ is the mesh spacing in the current node of the coarse grid and $a>b$. The filtered velocity $\widetilde{u_i}(i,k)$, where i,k are the coordinates x,z of the point on the fine grid, is:

$$\widetilde{u_i}(i,k) = \frac{1}{a^2}\sum_{i'=i-b}^{i+b}\sum_{k'=k-b}^{k+b} u_i(i',k'). \tag{2.57}$$

The coarse mesh for which the velocity field will be filtered can be thought of as the one we might use in a large eddy simulation of this flow. The situation for the filter $\widetilde{\Delta} = 3\Delta$ is illustrated in the schematic given by Fig. 2.1, which shows both the original fine mesh (of spacing Δ_i, Δ_j and Δ_k) and the coarse grid (of spacing $\widetilde{\Delta}_i$, $\widetilde{\Delta}_j$ and $\widetilde{\Delta}_k$) for a turbulent channel flow with the mesh refined near the walls. To compute the filtered

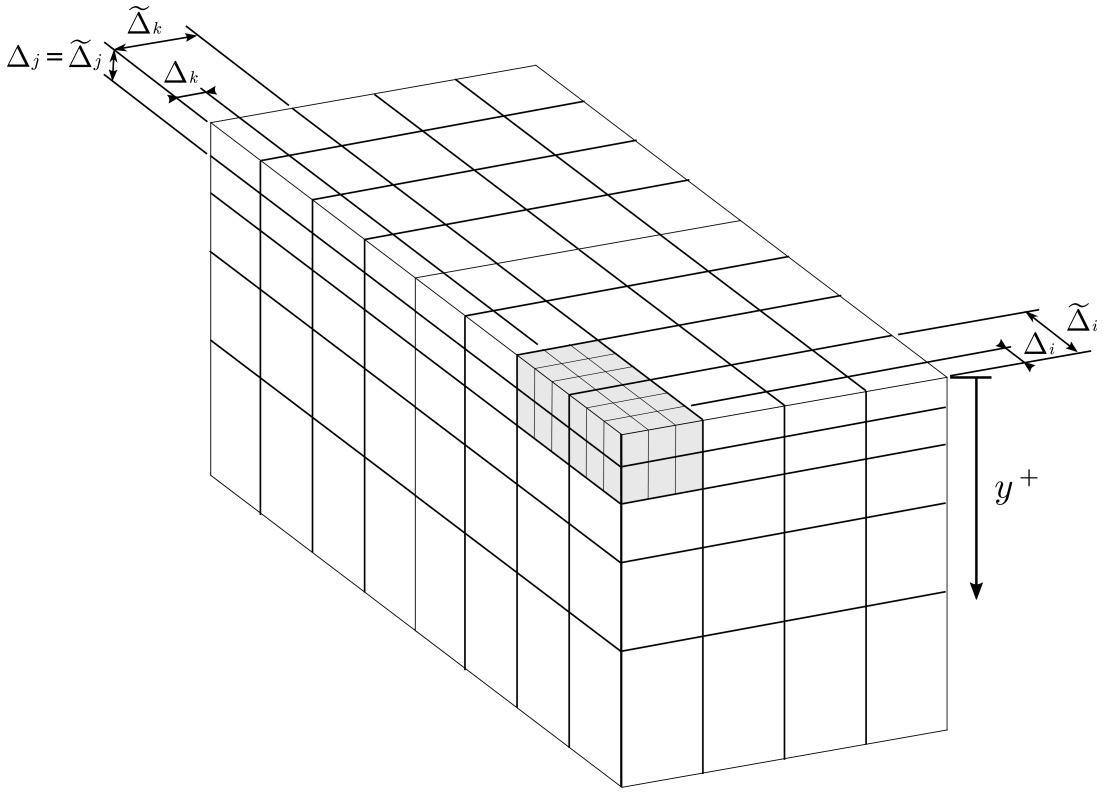

Figure 2.1 – Illustration of a fine mesh inside a coarse mesh in a channel flow. Δ_i, Δ_j and Δ_k stand for the discretization cell dimension in x, y and z direction, respectively, of the fine grid and $\widetilde{\Delta}_i$, $\widetilde{\Delta}_j$ and $\widetilde{\Delta}_k$ stand for the discretization cell dimension in x, y and z direction, respectively, of the coarse grid.

components, according to Liu et al. [95], two different approaches are possible. The first one, called "down-sample", removes the points from the field that are separated by a distance smaller than the filter scale $\widetilde{\Delta}$ and the second one preserves all the fine grid velocity points location. In present work, the down-sample technique is employed and the filtered variables are stored only in the coarse grid nodes, so we can capture a true representation of the effect gradient estimates on our SGS models and avoid enhanced correlations caused by filter overlap.

Tables 2.2 and 2.3 compare the resolutions of coarse grids for $Re_\tau = 180$ and $Re_\tau = 590$, respectively. The grid spacing of the filtered LES grids are about two, four and eight times the grid spacing of the corresponding DNS grid. Actual channel flow simulations applying similar resolutions have been performed by in the literature [122, 100, 56].

The constant coefficients corresponding to each tensor of the tensorial basis are ob-

	Domain		Grid				
$\widetilde{\Delta}$	L_x/h	L_z/h	$N_x \times N_y \times N_z$	δx^+	δy^+_{max}	δy^+_w	δz^+
2Δ	8π	$3\pi/2$	$256 \times 129 \times 64$	17.6	7.1	0.200	13.2
4Δ	8π	$3\pi/2$	$128 \times 129 \times 32$	35.2	7.1	0.200	26.4
8Δ	8π	$3\pi/2$	$64 \times 129 \times 16$	70.4	7.1	0.200	52.8

Table 2.2 – Geometric dimensions of the channel and grid resolution of the filtered grid in the filtered data at $Re_\tau = 180$.

	Domain		Grid				
$\widetilde{\Delta}$	L_x/h	L_z/h	$N_x \times N_y \times N_z$	δx^+	δy^+_{max}	δy^+_w	δz^+
2Δ	8π	$3\pi/2$	$256 \times 129 \times 64$	17.6	7.1	0.200	13.2
4Δ	8π	$3\pi/2$	$128 \times 129 \times 32$	35.2	7.1	0.200	26.4
8Δ	8π	$3\pi/2$	$64 \times 129 \times 16$	70.4	7.1	0.200	52.8

Table 2.3 – Geometric dimensions of the channel and grid resolution of the filtered grid in the filtered data at $Re_\tau = 590$.

tained from a minimization process of the deviation between the exact and the modeled SGS stress tensors. It is assumed that the DNS velocity field u_i is a good approximation for the Navier-Stokes exact solution. Since we are dealing with a turbulent plane channel flow, the model coefficients β_k (Eq. 2.47) found in the *a priori* test are assumed to be constants in time and in wall-parallel planes (xz) and vary only in the wall-normal direction as a function of the wall distance (y). Then, by setting the β_k to be constant on plane xz, the model coefficients are updated and are given by

$$C_k(y) = \langle \beta_k(x,y,z) \rangle_{xz}, \tag{2.58}$$

where $\langle\ \rangle_{xz}$ is the average calculated in plane xz. Then, Eq. 2.49 becomes:

$$\begin{aligned} \tau^M_{ij} - \frac{1}{3}\tau^M_{kk}\delta_{ij} = & -C_1\Delta^2|\widetilde{\boldsymbol{S}}|^2\delta_{ij} + C_2\Delta^2|\widetilde{\boldsymbol{S}}|\widetilde{S}_{ij} + C_3\Delta^2\widetilde{S}_{ik}\widetilde{S}_{kj} \\ & + C_4\Delta^2|\widetilde{\boldsymbol{P}}|\delta_{ij} + C_5\Delta^2\widetilde{P}_{ij} + C_6\Delta^2|\widetilde{\boldsymbol{P}}|^{-1}\widetilde{P}_{ik}\widetilde{P}_{kj}. \end{aligned} \tag{2.59}$$

The procedure that was developed in order to determine the C_k coefficients of Eq. 2.59 from the minimization of the deviation of the modeled SGS stress tensor, with respect to the exact one, is described next.

2.4.2 Model coefficients estimation based on SGS local error

The general and complete SGS model given by Eq. 2.59 depends on unknown coefficients $(C_1, ..., C_6)$ that are required to estimate the energetic influence of the SGS energy

behavior. In order to compute these coefficients in *a priori* test, a SGS local error tensor E_{ij}^{τ} can be defined by computing the difference between the modeled and the exact SGS stress. The SGS deviation function is therefore given by:

$$E_{ij}^{\tau} = \tau_{ij} - \tau_{ij}^{M}. \tag{2.60}$$

Introducing the SGS local quadratic error function $\mathcal{Q}^{\tau}$ given by:

$$\mathcal{Q}^{\tau} = E_{ij}^{\tau}\, E_{ij}^{\tau}. \tag{2.61}$$

Using Eq. 2.60 and making explicit the dependency of $\boldsymbol{\tau}^{M}$ on the coefficients C_k, where $C_k = [C_1,..., C_6]$, we have

$$\mathcal{Q}^{\tau}(C_k) = \tau_{ij}\ \tau_{ij} - 2\tau_{ij}^{M}(C_k)\ \tau_{ij} + \tau_{ij}^{M}(C_k)\ \tau_{ij}^{M}(C_k). \tag{2.62}$$

The local error function $\mathcal{Q}^{\tau}(C_k)$ can be minimized by the least square method as,

$$\frac{\partial}{\partial C_k}\left[\mathcal{Q}^{\tau}(C_k)\right] = 0. \tag{2.63}$$

The minimization expressed by Eq. 2.63 leads to the following condition

$$\begin{aligned} -\boldsymbol{\tau} T_{ij}^{(k)} + C_1 T_{ij}^{(k)} T_{ij}^{(1)} + C_2 T_{ij}^{(k)} T_{ij}^{(2)} + C_3 T_{ij}^{(k)} T_{ij}^{(3)} + \\ C_4 T_{ij}^{(k)} T_{ij}^{(4)} + C_5 T_{ij}^{(k)} T_{ij}^{(5)} + C_6 T_{ij}^{(k)} T_{ij}^{(6)} = 0. \end{aligned} \tag{2.64}$$

The index k varies from $k = 1$ to 6, the system given by Eq. 2.64 consists of a set of six linear equations that can be solved to estimate the model coefficients. Since the model coefficients are set to depend on the wall-distance y (Eq. 2.58), the averaging operation in wall parallel plans are applied to Eq. 2.64. Therefore, the linear equation system becomes

$$\begin{bmatrix} \left\langle T_{ij}^{(1)} T_{ij}^{(1)} \right\rangle_{xz} & \left\langle T_{ij}^{(1)} T_{ij}^{(2)} \right\rangle_{xz} & \cdots & \left\langle T_{ij}^{(1)} T_{ij}^{(6)} \right\rangle_{xz} \\ \left\langle T_{ij}^{(2)} T_{ij}^{(1)} \right\rangle_{xz} & \left\langle T_{ij}^{(2)} T_{ij}^{(2)} \right\rangle_{xz} & \cdots & \left\langle T_{ij}^{(2)} T_{ij}^{(6)} \right\rangle_{xz} \\ \vdots & \vdots & \ddots & \vdots \\ \left\langle T_{ij}^{(6)} T_{ij}^{(1)} \right\rangle_{xz} & \left\langle T_{ij}^{(6)} T_{ij}^{(2)} \right\rangle_{xz} & \cdots & \left\langle T_{ij}^{(6)} T_{ij}^{(6)} \right\rangle_{xz} \end{bmatrix} \begin{Bmatrix} C_1 \\ C_2 \\ \cdots \\ C_6 \end{Bmatrix} = \begin{Bmatrix} \left\langle \tau_{ij} T_{ij}^{(1)} \right\rangle_{xz} \\ \left\langle \tau_{ij} T_{ij}^{(2)} \right\rangle_{xz} \\ \vdots \\ \left\langle \tau_{ij} T_{ij}^{(6)} \right\rangle_{xz} \end{Bmatrix}, \tag{2.65}$$

where $T_{ij}^{(k)}$ are given by Eq. 2.48.

In order to estimate the model coefficients dependency on the wall-distance, one has to solve the system given by Eq. 2.65 at several y^{+} values. Equation 2.65 is designated

for the general model with the whole set of proposed tensor basis, i.e. $\widetilde{\boldsymbol{S}}$, $\widetilde{\boldsymbol{S}}\,\widetilde{\boldsymbol{S}}$, $\widetilde{\boldsymbol{P}}$, $\widetilde{\boldsymbol{P}}\,\widetilde{\boldsymbol{P}}$ and $\boldsymbol{I}$. However, from the proposed nonlinear SGS model it is possible to derive simpler models with a smaller set of tensor basis.

For instance, we can propose the Model I (given by Eq. 2.50) by keeping only the $\widetilde{\boldsymbol{S}}$ to represent the modeled SGS.

$$\tau_{ij}^{M} - \frac{1}{3}\tau_{kk}^{M}\delta_{ij} = C_2 T_{ij}^{(2)}, \tag{2.66}$$

where

$$T_{ij}^{(1)} = T_{ij}^{(3)} = T_{ij}^{(4)} = T_{ij}^{(5)} = T_{ij}^{(6)} = 0,$$

then, we have:

$$\left[\left\langle T_{ij}^{(2)} T_{ij}^{(2)} \right\rangle_{xz}\right]\{C_2\} = \left\{\left\langle \tau_{ij} T_{ij}^{(2)} \right\rangle_{xz}\right\},$$

$$C_2 = \frac{\left\langle \tau_{ij} T_{ij}^{(2)} \right\rangle_{xz}}{\left\langle T_{ij}^{(2)} T_{ij}^{(2)} \right\rangle_{xz}}. \tag{2.67}$$

Following the same procedure from Model I, it is possible to estimate the coefficients for the Model II, which incorporates the tensors: $\boldsymbol{I}$, $\widetilde{\boldsymbol{S}}$ and $\widetilde{\boldsymbol{S}}\,\widetilde{\boldsymbol{S}}$.

$$\tau_{ij}^{M} - \frac{1}{3}\tau_{kk}^{M}\delta_{ij} = C_1 T_{ij}^{(1)} + C_2 T_{ij}^{(2)} + C_3 T_{ij}^{(3)}, \tag{2.68}$$

where

$$T_{ij}^{(4)} = T_{ij}^{(5)} = T_{ij}^{(6)} = 0,$$

then, the linear system (Eq. 2.65) becomes:

$$\begin{bmatrix} \left\langle T_{ij}^{(1)} T_{ij}^{(1)} \right\rangle_{xz} & \left\langle T_{ij}^{(1)} T_{ij}^{(2)} \right\rangle_{xz} & \left\langle T_{ij}^{(1)} T_{ij}^{(3)} \right\rangle_{xz} \\ \left\langle T_{ij}^{(2)} T_{ij}^{(1)} \right\rangle_{xz} & \left\langle T_{ij}^{(2)} T_{ij}^{(2)} \right\rangle_{xz} & \left\langle T_{ij}^{(2)} T_{ij}^{(3)} \right\rangle_{xz} \\ \left\langle T_{ij}^{(3)} T_{ij}^{(1)} \right\rangle_{xz} & \left\langle T_{ij}^{(3)} T_{ij}^{(2)} \right\rangle_{xz} & \left\langle T_{ij}^{(3)} T_{ij}^{(3)} \right\rangle_{xz} \end{bmatrix} \begin{Bmatrix} C_1 \\ C_2 \\ C_3 \end{Bmatrix} = \begin{Bmatrix} \left\langle \tau_{ij} T_{ij}^{(1)} \right\rangle_{xz} \\ \left\langle \tau_{ij} T_{ij}^{(2)} \right\rangle_{xz} \\ \left\langle \tau_{ij} T_{ij}^{(3)} \right\rangle_{xz} \end{Bmatrix}. \tag{2.69}$$

Model III is composed by the tensor basis: $\mathbf{I}$, $\widetilde{\boldsymbol{S}}$, $\widetilde{\boldsymbol{S}}\,\widetilde{\boldsymbol{S}}$ and $\widetilde{\boldsymbol{P}}$:

$$\tau_{ij}^{M} - \frac{1}{3}\tau_{kk}^{M}\delta_{ij} = C_1 T_{ij}^{(1)} + C_2 T_{ij}^{(2)} + C_3 T_{ij}^{(3)} + C_5 T_{ij}^{(5)}, \tag{2.70}$$

where

$$T_{ij}^{(4)} = T_{ij}^{(6)} = 0,$$

then, the linear system (Eq. 2.65) becomes:

$$\begin{bmatrix} \left\langle T_{ij}^{(1)} T_{ij}^{(1)} \right\rangle_{xz} & \left\langle T_{ij}^{(1)} T_{ij}^{(2)} \right\rangle_{xz} & \left\langle T_{ij}^{(1)} T_{ij}^{(3)} \right\rangle_{xz} & \left\langle T_{ij}^{(1)} T_{ij}^{(5)} \right\rangle_{xz} \\ \left\langle T_{ij}^{(2)} T_{ij}^{(1)} \right\rangle_{xz} & \left\langle T_{ij}^{(2)} T_{ij}^{(2)} \right\rangle_{xz} & \left\langle T_{ij}^{(2)} T_{ij}^{(3)} \right\rangle_{xz} & \left\langle T_{ij}^{(2)} T_{ij}^{(5)} \right\rangle_{xz} \\ \left\langle T_{ij}^{(3)} T_{ij}^{(1)} \right\rangle_{xz} & \left\langle T_{ij}^{(3)} T_{ij}^{(2)} \right\rangle_{xz} & \left\langle T_{ij}^{(3)} T_{ij}^{(3)} \right\rangle_{xz} & \left\langle T_{ij}^{(3)} T_{ij}^{(5)} \right\rangle_{xz} \\ \left\langle T_{ij}^{(5)} T_{ij}^{(1)} \right\rangle_{xz} & \left\langle T_{ij}^{(5)} T_{ij}^{(2)} \right\rangle_{xz} & \left\langle T_{ij}^{(5)} T_{ij}^{(3)} \right\rangle_{xz} & \left\langle T_{ij}^{(5)} T_{ij}^{(5)} \right\rangle_{xz} \end{bmatrix} \begin{Bmatrix} C_1 \\ C_2 \\ C_3 \\ C_5 \end{Bmatrix} = \begin{Bmatrix} \left\langle \tau_{ij} T_{ij}^{(1)} \right\rangle_{xz} \\ \left\langle \tau_{ij} T_{ij}^{(2)} \right\rangle_{xz} \\ \left\langle \tau_{ij} T_{ij}^{(3)} \right\rangle_{xz} \\ \left\langle \tau_{ij} T_{ij}^{(5)} \right\rangle_{xz} \end{Bmatrix}. \tag{2.71}$$

Model IV is composed by the tensor basis: $\widetilde{\boldsymbol{S}}$ and $\widetilde{\boldsymbol{P}}$.

$$\tau_{ij}^{M} - \frac{1}{3}\tau_{kk}^{M}\delta_{ij} = C_2 T_{ij}^{(2)} + C_5 T_{ij}^{(5)}, \tag{2.72}$$

where

$$T_{ij}^{(1)} = T_{ij}^{(3)} = T_{ij}^{(4)} = T_{ij}^{(6)} = 0,$$

then, the linear system (Eq. 2.65) becomes:

$$\begin{bmatrix} \left\langle T_{ij}^{(2)} T_{ij}^{(2)} \right\rangle_{xz} & \left\langle T_{ij}^{(2)} T_{ij}^{(5)} \right\rangle_{xz} \\ \left\langle T_{ij}^{(5)} T_{ij}^{(2)} \right\rangle_{xz} & \left\langle T_{ij}^{(5)} T_{ij}^{(5)} \right\rangle_{xz} \end{bmatrix} \begin{Bmatrix} C_2 \\ C_5 \end{Bmatrix} = \begin{Bmatrix} \left\langle \tau_{ij} T_{ij}^{(2)} \right\rangle_{xz} \\ \left\langle \tau_{ij} T_{ij}^{(5)} \right\rangle_{xz} \end{Bmatrix}. \tag{2.73}$$

Model V is composed by the tensor basis: $\mathbf{I}$, $\widetilde{\boldsymbol{S}}$, $\widetilde{\boldsymbol{P}}$ and $\widetilde{\boldsymbol{P}}\widetilde{\boldsymbol{P}}$.

$$\tau_{ij}^{M} - \frac{1}{3}\tau_{kk}^{M}\delta_{ij} = C_2 T_{ij}^{(2)} + C_4 T_{ij}^{(4)} + C_5 T_{ij}^{(5)} + C_6 T_{ij}^{(6)}, \tag{2.74}$$

where

$$T_{ij}^{(1)} = T_{ij}^{(3)} = 0,$$

then, the linear system (Eq. 2.65) becomes:

$$\begin{bmatrix} \left\langle T_{ij}^{(2)} T_{ij}^{(2)} \right\rangle_{xz} & \left\langle T_{ij}^{(2)} T_{ij}^{(4)} \right\rangle_{xz} & \left\langle T_{ij}^{(2)} T_{ij}^{(5)} \right\rangle_{xz} & \left\langle T_{ij}^{(2)} T_{ij}^{(6)} \right\rangle_{xz} \\ \left\langle T_{ij}^{(4)} T_{ij}^{(2)} \right\rangle_{xz} & \left\langle T_{ij}^{(4)} T_{ij}^{(4)} \right\rangle_{xz} & \left\langle T_{ij}^{(4)} T_{ij}^{(5)} \right\rangle_{xz} & \left\langle T_{ij}^{(4)} T_{ij}^{(6)} \right\rangle_{xz} \\ \left\langle T_{ij}^{(5)} T_{ij}^{(2)} \right\rangle_{xz} & \left\langle T_{ij}^{(5)} T_{ij}^{(4)} \right\rangle_{xz} & \left\langle T_{ij}^{(5)} T_{ij}^{(5)} \right\rangle_{xz} & \left\langle T_{ij}^{(5)} T_{ij}^{(6)} \right\rangle_{xz} \\ \left\langle T_{ij}^{(6)} T_{ij}^{(2)} \right\rangle_{xz} & \left\langle T_{ij}^{(6)} T_{ij}^{(4)} \right\rangle_{xz} & \left\langle T_{ij}^{(6)} T_{ij}^{(5)} \right\rangle_{xz} & \left\langle T_{ij}^{(6)} T_{ij}^{(6)} \right\rangle_{xz} \end{bmatrix} \begin{Bmatrix} C_2 \\ C_4 \\ C_5 \\ C_6 \end{Bmatrix} = \begin{Bmatrix} \left\langle \tau_{ij} T_{ij}^{(2)} \right\rangle_{xz} \\ \left\langle \tau_{ij} T_{ij}^{(4)} \right\rangle_{xz} \\ \left\langle \tau_{ij} T_{ij}^{(5)} \right\rangle_{xz} \\ \left\langle \tau_{ij} T_{ij}^{(6)} \right\rangle_{xz} \end{Bmatrix}. \tag{2.75}$$

Results and validation for the *a priori* test are found in Sec. 3.3

2.4.3 Dynamic model coefficients estimation for nonlinear SGS models

Herein, a dynamic nonlinear SGS model is proposed and tested via *a posteriori* tests, where in a flow calculation, the model coefficients will vary and will be calculated each time step during the simulation with no need for *ad-hoc* coefficients depending on an exact velocity field. The dynamic coefficients are obtained by considering a test filter $\widehat{G}$ in a similar manner to Germano and Lilly's model (Section 1.3.4). It is considered a test filter width $\widehat{\Delta}$ taken to be equal twice the grid spacing filter $\widetilde{\Delta}$. More details about the grid and test filter applied in a dynamic LES is found in Section 1.3.4. By applying the filters $\widehat{G}$ and $\widehat{\widetilde{G}}$ to the incompressible Navier-Stokes equations one obtains the subgrid and the subtest stresses $\boldsymbol{\tau}$ and $\boldsymbol{T}$, Eqs. 1.20 and 1.21, respectively. The tensor components T_{ij}, τ_{ij} and $\mathcal{L}_{ij}$ are related by Eq. 1.23.

Alternatively to the modeled SGS stress, Eq. 2.59 can also be filtered by applying the test filter $\widehat{\widetilde{G}}$, then we have

$$\begin{aligned} T_{ij}^{M} = & -C_1\widehat{\Delta}^2|\widehat{\widetilde{\mathbf{S}}}|^2\delta_{ij} + C_2\widehat{\Delta}^2|\widehat{\widetilde{\mathbf{S}}}|\widehat{\widetilde{S}}_{ij} + C_3\widehat{\Delta}^2\widehat{\widetilde{S}}_{ik}\widehat{\widetilde{S}}_{kj} + \\ & + C_4\widehat{\Delta}^2|\widehat{\widetilde{\mathbf{P}}}|\delta_{ij} + C_5\widehat{\Delta}^2\widehat{\widetilde{P}}_{ij} + C_6\widehat{\Delta}^2|\widehat{\widetilde{\mathbf{P}}}|^{-1}\widehat{\widetilde{P}}_{ik}\widehat{\widetilde{P}}_{kj}. =, \end{aligned} \tag{2.76}$$

where T_{ij}^{M} are the components of the modeled subtest stress tensor. In the present modeled subtest stress tensor ($\boldsymbol{T}^{M}$), the assumption is made that the coefficients are independent to the filtering length, that is, for both $\boldsymbol{T}^{M}$ and $\boldsymbol{\tau}^{M}$ calculation, the coefficients $\{C_1, C_2, ..., C_6\}$ are held unchanged.

Then, the components of the modeled Leonard stress, $\mathcal{L}_{ij}$, (Eq. 1.23) for the nonlinear SGS become:

$$\mathcal{L}_{ij}^{M} = \sum_{k=1}^{6} C_k F_{ij}^{(k)} - \widehat{\sum_{k=1}^{6} C_k T_{ij}^{(k)}}, \tag{2.77}$$

where in a similar fashion to Eqs. 2.48, $F_{ij}^{(k)}$ are given by:

$$\begin{aligned} F_{ij}^{(1)} &= -\widehat{\Delta}^2|\widehat{\widetilde{\mathbf{S}}}|^2\widehat{\Delta}_{ij} & F_{ij}^{(2)} &= \widehat{\Delta}^2|\widehat{\widetilde{\mathbf{S}}}|\widehat{\widetilde{S}}_{ij} \\ F_{ij}^{(3)} &= \widehat{\Delta}^2\widehat{\widetilde{S}}_{ik}\widehat{\widetilde{S}}_{kj} & F_{ij}^{(4)} &= \widehat{\Delta}^2|\widehat{\widetilde{\mathbf{P}}}|\widehat{\Delta}_{ij} \\ F_{ij}^{(5)} &= \widehat{\Delta}^2\widehat{\widetilde{P}}_{ij} & F_{ij}^{(6)} &= \widehat{\Delta}^2|\widehat{\widetilde{\mathbf{P}}}|^{-1}\widehat{\widetilde{P}}_{ik}\widetilde{P}_{kj}. \end{aligned} \tag{2.78}$$

Since the coefficients $\{C_1, C_2, ..., C_6\}$ are independent from the filtering length, Eq. 2.77 become

$$\mathcal{L}_{ij}^{M} = \sum_{k=1}^{6} C_k \left[F_{ij}^{(k)} - \widehat{T_{ij}^{(k)}} \right]. \tag{2.79}$$

In a developed form, Eq. 2.79 become

$$\begin{aligned}\mathcal{L}_{ij}^{M} = & -C_1\left[\widehat{\Delta^2}|\widehat{\widetilde{\mathbf{S}}}|^2\delta_{ij} - \widehat{\Delta^2|\widetilde{\mathbf{S}}|^2\delta_{ij}}\right] + C_2\left[\widehat{\Delta^2}|\widehat{\widetilde{\mathbf{S}}}|\widehat{\widetilde{S}}_{ij} - \widehat{\Delta^2|\widetilde{\mathbf{S}}|\widetilde{S}_{ij}}\right] \\ & + C_3\left[\widehat{\Delta^2}\widehat{\widetilde{S}}_{ik}\widehat{\widetilde{S}}_{kj} - \widehat{\Delta^2\widetilde{S}_{ik}\widetilde{S}_{kj}}\right] + C_4\left[\widehat{\Delta^2}|\widehat{\widetilde{\mathbf{P}}}|\delta_{ij} - {}^2\widehat{\Delta|\widetilde{\mathbf{P}}|\delta_{ij}}\right] \\ & + C_5\left[\widehat{\Delta^2}\widehat{\widetilde{P}}_{ij} - \widehat{\Delta^2\widetilde{P}_{ij}}\right] + C_6\left[\widehat{\Delta^2}|\widehat{\widetilde{\mathbf{P}}}|^{-1}\widehat{\widetilde{P}}_{ik}\widehat{\widetilde{P}}_{kj} - \widehat{\Delta^2}|\widehat{\widetilde{\mathbf{P}}|^{-1}\widetilde{P}_{ik}\widetilde{P}_{kj}}\right].\end{aligned} \tag{2.80}$$

In the interest of simplification and coherence, it is appropriate to simplify Eq. 2.80 by introducing the tensors $\left\{\boldsymbol{M}^{(1)}, \boldsymbol{M}^{(2)}, ..., \boldsymbol{M}^{(6)}\right\}$ that are given by:

$$\begin{aligned} M_{ij}^{(1)} &= F_{ij}^{(1)} - \widehat{T_{ij}^{(1)}} & M_{ij}^{(4)} &= F_{ij}^{(4)} - \widehat{T_{ij}^{(4)}} \\ M_{ij}^{(2)} &= F_{ij}^{(2)} - \widehat{T_{ij}^{(2)}} & M_{ij}^{(5)} &= F_{ij}^{(5)} - \widehat{T_{ij}^{(5)}} \\ M_{ij}^{(3)} &= F_{ij}^{(3)} - \widehat{T_{ij}^{(3)}} & M_{ij}^{(6)} &= F_{ij}^{(6)} - \widehat{T_{ij}^{(6)}}, \end{aligned} \tag{2.81}$$

Therefore, Eq. 2.80 become

$$\mathcal{L}_{ij}^{M} = \sum_{k=1}^{6} C_k M_{ij}^{(k)}. \tag{2.82}$$

The mathematical procedure to obtain the dynamic nonlinear set of coefficients follows the least squares approach introduced by Lilly [93]. To characterize the deviation between the exact and the modeled Leonard stress tensors ($E_{ij}^{\mathcal{L}}$), a local error tensor is proposed by Eq. 2.83.

$$E_{ij}^{\mathcal{L}} = \mathcal{L}_{ij} - \mathcal{L}_{ij}^{M}, \tag{2.83}$$

where the components of the Leonard stress tensor $\mathcal{L}_{ij}$ is given by Eq. 1.22.

Now the Leonard local quadratic error function, $\mathcal{Q}^{\mathcal{L}}$, is introduced,

$$\mathcal{Q}^{\mathcal{L}} = E_{ij}^{\mathcal{L}} E_{ij}^{\mathcal{L}}. \tag{2.84}$$

Next, by applying the minimization technique to $\mathcal{Q}^{\mathcal{L}}$, we have:

$$\begin{bmatrix} M_{ij}^{(1)}M_{ij}^{(1)} & M_{ij}^{(1)}M_{ij}^{(2)} & \cdots & M_{ij}^{(1)}M_{ij}^{(6)} \\ M_{ij}^{(2)}M_{ij}^{(1)} & M_{ij}^{(2)}M_{ij}^{(2)} & \cdots & M_{ij}^{(2)}M_{ij}^{(6)} \\ \vdots & \vdots & \ddots & \vdots \\ M_{ij}^{(6)}M_{ij}^{(1)} & M_{ij}^{(6)}M_{ij}^{(2)} & \cdots & M_{ij}^{(6)}M_{ij}^{(6)} \end{bmatrix} \begin{Bmatrix} C_1 \\ C_2 \\ \cdots \\ C_6 \end{Bmatrix} = \begin{Bmatrix} \mathcal{L}_{ij}M_{ij}^{(1)} \\ \mathcal{L}_{ij}M_{ij}^{(2)} \\ \vdots \\ \mathcal{L}_{ij}ij^{(6)} \end{Bmatrix}. \tag{2.85}$$

The system of linear equation given by Eq. 2.85 is similar to the one given by Eq. 2.65. By obtaining its solutions, we are able to find the dynamic coefficients of the nonlinear SGS model. similar to what was shown in Sec. 2.4.2, we can also derive equations for

simpler models that involve fewer tensors in their composition, e.g. Model I:

$$\left[M_{ij}^{(2)}M_{ij}^{(2)}\right]\left\{C_2\right\} = \left\{\mathcal{L}_{ij}\mathcal{L}_{ij}M_{ij}^{(2)}\right\}, \tag{2.86}$$

$$C_2 = \frac{\mathcal{L}_{ij}M_{ij}^{(2)}}{M_{ij}^{(2)}M_{ij}^{(2)}}. \tag{2.87}$$

By analyzing the above model formulation, we can state that the conventional dynamic model formulation of Lilly [93] are somehow similar.

Results and validation for the *a posteriori* tests are found in Sec. 3.4

Chapter 3

Results

3.1 Statistical uncertainties and convergence for DNS

In this section, the results for statistical analysis of uncertainties and convergence for DNS are presented for turbulent channel flows. First, we present the turbulent plane channel data in Sec. 3.1.1 and then, we present the results of analyzes and comparisons with literature data in Sec. 3.1.2. Due to similarity in statistics, we also added circular pipe data from bibliographical references in comparisons with the turbulent flat channel. Experimental results were also analyzed for comparison reasons and application of the methodology presented in Sec. 2.2.

3.1.1 The turbulent channel and pipe flow data

Fully developed turbulent flows of incompressible Newtonian fluids are considered. For a channel flow, the usual notations for this geometry are used, namely, the channel streamwise direction is $x_1 = x$, the wall-normal direction is $x_2 = y$, and the spanwise direction is $x_3 = z$ with velocity field in the respective directions $(u_x, u_y, u_z) = (u_1, u_2, u_3)$. The solved momentum and continuity equations are given by

$$\frac{\partial u_i}{\partial t} + \frac{\partial (u_i u_j)}{\partial x_j} = -\frac{1}{\rho}\frac{\partial p}{\partial x_i} + \nu \frac{\partial^2 u_i}{\partial x_j^2}, \tag{3.1}$$

$$\frac{\partial u_i}{\partial x_i} = 0, \tag{3.2}$$

where p is the pressure.

The channel half-gap is denoted by h, while the two other directions are considered to be of infinite extent. Since the geometry for the pipe flow differs from that for a channel, some parts of the notation are slightly different, namely, the radial distance r, the circumferential direction $x_3 = R\theta$, where θ is the angle in a cylindrical coordinate,

and the velocity field (u_r, u_θ, u_x). A relation between y and r can be established in the form $x_2 = y = (R - r)$, where R is the radius of the pipe.

For the present work, new direct numerical simulations were conducted to provide the data used for the temporal convergence evaluation. Seeking to make comparisons with the results of other authors, in the present thesis DNS results from a literature review and an open online repository have been considered. The DNS come from the following research teams: Abe et al. [1], Del Álamo et al. [37], Del Álamo and Jiménez [36], Bernardini et al. [13], Eggels et al. [45], Fukagata and Kasagi [47], Hoyas and Jiménez [62], Khoury et al. [74], Iwamoto et al. [65], Lee and Moser [88], Lozano-Durán and Jiménez [96], Moser et al. [117], Thais et al. [146], Vreman and Kuerten [162], Vreman and Kuerten [163], Vreman and Kuerten [161], Wu et al. [171] and Wu and Moin [172], and the on-line database addresses are found in Table A.1. In these papers, direct numerical simulations of fully developed turbulent flow at different Reynolds numbers are reported and we can find results from $Re_\tau \approx 180$ up to $Re_\tau \approx 5200$.

For turbulent pipe flows, e.g. Wu et al. [171], the Kármán number, $R^+ \equiv u_\tau R/\nu$, based on the pipe radius, R, is equivalent to the friction Reynolds number Re_τ.

The main database parameters of the numerical simulations for different Reynolds numbers are given in Tables *A*.2–*A*.6 (Appendix A). The presented parameters are: the spatial discretization method, the Reynolds number, and the dimensionless averaging times, Tu_τ/h, and T^*. The so-called normalized eddy turnover time, T^*, takes into account in its calculation the computational domain in order to make a fair comparison between the different databases. This procedure is considered so that only the simulation time is taken into account in the error comparisons. For pipe flows, T^* is given by

$$T^* = \frac{Tu_\tau}{R}\left(\frac{L_x}{L_{x,min}}\right). \tag{3.3}$$

In parallel with the numerical studies listed above, many researchers have produced experimental data with different instrumentation setups and various levels of approximation to investigate turbulent channel flow [32, 68, 87, 137, 168]. While experimental studies are limited in their ability to collect three dimensional (3D) unsteady flow fields, they have the distinct advantage over DNS of allowing researchers to look at more realistic flows and over a much larger range of Reynolds numbers. In the present thesis, the method proposed by Thompson et al. [153] is also tested on the experimental studies of Schultz and Flack [137] and den Toonder and Nieuwstadt [38].

In Schultz and Flack [137], experiments were performed in a channel section of 25 mm in height, 200 mm in width, and 3.1 m in length. The available experimental data correspond to $Re_\tau = 1010$, $Re_\tau = 1956$, $Re_\tau = 4048$, and $Re_\tau = 5895$. Schultz and Flack [137] collected different amounts of sampled data at each Reynolds number. According to them, the velocity data was collected in such a way that the number of

velocity samples was sufficient to ensure the independence of the values of the statistics. At $Re_\tau = 1010$, between 15,000 and 18,000 velocity samples were taken; at $Re_\tau = 1956$ the number of acquisitions was between 35,000 and 40,000, and at higher Reynolds numbers, 50,000 velocity samples were collected.

The experiments with two-component laser Doppler anemometry of den Toonder and Nieuwstadt [38] were performed in a cylindrical perspex pipe with a length of 34 m and an inner diameter of 40 mm. They obtained 18,000 samples per position over 300 s. However, not all the samples were uncorrelated, due to each integral time scale of the turbulence. Hence, at least 6000 samples are effectively considered independent.

Uncertainties in data coming from experimental tests are generally found due to the inherent error sources present in measuring devices and setup control. These errors come from different sources, e.g. velocity and pressure gradient measurements, flow pressure control, control and measurement of the fluid temperature. Due to these uncertainties, the averaged fields extracted from experiments generally present errors larger than those calculated by DNS. For the experimental results analyzed in the present work, the results of Schultz and Flack [137] have total uncertainties of ±1.5% for the measurement of the mean velocity and ±5.1% for the measurement of the Reynolds shear stress. For the experimental data provided by den Toonder and Nieuwstadt [38], the relative measurement error in the mean streamwise velocity was ±0.3%. More details about the experiments can be found in Schultz and Flack [137] and den Toonder and Nieuwstadt [38].

3.1.2 Comparisons and validation

The results are organized according to similar Re_τ, selecting the flow cases, where $178 \leq Re_\tau \leq 5200$. The different flow cases were divided into five categories: (1) $178 \leq Re_\tau \leq 187$; (2) $543 \leq Re_\tau \leq 643$, (3) $934 \leq Re_\tau \leq 1000$, (4) $2000 \leq Re_\tau \leq 2200$, and (5) $4000 \leq Re_\tau \leq 5200$. The channel half-width is divided into four distinct regions (e.g. [127]): I: viscous sublayer ($0 < y^+ < 5$), II: buffer layer ($5 < y^+ < 30$), III: log-law region ($y^+ > 30, y/\delta < 0.3$), and IV: outer layer ($y^+ > 50$).

Figure 3.1 displays the residuals $E_R(y^+)$ and $E_U(y^+)$ obtained with Eqs. 2.8 and 2.11, respectively, across the channel half-width (or radius for pipe flow). Within the range $Re_\tau \leq 590$, the results from other authors are compared to the present results. We can see that particular patterns can be identified for each dataset, irrespectively of the Reynolds number. For Bernardini et al. [13], the maximum E_R is found to be in Region III, where the log-law holds, but the viscous contribution to the shear stress is still significant. For Del Álamo and Jiménez [36], the peak is located on the line separating the viscous sub-layer (Region I) and buffer layer (Region II), $y^+ \approx 5$, where the nonlinear TKE transfer has its positive peak [147]. The order of magnitude of

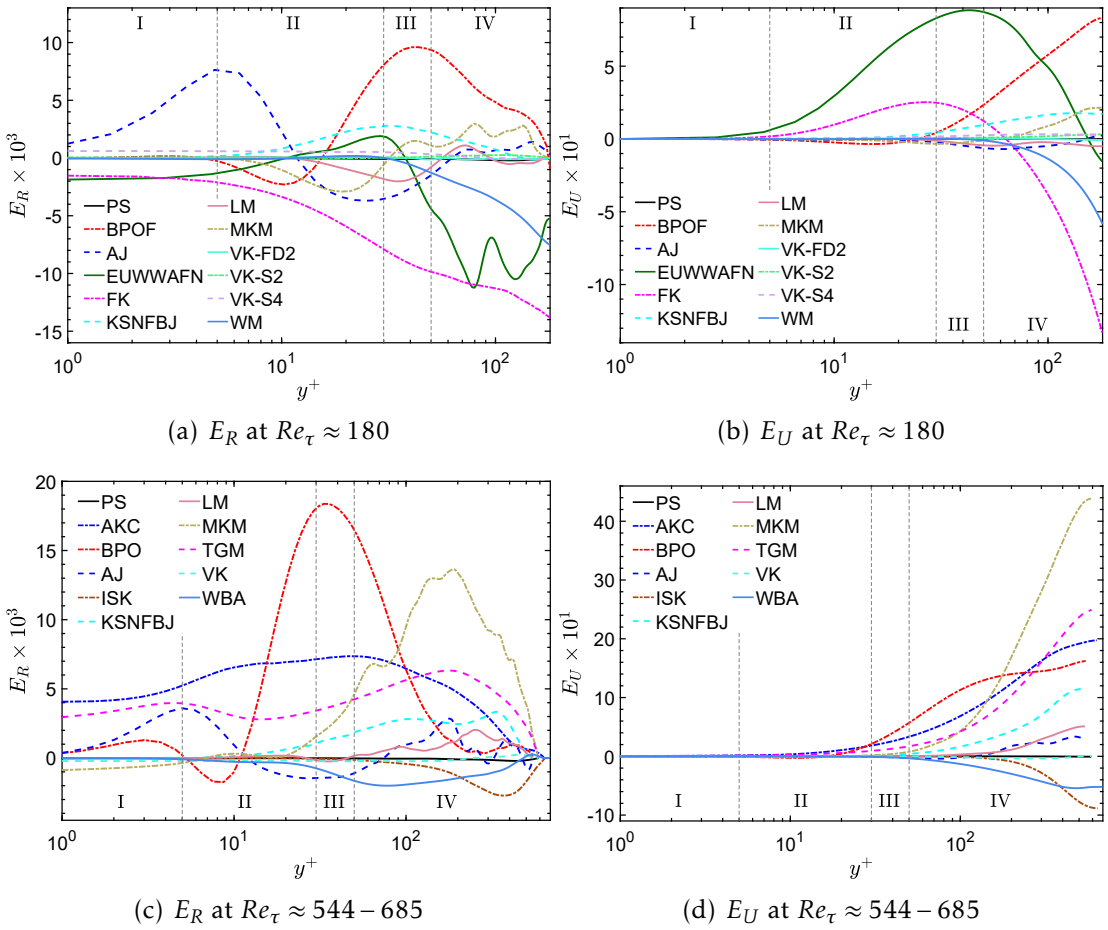

(a) E_R at $Re_\tau \approx 180$

(b) E_U at $Re_\tau \approx 180$

(c) E_R at $Re_\tau \approx 544 - 685$

(d) E_U at $Re_\tau \approx 544 - 685$

Figure 3.1 – Comparison of residual values, E_R (left column) and E_U (right column), between the present study and several DNS databases. Information about the numerical results is given by Table A.2 for $Re_\tau \approx 180$, and by Table A.3 for $Re_\tau \approx 544 - 685$. AKC [1]; BOP [13]; AJ [36]; EUWWAFN [45]; FK [47]; ISK [65]; KSNFBJ [74]; LM [88]; MKM [117]; TGM [146]; VK-FD2 [162]; VK [163]; VK-S2B3 [161]; VK-S4B3 [161]; WBA [171]; WM[172].

the residuals does not change with the Reynolds number. We can observe that the velocity residual E_U is negligible near the wall (Regions I and II) with a steepening in the outer layer, where the effects of viscosity on U begin to be negligible. This can be associated to the fact that in the outer region, the larger scales are predominant, and then the averaging time required for the convergence is higher than close to the walls. In addition, since this residual is associated to the cumulative y^+ error of R_{yx}, it is natural that there should be a growth tendency on departing from the wall.

In the range of Reynolds numbers $Re_\tau \approx 180$ and $Re_\tau \approx 590$ (Fig. 3.1) the high resolution results obtained by Vreman and Kuerten [162, 161, 163] and the present thesis are distinguished from the others by an extremely tiny residual; although the present thesis does not use an extra refined grid, it reached very small residual errors.

Figure 3.2 shows the residuals $E_R(y^+)$ and $E_U(y^+)$ for the experimental results of

Schultz and Flack [137] and den Toonder and Nieuwstadt [38], and some selected DNS results for similar Reynolds numbers for comparison. It can be seen that the experimen-

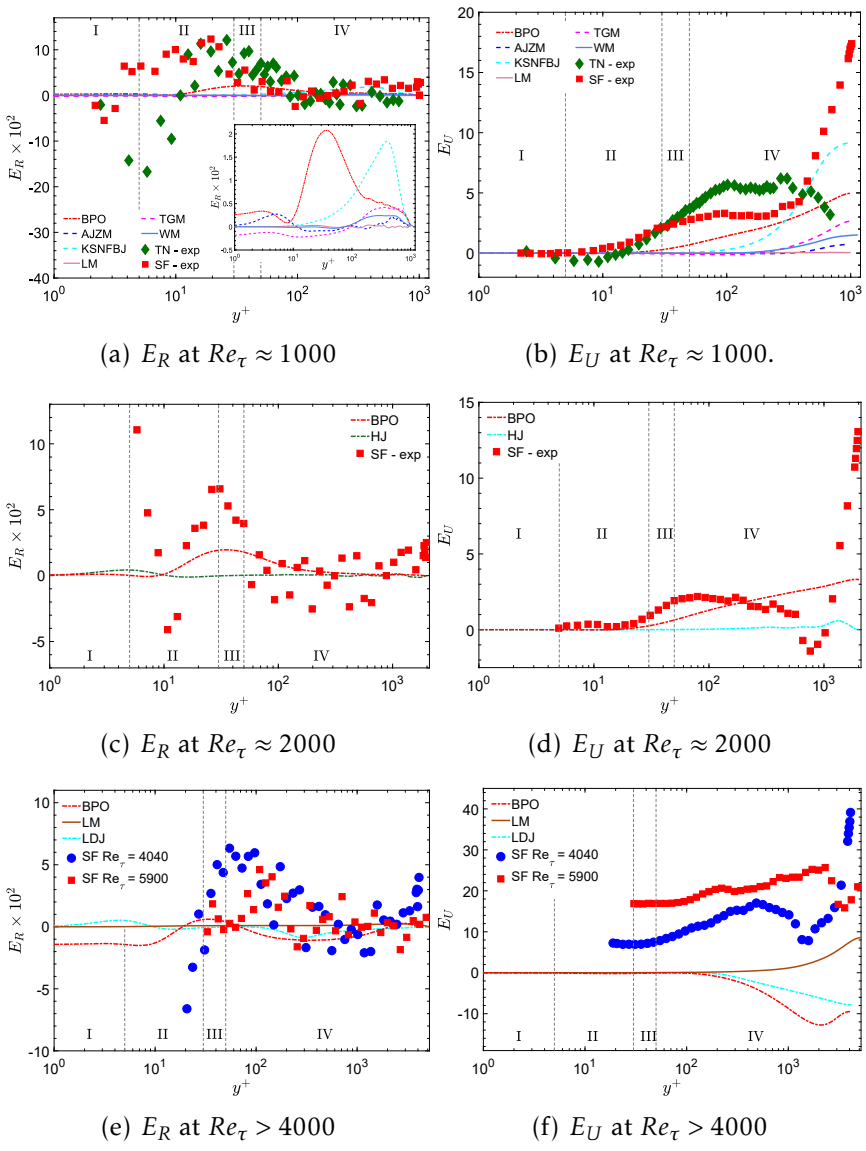

(a) E_R at $Re_\tau \approx 1000$ (b) E_U at $Re_\tau \approx 1000$.

(c) E_R at $Re_\tau \approx 2000$ (d) E_U at $Re_\tau \approx 2000$

(e) E_R at $Re_\tau > 4000$ (f) E_U at $Re_\tau > 4000$

Figure 3.2 – Experimental residual values, E_R (left column) and E_U (right column), computed from Schultz and Flack [137], den Toonder and Nieuwstadt [38] and selected DNS results for comparison, The zoomed inset in (a) allows visualization of the DNS errors

tal residual errors, as measured by $E_R(y^+)$ and $E_U(y^+)$, are higher than the corresponding DNS errors. This was expected, since the uncertainties of the equipment and measurements are quite influential on the experimental data. In this respect, Schultz and Flack [137] verify the accuracy of their experiments using DNS as a reference. The measure $E_R(y^+)$ and $E_U(y^+)$ are able to establish a direct quantitative comparison of DNS and experimental errors. Interestingly, some particular patterns can be identified in the experimental dataset, irrespectively of the Reynolds number and geometry (channel or

pipe). For $Re_\tau \approx 1000$, we notice that the channel case of Schultz and Flack [137] and the pipe case of den Toonder and Nieuwstadt [38] are in quite good agreement. The quantity $E_R(y^+)$ has similar dispersions. Both curves have negative values in the viscous layer and increase throughout the buffer layer, achieving a peak near the log-law region. In Region III, $E_R(y^+)$ decays significantly and has quite small values in the outer layer, switching between positive and negative near the center of the channel. In the case of the velocity residual, we can see that the integration process of Eq. (2.9) leads to smoother curves when compared to the original $E_R(y^+)$ function. The quantity $E_U(y^+)$ is small close to the wall and higher at the outer layer. The data provided by Schultz and Flack [137] presents an abrupt increase at the center of the channel. However, the residual error $E_U(y^+)$ of den Toonder and Nieuwstadt [38], unlike the other authors, shows a decline in the center of the channel due to the negative values of $E_R(y^+)$ in this region. Analyzing the overall results obtained from the data originating from the experiments conducted by Schultz and Flack [137] we can see that as Re_τ increases, it becomes harder to obtain near wall data since the characteristic length scale decreases significantly and the physical distance from the wall where measurements are able to be taken is nearly the same. Concerning the $E_R(y^+)$ curves, we can see a shift in the peak towards the center of the channel, from the perspective of the divisions of the regions, and we can also see a more erratic behavior of the data. The $E_U(y^+)$ curves for $Re_\tau > 1000$ systematically present a valley before the abrupt increase mentioned for the $Re_\tau \approx 1000$ case. Although the magnitudes of the residual errors of the Reynolds stress shear component were similar for the different Reynolds numbers, $E_U(y^+)$ experienced the impact of the cumulative residual and had very high values for $Re_\tau = 4040$ and 5900.

It is expected that experiments have higher errors than DNS. However, an interesting remark about the present convergence criterion in the analysis of experimental tests is the possibility to know in which positions y^+ present the largest errors without the need of a direct comparison with a reference DNS case. In other words, the present method can help by indicating the location of specific regions of the channel where the experimental measurements are providing less reliable statistical quantities and, consequently, where new sampling is needed in order to improve the quality of the results. In addition, this method enables one to compute the variation of the unbalance of the average forces as a function of the number of samples available, informing how many samples are needed for the field to be considered reliable, what can significantly help researchers who work with measurements on channel or pipe flows.

Still considering Fig. 3.2, as well as the results presented in Fig. 3.1, one can observe results from each dataset with patterns independent of the Reynolds number. For instance, Bernardini et al. [13] present the highest values of E_R, with peaks located in Region III. However, unlike other Reynolds values, Bernardini et al. [13] present

non-zero E_R close to the wall at $Re_\tau \approx 4000$ (Fig. 3.2-e). Also following a pattern, Khoury et al. [74] present a peak of E_R in the outer layer (Region IV) of the pipe, contributing to an increase of E_U in the central region; this behavior is similar to that shown in Fig. 3.1-c. It is remarkable that Lee and Moser [88] provide the lowest residuals compared to the other datasets. This can be explained by the high degree of refinement in the mesh used (see Table A.12).

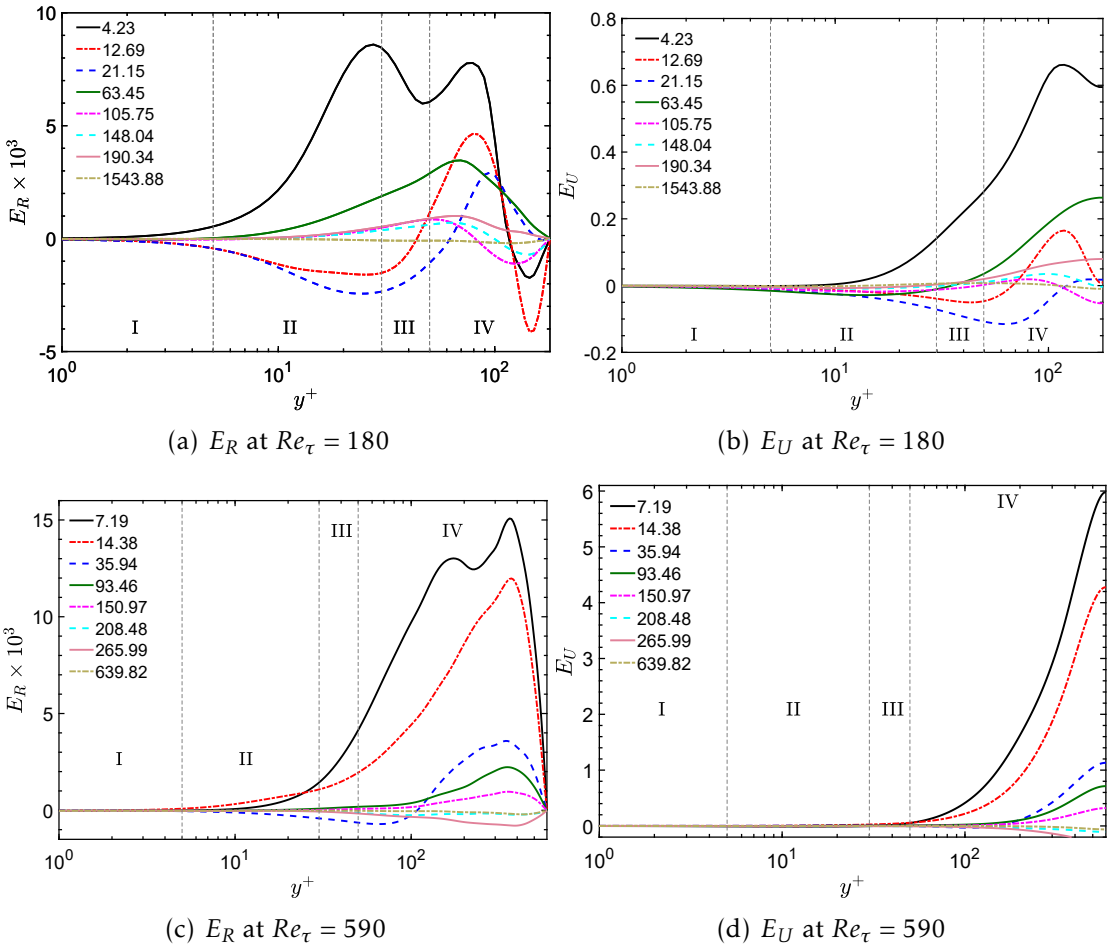

(a) E_R at $Re_\tau = 180$ (b) E_U at $Re_\tau = 180$

(c) E_R at $Re_\tau = 590$ (d) E_U at $Re_\tau = 590$

Figure 3.3 – Temporal development of residual profiles $E_R(y^+)$ (left column) and $E_U(y^+)$(right column) at several dimensionaless averaging time T^* at $Re_\tau = 180$ and 590.

Figure 3.3 shows the temporal evolution of residual profiles $E_R(y^+)$ and $E_U(y^+)$ computed from the DNS generated for the present study. In this figure, we can see that for both measures, E_R and E_U, the residual error has a tendency to decrease as the averaging time increases, being negligible along the domain in the limit of high values of T^*. The residual error oscillates between positive and negative values along the time and distance. The highest peaks of the residual error are concentrated in Region IV, even for E_R. This is probably due to the well known "outer layer effect" of turbulence, which contributes to an increase in the turbulent fluctuations.

A more detailed description of the evolution in time of the residuals $E_R(y^+, T^*)$ and $E_U(y^+, T^*)$ is shown in Fig. 3.4, which presents plots of the contours associated to both kinds of residual errors, as functions of T^* and y^+. It should be pointed out that the

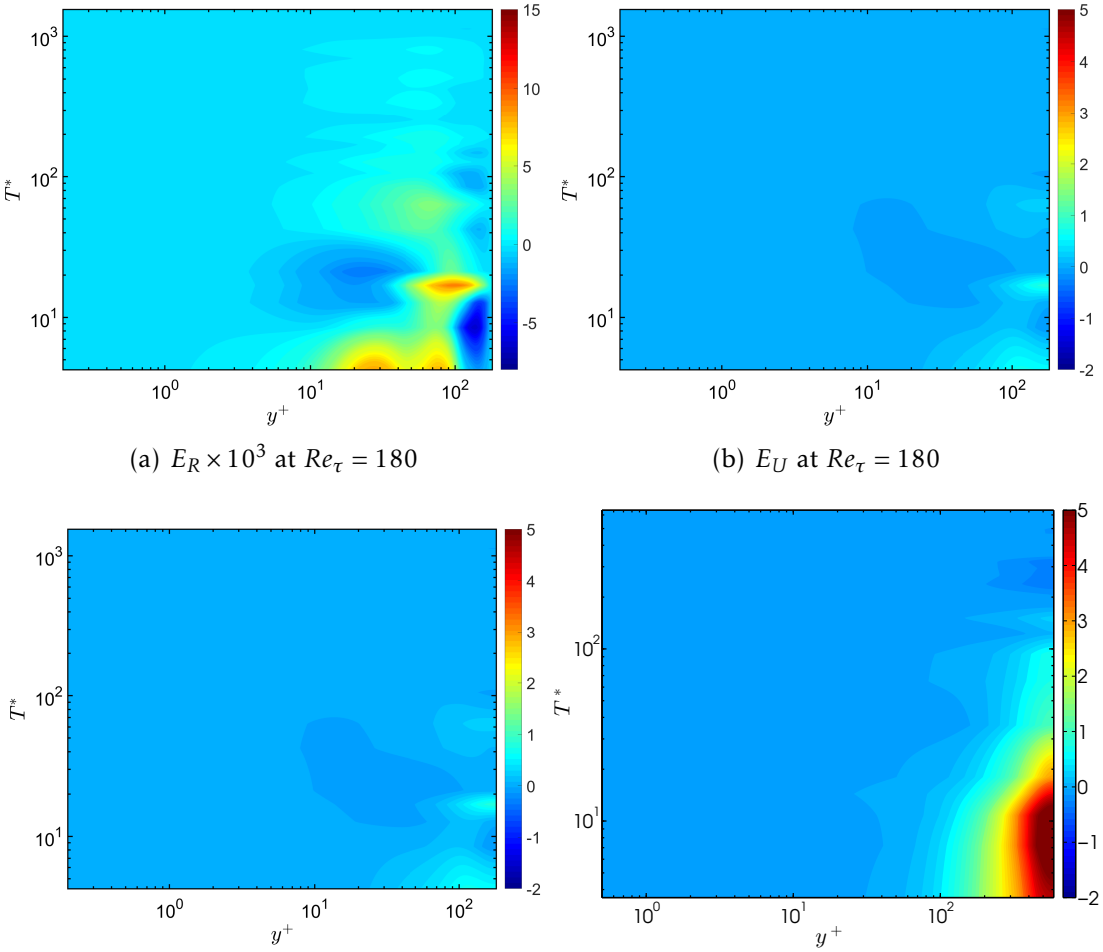

(a) $E_R \times 10^3$ at $Re_\tau = 180$ (b) E_U at $Re_\tau = 180$

(c) $E_R \times 10^3$ at $Re_\tau = 590$ (d) E_U at $Re_\tau = 590$

Figure 3.4 – Contours of temporal and spatial development of the residual profiles $E_R(y^+, T^*) \times 10^3$ (left column) and $E_U(y^+, T^*)$ (right column) at $Re_\tau = 180$ and 590.

smallest absolute residual errors are not necessarily the least scale value in the figure, since negative errors are found. As already shown in Fig. 3.3, it can be seen in Fig. 3.4 that the maximum errors are concentrated in the middle of the channel. The residuals oscillate between positive and negative and decrease with increasing averaging time. Higher peaks and lower oscillation frequencies are found for higher Reynolds numbers.

As discussed in the Methods section, we propose a norm with respect to the whole domain of the residual errors associated to the Reynolds stress shear component, $\|E_R\|$, and the mean velocity profiles, $\|E_U\|$, as a single measure of the error associated to a specific averaging time (see Eqs. 2.13 and 2.14). Fig. 3.5 shows the temporal evolution of these residual norms as functions of the dimensionless averaging time, T^*, associated to the DNS conducted for the present thesis. In addition, the same figure shows the

final norms obtained from the DNS and experimental data of the different groups here analyzed. In other words, the information associated to these data coming from the literature is displayed as a single point in the graph, corresponding to the pairs $(T^*, \|E_R\|)$ and $(T^*, \|E_U\|)$, where T^* is the total dimensionless averaging time employed by the respective group. For the cases where the information regarding the averaging time is missing for any reason, a straight horizontal line is plotted at the corresponding residual error value.

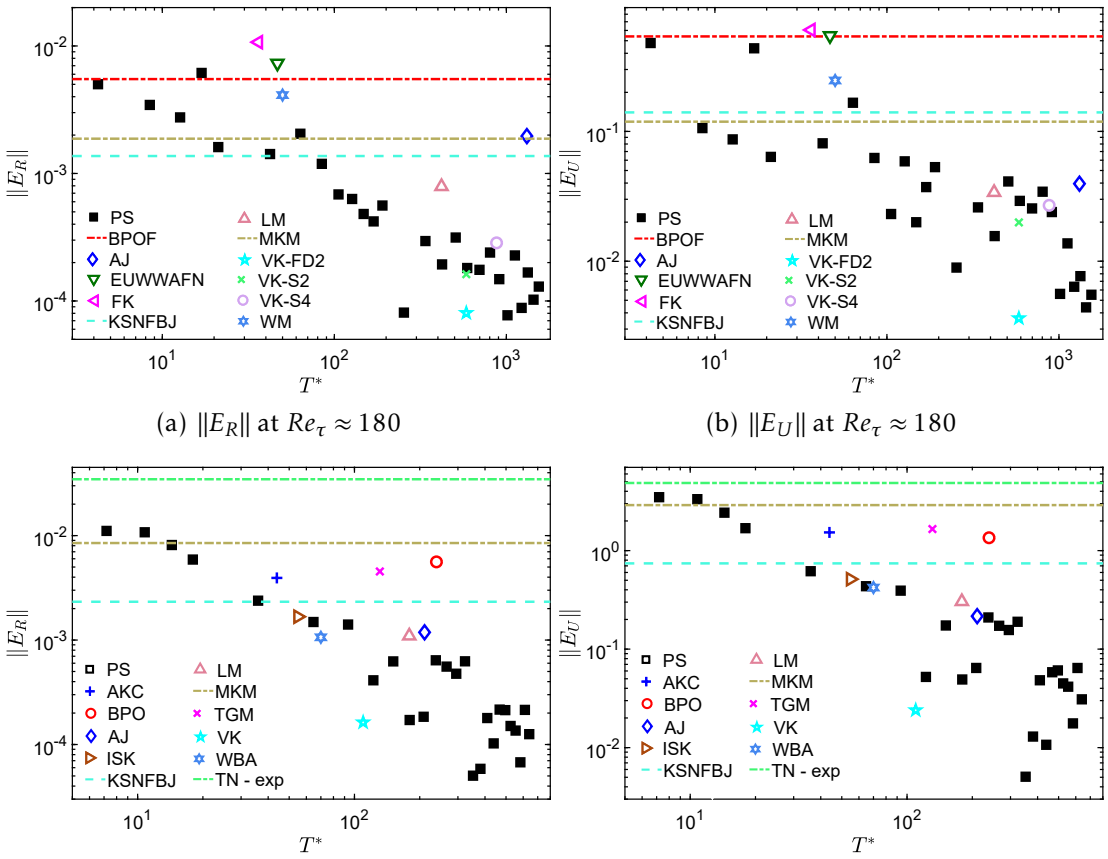

(a) $\|E_R\|$ at $Re_\tau \approx 180$ (b) $\|E_U\|$ at $Re_\tau \approx 180$

(c) $\|E_R\|$ at $Re_\tau \approx 544 - 685$ (d) $\|E_U\|$ at $Re_\tau \approx 544 - 685$

Figure 3.5 – Development of the residual norms, $\|E_R\|$ (left column) and $\|E_U\|$ (right column), as functions of the averaging time at $Re_\tau = 180$ and at $Re_\tau \approx 544 - 685$. Plotted horizontal lines report data with unidentified averaging time. AKC [1]; BOP [13]; AJ [36]; TN [38]; EUWWAFN [45]; FK [47]; ISK [65]; KSNFBJ [74]; LM [88]; MKM [117]; TGM [146]; VK-FD2 [162]; VK [163]; VK-S2B3 [161]; VK-S4B3 [161]; WBA [171]; WM [172].

From Fig. 3.5, it can be concluded that for low values of the averaging time, the residual errors decay faster and their convergence rate decreases along T^*. The convergence rate seems to decay logarithmically, since the log-log plot of Fig. 3.5 reveals an approximately linear behavior. The dispersions are more pronounced for high values of the averaging time. It is worth noting that, unlike with the mapping $E_R(y^+, T^*) \rightarrow E_U(y^+, T^*)$,

the mapping $\|E_R\|(T^*) \rightarrow \|E_U\|(T^*)$ does not lead to a smoother behavior. It can be seen that for friction Reynolds numbers of $Re_\tau = 180$ and 590, we were able to attain the very low error levels of Vreman and Kuerten [162, 161]. It is known that, to obtain a reliable converged state, relatively fine grid and long statistical averaging times are required. Based on the present results, we can conclude that the averaging time has a significant effect on the quality of the averaged field, since we were able to reach the very small mean forces unbalancing of Vreman and Kuerten [162, 161] by using a longer averaging time and a coarser grid (see Tabs. A.2, A.3 to averaging times and Tabs. A.7 and A.8 to grid information).

According to Vreman and Kuerten [162], a recent trend in the investigation of turbulence by means of DNS is to increase the numerical resolution without increasing the Reynolds number, the so-called high-resolution DNS (HR-DNS). This procedure is established in order to obtain reliable statistics and was shown to be essential for an accurate prediction of higher statistical moments analysis, e.g. the prediction of dissipation spectra. In their work, Vreman and Kuerten [162] demonstrated that the high spatial resolution is important for a more correct and more accurate calculation of the smallest physical scales in the turbulent dissipation. Other works also showed the importance of HR-DNS, e.g., Vreman and Kuerten [163], Kozuka et al. [81] and Ishihara et al. [64]. For this reason and due to the importance given to HR-DNS, by establishing comparisons with the results of Vreman and Kuerten [162, 161], the present work sought to analyze the data of this kind of simulation when dealing with the criteria developed in the present work. The present results showed that even with a lower spatial resolution, the mean fields presented reached errors smaller than those calculated through HR-DNS. However, a longer averaging time was required, this fact highlights the importance of HR-DNS, even for low statistical moments order.

Some authors that in principle used the same averaging time, reached very different convergence levels. On the other hand, authors with different averaging times reached almost the same residual error, which confirms the fact that other parameters are also very important for the convergence of the mean field, e.g., time step, domain size, spatial and temporal discretization method, mesh quality, etc.

According to Vinuesa et al. [159], a sufficient averaging time to obtain an accurate converged velocity field in turbulent plane channel flow is about $10L_x/U_b$, where L_x is the streamwise channel length, U_b is the bulk velocity and L_x/U_b is the time flow through periods. Table 3.1 shows the approximated residual value at $10L_x/U_b$. It can be seen that $T = 10L_x/U_b$ represents a higher T^* at $Re_\tau = 180$ than at $Re_\tau = 590$. It also noticeable the fact that even if $\|E_R\| = 10^{-3}$ at both Reynolds, $\|E_U\|$ is higher at $Re_\tau = 590$ than at 180, what brings up the question about adopting the averaging time of $10L_x/U_b$ as a general criterion for different Reynolds numbers. Direct numerical simulation seeks to resolve the whole spectrum of turbulent structures, from the smallest ones

Re_τ	$T^* \approx$	$\|E_R\| \approx$	$\|E_U\| \approx$
180	92	10^{-3}	4×10^{-2}
590	78	10^{-3}	3×10^{-1}

Table 3.1 – Residual norms $\|E_R\|$ and $\|E_U\|$ at $T = 10L_x/U_b$.

(Kolmogorov scales) up to the largest eddies in the flow. When sampling errors are neglected and insufficient intervals are applied in the calculations of the averaged fields, the unbalance of the largest scales, which require longer averaging times, induce higher errors in the balance of the mean forces. If due attention is not given to these parameters, the sampling uncertainties can have higher magnitude than discretization errors.

The residual error norms computed from DNS databases from the literature corresponding to $Re_\tau > 590$ are shown in Table 3.2. It can be seen that Lee and Moser [88]

Author	Re_τ	T^*	$\|E_R\|$	$\|E_U\|$
Bernardini et al. [13]	999	177	6.4×10^{-3}	3.6
Bernardini et al. [13]	2021	98	3.5×10^{-3}	2.8
Bernardini et al. [13]	4079	55	5.3×10^{-3}	1.0×10^{1}
Del Álamo et al. [37]	934	112	1.1×10^{-3}	3.9×10^{-1}
Hoyas and Jiménez [62]	2003	135	8.0×10^{-4}	3.0×10^{-1}
Khoury et al. [74]	999	-	1.1×10^{-2}	6.3
Lee and Moser [88]	1000	164	1.6×10^{-4}	4.0×10^{-2}
Lee and Moser [88]	5186	68	1.7×10^{-3}	5.3
Lozano-Durán and Jiménez [96]	4179	16	2.6×10^{-3}	6.0
Thais et al. [146]	1000	35	3.1×10^{-3}	1.6
Wu and Moin [172]	1142	20	1.6×10^{-3}	1.0

Table 3.2 – Residual norms $\|E_R\|$ and $\|E_U\|$ at DNS database at $Re_\tau \geq 999$.

attained the smallest $\|E_R\|$ and $\|E_U\|$ at $Re_\tau = 1000$. Within the range of $Re_\tau \approx 2000$, Hoyas and Jiménez [62] obtained the smallest residual errors at $Re_\tau = 2003$. For the high range of friction Reynolds numbers, $Re_\tau > 4000$, we can stress the relatively low value of $\|E_U\|$ for $Re_\tau = 5186$ obtained from the DNS of Lee and Moser [88].

The residual norms of the experimental databases of Schultz and Flack [137] and den Toonder and Nieuwstadt [38] are given in Tables 3.5 and 3.4, respectively. From the results of Schultz and Flack [137] (Table 3.5) it is possible to observe that both norms, $\|E_R\|$ and $\|E_U\|$, are smaller at $Re_\tau = 1956$ than at $Re_\tau = 1010$, an apparently unexpected result, since the error has a tendency to increase for higher Reynolds numbers. However, we can see that $15-18\ \times10^3$ velocity samples were taken into account for the computation of the statistics for $Re_\tau = 1010$, whereas, for $Re_\tau = 1956$,

Re_τ	Velocity samples	$\|\|E_R\|\|$	$\|\|E_U\|\|$
1010	15 - 18 $\times 10^3$	2.5×10^{-2}	9.8
1956	35 - 40 $\times 10^3$	1.6×10^{-2}	5.4
4048	50 $\times 10^3$	1.8×10^{-2}	1.8×10^1
5895	50 $\times 10^3$	1.2×10^{-2}	2.3×10^1

Table 3.3 – Residual norms $||E_R||$ and $||E_U||$ of experimental databases provided by Schultz and Flack [137].

Re_τ	Velocity samples	$\|\|E_R\|\|$	$\|\|E_U\|\|$
1000	6 – 18 $\times 10^3$	3.5×10^{-2}	4.9

Table 3.4 – Residual norms $||E_R||$ and $||E_U||$ of experimental database provided by den Toonder and Nieuwstadt [38].

the statistical quantities were computed with $35 - 40 \times 10^3$ velocity samples. Therefore, we can conclude that this difference in the samplings was able to compensate for the effect due to the increase of the Reynolds number. This reinforces the line of thought of the present thesis, namely, that the output of the statistical quantities provided by experiments and DNS needs more samples to achieve a representative mean value. The comparison between the $||E_U||$ norm associated to the data originating from the $Re_\tau = 4048$ and 5895 cases shows that since they have the same number of velocity samples, the higher Reynolds number case presents higher residual errors for U. If a similar error norm was a target, more samples were needed for higher Reynolds number.

Figure 3.6 shows the evolution of the norms $||E_R||$ and $||E_U||$ as functions of the averaging time for the different Reynolds numbers simulated in the present thesis, namely $Re_\tau = 180$ and $Re_\tau = 590$.

It may be noted that the value of $||E_R||$ and $||E_U||$ can be higher or lower for a given Re_τ depending on the averaging time. For example, for short averaging times ($T^* < 10^2$), the values of $||E_U||$ are higher at $Re_\tau = 590$ than at $Re_\tau = 180$, however, for longer averaging time ($T^* > 10^2$), the behavior of $||E_U||$ at both Reynolds numbers becomes scattered and it is no longer possible to predict in which Reynolds number the errors will be larger. Thus, a conclusion that can be made is that the number of samples or averaging time interval directly influences which Reynolds number will present the higher errors. This behavior seems to explain the fact shown at Tab. VIII, where at $Re_\tau = 5895$, the value $||E_R||$ is smaller than those obtained at smaller Reynolds number, $Re_\tau = 4048$, when the velocity samples are of some number.

To define the convergence rate of each criterion, logarithmic regression for $||E_R||$ and $||E_U||$ were computed and are also presented in the figures. It can be noted that, mainly

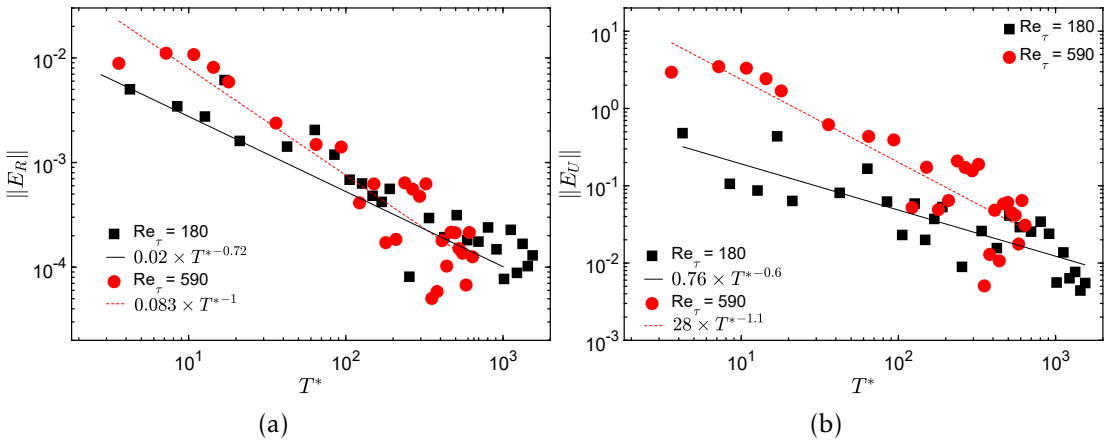

Figure 3.6 – Development of residual norms $\|E_R\|$ and $\|E_U\|$ at $Re_\tau = 180$ and $Re_\tau = 590$ as function of the averaging time. (a) Reynolds stress tensor residual norm $\|E_R\|$ and (b) mean velocity residual norm $\|E_U\|$.

for longer averaging time, the data become quite dispersed and a logarithmic regression is less representative and do not provide a fair representation of the results. However, the main reason for the employment of a representative curve obtained by logarithmic regression is the characterization of the decay tendency of the error depending on the averaging time. In this way, it is possible to obtain a quantitative comparison of the convergence rates of the different Reynolds numbers explored in the present work and also between E_R and E_U. In order to have a quantitative information of how close to a log pattern is the error distribution over the time, the correlation coefficient, R^2, were calculated. For the $\|E_R\|$ case, R^2 are given by 0.88 and 0.86 at $Re_\tau = 180$ and 590, respectively. For the $\|E_U\|$ case, R^2 was found to be 0.72 at $Re_\tau = 180$ and 0.79 at $Re_\tau = 590$. It is possible to verify that the norms computed from Eqs. 2.13 and 2.14 presented a similar behavior for the range of Reynolds numbers investigated in the present study. This result can be helpful for future studies on the convergence of the data statistics of DNS, since it provides a guideline. The logarithmic regression curves show a pattern behavior of each Reynolds number convergence criterion. At small averaging time, $Re_\tau = 590$ presents higher errors. However, since it presents a higher convergence rate than at $Re_\tau = 180$, i.e. T^{*-1} for $\|E_R\|$ and $T^{*-1.1}$ for $\|E_U\|$, its residual values achieve the same magnitudes computed at $Re_\tau = 180$ when the averaging time is increased. The criterion proposed in the present work measures the mean force unbalance through the analysis of the mean streamwise velocity and the Reynolds shear stress fields. This unbalance comes from the comparison between well known theoretical relations and the values coming from DNS or experimental test. It is known that the mean field of a given turbulent flow is influenced by several wavelengths in a continuous spectrum that extends from the smallest (Kolmogorov) scales up to the larger scales influenced by the flow geometry. Based on this rationale, one can attribute

the dependence of the exponents values on the Reynolds number to the fact that for higher values of Re, the Kolmogorov scales are smaller and these small scales tend to a faster convergence of statistical quantities, since they have higher frequencies.

A more detailed procedure can be used to distinguish the behaviors of the norms in each region, in order to examine the similarities among the different Reynolds numbers at the viscous sublayer, the buffer layer, and the log-law regions. Hence, an integral residual norm based on Eqs. 2.13 and 2.14 can be defined:

$$\|E_E\|_{y_1^+,y_2^+} = \sqrt{\frac{1}{\left(y_2^+ - y_1^+\right)} \int_{y_{min}^+}^{y_{max}^+} [E_R(y')]^2 \, dy'}. \tag{3.4}$$

$$\|E_U\|_{y_1^+,y_2^+} = \sqrt{\frac{1}{\left(y_2^+ - y_1^+\right)} \int_{y_{min}^+}^{y_{max}^+} [E_U(y')]^2 \, dy'}, \tag{3.5}$$

where y_{min}^+ and y_{max}^+ are, respectively, the y^+ minimum and maximum for each region, i.e., at the viscous sublayer: $(y_{min}^+, y_{max}^+) = (0, 5)$, at the buffer layer, $(y_{min}^+, y_{max}^+) = (5, 30)$, and in the log-law region, $(y_{min}^+, y_{max}^+) = (30, Re_\tau)$. Figure 3.7 shows the evolution of the residual norms $\|E_R\|_{y_1^+,y_2^+}$ and $\|E_U\|_{y_1^+,y_2^+}$ as functions of the averaging time for the different regions. Within the viscous sublayer, both $\|E_R\|$ and $\|E_U\|$ present, even for short averaging times, residuals of the same order of magnitude as those achieved by the global residuals with the longest averaging time employed (see Fig. 3.6). This indicates that the convergence there occurs much faster than in higher layers. Moreover, it is remarkable how $\|E_R\|_{0,5}$ at $Re_\tau = 590$ shows very small variations compared to all the other residuals analyzed in Fig. 3.7. This behavior suggests that the mean velocity field converged very quickly in that case. Regarding the residuals within the buffer layer, the order of magnitude of $\|E_R\|$ is comparable to that of the residuals within the log-law region. The mean velocity residuals have an order of magnitude comparable to those within the viscous sublayer. One can conclude that the statistically converged state for the Reynolds stress tensor is achieved faster than the corresponding state for the mean velocity in the buffer layer. Comparing Fig. 3.7 with Fig. 3.6, we can see the influence of the log-law region on the overall result.

In order to establish comparisons between the uncertainty criteria applied in the present work ($\|E_R\|$ and $\|E_U\|$) and the convergence evolution of different flow statistical moments, like the enstrophy and the TKE, we evaluate and examine a relative deviation of several mean fields (coming from different parcial averaging time) with respect to the previous one. The relative deviation of a quantity θ between the mean field calculated over an interval of T^* and its neighborhood (in time) value is calculated as follows

$$\Delta\theta(T^* + \Delta T^*, y^+) = \frac{\theta(T^*, y^+) - \theta(T^* + \Delta T^*, y^+)}{\theta(T^* + \Delta T^*, y^+)} \tag{3.6}$$

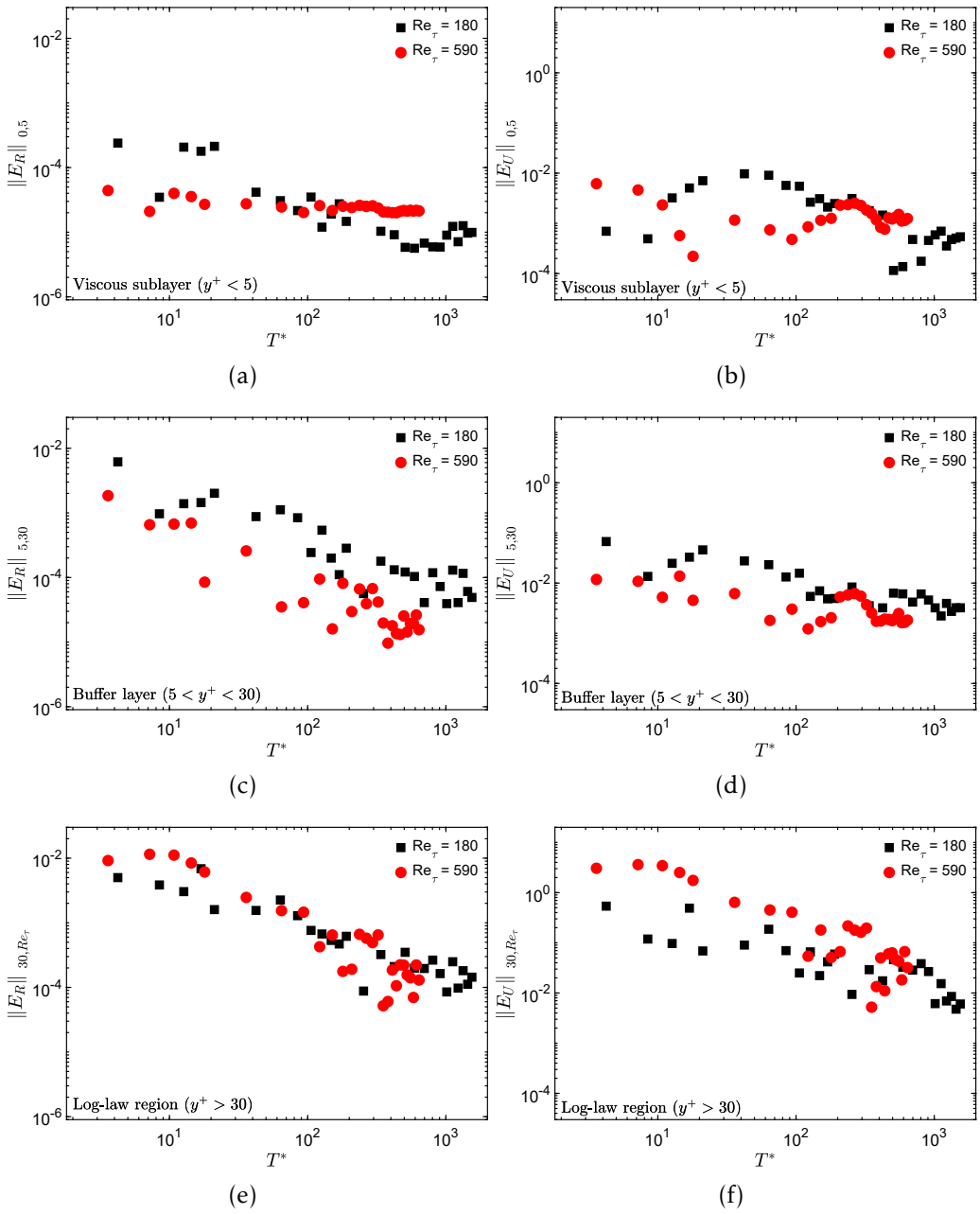

Figure 3.7 – Development of residual norms $\|E_R\|$ and $\|E_U\|$ at $Re_\tau = 180$ and $Re_\tau = 590$ in different regions as function of the averaging time. (a) Reynolds stress tensor residual norm $\|E_R\|$ and (b) mean velocity residual norm $\|E_U\|$.

In this sense, this error measurement has an instantaneous character. The logarithmic regressions applied in Fig. 3.7 are useful for a direct comparison between the decay rate for the two Reynolds numbers studied, even when these data are scattered. These exponents reflect the convergence behavior of different statistical moment orders with respect to a more converged field and seems to be related to the highest intensity wavelengths of each of the variables.

The normalized enstrophy in wall-scale unit is defined as the vorticity fluctuations

amplitude, yielding:

$$\xi^+ = \frac{h^2}{u_\tau^2}\frac{\overline{\omega_i'\omega_i'}}{2}, \tag{3.7}$$

where ω_i' are the components of the fluctuating part of the vorticity first order tensor ($\omega_i = 0.5\epsilon_{ijk}\partial u_k/\partial x_j$).

The turbulent kinetic energy is defined as:

$$K^+ = \frac{1}{u_\tau^2}\frac{\overline{u_i'u_i'}}{2}. \tag{3.8}$$

Figure 3.8 displays the TKE profile across channel half-width computed by applying different averaging times as well as its residual. The non-dimensional mean kinetic

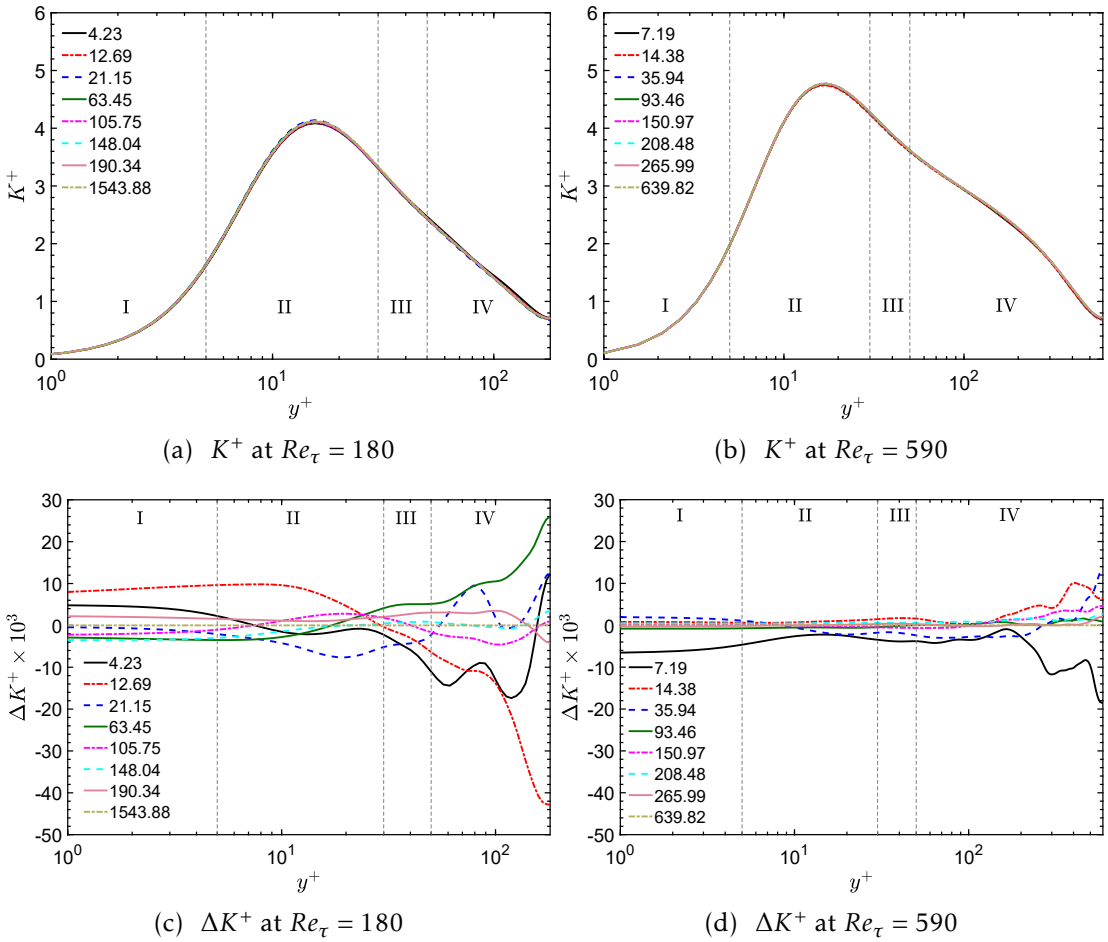

(a) K^+ at $Re_\tau = 180$ (b) K^+ at $Re_\tau = 590$

(c) ΔK^+ at $Re_\tau = 180$ (d) ΔK^+ at $Re_\tau = 590$

Figure 3.8 – Mean turbulent kinetic energy, K^+, and its relative deviation from the most converged field, ΔK^+ for several averaging time at $Re_\tau = 180$ and 590.

energy K^+ intensity not surprisingly increases with Reynolds number. However, its peak is approximately located at the same position in the buffer layer, $y^+ \approx 16$, and does not change for the higher Reynolds number. Despite its peak is found in Region *II*,

the largest relative deviations are not necessary located in this region, the residual is approximately constant in Regions I, II and III with an increase in Region IV. The residuals at $Re_\tau = 180$ have apparently revealed to be higher than at $Re_\tau = 590$ for smaller averaging times, what can possibly be associated to other simulation parameters such as the number of grid points, for instance.

The normalized enstrophy in wall-scale unit, ξ^+, and its deviation are presented in Fig. 3.9. It can be noticed that, as for the TKE, the peak level increases with the increase

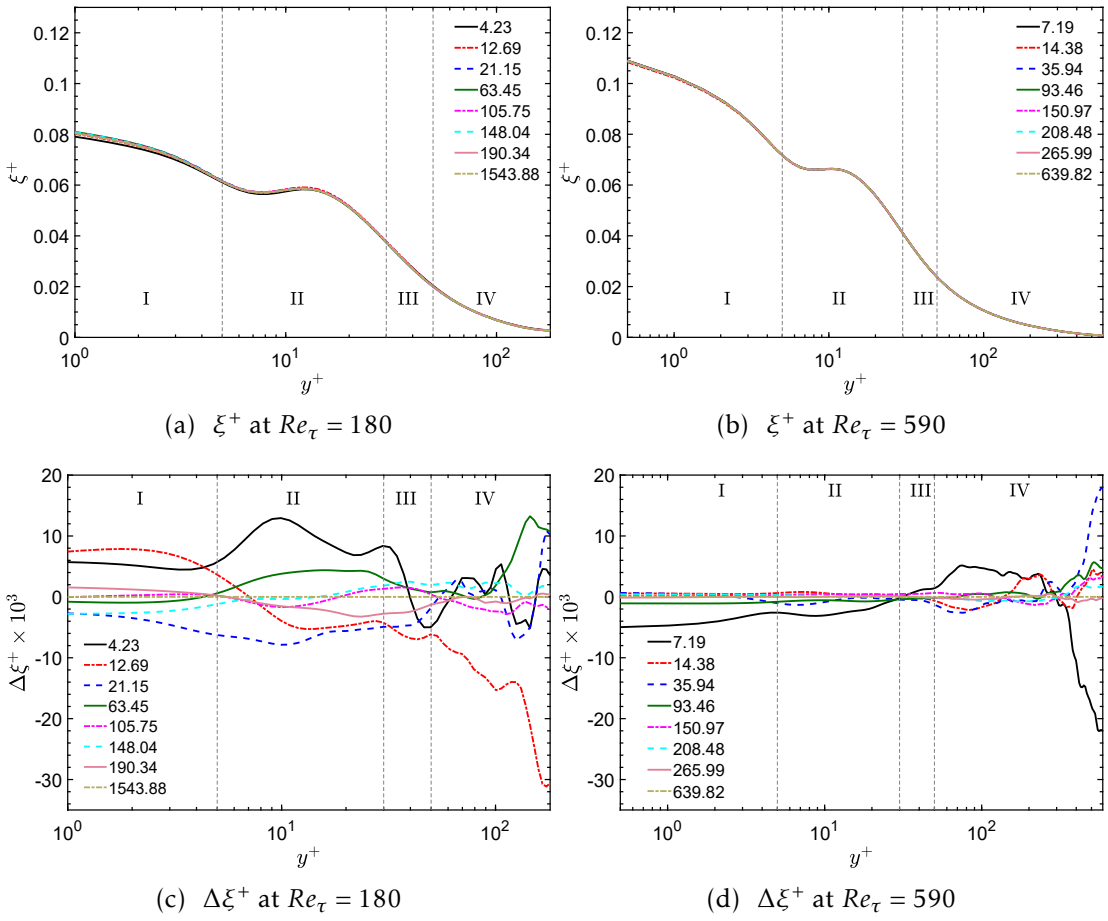

(a) ξ^+ at $Re_\tau = 180$ (b) ξ^+ at $Re_\tau = 590$

(c) $\Delta\xi^+$ at $Re_\tau = 180$ (d) $\Delta\xi^+$ at $Re_\tau = 590$

Figure 3.9 – Mean enstrophy, ξ^+, and its relative deviation from the most converged field, $\Delta\xi^+$ for several averaging time at $Re_\tau = 180$ and 590.

of the Reynolds number. On the other hand, the two peak locations remain in the same position. The enstrophy deviation presents approximately constant values in Regions I, II and III with a peak in the center of the channel. It also revealed higher values at $Re_\tau = 180$ than at 590 for small averaging time.

Figure 3.10 displays the evolution of the root-mean-square (RMS) norm of the TKE and the enstropy relative deviation as function of the averaging time for different Reynolds number. The logarithmic regression curve is also plotted in the figure and indicates the decaying order of each scalar convergence.

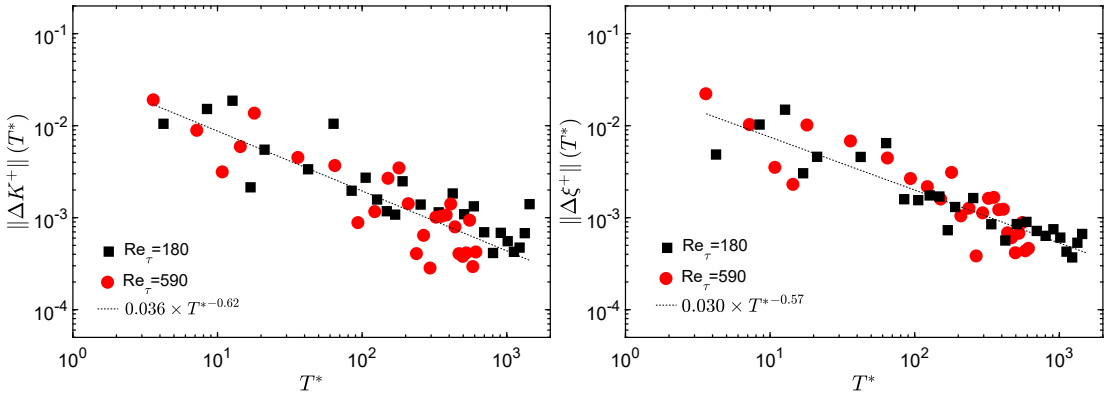

(a) K^+ (b) ξ^+

Figure 3.10 – Development of relative deviation RMS norms $\|\Delta K^+\|(T^*)$ and $\|\Delta \xi^+\|(T^*)$ at $Re_\tau = 180$ and $Re_\tau = 590$ as function of the averaging time.

It can be noticed that the decaying order of $\|\Delta K^+\|$ and $\|\Delta \xi^+\|$ are similar for both Reynolds number. This shows that, mathematically, the averaged fields tend to a final mean field in a similar fashion, independently of the Re. However, this behavior is different from what was observed for $\|E_U\|$ and $\|E_R\|$, where the $Re_\tau = 590$ shows convergence rates higher than $Re_\tau = 180$ (see Fig. 3.6). One can attribute this difference in methodologies to the fact that the results displayed in Fig. 3.7 are purely numerical and do not take into account physical aspects. On the other hand, in Fig. 3.6, the convergence rate is higher at $Re_\tau = 590$, what can be possibly attributed to the fact that at higher Reynolds number, smaller turbulent structures are found and their averaging value converges faster, as explained previously. An interesting fact that can be observed is that the decaying order is higher for the TKE than the enstrophy. This can be explained by the fact that the enstrophy represents a higher statistical moment order than the TKE.

It is known that ξ^+ and K^+ have their peaks in different regions of the channel, as can be seen in Figs.3.8 and 3.9. This fact motivated us to understand the convergence of these variables, since they are more intense on different regions of the channel. Another important physical behavior that motivated the study of the convergence of these two variables, K^+ and ξ^+, is the fact that they are dominated by wavenumber lengths that belong to different regions of the wave-number spectrum (κ). While K^+ is more intense at the smaller wave-numbers, ξ^+ is dominated by the largest κ. The logarithmic regression applied in Fig. 3.10 are useful for a direct comparison between the decay rate for the two Reynolds numbers studied, even when these data are scattered. In this sense, the residuals ΔK^+ and $\Delta \xi^+$ are associated to a reference. In this case the corresponding previous value of averaging time. The trajectory of the residual, as measured by this second method, does not reflect an evolution of accuracy, it measures a convergence

rate without approaching the matter of accuracy.

Table 3.5 presents the convergence decay order of several properties of the flow. The variables are listed as A and B, representing the coefficients of logarithmic regression given by: $\Delta\theta(T^*) = AT^{*B}$.

	$Re_\tau = 180$		$Re_\tau = 590$	
θ	A	B	A	B
ξ^+	0.024	−0.57	0.036	−0.58
K^+	0.032	−0.61	0.039	−0.63
U^+	0.0048	−0.51	0.0025	−0.54
u^+_{RMS}	0.025	−0.56	0.020	−0.57
v^+_{RMS}	0.030	−0.63	0.024	−0.66
w^+_{RMS}	0.024	−0.63	0.029	−0.74

Table 3.5 – Logarithmic regression coefficients A and B of several mean field convergence of variables of the flow, where $\Delta\theta(T^*) = AT^{*B}$. ξ^+ is the enstrophy, K^+ is the turbulent kinetic energy, U^+ is the mean streamwise velocity, u^+_{RMS}, v^+_{RMS} and w^+_{RMS} are the RMS value of the fluctuating part of velocity in x, y and z directions, respectively. All variables are listed in wall unit.

Conclusions are found in Sec. 4.1.

3.2 Evaluation of spectral budget in DNS data of turbulent channel flow

In this section, the results of the evaluation of spectral budget in DNS data of turbulent channel flow for turbulent channel flows are presented and compared with those coming from literature.

To compute the various source terms of the energy transfer process (Eq. 2.25), several instantaneous three-dimensional velocity flows field are required. The terms of Eq. 2.25 were computed by using DNS data in the form of snapshots. Data were obtained with the NNEWT code (Sec. 3.1.1). A total of 105 snapshots during 1050 s of simulation were used for $Re_\tau = 180$ and 460 snapshots during 92 s were used for $Re_\tau = 1000$. In wall units, the sampling time is given by $Tu_\tau/h = 67.5$ and 4.7 at $Re_\tau = 180$ and 1000, respectively. These values represent, respectively, $\approx 50L_x/U_b$ and $\approx 6L_x/U_b$. In the present work, we have focused on the spatial/spectral analysis at a selection of homogeneous planes. According to Marati et al. [102], temporally uncorrelated configurations are needed to obtain reliable statistics. According to Oliver et al. [118], to reduce the correlation, the samples used to compute statistics are sometimes taken "far" apart in time and then treated as independent, it can lead to underestimated uncertainty if the snapshots are not sufficiently separated. If is necessary that the time snapshots be

sufficiently separated and independent, at a fixed spatial point this requires that the time separation be such that the two-point time correlation of the random variables be small. Since the low Reynolds number cases are dominated by large structures which have long time constants, it is reasonable that the 180 case have a snapshot separation time much larger than the 1000 case.

First, in Fig. 3.11 we present the Kolmogorov time and length scales depending on the distance from the wall at $Re_\tau = 180$ and 1000, both are in wall units. Good

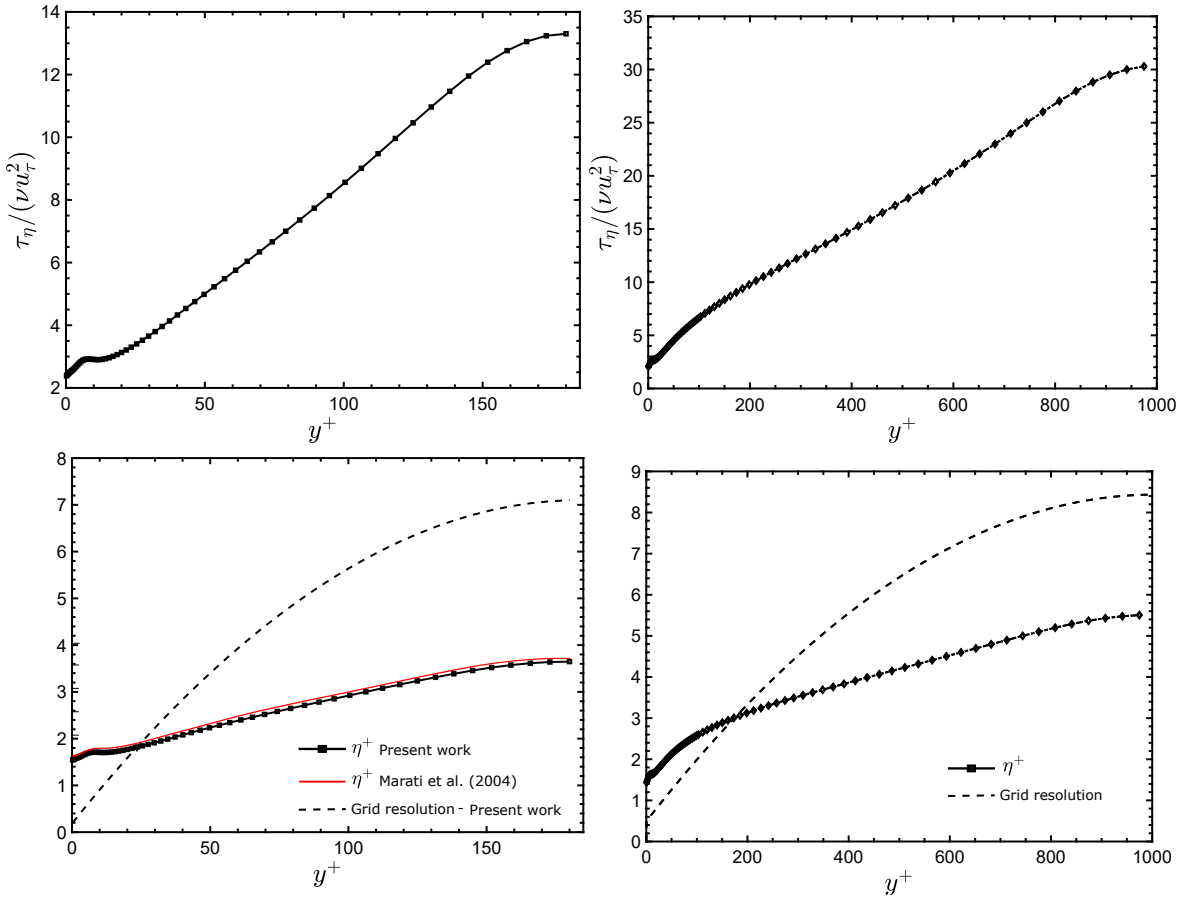

Figure 3.11 – The Kolmogorov scale vs. distance from the wall y^+ at $Re_\tau = 180$ and $Re_\tau = 1000$. (a) and (b) Kolmogorov time scale normalized by the inner time scale (ν/u_τ^2) at $Re_\tau = 180$ and 1000, respectively; (c) and (d) length scale in wall unit and grid resolution in x_2-direction at $Re_\tau = 180$ and 1000, respectively. Comparisons are established with Marati et al. [102] at $Re_\tau = 180$.

match are found between our results and those of Marati et al. [102] at $Re_\tau = 180$. In Figs. 3.11-(c) and (d) we present comparisons between the Kolmogorov length scale and the grid resolution in x_2-direction applied in the present work. It is apparent that the orders of the smallest length and time scales are respected in the present simulation and the parameters are sufficient to achieve a well-resolved DNS. Since it is required that the smallest resolved lengthscale is of $O(\eta)$ Moin and Mahesh [111].

Comparison of the total turbulent kinetic energy (Eq. 2.34) and the ratio of pro-

duction to dissipation between the present thesis and results of Moser et al. [117], Del Álamo et al. [37] and Thais et al [147] is shown in Fig. 3.12, where statistical quantities were calculated directly from the spatially averaged quantities with no reconstruction from the spectral domain.

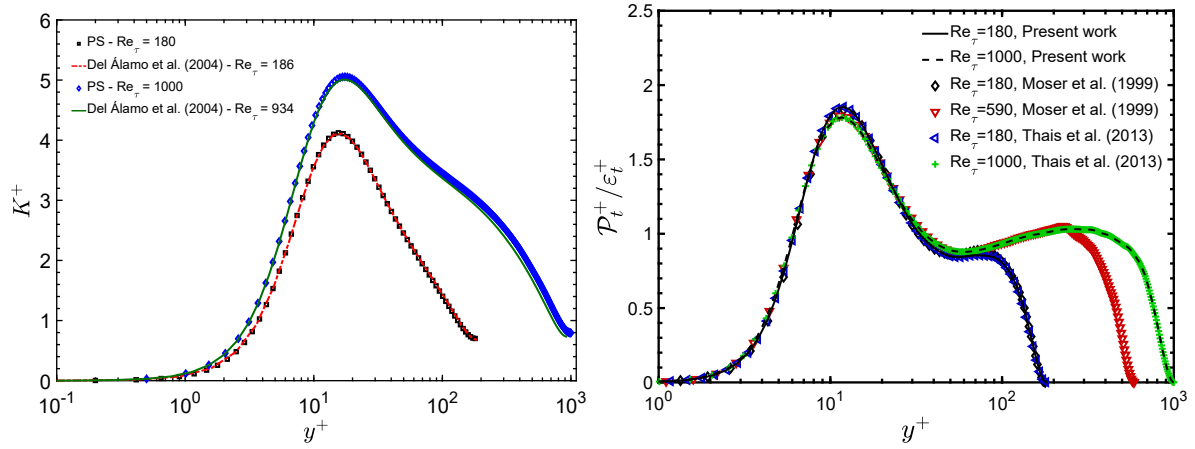

Figure 3.12 – Comparisons with results of Moser et al. [117], Del Álamo et al. [37] and Thais et al [147]: (a) Total turbulent kinetic energy dependence on the normalized distance from the wall and (b) ratio of production to dissipation of turbulent kinetic energy.

From Fig. 3.12-(a), at $Re_\tau = 180$, the present result is in good agreement with that of Del Álamo et al. [37]. At $Re_\tau = 1000$, the maximum occurs at the same y^+ location as $Re_\tau = 180$, at a slightly higher value. Figure 3.12-(b) shows the same behavior for all the Reynolds numbers up to $y^+ \approx 80$. The lines reach a peak at $y^+ \approx 12$ and then decline followed by a bottoming until the center of the channel. An expected behavior for high-Reynolds number channel flows is that the production and dissipation of turbulent kinetic energy will be approximately balanced in the log region. From the present results, the ratio of production to dissipation is about one over the range $50 < y^+ < 350$. In particular, at $Re_\tau = 1000$, the ratio is closer to one than at $Re_\tau = 180$. At $Re_\tau = 180$, since it is a low Reynolds number, the log layer region is narrow, and the region where production balancing dissipation holds is restricted.

The TKE balance across the channel half-width is shown in Fig. 3.13 at $Re_\tau = 180$ and 1000. Its calculation was computed from the summing over all κ^+ of each spectral term of Eq. 2.25, that is

$$\theta_t^+(y^+) = \int_{\kappa^+} \theta^+(\kappa^+, y^+) d\kappa^+, \tag{3.9}$$

where each term of Eq. 2.25 is integrated across the entire wavenumber spectrum and becomes function only of y^+ (Eq. 2.36). The dynamic balance depending on the distance from the wall is well-known and presented here for validation. For both Reynolds number, $Re_\tau = 180$ and 1000, there is a peak of turbulent production located at $y^+ \approx 12$

and the balance between viscous diffusion and turbulent energy dissipation rate is evident. The pressure transport plays a relatively minor role. Both components of the energy dissipation rate are negative, as expected. The rate of inter-plane dissipation makes a significant contribution to the overall balance across the whole wall-distance y^+ with a maximum value at the wall. On the other-hand, the in-plane dissipation component reaches a peak at $y^+ \approx 15$ and tends to zero elsewhere. For the turbulent transport, for $y^+ < 9.9$ there is a competition between both terms, for which the in-plane turbulent transport is negative and the inter-plane turbulent transport is positive, whereas for $y^+ > 9.9$ both terms are negative and become a sink of energy. The residual is referenced in the figure as "Balance".

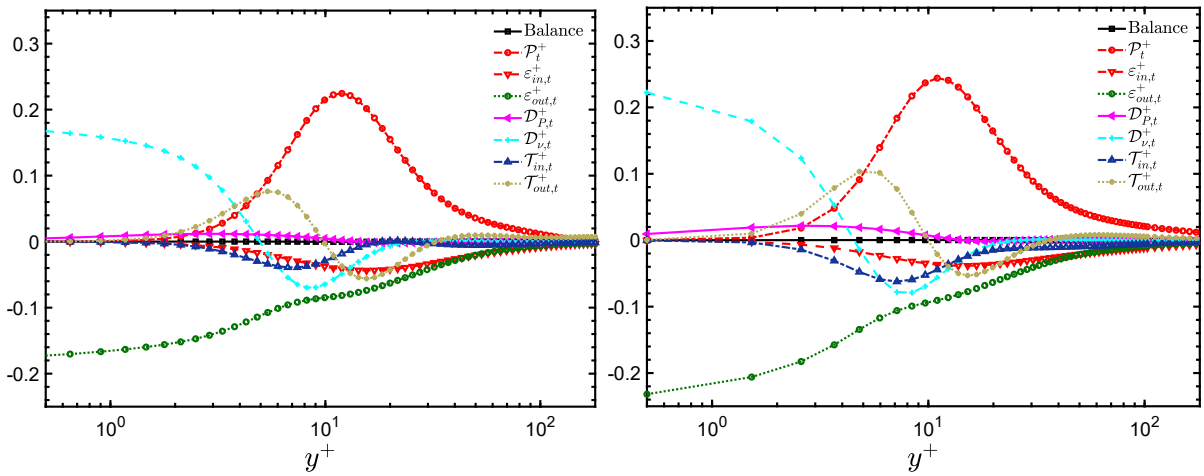

Figure 3.13 – Turbulent kinetic energy budget (Eq. 2.36) at $Re_\tau = 180$ and 1000, respectively.

In order to understand the role of each term in terms of spatial influence, the channel half-width is divided into four distinct regions (e.g., Pope [127]): I–viscous sub-layer ($y^+ < 5$), II–buffer layer ($5 < y^+ < 30$), III–log-law region ($y^+ > 30, y/h < 0.3$) and IV–outer layer ($y^+ > 50$).

Seeking to look into the differences between the in- and inter-plane energy dissipation rate, Fig. 3.14 shows both terms as well as its sum, $\varepsilon_{tot,t}^+$, compared to the results of Moser et al. [117] and Thais et al [147]. Although there is a difference between $Re_\tau = 180$ and 1000, both results present a similar behavior. The total energy dissipation rate is in good agreement with the reference results. At $Re_\tau = 1000$, one can notice that the ratio of inter-plane to in-plane dissipation is higher than at $Re_\tau = 180$. Discrepancies between the total dissipation of the present work and the one obtained by Thais et al [147] at $Re_\tau = 1000$ are noticed. This difference can be consequence of the calculation procedure established to compute this statistics, for which the data are firstly decomposed to a partially Fourier domain (wall parallel directions) and, then, we reconstruct from the spectral domain the averaged quantities through an integration

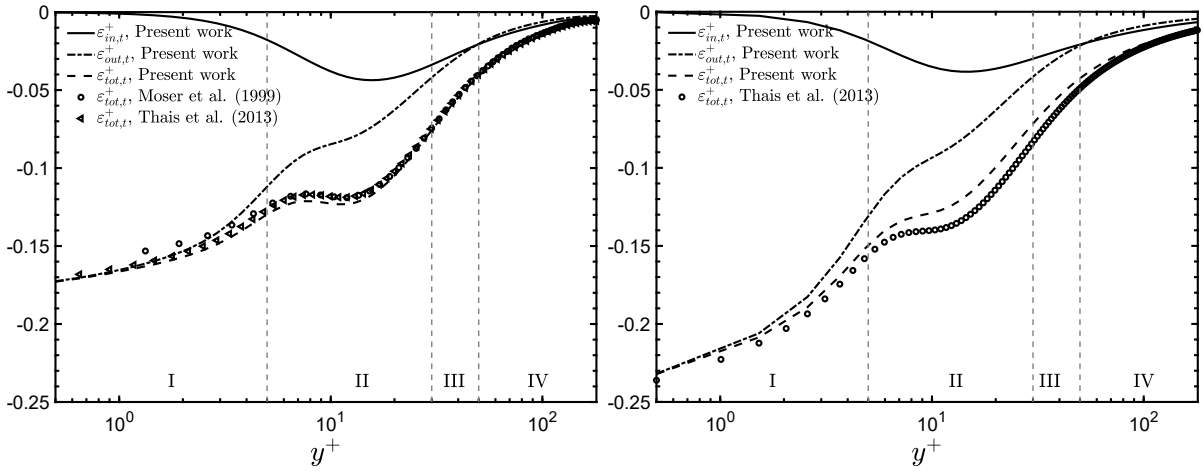

Figure 3.14 – In-plane, $\varepsilon^+_{in,t}$, and inter-plane, $\varepsilon^+_{out,t}$, dissipation contributions to the total dissipation, $\varepsilon^+_{tot,t}$, at $Re_\tau = 180$ and 1000, respectively. Comparisons with results of Moser et al. [117] and Thais et al [147].

process over the wave-number (Eq. 3.9). Since the κ^+ range is (numerically) limited, the integration process does not reach the complete wave-number bandwidth necessary to restore the terms again to the physical domain and information is lost in this procedure. These deviations come from the post-processing procedure and do not compromise the analysis of the results.

As noticed in Fig. 3.14, the inter-plane dissipation rate is dominant and dictates the total dissipation close to the wall (Region I). This behavior comes from the fact that the velocity gradient is maximum at this location, while the in-plane dissipation is negligible due to the behavior of K^+ (cf. Fig. 3.12). The in-plane dissipation has a peak at $y^+ \approx 12$ (Region II), where TKE and production are maximum (cf. Figs. 3.12 and 3.13). At the outer-layer, Region IV, $\varepsilon^+_{in,t}$ becomes dominant and this behavior is maintained up to the mid-channel region. The inter-plane dissipation is higher at $Re_\tau = 1000$, while the in-plane dissipation presents similar values at both Reynolds number.

It is also relevant to understand the differences between the in- and inter-plane turbulent transfer rate, whose behavior and sum are presented in Fig. 3.15. Two peaks of total transfer are noticed in the plot. The first one, positive, is located at $y^+ \approx 5$ and the second, negative, is located at $y^+ \approx 12$. They are both dictated by the inter-plane transfer term. In Region I, in-plane transfer acts as a sink of energy and the inter-plane term acts as a source, but this behavior is inverted in Region II. At $Re_\tau = 1000$, due to its broad log-law layer, the in- and inter-plane terms tend to zero in the center of the channel. While at $Re_\tau = 180$, as a consequence of the narrow log-law layer, the inter-plane transfer contributes to a non zero turbulent transfer close to the channel centerline, this behavior was also noticed by Bolotnov et al. [17]. In Region IV, the

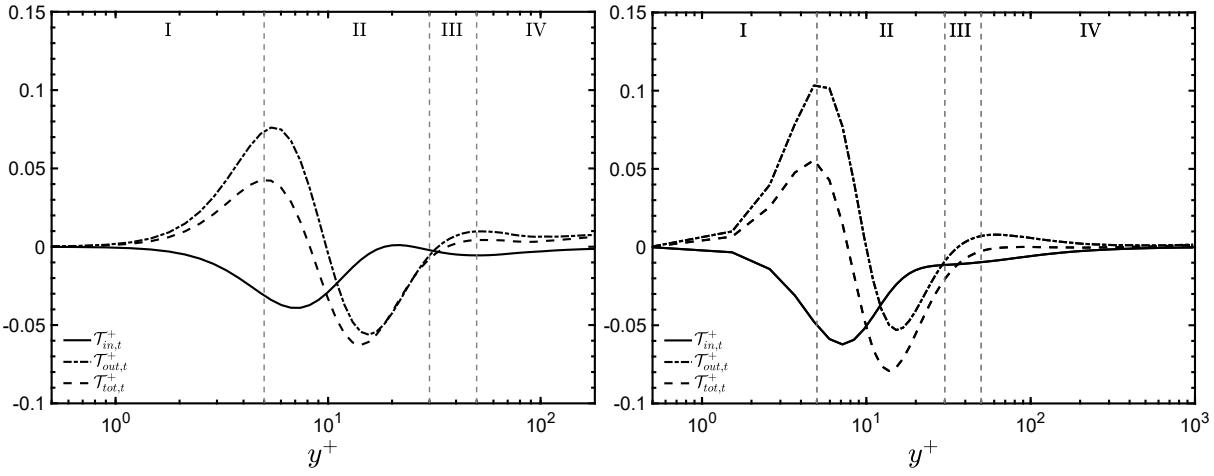

Figure 3.15 – In-plane, $\mathcal{T}^+_{in,t}$, and inter-plane, $\mathcal{T}^+_{out,t}$, nonlinear transfer contributions to the total nonlinear transfer, $\mathcal{T}^+_{tot,t}$, at $Re_\tau = 180$ and 1000, respectively.

in- and inter-plane transfer will be approximately balanced. Is is important to point out that the simulations were run with appropriate mesh resolution, time step and averaging time. However, when it comes to the post-processing, a reduced number of grid points is considered in the wall normal direction since the number of discretized points in the simulation grid would be unnecessary to the developed analysis.

It is interesting to compare the energy spectrum density at a fixed position from the wall ($y^+ \approx 40$) at several Reynolds numbers (Fig. 3.16). Note that the spectral densities are normalized here using wall units. As shown in Fig. 3.16, the results at higher wavenumbers ($\kappa^+ \geq 3 \times 10^{-2}$), coincide. However, at lower κ^+, each result presents a different behavior depending on the Reynolds number.

According to Marati et al. [102], since the inhomogeneity present in near-wall turbulence creates energy fluxes in the spatial domain that correspond to the spatial redistribution of turbulent kinetic energy, it is worth to analyze the spatial variation of turbulent kinetic energy spectral density at various y^+ locations (Fig. 3.17). The spectra are given for 8 wall-normal positions extending from the wall to the channel center. A first observation that can be established is the fact that the spectral band for $Re_\tau = 1000$ ($5 \times 10^{-4} \geq \kappa\eta \geq 1$) is wider than that of $Re_\tau = 180$ ($1 \times 10^{-3} \geq \kappa\eta \geq 1$), where η is the Kolmogorov length scale [126]. At higher Reynolds number, at mid-channel region, the energy spectrum density matches the $-5/3$ slope of the inertial subrange in the region $2 \times 10^{-2} \geq \kappa\eta \geq 2 \times 10^{-1}$, which can be taken as an indication of an approach to local isotropy. On the other hand, closer to the wall, the spectrum shape is more distributed along $\kappa\eta$ and is less intense indicating the constriction of larger scales in this region.

Figure 3.18 shows the in-plane and inter-plane dissipation rate contributions to the total dissipation in the middle of the channel depending on the wavenumber. In an isotropic and homogeneous turbulent flow Tennekes and Lumley [145], the total

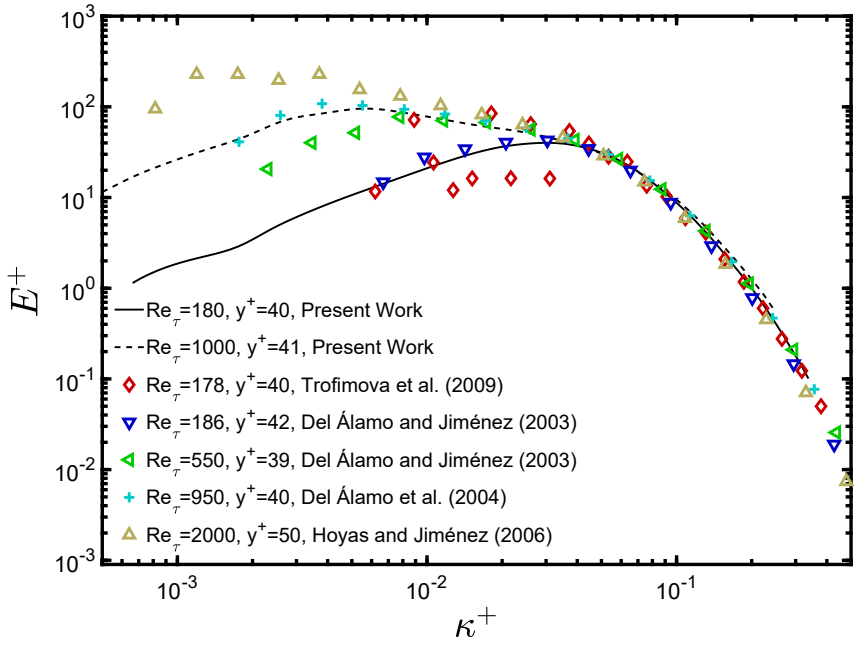

Figure 3.16 – Energy spectrum density at $y+ \approx 40$: present results compared to DNS data from Trofimova et al. [155], Del Álamo and Jiménez [36], Del Álamo et al. [37], and Hoyas and Jiménez [62].

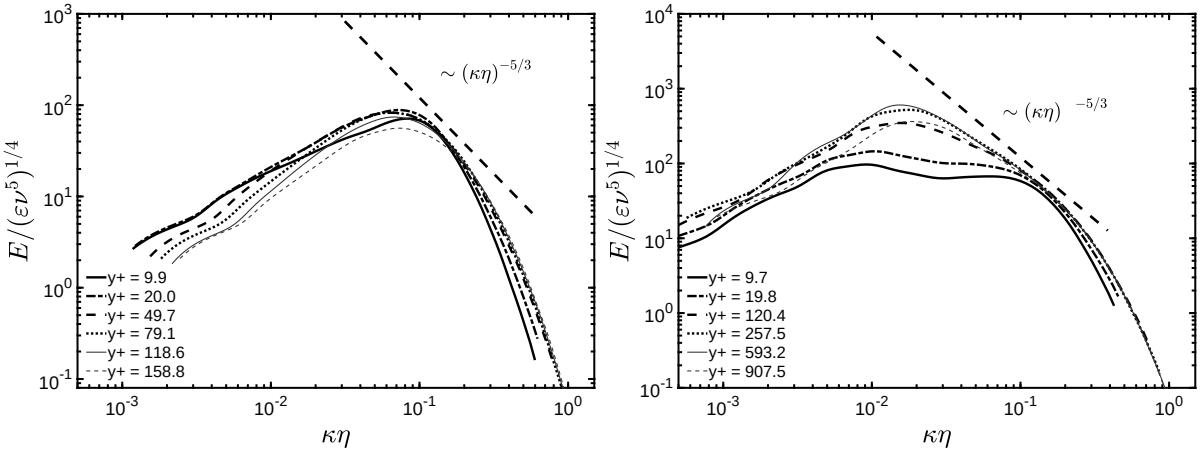

Figure 3.17 – Non-dimensional energy spectrum density $E/(\varepsilon\nu^5)^{1/4}$ at various y^+ locations at $Re_\tau = 180$ and 1000, respectively.

energy dissipation rate spectrum density should match the 1/3 slope in the inertial subrange, that is, close to the mid-channel region. This behavior is more evident at $Re_\tau = 1000$. It also can be noticed that each term (in-plane and inter-plane) dictate the total dissipation rate at a different range. The inter-plane is more influential at small $\kappa\eta$, i.e. $\kappa\eta \leq 0.045$ at $Re_\tau = 180$ and $\kappa\eta \leq 0.02$ at $Re_\tau = 1000$, while the in-plane dissipation dominates at higher wavenumbers. The geometric symmetry at the channel centerline would preclude any cross-plane transfer at the centerline itself. As the centerline is approached only smaller scale in-plane motions can contribute to the

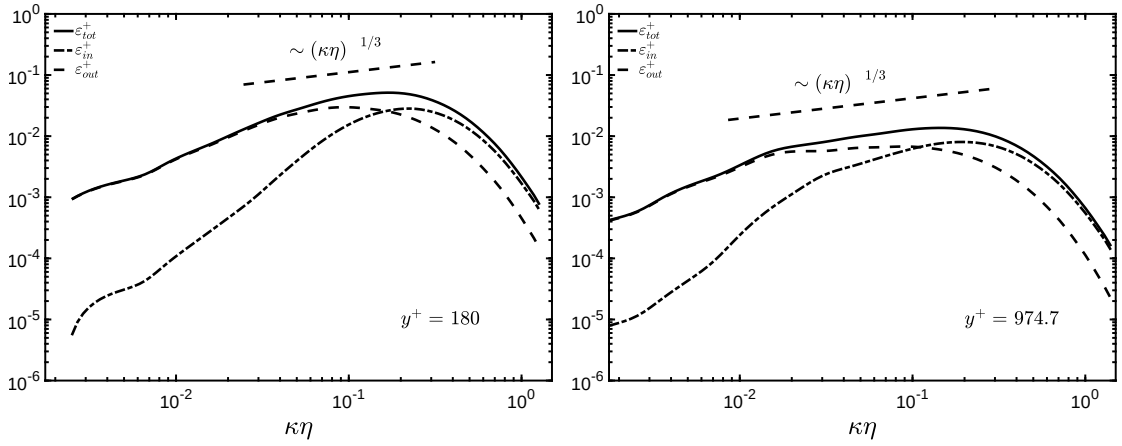

Figure 3.18 – Turbulent dissipation spectra in the middle of the channel at $Re_\tau = 180$ and 1000, respectively.

energetic dynamics.

3.2.1 Spectral density of source terms to the TKE

In Figs. 3.19-3.28 a comparison between $Re_\tau = 180$ and 1000 of the spectral density of the various source terms on the right-hand side (RHS) in Eq. 2.25 as a function of $\kappa\eta$ is shown. The terms are normalized according to Eq. 2.37.

The turbulence production spectra density (Eq. 2.27) is shown in Fig. 3.19. The

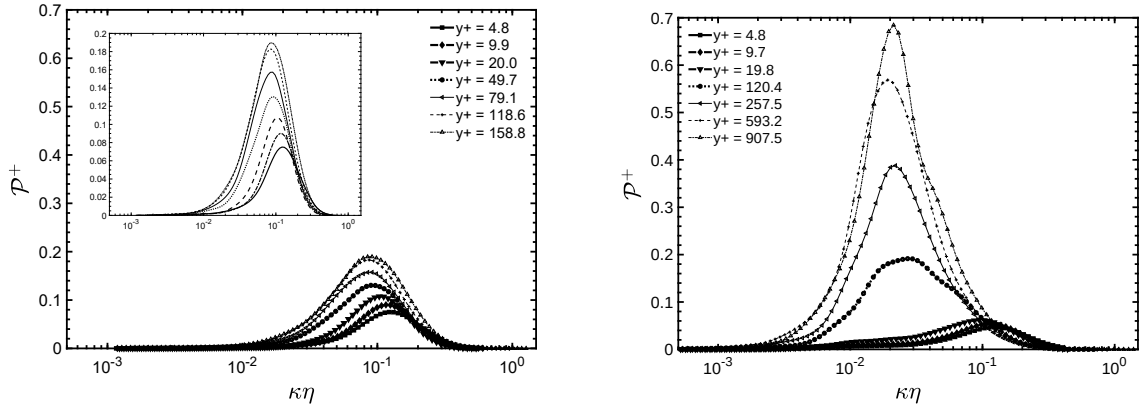

Figure 3.19 – Turbulent production spectral density, $\mathcal{P}^+$, at various y^+ location at $Re_\tau = 180$ and 1000, respectively.

significant influence of increased Reynolds number is evident. At $Re_\tau = 1000$, the range of affected spectral scales increases with distance from the wall relative to the $Re_\tau = 180$ flow. Nevertheless, in both cases there is a shift in the location of the peak of energy production towards larger scales ($\kappa\eta$ decreases) of motion with increasing distance from the wall. This behavior comes from the fact that close to the wall, the largest scales are

spatially restricted. This fact results in the observed shift in the production spectrum. Associated with this shift is a significant increase in the peak energy production level at the lower wavenumber range especially as the channel centerline is approached. At the higher wavenumbers in close proximity to the wall, the energy production at both low and high Reynolds number is similar. This suggests a relatively small change with Reynolds number in energy being supplied to the small scale motions near the wall.

The in-plane dissipation rate spectral density (Eq. 2.28) is presented in Fig. 3.20. Similar to the spectral contribution from production there is a broadening of affected

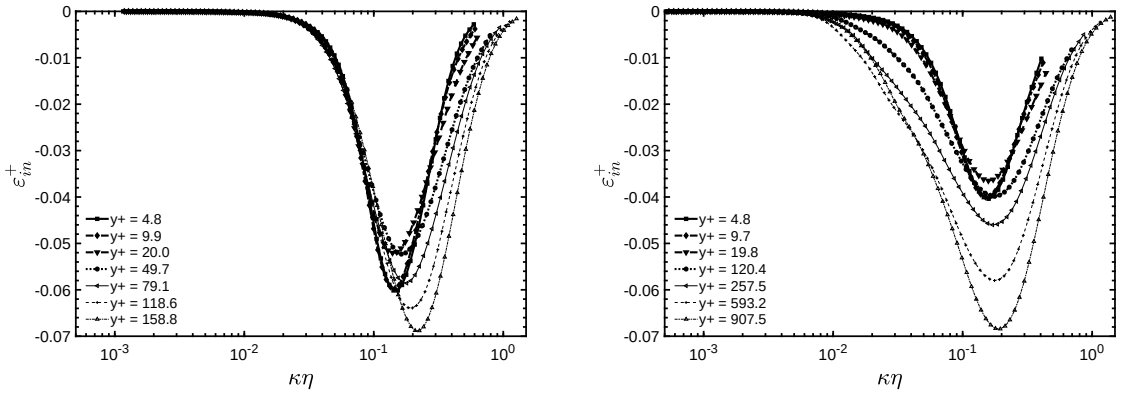

Figure 3.20 – In-plane dissipation spectral density, ε_{in}^{+}, at various y^{+} locations at $Re_\tau = 180$ and 1000, respectively.

spectral range with increasing distance from the wall. However, unlike the spectral contribution from production, there is a relatively minor shift in $\kappa\eta$ location of peak intensity values across the channel. From Fig. 3.19, there was a monotonic increase in peak intensity with wall distance across most of the channel half-width. This behavior is not replicated with in-plane dissipation rate spectral density. For $Re_\tau = 180$, the peak intensity levels decrease overall through the sub-layer and the buffer layer regions. As y^{+} increases, the peak intensity values increase with a shift to higher wavenumbers. This trend is similar for the $Re_\tau = 1000$ case, although this shift in peak intensity location is less evident. In this outer layer region, the peak intensity levels and spectral locations are the same at both Re_τ. In the inner layer region, the peak intensity levels of the in-plane dissipation rate are lower for $Re_\tau = 1000$. This indicates that in this inner layer other contributors to the spectral energy budget significantly impact the energy cascade process. It is interesting to note that, at $Re = 1000$, we have very good separation between the dissipation and production peaks, promoting a well-defined inertial region.

The inter-plane dissipation rate spectral density (Eq. 2.29) is shown in Fig. 3.21. There is a decrease in peak intensity values for both Reynolds numbers through the wall region through $y^{+} \leq 50$. In the $Re_\tau = 1000$ case, two local peak intensities in the

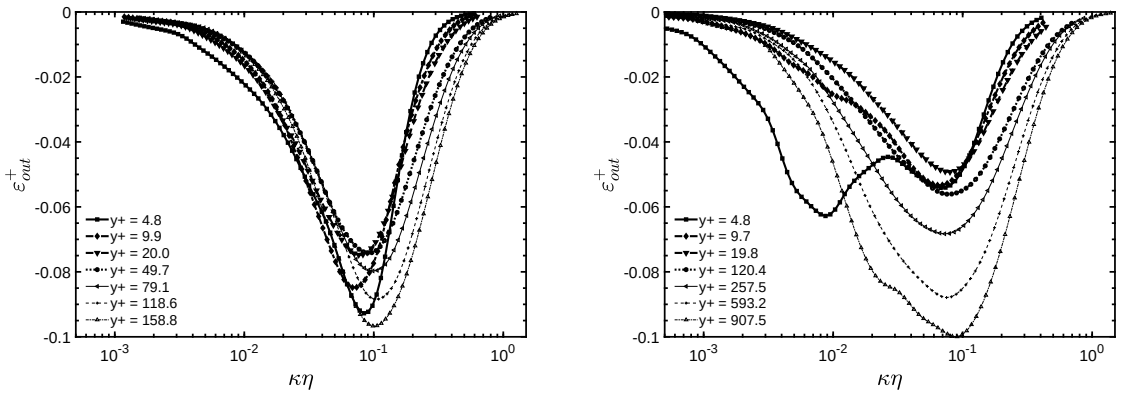

Figure 3.21 – Inter-plane dissipation spectral density, ε^+_{in}, at various y^+ locations.

inter-plane dissipation are observed. The results in Fig. 3.20 suggest no affect on the in-plane dissipation contribution; whereas, for $Re_\tau = 1000$ shows that the wall-normal spatial variations inherent in the inter-plane dissipation are influenced. In the region farther away from the wall the intensity levels increase and with a slight shift to higher wavenumbers. Most notably, there is large spectral broadening at all y^+ locations for $Re_\tau = 1000$ which is skewed towards the lower wavenumbers. Since these lower wavenumbers are associated with the larger scale motions in the flow, the inter-plane dissipation rate has a broader influence on both the physical and spectral scales across the flow compared to the in-plane contribution.

Since a second peak of inter-plane dissipation rate is found in the close-to-wall region at $Re_\tau = 1000$, it is convenient to analyze more specifically its behavior within the viscous sub-layer and in the initial region of the buffer layer. For this purpose, Fig. 3.22 presents ε^+_{out} at various y^+ locations restricted to regions I and II. Two peaks are

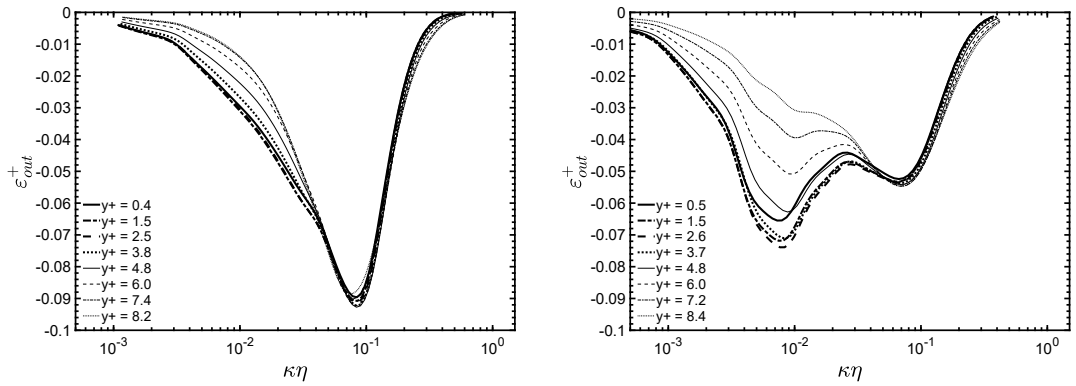

Figure 3.22 – Inter-plane dissipation spectral density, ε^+_{out}, at various y^+ locations in the viscous sub-layer and in the initial region of the buffer layer at $Re_\tau = 180$ and 1000, respectively.

noticed in the vicinity of the wall only at $Re_\tau = 1000$, indicating that this phenomenon

does not occur at low Reynolds numbers. In close proximity of the wall, both ejections and sweeps of fluid occur. This action results in the production of energy at finer scales of motion. At $Re_\tau = 180$ only one peak intensity is observed at $y^+ = 4.8$ due to the stronger influence of viscous effects at this low Reynolds number (cf. Fig. 3.27). For both Reynolds numbers, at low wavenumbers ($\kappa\eta < 4 \times 10^{-2}$), ε^+_{in} intensity increases for y^+ values through $y^+ \leq 2.5$ and then decreases in value with increasing distance from the wall. It seems likely that at this close wall proximity location any change in spectral behavior would be affected by the diminished effect of viscosity with the distance from the wall. An increase in the energetics at a higher Reynolds number is consistent with this thinking. The appearance of a double peak may simply be an intermediate effect at this one Re (= 1000) so that at higher Re only one peak would be present and that would be at the higher $\kappa\eta$.

It is also interesting to discuss the ratio of production spectral density to total dissipation spectral density depending on both y^+ and $\kappa\eta$. It is known that the ratio $\mathcal{P}^+_t/\varepsilon^+_{tot,t}$ is close to 1 in the log-layer and is approximately 1.8 in the area where the peak of production occurs (Fig. 3.12). The objective here is to understand which spectral modes dominate in each region. The ratio $\mathcal{P}^+/\varepsilon^+$ is presented in Fig. 3.23. In the viscous

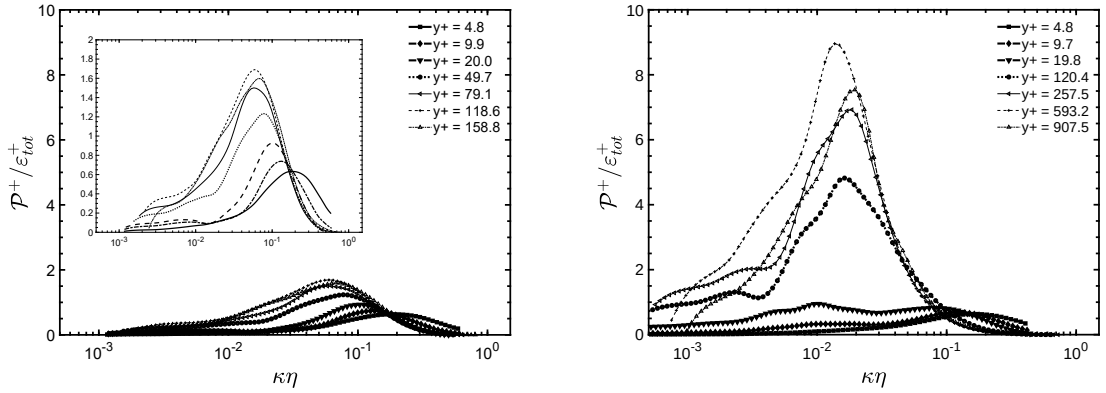

Figure 3.23 – Ratio of production to total dissipation spectral density at various y^+ locations at $Re_\tau = 180$ and 1000, respectively.

sublayer, the behavior is the same comparing the two Reynolds numbers, monotonic inscreases in log and buffer layer are found. As y^+ inscreases, the intensity peak shifts towards smaller wavenumber. It can be noticed that the dissipation is more important than production at higher wavenumber and it inverts as $\kappa\eta$ decreases.

Figure 3.24 shows the scaled in-plane nonlinear transfer spectral density (Eq. 2.30). For $Re_\tau = 180$, the transfer is negative at lower wavenumber values and positive at higher wavenumbers. This affirms the usual transfer of energy from larger to smaller scales in the flow. There is a shift in the $\kappa\eta$ location of both the maximum and minimum in-plane values with distance from the wall. The shift tends to larger scales for wall

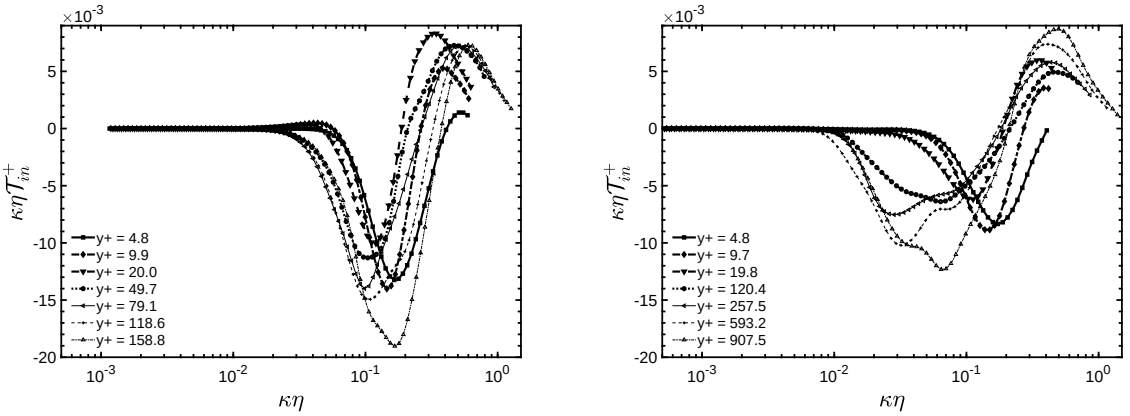

Figure 3.24 – In-plane nonlinear transfer spectral density, $\kappa\eta\mathcal{T}_{in}^{+}$, at various y^{+} locations at $Re_\tau = 180$ and 1000, respectively.

distances through the buffer layer and to smaller scales for the remainder of the channel half-width. For $\kappa\eta\mathcal{T}_{in}^{+} < 0$, peak intensity decreases for y^{+} values through the buffer layer and then increase in value with increasing distance from the wall. For $\kappa\eta\mathcal{T}_{in}^{+} > 0$, peak intensity increases for y^{+} values through the buffer layer and then decrease in value with increasing distance from the wall. This behavior is in accordance with the characteristic of this term to transfer energy from the inertial subrange (generated by the production term) into the high wave-number range (dissipation region)

In contrast to the $Re_\tau = 180$ case, the relevant spectral range covered by the scaled in-plane nonlinear transfer spectral density increases for $Re_\tau = 1000$. Additionally, in the region where the energy is transferred from the larger scales ($\kappa\eta\mathcal{T}_{in}^{+} < 0$) the magnitude of the nonlinear spectral density is smaller than its $Re_\tau = 180$ counterpart. For the higher wavenumber contributions ($\kappa\eta\mathcal{T}_{in}^{+} > 0$) the relative magnitudes of nonlinear spectral density between Reynolds numbers is similar. This spectral broadening is consistent with the fact that, as the Reynolds number increases in wall-bounded flow, a wider range of spatial scales (structures) is observed. While the $\kappa\eta$ locations of the maximum and minimum nonlinear spectral density distributions are generally consistent with the $Re_\tau = 180$ locations, a shift to lower wavenumbers is observed for the spectral density distributions near the channel centerline. This implies the presence of larger scale motions in the bulk flow relative to the lower Re_τ case.

As with the spectral dissipation rate there is an additional contribution to the nonlinear transfer spectral density that accounts for the inter-(spatial) plane nonlinear transfer spectral density. When combined with the in-plane results the total effect of this nonlinear transfer term on the flow can be assessed. The inter-plane nonlinear transfer term (Eq. 2.31) is presented in Fig. 3.25. Both the inter- and in-plane nonlinear turbulent transport have very little influence until $\kappa\eta \approx 2\times10^{-2}$ (cf. Figs. 3.24 and 3.25).

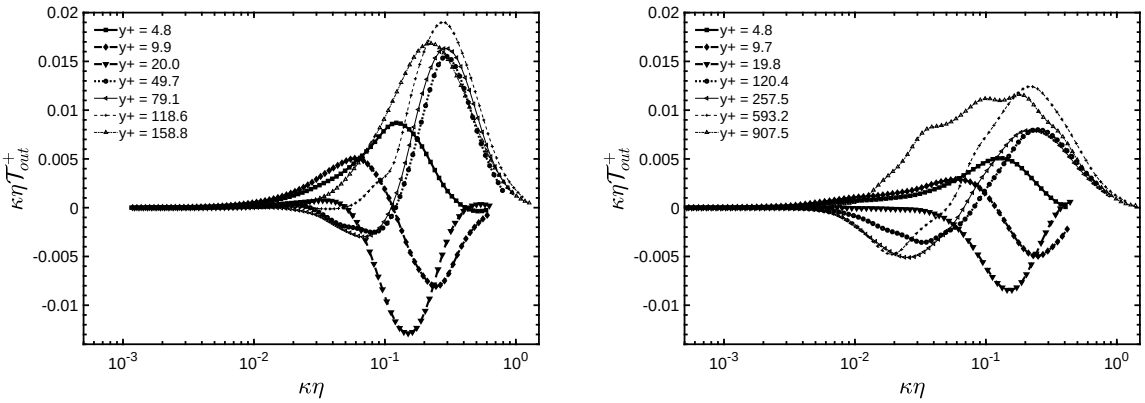

Figure 3.25 – Inter-plane nonlinear transfer spectral density, $\kappa\eta\mathcal{T}^+_{out}$, at various y^+ locations at $Re_\tau = 180$ and 1000, respectively.

For both Reynolds numbers, the spectral distributions adjacent to the wall show that there is a transfer of energy into a broad range of scales. In addition, at $y^+ \approx 10$, an inverse energy cascade from intermediate to large spectral scales appears. In the buffer layer region $y^+ \approx 20$ the inter-plane nonlinear transfer term acts to transfer energy out of these intermediate scales. Farther away from the wall another inverse cascade appears but with slightly different characteristics depending on Re_τ. At the lower Reynolds number, the intensity level of the energy transfer from the lower wavenumbers is less intense than the level of the increase of energy at the higher wavenumbers. At the higher Reynolds number, the difference in intensity levels is not as great, and the energy transfer from the larger scales extends over a wider wavenumber range. As the mid-channel is approached, a net transfer of energy to a broad range of scales is found.

Similar to the spectral dissipation rate, the total nonlinear transfer spectral density is composed by its in- and inter-plane contributions. When combined both results, the total effect of the nonlinear transfer term on the flow can be analyzed. The total nonlinear term, $\mathcal{T}^+_{tot} = \mathcal{T}^+_{in} + \mathcal{T}^+_{out}$, is presented in Fig. 3.26. The inverse cascade energy flux is noticed in the near-to-wall region at both Reynolds number, for which at intermediate wavenumber range ($\kappa\eta \leq 0.1$), the total nonlinear transfer acts as a source of energy, injecting energy coming from higher wavenumber. The inverse cascade come from the combination of in- and inter-plane terms, for which, at $y^+ = 4.8$, $\kappa\eta\mathcal{T}_{in}$ acts as a sink of energy and $\kappa\eta\mathcal{T}_{out}$ acts as a source. In regions II, III and IV, the total nonlinear transfer tends to transfer energy from larger to the smaller scales.

Figure 3.27 shows the distribution of the viscous diffusion spectral density (Eq. 2.32). For $Re_\tau = 180$, adjacent to the wall and in the bulk flow, the diffusion spectral density acts primarily as a source of energy over a broad spectrum of scales. However, over the intermediate distances, the diffusion alternates between a sink/source contributor covering a broad spectrum of scales. For $Re_\tau = 1000$ the trends are less obvious. Adja-

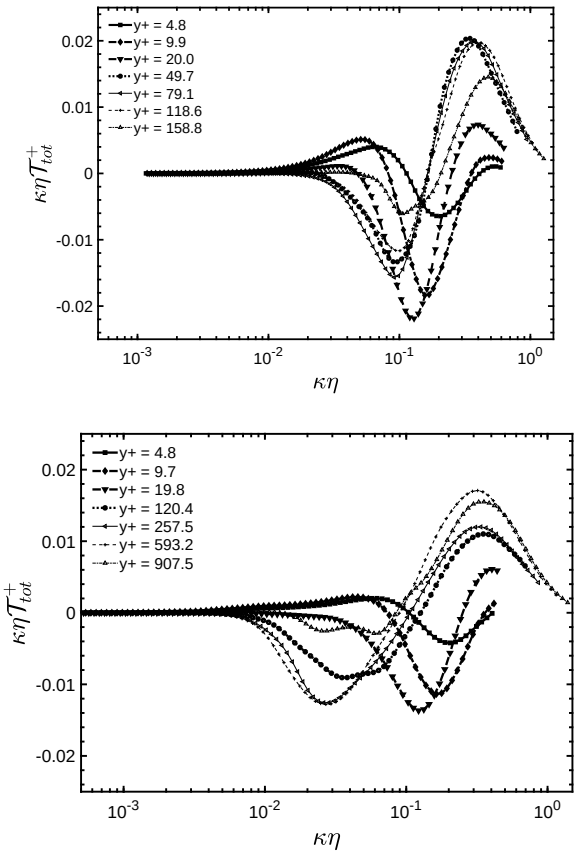

Figure 3.26 – Total nonlinear transfer spectral density, $\kappa\eta\mathcal{T}^+_{tot}$, at various y^+ locations at $Re_\tau = 180$ and 1000, respectively.

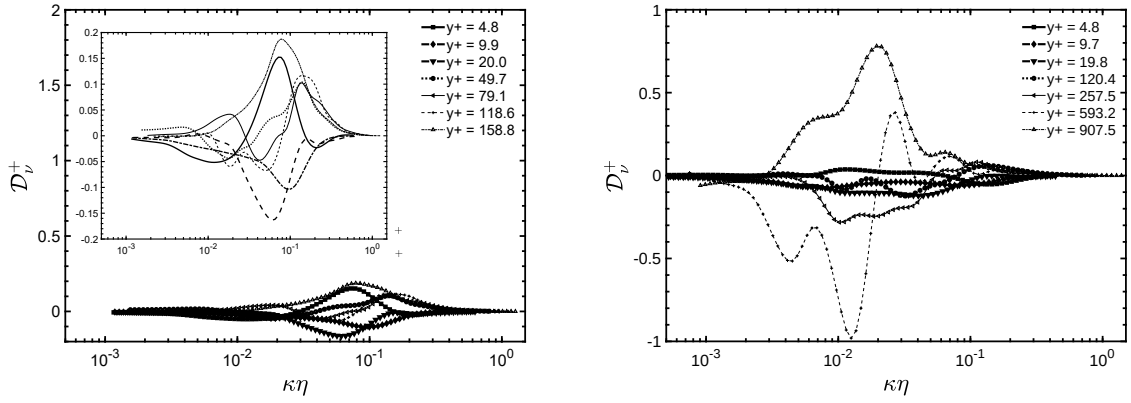

Figure 3.27 – Viscous diffusion spectral density, $\mathcal{D}^+_\nu$, at various y^+ locations at $Re_\tau = 180$ and 1000, respectively.

cent to the wall and in the bulk region of the channel the viscous spectral density acts as a source of energy over a broad spectrum of scales. Intermediate to these regions, the effect of the sink/source variations is less clear. These results are in contrast to the energy budget in physical space shown in Fig. 3.13, in which the contribution of the

viscous diffusion across the channel is clear. This terms is responsible for an energy exchange where the energy is distributed to practically the whole wave-number spectrum. Possibly, higher-order reconstruction of the second derivative spectral function is required to develop a more precise representation of this term.

Figure 3.28 shows the pressure diffusion spectral density (Eq. 2.33). For $y^+ \leq 10$

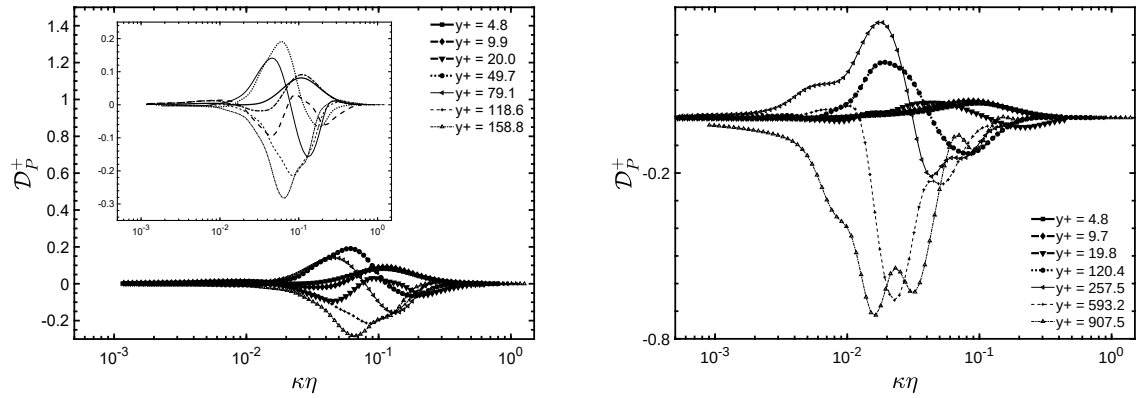

Figure 3.28 – Pressure diffusion spectral density, $\mathcal{D}_P^+$, at various y^+ locations at $Re_\tau = 180$ and 1000, respectively.

in the lower Reynolds number flow, the pressure diffusion acts as an energy source; whereas, as the mid-channel is approached, the term acts as sink across the affected scales. In the intermediate spatial flow regions, there are spectral oscillations resulting in sink and source contributions. At the higher Reynolds number, the behavior of the pressure diffusion as a source term for $y^+ \leq 10$ is similar to the low Reynolds number case. Additionally, in the bulk flow near the mid-channel, the effect reverses and the term acts as a sink. At intermediate distances from the wall, there is a migration from source to sink energy contribution with wall distance, and also characterized by a spectral sink/source variation with wavenumber.

3.2.2 TKE budget in spatial domain by wavenumber bands

In this section, we show the various source terms in Eq. 2.25 as function of the wall distance, y^+, at several wavenumber bands, termed here as bins. These terms are locally normalized according to Eq. 2.42. Following the approach by Bolotnov et al. [17], the bin size and its distribution are shown in Fig. 3.29, for which the turbulent kinetic energy spectral density is illustrated at $y^+ \approx 40$. A total of 28 bins are defined, but for simplification, only 8 bins are plotted, which are highlighted in Figs. 3.30-3.37.

Figure 3.30 shows the distribution of the turbulent kinetic energy. For both Reynolds numbers, the peaks of turbulent kinetic energy are located in the same region ($y^+ \approx 10$) and at the same spectral band (bin $m = 6$). For the $Re_\tau = 180$ flow, the energy bins

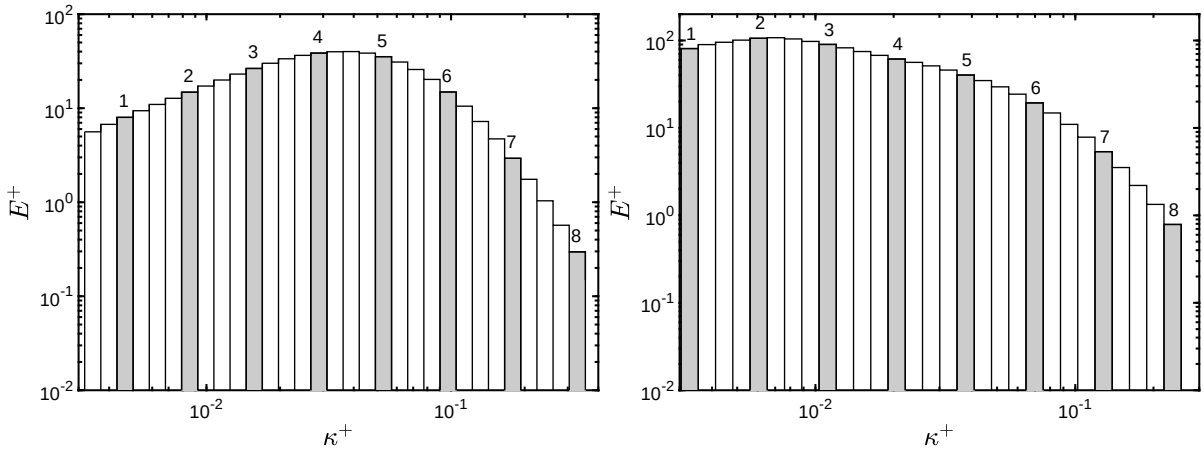

Figure 3.29 – Wavenumber bin distribution at $y^+ \approx 40$ and numeration plotted in Figs. 3.30-3.37 at $Re_\tau = 180$ and 1000, respectively.

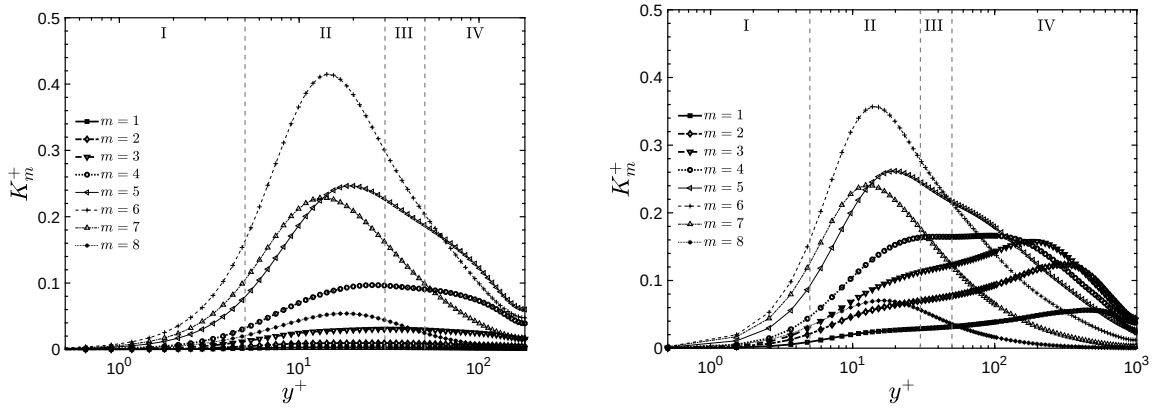

Figure 3.30 – Band distribution for turbulent kinetic energy of various wavenumber bins, K_m^+, vs. distance to the wall, y^+.

$m = [1, 5]$ result in both an increase in turbulent kinetic energy as well as a shift in spatial location of peak energy within Region II. Consistent with the trends shown in Fig. 3.29, bins $m = 6$ and 8 contribute decreasing amounts of energy with increasing wavenumber. At $Re_\tau = 1000$ the spectral contributions are complicated by the emergence of a second peak in energy input from bins $m = [1, 3]$ affecting the outer layer (Region IV) of the channel. As Fig. 3.29 shows, these bins contain significant energy, although at lower wavenumbers (larger scales) than contributions relevant to the region of maximum turbulent kinetic energy (Region II). Due to the broader inertial range shown for the high Reynolds number case in Fig. 3.29, bins $m = [4, 6]$ result in both the increase in energy in Region II as well as the shift to the spatial location of peak turbulent energy. Energy input from bins $m = 7$ and 8 continue but at a lower level consistent with their spectral energy content.

The turbulent production contribution to the energy budget (Eq. 2.25) is shown

in Fig. 3.31. Although there is very little change in spatial distribution with Reynolds

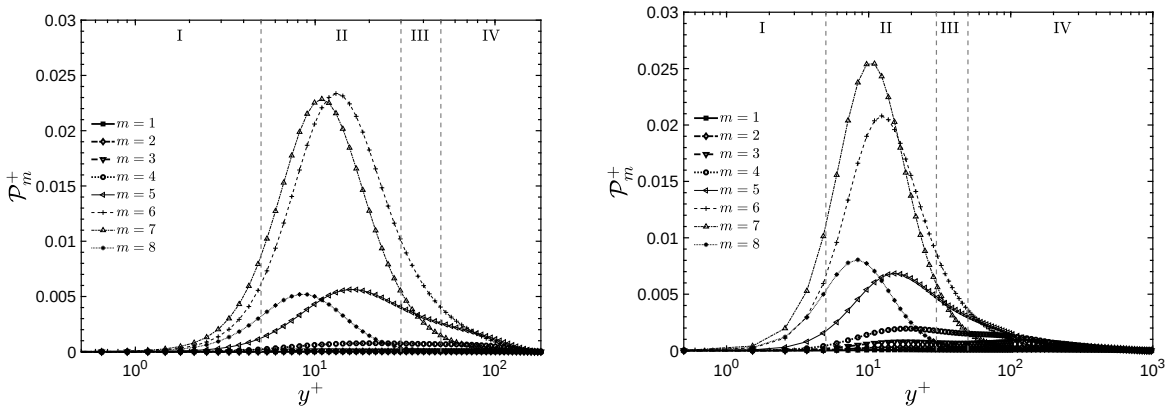

Figure 3.31 – Band distribution for turbulent production for various wavenumber bins, $\mathcal{P}_m^+$, vs. distance to the wall, y^+, at $Re_\tau = 180$ and 1000, respectively.

number, a difference in energy content is found at the peak level of production. At the lower Reynolds number, there is an equal contribution from bins $m = 6$ and 7 to the energy production with the contribution from bin $m = 7$ (higher wavenumber band) resulting in a slight shift towards the wall in peak production location. In contrast, at the higher Re_τ the energy contribution from bin $m = 6$ is less intense than that from bin $m = 7$ with peak production location remaining the same as in the lower Re_τ flow. Even though the energy content in the spectral band of bin $m = 7$ is larger for $Re_\tau = 180$ than $Re_\tau = 1000$, the peak of energy production is larger in the higher Reynolds number flow. Even in a higher Reynolds number, the peak of production is still located in the buffer layer, where TKE is created and then transferred to the center of the channel.

Figure 3.32 shows the in-plane turbulent dissipation band distribution. The most

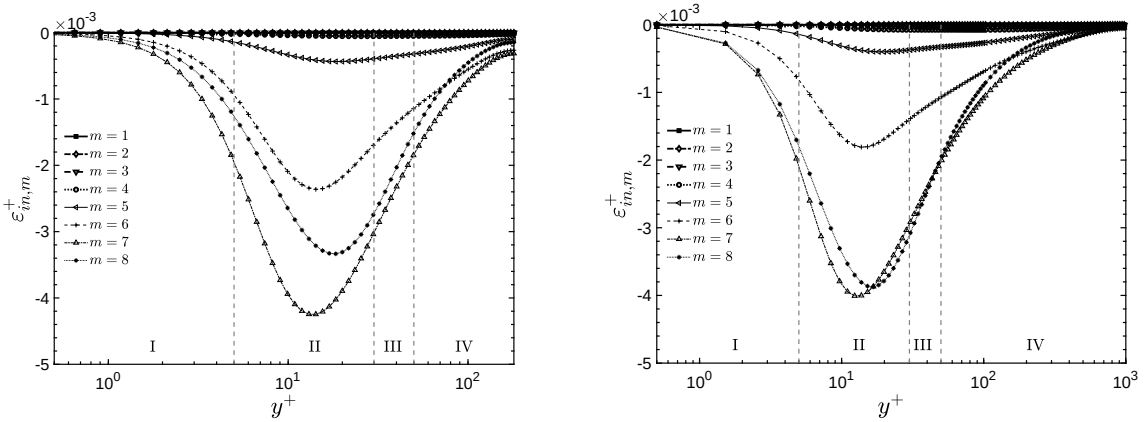

Figure 3.32 – Band distribution for in-plane turbulent dissipation for various wavenumber bins, $\varepsilon_{in,m}^+$, vs. distance to the wall, y^+, at $Re_\tau = 180$ and 1000, respectively.

relevant spectral band contributions come from bins $m = [5, 8]$ and, once again, peak intensity values occur near $y^+ \approx 12$, consistent with the results previously presented. The main difference between Reynolds number distributions lies in the relative contributions from bins $m = 7$ and 8. In the $Re_\tau = 180$ case, bin $m = 7$ is the primary contributor to peak dissipation intensity; whereas for the $Re_\tau = 1000$ case, both bins $m = 7$ and 8 provide relatively equal contributions albeit at a slight shift in peak intensity location.

The remaining contribution to the energy dissipation is the inter-plane dissipation rate component. As shown in Fig. 3.33, this component acts as an overall drain of energy throughout primarily regions I, II, and III. Unlike the in-plane component,

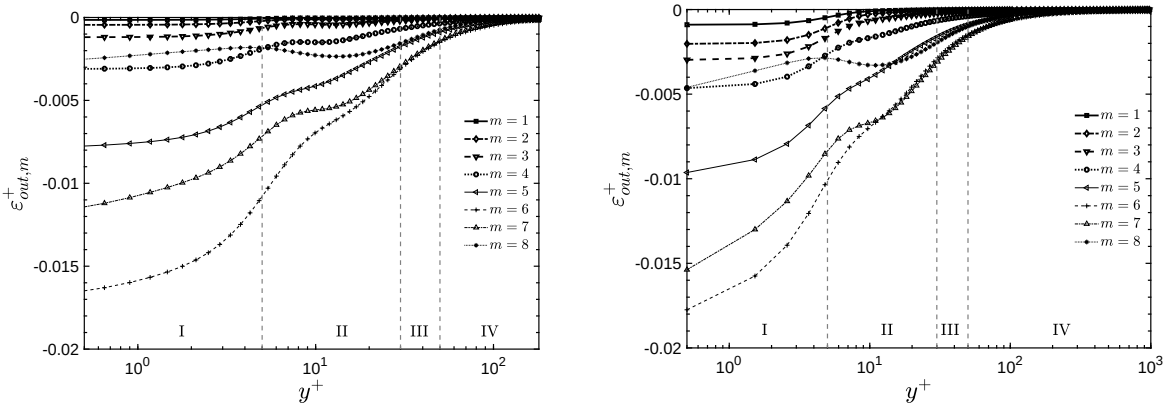

Figure 3.33 – Band distribution for inter-plane turbulent dissipation for various wavenumber bins, $\varepsilon^+_{out,m}$, vs. distance to the wall, y^+, at $Re_\tau = 180$ and 1000, respectively.

the inter-plane component is composed of spectral band contributions spanning all the selected bins. For both Reynolds numbers, there is a monotonic increase in inter-plane intensity distribution across the channel with increasing wavenumber band (bins $m = [1, 5]$). The largest contribution to the inter-plane intensity comes from bin $m = 6$, with subsequent higher wavenumber bins (bins $m = 7$ and 5). Since this term comes from the mean velocity gradients close to the wall, it shows a decreasing intensity distributions across the channel, where the velocity gradient decreases. Unlike the in-plane distributions, whose maximums were in Region II, all the maximum values in the inter-plane distributions occurred at the channel wall. The larger inter-plane intensity values relative to the in-plane contributions show that the spatial inhomogeneity in the wall-normal direction induces a much stronger energetic sink (across a broad spectrum of scales) than the in-plane spectral interaction.

The in-plane (Fig. 3.34) and inter-plane (Fig. 3.35), nonlinear contributions are characterized by both a spectral band and a cross-channel energy transfer. For the in-plane nonlinear transfer at $Re_\tau = 180$, low wavenumber energy bands (bins $m = [1, 3]$) make minimal contribution. Contributions from spectral bands bins $m = 4$,

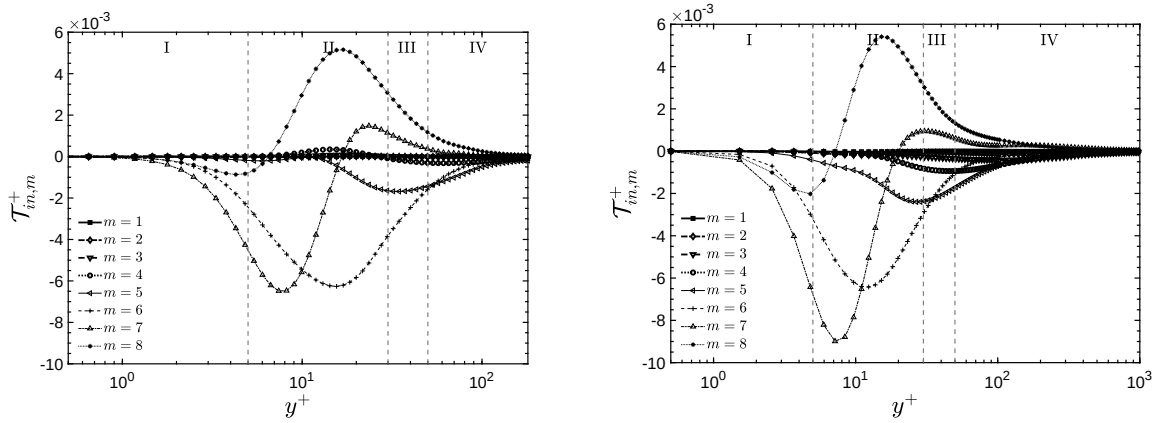

Figure 3.34 – Band distribution for in-plane nonlinear transfer for various wavenumber bins, $\mathcal{T}^+_{in,m}$, vs. distance to the wall, y^+, at $Re_\tau = 180$ and 1000, respectively.

5 and (primarily) 6 affect broad regions of the flow through large- to small-scale energy transfers acting as an overall sink in the energy budget. Across the buffer layer (Region II), the contribution from the spectral band in bin $m = 7$ acts as both a sink and a source of energy. The cross-over location appears to be above the production peak location at $y^+ \approx 16$. At the highest wavenumber band, bin $m = 8$, the nonlinear term becomes an energy source over most of the outer layer; although, in a small spatial length in the lower buffer layer it acts as a sink. For the highest Reynolds number flow, $Re_\tau = 1000$, the qualitative features of the spectral distributions are similar; however, the lower wavenumber contributions from bins $m = 3$ and 4 become evident. Also, the higher wavenumber contributions from bins $m = [5, 8]$ penetrate closer to the wall and act as an energy sink to the smaller scale motions.

For the inter-plane nonlinear transfer, Fig. 3.35, there is a spatial flux of energy toward the channel wall across a broad range of spectral scales (bins $m = [1, 4]$). For the higher spectral bands (bins $m = [5, 8]$), the spatial flux of energy shifts towards the bulk part of the flow. In addition to being dependent on spectral band, this shift is also dependent on the distance from the wall. These qualitative features are similar for both Reynolds numbers; although differences in magnitude and maximum intensity (spatial) location occur between $Re_\tau = 180$ and $Re_\tau = 1000$. The inter-plane nonlinear transfer is responsible for an energy transfer from the buffer layer, where production holds its peak, adjacent regions. This energy flux results in an inverse cascade as noticed in Fig. 3.25.

The turbulent viscous diffusion contribution is shown in Fig. 3.36. Once again, there is little qualitative differences between Reynolds numbers. For both flows, the entire spectral band acts as a source of energy in Region I and as a sink in Region II, in other words, transferring energy from the buffer layer to the viscous sublayer. Quantitative differences in magnitude and maximum intensity location appear between flows but

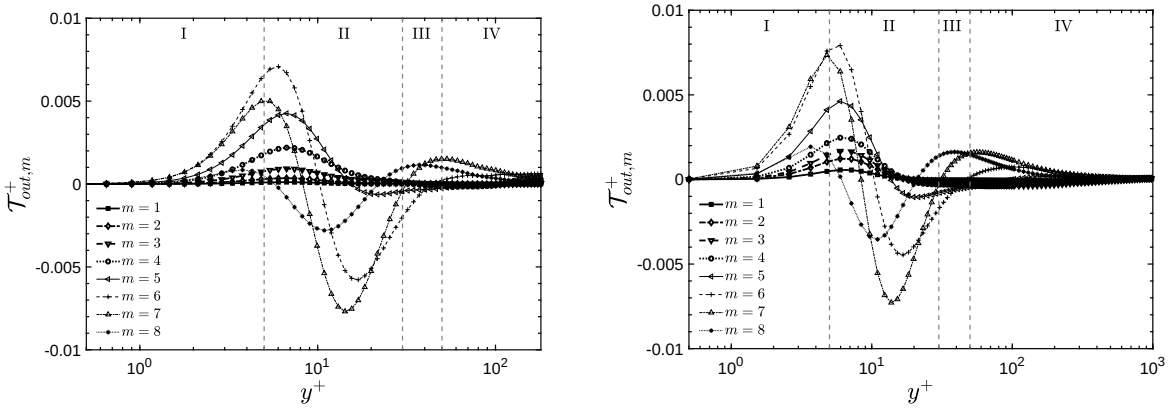

Figure 3.35 – Band distribution for inter-plane nonlinear transfer for various wavenumber bins, $\mathcal{T}^+_{out,m}$, vs. distance to the wall, y^+, at $Re_\tau = 180$ and 1000, respectively.

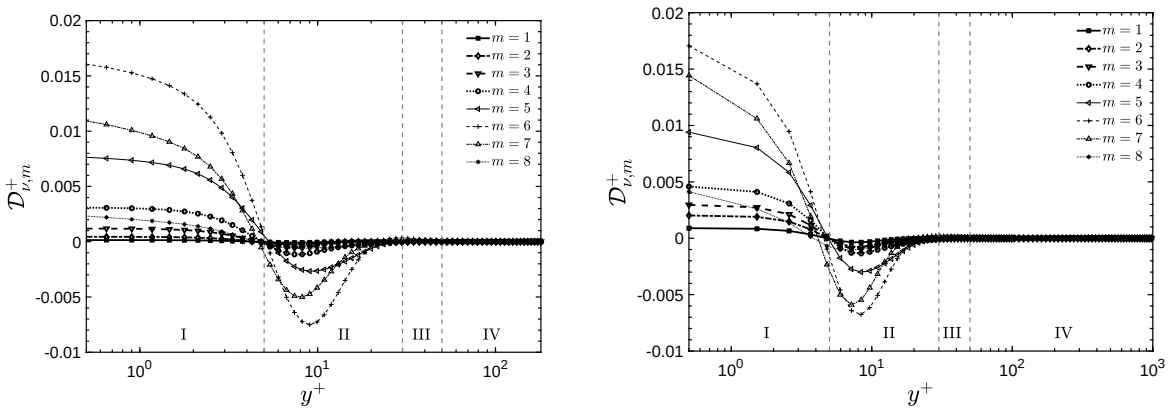

Figure 3.36 – Band distribution for turbulent viscous diffusion for various wavenumber bins, $\mathcal{D}^+_{\nu,m}$, vs. distance to the wall, y^+, at $Re_\tau = 180$ and 1000, respectively.

each shows an intense source of energy near the wall with a weaker energy sink in the buffer layer. As it was noticed in Fig. 3.27, it may be noticed an inversion in the behavior of the viscous diffusion as it approaches the mid-channel region, switching from an energy source to a sink. This inversion is found to be closer to the wall at $Re_\tau = 1000$ than at $Re_\tau = 180$. This fact indicates that this term is responsible for an energy transfer in the physical domain rather than a scale-to-scale diffusion.

The pressure diffusion contribution is shown in Fig. 3.37. Although the pressure diffusion is small when compared to the other terms (see Fig. 3.13), it contributes to the energy transfer from the mid-channel region to the close to the wall region, removing turbulent kinetic energy from the homogeneous and injecting in the inhomogeneous region. This transfer behavior occurs more significantly at larger wavenumbers (bins $m = [5, 8]$). At lower wavenumber (bins $m = [1, 4]$), since the average pressure term is homogeneous along the normal-to-wall direction, it presents a less pronounced

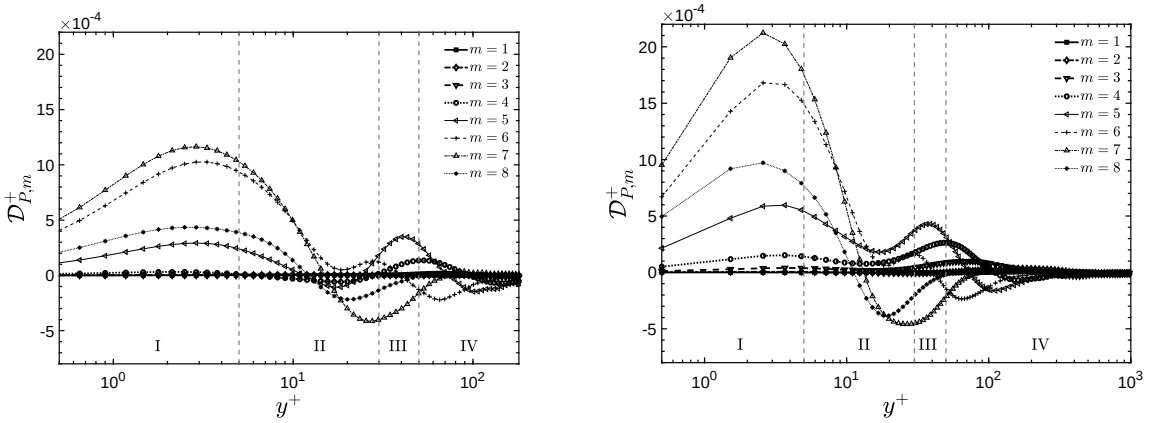

Figure 3.37 – Band distribution for pressure diffusion for various wavenumber bins, $\mathcal{D}^+_{P,m}$, vs. distance to the wall, y^+, at $Re_\tau = 180$ and 1000, respectively.

dynamic to the spectral budget (see Fig. 3.28), and it becomes negligible. Two energy injection peaks are noticed, the higher one in the viscous sublayer (Region *I*), and the second at the logarithmic layer (Region *III*). In the center of the channel, the transfer is negligible. The Reynolds number influence on the pressure diffusion occurs mainly in the close-to-wall region (Region *I*), with an increasing peak intensity when the Reynolds number is increased.

Conclusions are found in Sec. 4.2.

3.3 *A priori* test of a novel nonlinear subgrid-scale model

In this section we present the results showing the evaluation of Models *I* to *V* (Eqs. 2.50–2.54, respectively) by calculating its coefficients by means of the mathematical procedures depicted in Sec. 2.4.2. The influences of the filtering grid (Tabs. 2.2 and 2.3) and the Reynolds number ($Re_\tau = 180$ and $Re_\tau = 590$) are also investigated and are presented in the next section. In this section, it is shown and compared the behavior of the exact and modeled SGS stress tensor components.

In order to analyze the correlation between $\boldsymbol{\tau}$ and $\boldsymbol{\tau}^M$, it will be employed here a normalized parameter, R_M, given by Thompson [149], that measures how important is the tensor $\boldsymbol{\tau}^M$ when compared with tensor $\boldsymbol{\tau}$. This parameter is given by:

$$R_M = 1 - \frac{2}{\pi}\cos^{-1}\left(\frac{\left\|\boldsymbol{\tau}^M\right\|}{\|\boldsymbol{\tau}\|}\right), \tag{3.10}$$

where the operator $\|\boldsymbol{A}\|$ that can be applied to a generic second order tensor $\boldsymbol{A}$ is defined as $\|\boldsymbol{A}\| = \sqrt{\mathrm{tr}\left(\boldsymbol{A}^T \cdot \boldsymbol{A}\right)}$. The quantity $R_M \in [0,1]$.

All variables presented in this section are averaged in several parallel-to-wall plans,

varying on the wall-distance. The averaged variables are presented as $\langle\phi\rangle$, where ϕ is a generic variable. Section 3.3.1 presents the influence of the filtering width and the Reynolds number on the filtered data by means of the *a priori* test. Sec. 3.3.2 presents the evaluation of $\boldsymbol{\tau}^M$ in relation to the exact subgrid-scale tensor.

3.3.1 The filtered data

Regarding the influence of the filtering process in the modeled SGS stress tensor. The filter widths applied in the present work are presented in Tabs. 2.2 and 2.3. Figure 3.38 reports the comparison of the exact stress components τ_{11} and τ_{12} (Eq. 1.15) at $Re_\tau = 180$ with results of Majander and Siikonen [100] and Salvetti and Banerjee [134]. Since each result shown in Fig. 3.38 was obtained by applying a different DNS grid and filtering operation, only a qualitative comparison can be established. It is shown

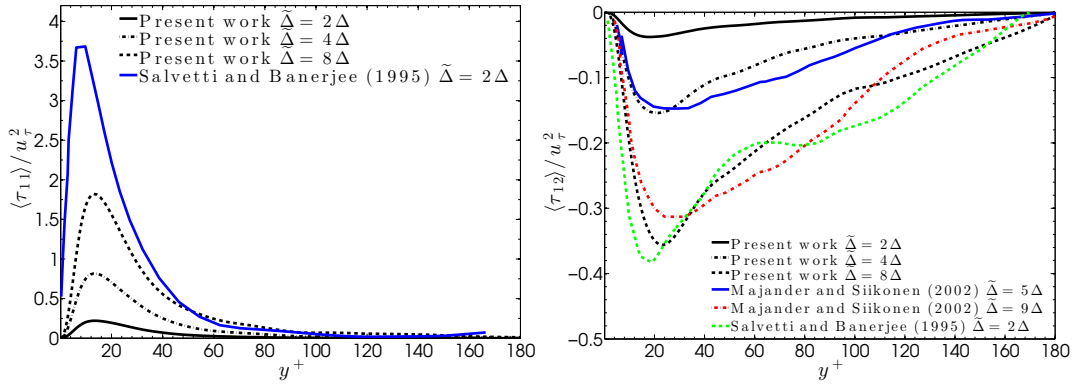

(a) τ_{11} (b) τ_{12}

Figure 3.38 – Profile of τ_{11} and τ_{12} scaled by u_τ^2 across channel half-width at $Re_\tau = 180$ compared to Majander and Siikonen [100] and Salvetti and Banerjee [134]

that, as expected, by increasing the filter width, the intensity of the SGS stress tensor components also increases. It also can be noted that the peak of the τ_{11} (Fig. 3.38-a), localized at $y^+ \approx 10$, is close to the results of Majander and Siikonen [100], which carried out a similar procedure by applying a grid size of $128 \times 64 \times 128$ with a trapezoidal filter. Comparison is also made with Salvetti and Banerjee [134], which presents a turbulent pipe flow at $Re_\tau = 170$ in a DNS grid size of $64 \times 64 \times 65$ with box filter in all directions. The behavior and the peak of the τ_{12} (Fig. 3.38-b) are also in agreement with results found by Majander and Siikonen [100] and Salvetti and Banerjee [134]. In all cases, τ_{12} decreases at the same rate, vanishing at the center of the channel.

In a turbulent channel flow, when it comes to spatial characteristics, the flow domain presents well-defined regions where there are different contributions to the velocity field [127], i.e., I - viscous sublayer ($0 < y^+ < 5$), II - buffer layer ($5 < y^+ < 30$), III - log-law region ($y^+ > 30$) and IV - outer layer ($y^+ > 50$). To improve the analysis of the results, these regions are shown in the following figures.

According to Cimarelli and De Angelis [27], the most important feature of the SGS models should be their ability to accurately reproduce the energy transfer between resolved and SGS scales ($\mathcal{P}_r$). In a wall bounded turbulent flow, the physical process of $\mathcal{P}_r$ can behave very differently depending on the range of scales removed by the filter and on the wall-distances considered [57]. To evaluate the different behavior of $\mathcal{P}_r$, Fig. 3.39 presents the comparison of turbulent kinetic energy transfer from the large to the small scales $\mathcal{P}_r$ for different filter widths and at $Re_\tau = 180$ and $Re_\tau = 590$, where $\mathcal{P}_r$ is given by:

$$\mathcal{P}_r = \left\langle \tau_{ij} \widetilde{S}_{ij} \right\rangle. \tag{3.11}$$

Regarding the influence of the Reynolds number, it was found that $\mathcal{P}_r$ presents higher

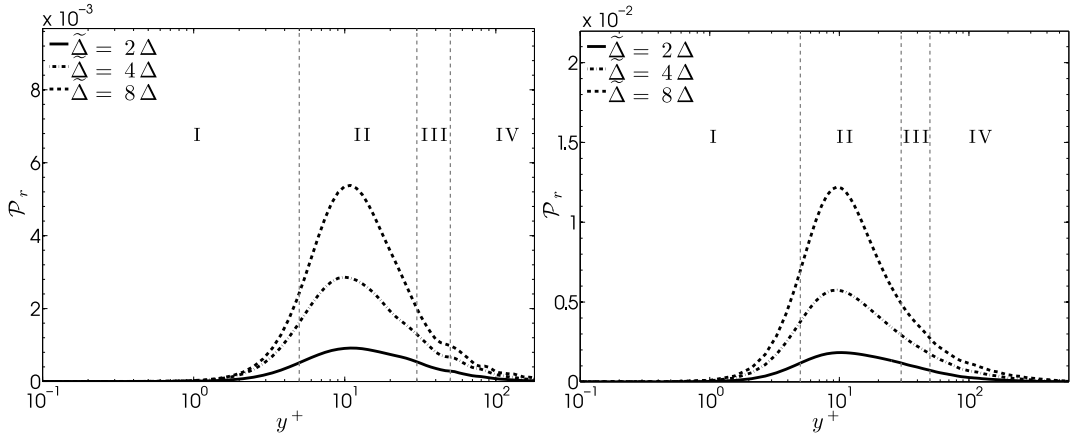

(a) $Re_\tau = 180$ (b) $Re_\tau = 590$

Figure 3.39 – Profile of reference $\mathcal{P}_r$ across channel half-width at $Re_\tau = 180$ and $Re_\tau = 590$.

values for larger Reynolds number. However, no significant qualitative difference was observed between $Re_\tau = 180$ and $Re_\tau = 590$, with each peak located in the same region ($y^+ \approx 10$) in the buffer layer. These results are in accordance with the previously results in Sec. 2.3. Turning now to the analysis of the filtering influence, it is apparent that in a coarser grid, the energy injected in the SGS scales is larger. This result can be explained by the fact that for a coarser grid, the modeled spectral range is larger and, consequently, the energy change is higher.

Figures 3.40 and 3.41 present the components $\langle \tau_{11} \rangle$ and $\langle \tau_{12} \rangle$ of the SGS stress tensor (Eq. 1.15). They are presented at $Re_\tau = 180$ and 590 for the three tested filter widths. From the results we can notice that by increasing the filter width, the filtered SGS stress intensity is increased proportionally. These figures also indicate where the peaks of $\langle \tau_{11} \rangle$ and $\langle \tau_{12} \rangle$ are located. The maximum value of $\langle \tau_{11} \rangle$ is found in the Region II around $y^+ \approx 13$ and for $\langle \tau_{12} \rangle$, the peak is localized around $y^+ \approx 22$, also in Region II. It may be noted that the Reynolds number has no significant influence under the location of the peaks. For both $\langle \tau_{11} \rangle$ and $\langle \tau_{11} \rangle$, the buffer layer has shown to be the

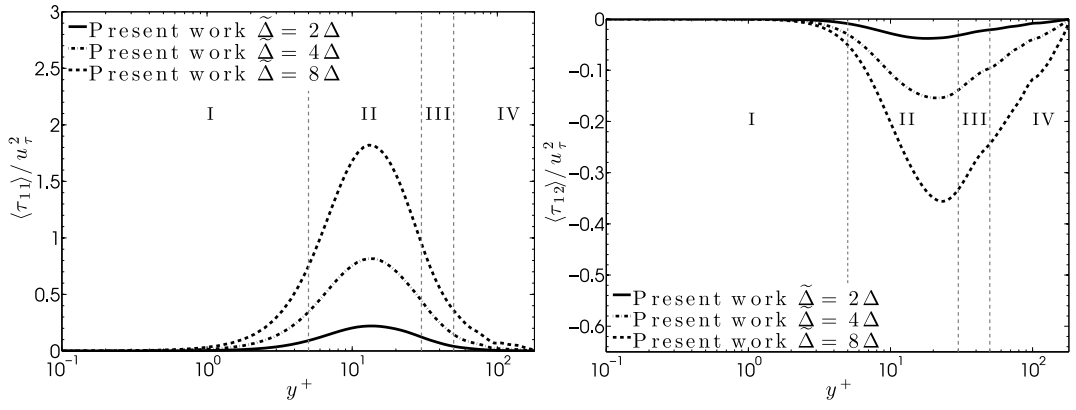

(a) $\langle\tau_{11}\rangle/u_\tau^2$ (b) $\langle\tau_{12}\rangle/u_\tau^2$

Figure 3.40 – Profile of $\langle\tau_{11}\rangle/u_\tau^2$ and $\langle\tau_{12}\rangle/u_\tau^2$ across channel half-width at $Re_\tau = 180$.

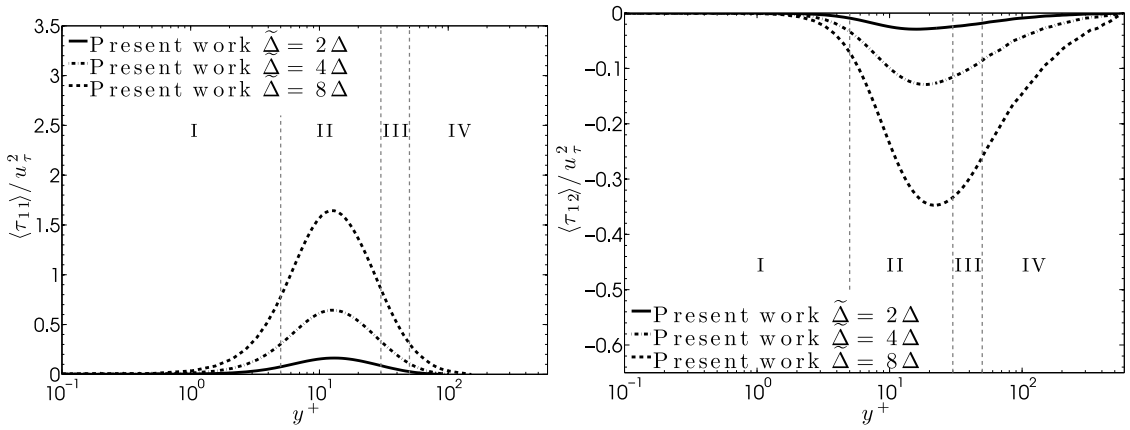

(a) $\langle\tau_{11}\rangle/u_\tau^2$ (b) $\langle\tau_{12}\rangle/u_\tau^2$

Figure 3.41 – Profile of $\langle\tau_{11}\rangle/u_\tau^2$ and $\langle\tau_{12}\rangle/u_\tau^2$ across channel half-width at $Re_\tau = 590$.

most important region, where are found the peak of turbulent kinetic energy and the maximum ratio of production to dissipation of the turbulent kinetic energy.

3.3.2 The nonlinear SGS models

In this section, we now turn to the analysis of the proposed nonlinear SGS models. As was described in Sec. 2.4, five models were proposed based on the complete tensorial basis given by Eq. 2.49.

In order to predict the maximum correlation that the proposed model can achieve, a mathematical procedure to determine the set of scalar coefficients based on the minimization of the discrepancy between the exact and the modeled SGS stress is applied. This procedure is found in Sec. 2.4.2. Additionally, since the exact velocity field is known in an *a priori* test, a conventional correlation coefficient between the exact and the modeled SGS stress tensor is defined to examine the degree to which the closure model represents the local and instantaneous stress in a quantitative frame

with numerical values. The *a priori* test is performed by means of a turbulent plane channel flow canonical case at two different Reynolds numbers, i.e., $Re_\tau = 180$ and 590, respectively.

The correlation (Eq. 3.10) between the exact and the modeled SGS stress tensor, $\boldsymbol{\tau}$ and $\boldsymbol{\tau}^M$, respectively, was tested and the corresponding results are shown in Fig. 3.42. This set of analyses investigates how close the modeled tensor can get to the exact SGS stress tensor field. The coefficients of the model are computed by applying the procedure described in Sec. 2.4.2 and the evaluation of the correlation between both tensors is performed by applying the correlation coefficient R_M (Eq. 3.10). These tests

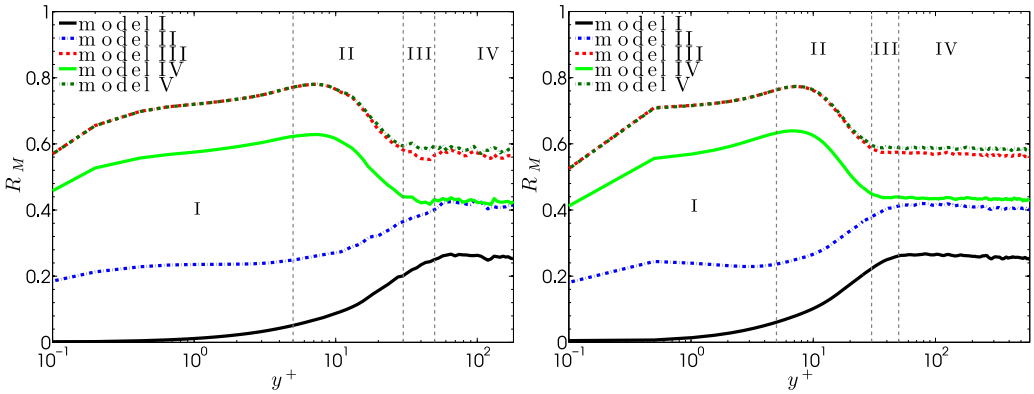

(a) $Re_\tau = 180$ (b) $Re_\tau = 590$

Figure 3.42 – Correlation coefficient, R_M, applied to Models I to V at (a) $Re_\tau = 180$ and (b) $Re_\tau = 590$.

revealed that there is an important gain in correlation between $\boldsymbol{\tau}$ and $\boldsymbol{\tau}^M$ when a more complex nonlinear SGS model is applied. From the figure we can notice that the models III and V present the most significant positive correlation. They reach a maximum value of $R_M \approx 0.76$ and a minimum of $R_M \approx 0.53$. Model I, the linear SGS model, was found to be the worst one, where the figure suggests that the correlation tends to zero around the viscous sublayer regions with a maximum value of $R_M \approx 0.24$ at the outer layer, this result indicates the poor correlation between $\boldsymbol{\tau}$ and $\widetilde{\boldsymbol{S}}$ in the whole channel, reaching the lowest values in the close-to-wall region. This behavior can be attributed to the highly anisotropic behavior of the smallest scales in the region. These results was expected, since Model I imposes an eigenvector alignment and eigenvalues proportion between the SGS stress and the resolved rate-of-strain tensor. The correlation coefficient of Model II is better than the Model I uniformly throughout the channel, in this model, the eigenvector alignment between $\boldsymbol{\tau}$ and $\widetilde{\boldsymbol{S}}$ are imposed, but there is no proportion between its eigenvalues. For models III, IV and V, we observe a great improvement of the correlation coefficient, mainly in the close-to-wall region, where R_M reaches a peak in the buffer layer. These models (III, IV and V) are the ones that include the tensor $\widetilde{\boldsymbol{P}}$ in their composition. On the basis of this evidence, it seems fair to suggest that this was

the most remarkable result to emerge from the DNS data, since by incorporating the non-persistence-of-straining tensor to the tensorial basis of the SGS model, the near-wall region was satisfactorily modeled. A last conclusion worth mentioning is that the procedure outlined showed that the Reynolds number does not affect R_M significantly for the range analyzed here, since there is no substantial differences between $Re_\tau = 180$ e $Re_\tau = 590$.

To assess the correlation coefficient R_M, it was necessary to compute the model coefficients C_k (Eq. 2.58). In the present work, these coefficients were determined by minimizing deviations between $\boldsymbol{\tau}$ and $\boldsymbol{\tau}^M$. Figure 3.43 presents C_k for models I and V, the best and the worst models, respectively. The results are shown only for $Re_\tau = 590$, since no remarkable dependence on the Reynolds number was found. Model V is

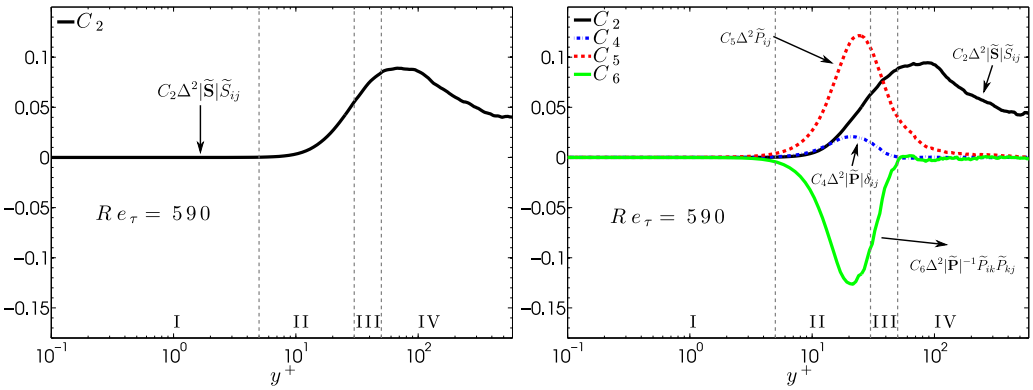

(a) Model I (b) Model V

Figure 3.43 – Coefficients for SGS model: (a) Model I and (b) Model V.

composed by more components in its tensorial basis than Model I. One can notice that the coefficient C_2 for both models (I and V) have a similar behavior. This fact indicates that the tensors $|\widetilde{\boldsymbol{P}}|\delta_{ij}$, $\widetilde{P}_{ij}$ and $|\widetilde{\boldsymbol{P}}|^{-1}\widetilde{P}_{ik}\widetilde{P}_{kj}$ do not affect the role of the tensor $|\widetilde{\boldsymbol{S}}|\widetilde{S}_{ij}$ in the SGS model. It can be explained by the property of orthogonality between $\widetilde{\boldsymbol{S}}$ and $\widetilde{\boldsymbol{P}}$, as was mentioned in the Sec. 2.4. It can be seen that coefficient C_2 tends to be more important in the outer layer whereas the other coefficients have their peaks in the buffer layer. This result is consistent with previous ones from literature, for which it was found that the tensor $\boldsymbol{P}$ promotes a better improvement in the buffer layer. By analyzing Fig. 3.43-(b), it can be remarked that all coefficients have a similar peak intensity, around ≈ 0.12, the only exception is C_4, where its maximum value reaches ≈ 0.02.

With regard to the correlation coefficients between the SGS and the modeled SGS stress tensors for Models I and V, in order to understand its behavior, we present Fig. 3.44, where the modeled and the exact components $\langle\tau_{11}\rangle$ and $\langle\tau_{12}\rangle$ at $Re_\tau = 590$ are plotted.

From Fig. 3.44, we can observer that the exact $\langle\tau_{11}\rangle$ component is positive and

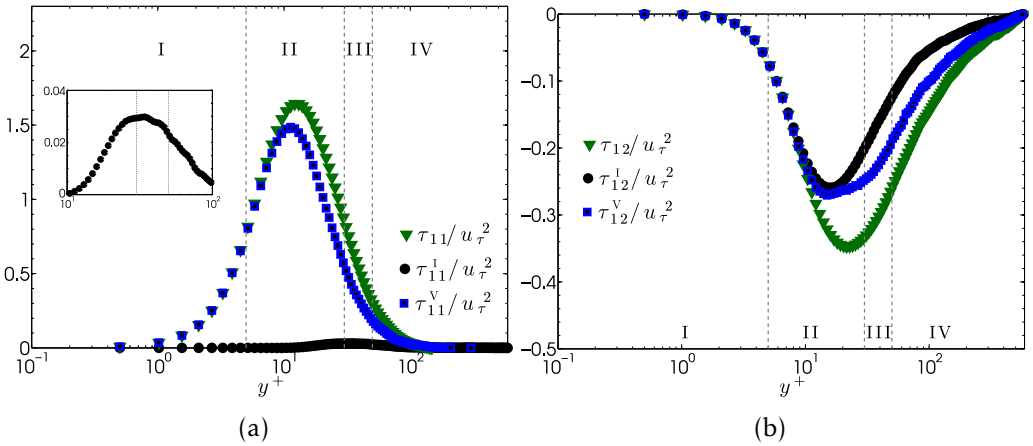

Figure 3.44 – Modeled and exact components of SGS stress tensor by applying: (a) Model I and (b) Model V.

reaches its peak at $y^+ \approx 11$, while $\langle\tau_{12}\rangle$ is always negative and has its maximum intensity at $y^+ \approx 25$. Both the components tend to a maximum value at the buffer layer whereas they decay to zero in the other regions. Concerning $\langle\tau_{11}\rangle$, it was found dramatic differences between Model I and the exact data, both results presenting very different intensities. On the other hand, Model V shows a peak almost in the same region of the exact tensor. We observe from Fig. 3.44-(b) that both models are quite similar to the exact $\langle\tau_{12}\rangle$-component. From this figure we can still state that the Model V shows a result closer to the reference results than Model I. This finding confirms the importance of non-persistence-of-straining tensor in the composition of the modeled SGS stress tensor basis.

3.4 *A posteriori* test of a novel nonlinear subgrid-scale model

In order to establish comparisons and to analyze the proposed nonlinear SGS models, a mathematical procedure to determine the set of scalar coefficients based on dynamic procedure is applied.

Attempts to run nonlinear SGS models III and V (Eqs. 2.50-2.54) without any artificial mathematical artifice have not converged, this behavior can be explained by the fact that inverse cascade creates negative eddy viscosities that may lead to numerical instabilities without any special procedure. In order to understand this problem, further work must be done.

In the *a posteriori* evaluation for the nonlinear SGS models, a lid-driven cubic cavity flow and a backward step simulation flow are considered.

3.4.1 Large-eddy simulation of the lid-driven cubic cavity flow

To ascertain the implications of a nonlinear subgrid-scale model in the AMR3D algorithm, as the first test case, it was chosen the large-eddy simulation of the lid-driven cubic cavity flow by means of a dynamic model. This case was applied due to the fact that it presents a simple geometry with well defined boundary condition. However, a complex physical phenomenon is found when a turbulent regime is reached. Finally, it is a well-adapted problem to the AMR code where the simulations were performed. The cubic cavity case has no homogeneous direction, where walls confine the whole turbulent process and dictate it pattern. Noticeable description of the physics behind the lid-driven cubic cavity flow can be found in Jordan and Ragab [70], Koseff and Street [79], Leriche and Gavrilakis [91] and Shankar and Desphande [138].

Figure 3.45 presents the sketch of the cubical cavity. The flow movement is incited by the moving top wall, which is moving in the x-direction with a wall velocity $U_0 = 1\ m/s$. Except for the top wall, all the others ones are stationaries. The Reynolds number in this simulation is given by $Re = U_0 L/\nu$ and the flow properties were chosen in such a way that a desired Reynolds number of $Re = 10,000$ is applied. Comparisons are established with experimental results of Prasad and Koseff [128]. The literature shows that flow in a lid-driven cubic cavity flow with Reynolds number higher than 3200 is already in transition, and the higher the number of Reynolds the more turbulent is the flow regime.

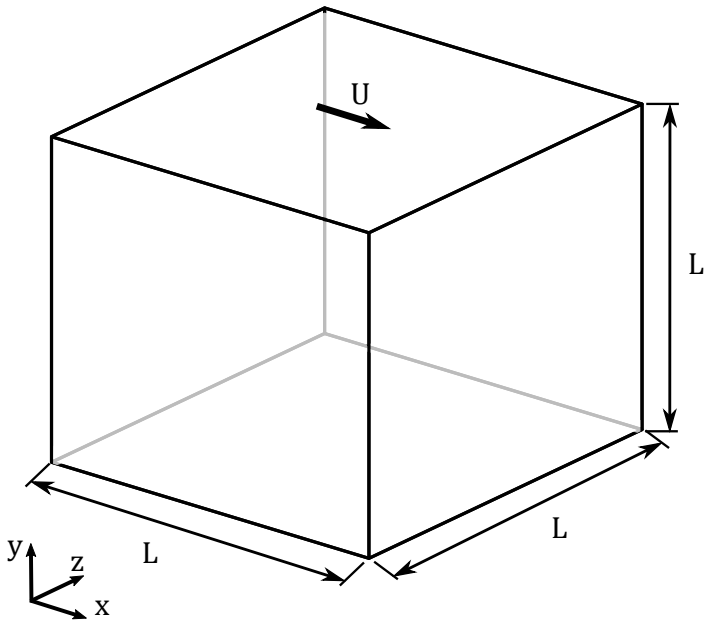

Figure 3.45 – Sketch of the geometry of the lid-driven cubical cavity.

A base grid with 64^3 volumes and three physical levels was applied. All simulations were performed using dynamic adaptive over time and with parallel processing, the

domain was divided into 64 processes ($8 \times 8 \times 8$). The chosen refinement criterion was vorticity. The time step is controlled by taken the CFL factor smaller than 0.25.

The mesh applied in the simulation is illustrated in the Fig. 3.46 at a given instant of time, it can be noticed that in the regions of high vorticity and, consequently, high turbulent intensity, a greater refinement is needed.

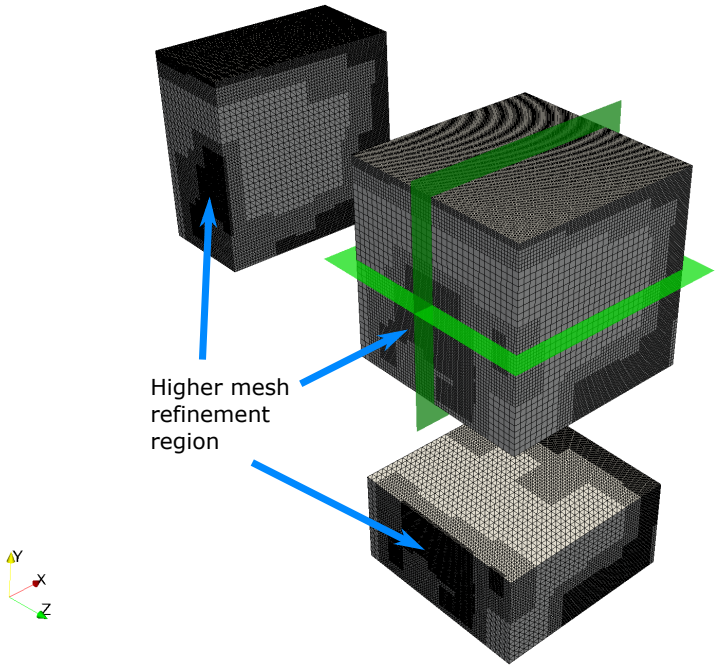

Figure 3.46 – Grid distribution in a given instant of time in the lid-driven cubical cavity flow.

As stated by Bouffanais et al. [20], the viscous diffusion is the responsible for the TKE transport from the top wall to the mean flow by means of the shear stress. A region of high pressure is found in the upper corner of the downstream wall, and the fluid flow is forced to move vertically downwards. The flow recirculates due to this high pressure region, moving in a parallel to the vertical wall plane toward the bottom wall, where there is a turbulence generation and a injection of turbulent kinetic energy in the cubic center.

Figure 3.47 shows a qualitative comparison of instantaneous isosurfaces of the Q-criterion $Q = 5$ for Models I and IV at $t = 150$ s. Such comparison is only able to perform a qualitative analysis of the turbulent structures at different cavity regions, it is noted that there are no remarkable differences between the two models. Great similarity is observed in the flow characteristic for both models, where a large structure is generated near the sliding wall, at $y/L = 1$. This structure starts at $x/L = 0$ and extends to $x/L = 1$, and has boundary layer characteristics. A large rotating structure inside the cavity is also observed for both cases, this main structure induces secondary structures

near the stationary walls.

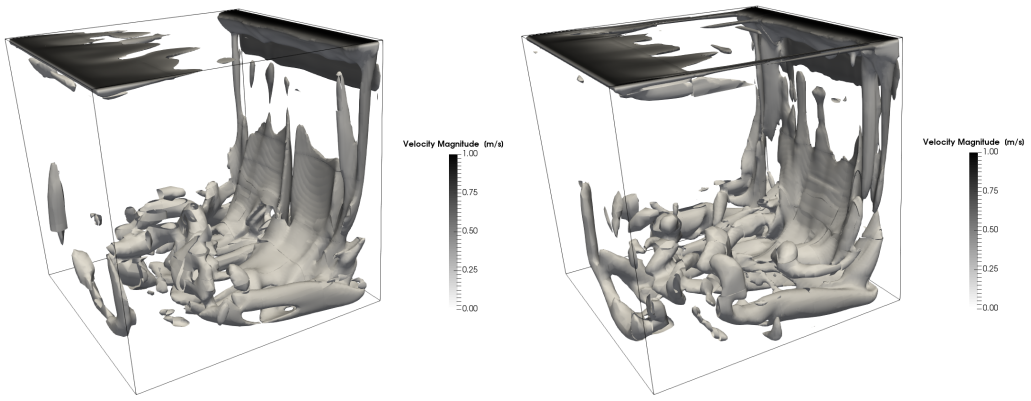

(a) Model I (b) Model IV

Figure 3.47 – Contour plots of instantaneous isosurfaces of the Q-criterion ($Q = 5$) showing the comparison between the turbulent structures of SGS Model I and IV.

Quantitative results are presented below. Data are compared with experiments obtained by Prasad and Koseff [128]. The subgrid-scale Models I, II and IV (Eq. 2.50-2.54) are compared, these models were chosen because they present different characteristics between them, where Model I is the simplest one (linear model), Model II presents the subgrid tensor as a function of combinations of the rate-of-strain tensor and Model IV presents the subgrid-scale model depending on $\widetilde{\boldsymbol{S}}$ and $\widetilde{\boldsymbol{P}}$. Models III and V presented highly instabilities when calculating the set of SGS model coefficients (Eq. 2.85), and its results are not showed. The measurements reported here were taken in the midplane $z/L = 0.5$, which is a statistical symmetry plane of the flow domain.

The mean velocity components along the symmetry axes in mid-plane ($z = 0.5$) are presented in Fig. 3.48, where Fig. 3.48-(a) presents the mean velocity in x direction, $\langle U \rangle$ versus y/L, while Fig. 3.48-(b) shows the mean velocity in y direction, $\langle V \rangle$, versus x/L. Comparisons with experimental data from Prasad and Koseff [128] are established. It is seen that reasonably good agreements are obtained between the present models and previous experimental results. Good agreement of the results with the experimental profile was achieved, capturing well the minimum velocity point, where the highest velocity gradient is found. No substantial differences were observed between the three SGS models.

Figure 3.49 depicts the comparison of the velocity fluctuation (RMS) along the horizontal and vertical lines in the channel mid-plane ($z = 0$) with Prasad and Koseff [128]. Good performance of the nonlinear SGS modelling was reached. The differences of the SGS Model II and IV could possibly be explained by tensorial basis composing each modeling. It can be seen that Model IV (containing the non-persistence-of-straining) reached better results in the close to wall region, while Model II only showed improve-

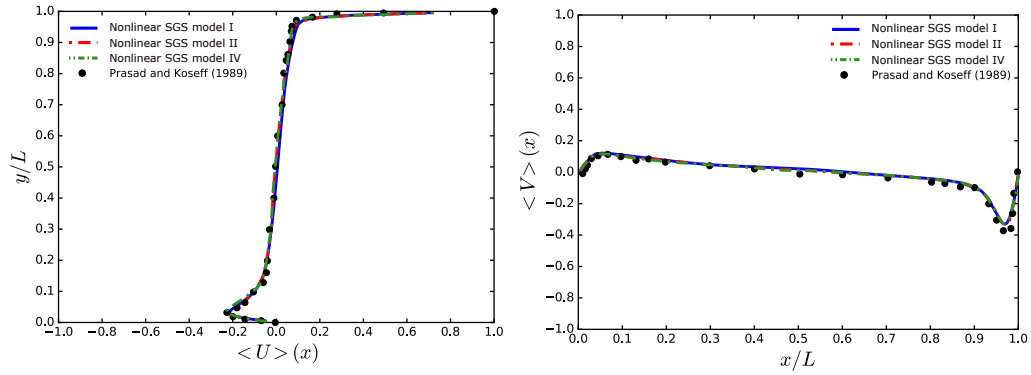

(a) (b)

Figure 3.48 – Comparison of mean velocity profiles in the mid-plane ($z = 0$) along a vertical and horizontal lines, respectively. Results for SGS Models I, II and IV are presented.

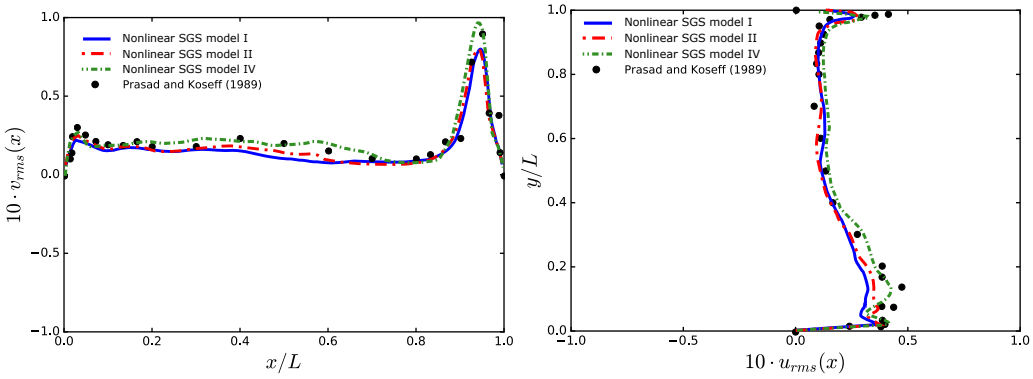

(a) (b)

Figure 3.49 – Comparison of RMS velocity fluctuation profiles in the mid-plane ($z = 0$) along a vertical and horizontal lines, respectively. Results for SGS Models I, III and IV are presented.

ment in the center of the geometry, where the flow presents isotropic characteristics. All the models capture the double-peak behavior near the bottom wall, but only the SGS Model IV had a better defined behavior.

In comparison with earlier findings [128], our results for SGS Model IV just slightly differ under the moving lid. This apparent lack of correlation can be attributed to the reason that, in this region, the amplitude of the SGS stress is negligible and indicates that the flow is mainly laminar and transient. In a general analysis, all models well captured the mean flow for the turbulent lid-driven cubic cavity problem at $Re = 10,000$. However, when the velocity fluctuation was analyzed, improvement in results were obtained by the addition of nonlinear terms in the modeled SGS tensor.

3.4.2 Large-eddy simulation of the backward facing step flow simulation

In this section, the validation results of a backward facing step flow are presented. This case presents a simple geometry domain. However, the induced flow, mainly at higher Reynolds numbers, is considered a complex phenomenon. Since it presents a parietal flow with boundary layer separation and reattachment, and generation of turbulent structures.

The setup configurations of this numerical simulation are based on the experiments performed by Jovic and Driver [71]. Where, through wind tunnel tests and Doppler laser velocimetry, several flow properties were characterized. The Reynolds number based on the step height, h, is given by $Re_h = 5000$.

Figure 3.50 illustrates the wind tunnel scheme used to obtain the experiments results. Firstly, it can be noted that the air flow crosses the honeycomb-screen, seeking to stabilize the turbulent flow fluctuations. Next, the air passes through the development section, where the inlet conditions are well controlled and the maximum turbulence intensity in the free stream is given by 1%. Although being well controlled, the inlet condition is a turbulent boundary layer. Where a $0.1667h$ diameter wire was used to force the boundary layer transition, which approaches the step with a thickness of $1.15h$. After the development section, the air reaches the test section, which has symmetrical expansion, and the distance between the upper and lower wall in the step region is given by $10h$.

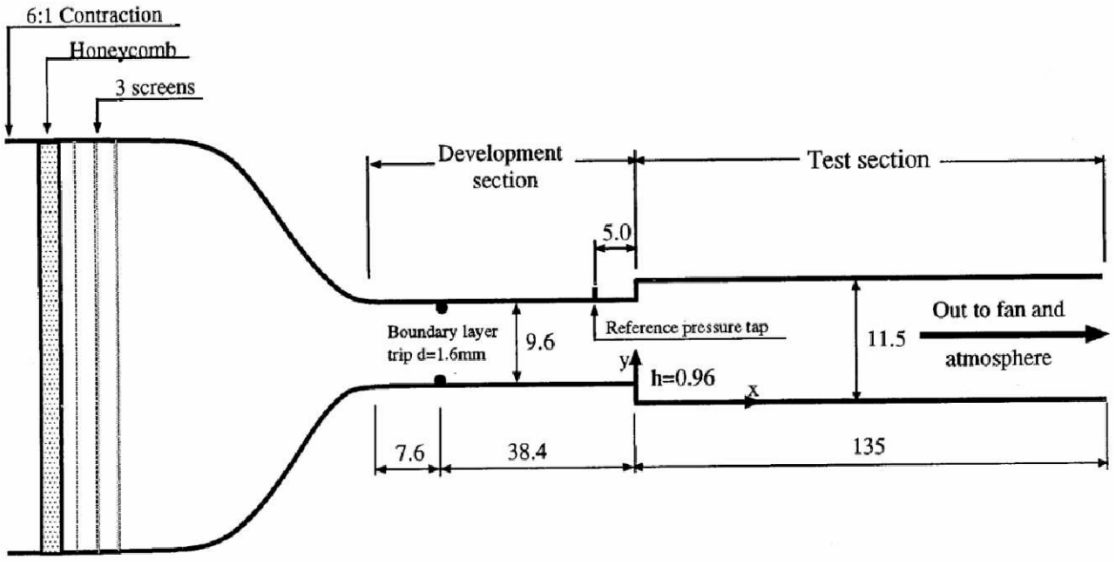

Figure 3.50 – Wind tunnel scheme, reprinted from Jovic and Driver [71].

The experimental results presented by the authors show that, in the region where the data were sampled, the characteristics of the lower step flow are independent from

the upper step flow. Thus, the domain chosen to perform the numerical simulations in the present thesis was only one of the steps. Figure 3.51 shows the domain scheme used for the numerical simulations, its geometric characteristics are: h= 0.5m, L= 32h, H= 6h, W= 4h and X_i= 3h, where h = 0.5 m. Since the domain horizontal length is of the order of 30h, elliptic effects of the imposed outlet boundary condition are avoided [139]. The domain height, H, was defined as 6h, this dimension is close to the plane of symmetry of the expansion region. Finally, the value of W is based on the work of other authors [139], which indicates that a minimum depth of 4h is enough to capture the three-dimensional effects.

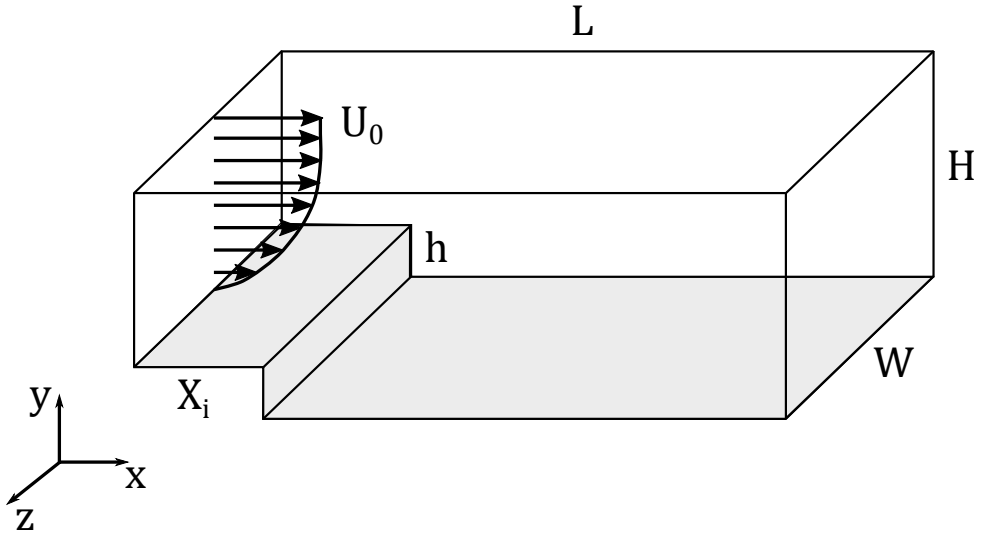

Figure 3.51 – Domain scheme used for the numerical simulations of the backward facing step flow.

Inlet boundary condition is imposed at $x = 0$, where the average velocity profile in the boundary layer coming from the experiment is imposed. The advective condition was chosen as output boundary condition. Therefore, the structures leaving the domain do not cause non-physical numerical interference in the flow. Periodicity is applied to the z-directions boundary conditions. Symmetric boundary condition was defined to the upper domain face. Finally, the non-slip boundary condition is applied to the lower wall and the step. The step was modeled by using the immersed boundary method.

The flow properties were defined in such way that the Reynolds number was given by $Re = 5000$. The time step is controlled by taken CFL factor smaller than 0.2.

Since a dynamic adaptive refinement mesh methodology is applied in the present procedure, the number of volumes and the refinement regions are variable throughout the simulation. For illustration purposes, Fig. 3.52 shows the simulation grid when the calculation starts and at a given time step. The adaptive refinement follows the regions with higher shear stresses, that is, regions that present high values of vorticity.

The topological flow data are presented below. Figure 3.53 presents instantaneous

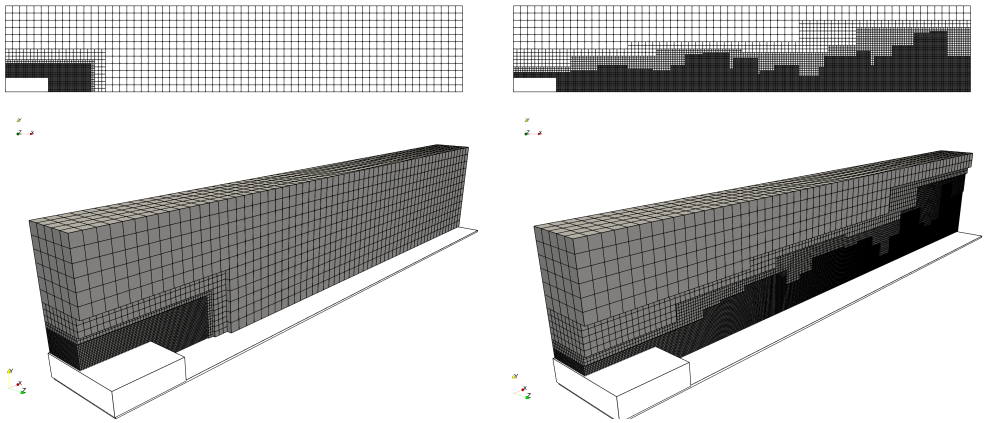

(a) (b)

Figure 3.52 – Eulerian mesh refinement regions at the begin of the simulation and at a given time step, respectively.

vorticity-magnitude fields, $|\boldsymbol{W}|$, in the center plane at $z = 2h$ and snapshots of the instantaneous isosurfaces of the Q-criterion, $Q = 0.1$, of the turbulent flow for the different turbulence models tested. The flow seems to present similar behavior for all simulated cases.

It is possible to observe some transient characteristics in the flow, where expressive velocity fluctuations is found. Turbulent structures generated after the boundary layer detachment on the step also can be noted. These structures collides on the lower wall of the domain, leaving the instantaneous undefined reattachment point.

It is noted that there is an expressive vorticity intensity above the step due to the boundary layer as well as just after the detachment point between the free flow and the unstable recirculation region. This strong shear stress, just after the detachment point, gives rise to Kelvin-Helmholtz structure, with unstable and rotational structures. With the development of the flow along the x-direction, the rotational structures interact with each other, giving rises to elongated and deformed rotating bigger structures, called as hairpin vortex.

Bellow, quantitative results comparing all the SGS models are presented. In order to establish statistical quantitative comparisons, numeric probes are placed inside the domain. The probes are given as vertical lines in the mid-plane and arranged in the following position: $x/h = 4$, $x/h = 6$, $x/h = 10$, $x/h = 15$ and $x/h = 19$, where $x/h = 0$ is the edge of the step. Fig. 3.54 presents the illustration of the probes positions.

Figure 3.55 presents the mean streamwise velocity profile, $\overline{u}$, depending on y/h distance. Comparisons are established with experimental data coming from Jovic and Driver [71]. For each one of the SGS models, in the section $x/h = 4$, a negative part is

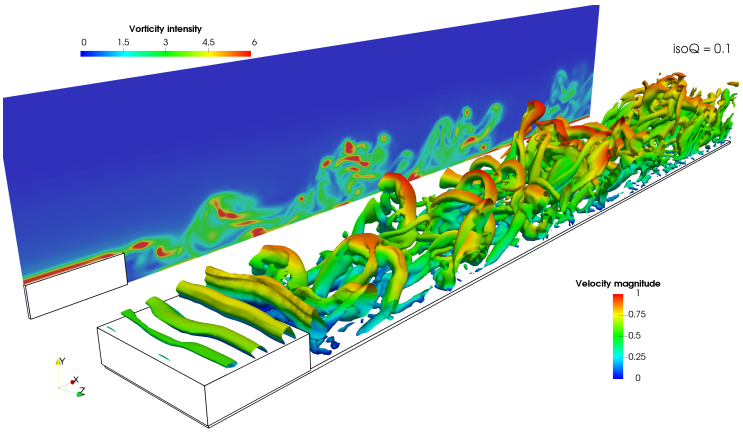

(a) Nonlinear SGS Model I

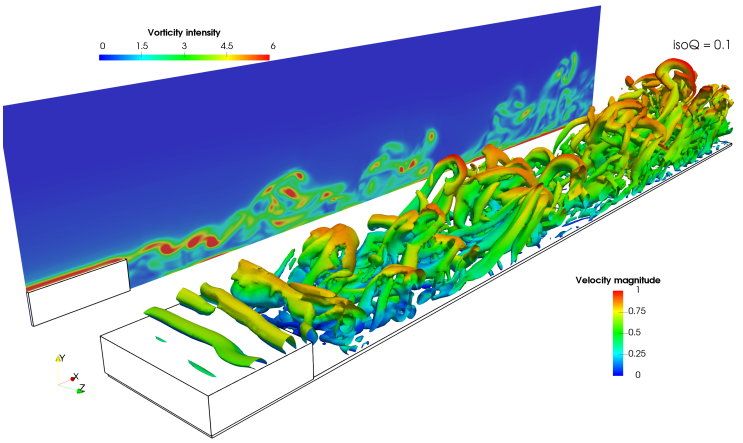

(b) Nonlinear SGS Model II

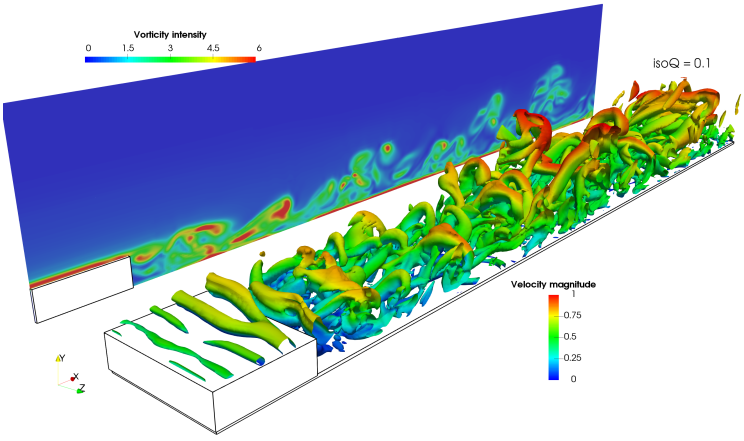

(c) Nonlinear SGS Model IV

Figure 3.53 – Instantaneous vorticity-magnitude fields, $|\boldsymbol{W}|$, in the center plane at $z = 2h$ and contour plots of instantaneous isosurfaces of the Q-criterion ($Q = 0.1$) showing the comparison between the turbulent structures of SGS models: (a) Model I, (b) Model II and (c) Model IV.

observed in the velocity profile, more specifically in the region close to the bottom wall.

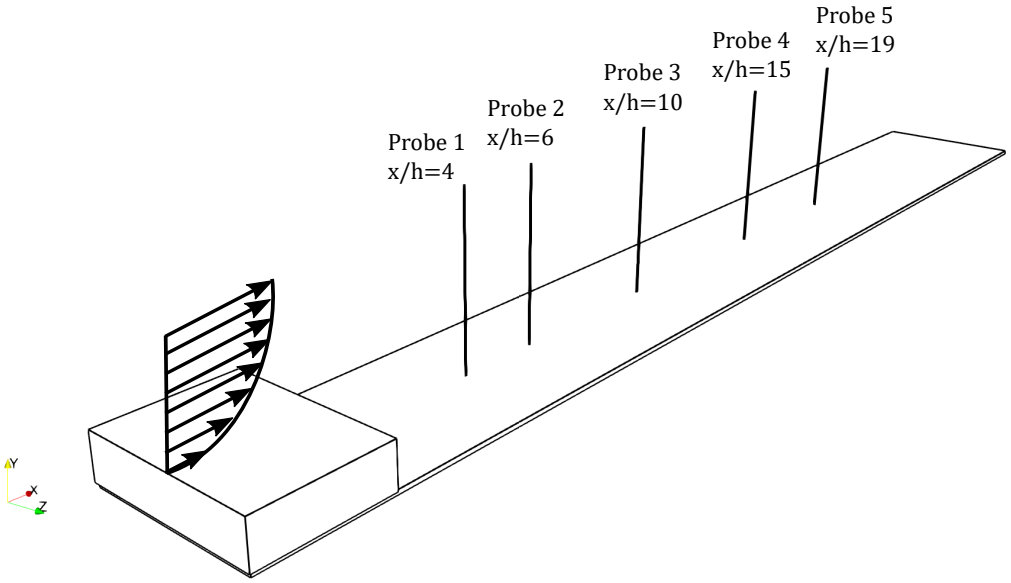

Figure 3.54 – Illustration of the velocity probes positions at the backward facing step domain.

This fact is in agreement with the experiment and it is an indication of the presence of a recirculation zone. In the velocity profile in the section $x/h = 6$, it is noticed that in the region close to the inferior wall, the mean streamwise velocity has an almost negligible intensity. We can also note that there are no expressive gradients in the y-direction. This fact indicates that the reattachment point of the boundary layer is close to this section. From the $x/h = 10$ section, the development of a mean boundary layer is initiated, as expected from this point. Moreover, from this point, in the region $(1 < y/h < 2)$ there is a larger deviation between the experimental and numerical results. This behavior is possibly associated to the formation of the boundary layer in this region and to the fact that the applied grid does not have a suitable refinement close to the wall to adequately capture the phenomenon. In general, the results are close to those obtained by experiments, even in the region very close to the bottom wall, where due to its turbulent structure, great difficulty in modeling is presented. No significant difference was observed in the mean velocity in x-direction when using the different SGS models.

Figure 3.56 presents the streamwise velocity fluctuation intensities depending on y at the several x sections for each different tested SGS model. High fluctuation values are observed in the region near the bottom wall $(y/h < 2)$. This behavior is evidenced in all the analyzed x/h-sections. This phenomenon can be possibly explained by the presence of structures that are formed in the step and propagate along the geometry, which is consistent with what is observed in the experiments. This fluctuation is high in the recirculation region, at $x/h = 4$, and intensifies closer to the section at $x/h = 6$. Then the fluctuation decreases along x, where its intensity in the region $0 < y/h < 2$ is

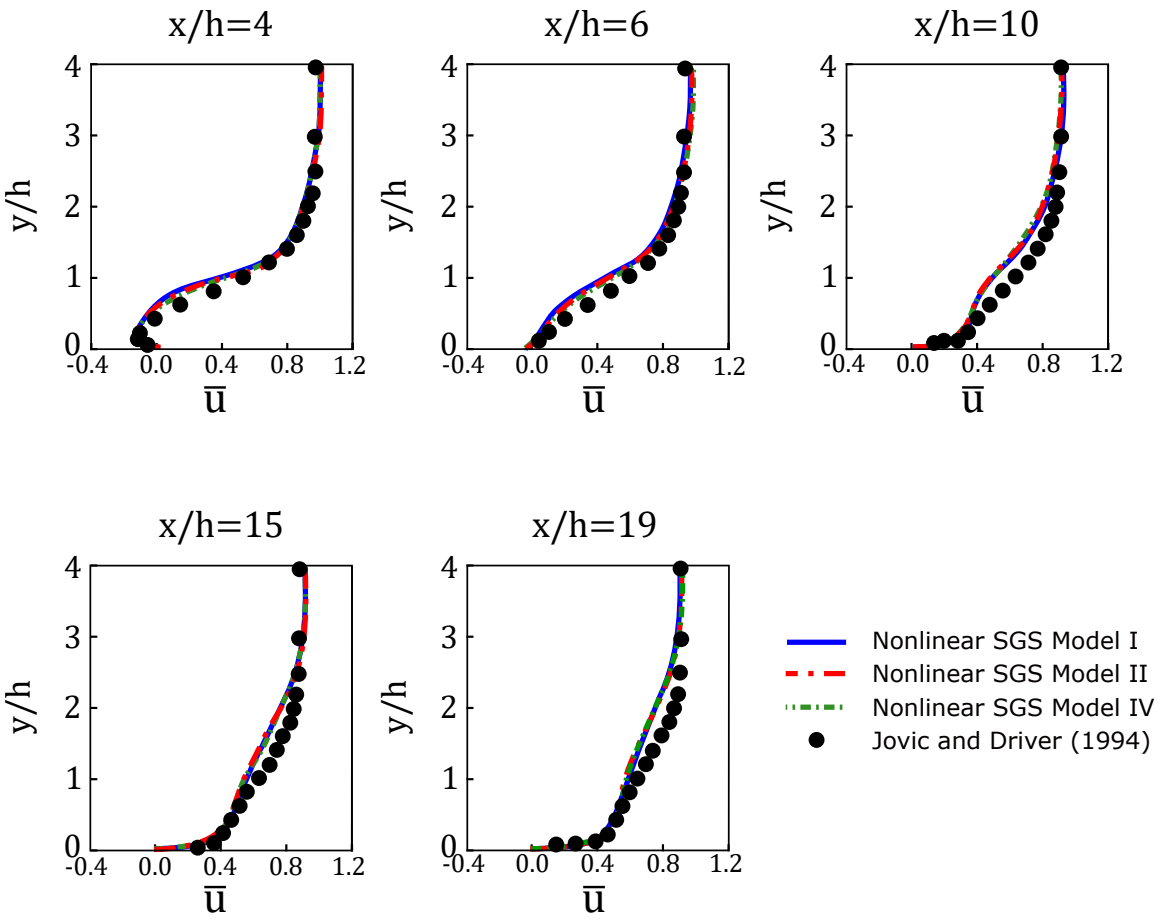

Figure 3.55 – Mean velocity profiles in the x-direction as a function of y/h in several sections in the midplane, comparisons are established with Jovic and Driver [71].

attenuated, and is intensified at $y/h > 2$. This fact indicates that the structures are being launched from the region close to the wall into the interior of the domain. Regarding the comparison of the turbulence tested models, it is noted that, despite they present all similar results, Model IV presents results that are closer to the experimental data, followed by Model II and, finally, Model I. This fact is consistent with what was presented throughout the present work.

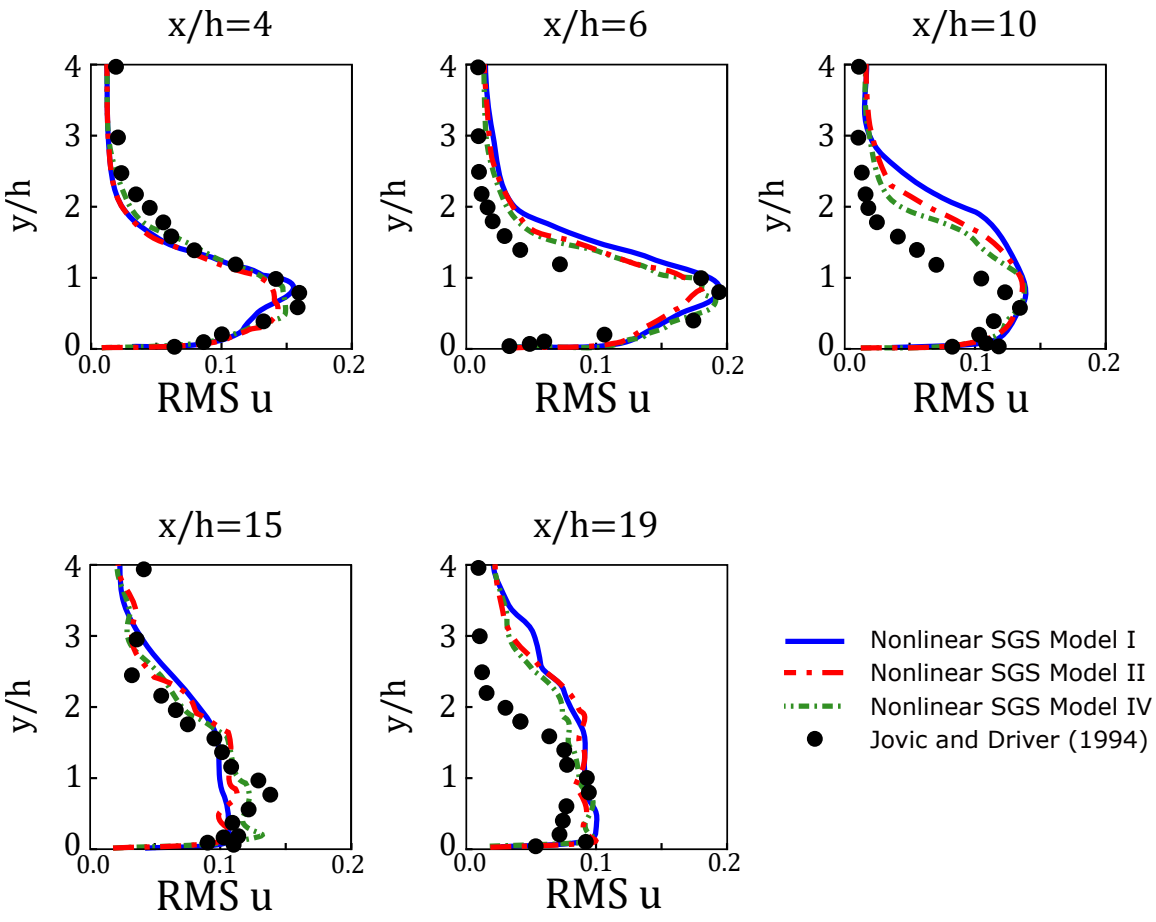

Figure 3.56 – Root-mean-square velocity profiles in the x-direction as a function of y/h in several sections in the midplane $z/L = 0.5$, comparisons are established with Jovic and Driver [71].

Chapter 4

Discussion and conclusions

The goal of the present thesis is divided into three main objectives. First, we analyzed the statistical uncertainties of direct numerical simulation of turbulent plane channel flow in order to ensure the quality of the data used in the present work. Then, fully spectral approach has been followed that isolates the effect of the mean shear inhomogeneity and the planar homogeneity characteristic of the fully developed channel flow as well as offering a comparative analysis of results at $Re_\tau = 180$ and $Re_\tau = 1000$, in this way we are able to understanding the small eddies behavior in a turbulent wall bounded flow. Finally, the present work investigated the influence of nonlinear modeling of the SGS stress tensor by means of an *a priori* test using DNS data of a turbulent plane channel flow and *a posteriori* test in a lid-driven cubic cavity and a backward step flows. The novel nonlinear subgrid-scale model for large eddy simulation includes combinations of the tensors $\widetilde{\boldsymbol{S}}$ and $\widetilde{\boldsymbol{P}}$, both objectives.

4.1 Statistical uncertainties and convergence for turbulent plane channel flows

In order to analyze the statistical data quality of the DNS applied in the present work, from the perspective of the momentum balance equation or its integrated form, the mean streamwise velocity and Reynolds stress tensor can be interpreted as dual statistical quantities. Considering one of this quantities as a given, the other can be computed. The deviation between the computed value and the corresponding provided value can be considered an error estimation for the evaluated statistical quantity. we performed new direct numerical simulations for $Re_\tau = 180$ and $Re_\tau = 590$, in order to evaluate the time evolution of these uncertainties. These error estimations became functions of the dimensionless averaging time, with a correction that takes the box size into account, leading to $E_R(y^+, T^*)$ and $E_U(y^+, T^*)$. These functions are shown in a plot of T^* versus y^+, revealing the highest errors at high y^+ and low T^*, as expected. Some

line samples of $E_R(y^+, T_i^*)$ and $E_U(y^+, T_i^*)$, for chosen values of T_i^*, are shown in order to illustrate the uncertainty as a function of the position that would have been achieved if T_i^* had been adopted to end the numerical simulation. The final averaging time considered in the present thesis was compared with other databases for similar values of Re_τ, leading to the lowest error estimates of the available literature. The RMS-norms of the functions $E_R(y^+, T^*)$ and $E_U(y^+, T^*)$ were obtained by integrating over the whole domain and in each of the classical layers of wall turbulence, leading to quantities that depend on time, but not on the position in wall units, i.e., $\|E_R\|(T^*)$ and $\|E_U\|(T^*)$. The evolution in time of the whole domain norms is compared with the RMS-norms of $E_R(y^+, T_f^*)$ and $E_U(y^+, T_f^*)$, of the databases of the different groups investigated in the present thesis (T_f^* is the final averaging time reported by the respective group). In this way, we could obtain a clear picture of the behavior of the decay of the uncertainty, and how it meets the final uncertainty reported by the different groups.

4.2 Evaluation of spectral budget in DNS data of turbulent channel flow

To analyze the behavior of the terms composing the balance of turbulent kinetic energy equation, the transport equation for the energy spectral density has been derived and partitioned into terms representing in-plane (homogeneous direction) and inter-plane (inhomogeneous direction) energetic transfer. The energetic scale transfer has been analyzed as a function of wavenumber at various locations across the channel. The results showed that the spectral range of the relevant energetic dynamics for the $Re_\tau = 180$ case were narrower than the corresponding range for the $Re_\tau = 1000$ case. Among the results, a spectral broadening at the higher Reynolds number due to an increase in the lower wavenumber scales was shown. This increase was found to primarily affect the bulk region of the flow for the majority of energetic budget terms. Also presented was an analysis of the energetic scale transfer as a function of wall distance at different wavenumber bands. These results showed that the primary contributions to the energetic dynamics across the channel were due to spectral scales in the inertial range and higher. Near the wall the spectral content of the budget terms varied little between Reynolds numbers. Away from the wall, in the buffer layer and into the bulk layer, more variation in energy band contributions was found. A validation of the methodology has also been performed with a comparison with results from a previous study [17] at low Reynolds number.

In addition to the insights into the energetic dynamics provided by this spectral budget study, the results obtained here are relevant to the improved development of SGS models for use in multi-scale methods including both LES and hybrid RANS/LES.

Demands on multi-scale methods, such as LES and hybrid RANS-LES, to yield flow field solutions to ever increasing complex flows is increasing. While increased temporal and spatial resolution will inherently improve the solution accuracy, the associated increased costs severely curtail the feasibility of using such methodologies. As with all turbulent solution methodologies requiring some form of modeling, it is the quality of the models to accurately replicate the effects of the unresolved motions that correlates with of the overall flow field solution. For LES and hybrid methods, this means that the effects of the unresolved and/or subfilter scale motions need to be accurately replicated. It has long been known that backscatter [124] plays a pivotal role in the energetic dynamics. A detailed knowledge of the influence of inhomogeneity and anisotropy as well as the influence of Reynolds on the spectral behavior can significantly improve the predictability of the functional modeling of the subgrid and subfilter scales (see Sagaut [133]). For instance, Chaouat and Schiestel [22], by using the spectral transfer concept, proposed a new large eddy simulation model, where the energy transfers for the subgrid turbulent TKE was tracked. Cimarelli and De Angelis [27] studied how new subgrid-scale modeling approach could be enhanced by new physical concepts based on the multi-dimensional feature of energy transfer. On the side of RANS models, DNS are able to provide very detailed data in order to estimate the quality of different turbulence modeling approaches. For instance, as pointed out by Bolotnov et al. [18], the understanding of the spectral and spatial turbulent kinetic energy transfer can help the modeling of the energy transfers between liquid eddies of different sizes and the energy exchanges between dispersed bubbles and liquid eddies.

4.3 A new nonlinear SGS model for large eddy simulation

Concerning the *a priori* test of the new nonlinear subgrid-scale model for large eddy simulation proposed in the present work, by analyzing the linear closure model employing the rate-of-strain, it was showed that the SGS model composed by only the rate-of-strain tensor (Smagorinsky model) is not a good assumption, mainly in the close-to-wall region, even when an ideal and exact distribution field of the turbulent viscosity is applied. This behavior can be explained by the poor prediction of the SGS anisotropy when the rate-of-strain is employed. Good correlation was found between the subgrid-scale tensor and the most complete nonlinear SGS model. This result can be considered a significant improvement, since this is found to increase its correlation in the close-to-wall region, where most closure models fail. Therefore, the proposed model possesses a great potential to predict a more accurate dissipation of energy in regions of great complexity. The findings of the present study suggest that by using a more

complete SGS model, the dissipation of the turbulent kinetic energy is better estimated, since we do not impose neither alignment between the eigenvectors nor proportionally between the eigenvalues of $\boldsymbol{\tau}$ and $\widetilde{\boldsymbol{S}}$. Regarding the parameters of influences, it was shown that the Reynolds number does not influence in the correlation of the tested models. It is worth mentioning that the closure models applied in the present work are solely based on objective tensorial basis, where its components are invariant under changes of reference frame.

With respect to the *a posteriori* test, time integration results of three nonlinear SGS models for LES of the lid-driven cubical cavity flow at a Reynolds number of 10,000 and the backward facing step flow at $Re = 5,000$ have been presented for a dynamic subgrid-scale approach. These simulations have been carried out on a parallel architecture algorithm based on a finite difference scheme in an adaptive mesh refinement approach. In general, the results for the SGS models have shown qualitatively good agreement with experimental reference results from Prasad and Koseff [128] and Jovic and Driver [71]. When comparisons of the velocity fluctuation of the tested nonlinear SGS models are established, we found that among the three SGS models, Model IV found to give better performance compared with Models I and II. And consequently, Model II obtained results closer to the experimental results than Model I. In other words, by means of LES simulations, it was confirmed that the inclusion of new tensors to the tensor basis modeling the subgrid-scale tensor presented improvements to the analyzed correlations, both in close to the walls and in central regions.

Chapter 5

Curriculum vitae and publications

5.1 Curriculum vitae

Degrees

- 2015-2019: **Double doctorate PhD program** (*Cotutelle-de-Thèse*) in Fluid Mechanics. **Title**: Spectral analysis of the turbulent energy cascade and the development of a novel nonlinear subgrid-scale model for large eddy simulation. **Supervisors**: Professors Gilmar Mompean, Aristeu da Silveira Neto and Roney Leon Thompson. **Universities**: *Université de Lille* and *Universidade Federal de Uberlândia*. **Scholarships**: PhD scholarships provided by the Brazilian government and Petrobras.

- 2014-2015: **Master of Sciences** in Fluid Mechanics. **Title**: Immersed boundary methods for flow over thin plates and sharp edges. **Supervisor**: Professor Aristeu da Silveira Neto. **University**: *Universidade Federal de Uberlândia*. **Scholarships**: PhD scholarships provided by the Brazilian government and Petrobras.

- 2013: **Master of Sciences** in Vibro Acoustics. **Title**: *Modélisation vibro-acoustique d'un démarreur VALEO*. **Supervisor**: Nacer Hamzaoui and Nicolas Totaro. **University**: *Institut National des Sciences Appliquées de Lyon (INSA)*.
  Scholarships: PhD scholarships provided by the Brazilian government.

- 2008-2013: **Double degree (Bachelor of Engineering)** in Mechanical Engineering. **University**: *Institut National des Sciences Appliquées de Lyon (INSA)*.

- 2008-2013: **Bachelor of Engineering** in **Mechanical Engineering**. **University**: *Universidade Federal de Uberlândia*.

Employment History

- 2017-2019: Assistant Professor, *Centro Universitário de Patos de Minas (UNIPAM)*, Department of Mechanical Engineering, Patos de Minas-Brazil.

- 2011-2012: Internship, *Institut National de l'Énergie Solaire*.

Teaching Activities

- **Undergraduate Courses**: Fluid Mechanics, Heat Transfer, Numerical Methods, *Centro Universitário de Patos de Minas* (2017 – 2019).

Journal reviewer

- Reviewer for the **Journal of the Brazilian Society of Mechanical Science and Engineering**, 2018-2019.

- Reviewer for the **Physics of Fluids**, 2018-2019.

Languages

- **Portuguese**, native. **French**, full professional proficiency. **English**, full professional proficiency. **Spanish**, basic knowledge.

5.2 Publications

Journal publications

- Andrade, J. R., Martins, R. S., Mompean, G. Laurent Thais, L., and B. Gatski, T. B., 2018. "Analyzing the spectral energy cascade in turbulent channel flow". *Phys Fluids*, 30(6), p. 065110.

- Andrade, J. R., Martins, R. S., Thompson, R. L., Mompean, G., and Silveira-Neto, A., 2018. "Analysis of uncertainties and convergence of the statistical quantities in turbulent wall-bounded flows by means of a physically based criterion". *Phys Fluids*, 30(4), p. 045106.

- Andrade, J. R., Martins, R. S., Silveira-Neto, A. and Vedovoto, J. M. =, 2018. "Assessment of two immersed boundary methods for flow over thin plates and sharp edges". *J. Braz. Soc. Mech. Sci. & Eng.*, 40:288.

Submitted journal articles

- Andrade, J. R., Martins, R. S., Thompson, R. L., Mompean, G., and Silveira-Neto, A., 2019. "A nonlinear subgrid-scale closure model employing the non-persistence-of-straining tensor". *J Fluid Eng*.

Articles in preparation

- Andrade, J. R., Martins, R. S., Thompson, R. L., Mompean, G., and Silveira-Neto, A., 2019. "Analysis of a objective nonlinear subgrid-scale model for Large Eddy Simulation". *Comp Fluids*.

- Andrade, J. R., Martins, R. S., Mompean, G. Laurent Thais, L., and B. Gatski, T. B., 2019. "Analyzing the spectral energy cascade in viscoelastic turbulent flow". *J Nonnewton Fluid Mech*.

- Andrade, J. R., Martins, R. S., Thompson, R. L., Mompean, G., 2019. "Analysis of uncertainties and convergence of the statistical quantities in viscoelastic turbulent flows". *J Nonnewton Fluid Mech*.

More recent conference presentations

- Andrade, J. R.; Martins, R. S. ; Mompean, G. ; Thais, L. ; Gatski, T. B. "A simultaneous spectral/spatial analysis of turbulent kinetic energy in turbulent channel flow: the effect of the Reynolds number". In: *Conference on Turbulence, Heat and Mass Transfer.*, 2018, Rio de Janeiro-Brazil.

- Andrade, J. R.; Martins, R. S. ; Mompean, G. ; Thompson, R. L. "Quantification of statistical imbalance in DNS of plane channel flows of viscoelastic fluids". In: *VIII Brazilian Conference on Rheology*, 2018, São Leopoldo-Brazil.

- Andrade, J. R.; Martins, R. S. ; Mompean, G. ; Thompson, R. L.; Silveira-Neto, A. "Evaluation of the statistical convergence of turbulent flow data." In: *24th International Congress of Mechanical Engineering*, 2018, Curitiba-Brazil.

Bibliography

[1] H. Abe, H. Kawamura, and H. Choi. "Very Large-Scale Structures and Their Effects on the Wall Shear-Stress Fluctuations in a Turbulent Channel Flow up to $Re_\tau = 640$". In: *J Fluid Eng* 126(5), 83 (2004). DOI: https://doi.org/10.1115/1.1789528.

[2] M. Alves, P. Oliveira, and F. Pinho. "A convergent and universally bounded interpolation scheme for the treatment of advection". In: *Int. J. Numer. Meth. Fluids* 41.1994 (2003), pp. 47–75. DOI: https://doi.org/10.1002/fld.428.

[3] J. R. Andrade et al. "Analysis of uncertainties and convergence of the statistical quantities in turbulent wall-bounded flows by means of a physically based criterion". In: *Phys Fluids* 30(4) (2018), p. 045106. DOI: https://doi.org/10.1063/1.5023500.

[4] J. R. Andrade et al. "Analyzing the spectral energy cascade in turbulent channel flow". In: *Phys Fluids* 30(6) (2018), p. 065110. DOI: https://doi.org/10.1063/1.5022653.

[5] R. Antonia, B. Satyaprakash, and A. Hussain. "Statistics of fine-scale velocity in turbulent plane and circular jets". In: *J Fluid Mech* 119 (1982), pp. 55–89. DOI: 10.1017/S0022112082001268.

[6] G. Astarita. "Objective and generally applicable criteria for flow classification". In: *J Non-Newton Fluid Mech* 6.1 (1979), pp. 69–76. ISSN: 03770257. DOI: 10.1016/0377-0257(79)87004-4.

[7] F. Aulery et al. "Energy transfer process of anisothermal wall-bounded flows". In: *Physics Letters A* 379 (2015), pp. 1520–1526. DOI: https://doi.org/10.1016/j.physleta.2015.03.022.

[8] F. Aulery et al. "Spectral analysis of turbulence in anisothermal channel flows". In: *Computers & Fluids* 000 (2016), pp. 1–17.

[9] J. S. Baggett, J. Jiménez, and A. G. Kravchenko. "Resolution requirements in large-eddy simulations of shear flows". In: *Center for Turbulence Research Annual Research Briefs* Chapman 1979 (1997), pp. 51–66.

[10] J. L. Balint, P. Vukoslavčecić, and J. M. Wallace. "European Turbulence Conf." In: *Proc Adv in Turb*. Ed. by G. Comte-Bellot and J. Mathieu. Springer, 1987, p. 456.

[11] J. Bardina, J. H. Ferziger, and W. C. Reynolds. "Improved subgrid-scale models for large eddy simulation." In: *AIAA* Paper 80-1 (1980).

[12] M. J. Berger and P. Colella. "Local adaptive mesh refinement for shock hydrodynamics". In: *J Comput Phys* 82 (1989), pp. 64–84. DOI: https://doi.org/10.1016/0021-9991(89)90035-1.

[13] M. Bernardini, S. Pirozzoli, and P. Orlandi. "Velocity statistics in turbulent channel flow up to $Re_\tau = 4000$". In: *J Fluid Mech* 742.2014 (2014), pp. 171–191. ISSN: 0022-1120. DOI: 10.1017/jfm.2013.674.

[14] R. F. Blackwelder and H. Eckelmann. "Streamwise vortices associated with the bursting phenomenon". In: *J Fluid Mech* 94.3 (1979), pp. 577–594. DOI: 10.1017/S0022112079001191.

[15] R. F. Blackwelder and J. H. Haritonidis. "Scaling of the bursting frequency in turbulent boundary layers". In: *J Fluid Mech* 132 (1983), pp. 87–103. ISSN: 0022-1120. DOI: 10.1017/S0022112083001494.

[16] J. Blazek. *Turbulence modelling, Computational Fluid Dynamics: Principles and Applications*. second. Elsevier Science, Oxford, 2005, pp. 227–270.

[17] I. A. Bolotnov et al. "Spectral analysis of turbulence based on the DNS of a channel flow." In: *Computer & Fluids* 39(4):640–55 (2010). DOI: https://doi.org/10.1016/j.compfluid.2009.11.001.

[18] I. A. Bolotnov et al. "Turbulent cascade modeling of single and bubbly two-phase turbulent flows". In: *Int J Multiphase Flow* 34 (2008), pp. 1142–1151. DOI: https://doi.org/10.1016/j.ijmultiphaseflow.2008.06.006.

[19] V. Borue and S. A. Orszag. "Local energy flux and subgrid-scale statistics in three-dimensional turbulence". In: *J Fluid Mech* 366.1 (1998). ISSN: 00221120. DOI: 10.1017/S0022112097008306.

[20] R. Bouffanais et al. "Large-eddy simulation of the lid-driven cubic cavity flow by the spectral element method". In: *J Sci Comput* 27 (2006), p. 151. DOI: https://doi.org/10.1007/s10915-005-9039-7.

[21] T. Brandt. "A priori tests on numerical errors in large eddy simulation using finite differences and explicit filtering". In: *Int J Numer Meth Fluids* 00:1–36 (2005).

[22] B. Chaouat and R. Schiestel. "A new partially integrated transport model for subgrid-scale stresses and dissipation rate for turbulent developing flows." In: *Phys Fluids A* 17 (2005), p. 065106. DOI: https://doi.org/10.1063/1.1928607.

[23] P. Chassaing. *Turbulence en mécanique des fluides : analyse du phénoméne en vue de sa modélisation à l'usage de l'ingénieur*. Polytech, 2000.

[24] H. Choi and P. Moin. "Grid-point requirements for large eddy simulation: Chapman's estimates revisited". In: *Phys Fluids* 24.1 (2012). ISSN: 10706631. DOI: 10.1063/1.3676783.

[25] A. J. N. Chorin. "Numerical solution of the navier-stokes equations". In: *Math Comput* 22 (1968), pp. 745–762. DOI: https://doi.org/10.1090/S0025-5718-1968-0242392-2.

[26] F. K. Chow and P. Moin. *A further study of numerical errors in large-eddy simulations*. Vol. 184. 2. 2003, pp. 366–380. ISBN: 0021-9991. DOI: 10.1016/S0021-9991(02)00020-7.

[27] A. Cimarelli and E. De Angelis. "The physics of energy transfer toward improved subgrid-scale models." In: *Phys Fluids* 26(5):055103 (1994). DOI: https://doi.org/10.1063/1.4871902.

[28] A. Cimarelli, E. De Angelis, and C. Casciola. "Paths of energy in turbulent channel flows." In: *J Fluid Mech* 715:436–51 (2013). DOI: https://doi.org/10.1017/jfm.2012.528.

[29] R. A. Clark, J. H. Ferziger, and W. C. Reynolds. "Evaluation of subgrid-scale models using an accurately simulated turbulent flow." In: *J Fluid Mech* 91 part 1: (1979). DOI: https://doi.org/10.1017/S002211207900001X.

[30] H. W. Coleman and W. G. Steele. "Engineering application of experimental uncertainty analysis". In: *AIAA J* 33.10 (1995), pp. 1888–1896. ISSN: 1533-385X. DOI: http://dx.doi.org/10.2514/3.12742.

[31] G. Comte-Bellot and S. Corrsin. "The use of a contraction to improve the isotropy of grid-generated turbulence". In: *J Fluid Mech* 25 (1966), p. 657. DOI: https://doi.org/10.1017/S0022112066000338.

[32] Geneviève Comte-Bellot. *Écoulement turbulent entre deux parois parallèles*. France: Publications Scientifiques et Techniques du Ministère de l'Air No. 419, 1965, 159 p.

[33] S. Corrsin. "Local isotropy in turbulent shear flow". In: *Naca RM 58B11* (1958).

[34] G. De Stefano, O. V. Vasilyev, and D. E. Goldstein. "A-priori dynamic test for deterministic/stochastic modeling in large-eddy simulation of turbulent flow". In: *Computer Physics Communications*. Vol. 169. 1-3. 2005, pp. 210–213. DOI: 10.1016/j.cpc.2005.03.047.

[35] J. W. Deardorff. "A numerical study of three-dimensional turbulent channel flow at large Reynolds numbers". In: *J Fluid Mech* 41.1970 (1970), pp. 453–480. ISSN: 0022-1120. DOI: 10.1017/S0022112070000691.

[36] J. C. Del Álamo and J. Jiménez. "Spectra of the very large anisotropic scales in turbulent channels". In: *Phys Fluids* 15.6 (2003). ISSN: 10706631. DOI: 10.1063/1.1570830. eprint: 1309.2322.

[37] J. C. Del Álamo et al. "Scaling of the energy spectra of turbulent channels". In: *J Fluid Mech* 500 (2004), pp. 135–144. ISSN: 0022-1120. DOI: 10.1017/S002211200300733X.

[38] J. M. J. den Toonder and F. T. M. Nieuwstadt. "Reynolds number effects in a turbulent pipe flow for low to moderate Re". In: *Phys Fluids* 9.11 (1997), p. 3398. ISSN: 10706631. DOI: 10.1063/1.869451.

[39] J. A. Domaradzki and W. Liu. "Energy transfer in numerically simulated wall–bounded turbulent flows." In: *Phys Fluids* 6(4):1583–99 (1994). DOI: https://doi.org/10.1063/1.868272.

[40] J. A. Domaradzki, W. Liu, and M. E. Brachet. "An analysis of subgrid-scale interactions in numerically simulated isotropic turbulence". In: *Phys Fluids A: Fluid Dynamics* 5.7 (1993), p. 1747. ISSN: 08998213. DOI: 10.1063/1.858850.

[41] J. A. Domaradzki and R. S. Rogallo. "Local energy transfer and nonlocal interactions in homogeneous, isotropic turbulence". In: *Phys Fluids* 2(3):413–26 (1990). DOI: https://doi.org/10.1063/1.857736.

[42] J. A. Domaradzki and E. M. Saiki. "A subgrid-scale model based on the estimation of unre- solved scales of turbulence." In: *Physics Fluids* 9(7):2148 (1997). DOI: https://doi.org/10.1063/1.869334.

[43] D. A. Donzis, P. K. Yeung, and K. R. Sreenivasan. "Dissipation and enstrophy in isotropic turbulence: resolution effects and scaling in direct numerical simulations". In: *Phys Fluids* 20 (2008), p. 045108. DOI: https://doi.org/10.1063/1.2907227.

[44] D. C. Dunn and J. F. Morrison. "Analysis of the energy budget in turbulent channel flow using orthogonal wavelets". In: *Computers & Fluids* 34 (2005), p. 199. DOI: https://doi.org/10.1016/j.compfluid.2004.04.003.

[45] J. G. Eggels et al. "Fully Developed Turbulent Pipe Flow: A Comparison Between Direct Numerical Simulation and Experiment". In: *J Fluid Mech* 268.1994 (1994), pp. 175–209. DOI: https://doi.org/10.1017/S002211209400131X.

[46] A. Eppler and K. Bernert. *Two-Stage Testing of Advanced Dynamic Subgrid-Scale Mo dels for Large-Eddy Simulation on Parallel Computers*. Tech. rep. Eppler1999: Chemnitz University of Technology, 1999.

[47] K. Fukagata and N. Kasagi. "Highly Energy-Conservative Finite Difference Method for the Cylindrical Coordinate System". In: *J Comput Phys* 181.2 (2002), pp. 478–498. ISSN: 0021-9991. DOI: http://dx.doi.org/10.1006/jcph.2002.7138.

[48] T. B. Gatski and C. G. Speziale. "On explicit algebraic stress models for complex turbulent flows". In: *J Fluid Mech* 254 (1993), pp. 59–78. DOI: https://doi.org/10.1017/S0022112093002034.

[49] W. K. George. "The decay of homogeneous isotropic turbulence". In: *Phys Fluids* 4 (1992), p. 1492.

[50] W. K. George, P. D. Beuther, and J. L. Lumley. "Processing of random signals". In: *Proceedings of the dynamic flow conference 1978 on dynamic measurements in unsteady flows*. Ed. by B. W. Hansen. Springer Netherlands, 1978, pp. 757–800. ISBN: 978-94-009-9565-9. DOI: 10.1007/978-94-009-9565-9_43.

[51] M. Germano et al. "A dynamic subgrid-scale eddy viscosity model." In: *Phys Fluids* 3, 1760 (1991).

[52] B. J. Geurts and J. Fröhlich. "A framework for predicting accuracy limitations in large-eddy simulation". In: *Phys Fluids* 14.6 (2002). ISSN: 10706631. DOI: 10.1063/1.1480830.

[53] S. Ghosal. "An Analysis of Numerical Errors in Large-Eddy Simulations of Turbulence". In: *J Comput Phys* 125.1 (1996), pp. 187–206. ISSN: 00219991. DOI: 10.1006/jcph.1996.0088.

[54] H. Gong. "Testing of Subgrid-Scale Stress Models by Using Results from Direct Numerical Simulations". In: *Commun Nonlinear Sci Numer Simul* 3.2 (1998), pp. 87–91.

[55] P. Gualtieri et al. "Preservation of statistical properties in large-eddy simulation of shear turbulence". In: *J Fluid Mech* 592 (2007), pp. 471–494. DOI: https://doi.org/10.1017/S0022112007008609.

[56] Gullbrand, J. "Explicit filtering and subgrid-scale models in turbulent channel flow". In: *Center for Turbulence Research, Annual Research Briefs*. 2001, pp. 31–42.

[57] C. Härtel et al. "Subgrid-scale energy transfer in the near–wall region of turbulent flows." In: *Phys Fluids* 6(9):3130 (1994). DOI: https://doi.org/10.1063/1.868137.

[58] R. J. Hill. "Equations relating structure functions of all orders". In: *J Fluid Mech* 434 (2001), pp. 379–388. DOI: https://doi.org/10.1017/S0022112001003949.

[59] R. J. Hill. "Exact second-order structure-function relationship". In: *J Fluid Mech* 468 (2002), pp. 317–326. DOI: https://doi.org/10.1017/S0022112002001696.

[60] J. H. Hogenes and T. J. Hanratty. "The use of multiple wall probes to identify coherent flow patterns in the viscous wall region". In: *J Fluid Mech* 124, 363 (1982). ISSN: 14697645. DOI: 10.1017/S0022112082002547.

[61] K. Horiuti. "Roles of non-aligned eigenvectors of strain-rate and subgrid-scale stress tensors in turbulence generation". In: *J Fluid Mech* 491.August (2003), pp. 65–100. ISSN: 00221120. DOI: 10.1017/S0022112003005299.

[62] S. Hoyas and J. Jiménez. "Scaling of the velocity fluctuations in turbulent channels up to $Re_\tau = 2003$". In: *Phys Fluids* 18(1):0117 (2006).

[63] J. C. R. Hunt, A. A. Wray, and P. Moin. "Eddies, Stream, and Convergence Zones in Turbument Flows". In: *Center for Turbulence Research, Proceeding of the Summer Program*. 1. 1988, pp. 193–208. ISBN: CTR-S88. DOI: CTR-S88.

[64] T. Ishihara et al. "Small-scale statistics in high-resolution direct numerical simulation of turbulence: Reynolds number dependence of one-point velocity gradient statistics". In: *J Fluid Mech* 592, pp. 335-366 (2007). DOI: https://doi.org/10.1017/S0022112007008531.

[65] K. Iwamoto, Y. Suzuki, and N. Kasagi. "Reynolds Number Effect on Wall Turbulence: Toward Effective Feedback Control". In: *Control* 23 (2002), pp. 678 –689. DOI: https://doi.org/10.1016/S0142-727X(02)00164-9.

[66] J. Jiménez. "The physics of wall turbulence". In: *Physica A* 263 (1999), pp. 252–262.

[67] J. Jiménez and R. D. Moser. *A Selection of Test Cases for the Validation of Large-Eddy Simulations of Turbulent Flows*. Tech. rep. Advisory group for aerospace research and development, 1998, p. 5.

[68] A. V. Johansson and P. H. Alfredsson. "On the structure of turbulent channel flow". In: *J Fluid Mech* 122 (1982), pp. 295–314. ISSN: 0022-1120. DOI: 10.1017/S0022112082002225.

[69] S. A. Jordan. "A Priori Assessments of Numerical Uncertainty in Large-Eddy Simulations". In: *J Fluid Eng* 127 (2005), p. 1171. ISSN: 00982202. DOI: 10.1115/1.2060735.

[70] S. A. Jordan and S. A. Ragab. "On the unsteady and turbulent characteritics of the three-dimensional shear-driven cavity flow." In: *J. Fluids Eng.* 116 (1994), pp. 439–449. DOI: https://doi.org/10.1115/1.2910296.

[71] S. Jovic and D. M. Driver. *Backward-facing step measurements at low Reynolds number, Re(sub h)=5000*. Tech. rep. February. NASA, 1994, p. 25.

[72] E. G. Kastrinakis and H. Eckelmann. "Measurement of streamwise vorticity fluctuations in a turbulent channel flow". In: *J Fluid Mech* 137.1 (1983), pp. 165–186. ISSN: 0022-1120. DOI: 10.1017/S0022112083002347.

[73] A. Keating et al. "A priori and a posteriori tests of inflow conditions for large-eddy simulation". In: *Phys Fluids* 16.12 (2004), pp. 4696–4712. ISSN: 10706631. DOI: 10.1063/1.1811672.

[74] G. K. E. Khoury et al. "Direct Numerical Simulation of Turbulent Pipe Flow at Moderately High Reynolds Numbers". In: *Flow Turbul Combust* 91, 475-49 (2013), pp. 475–495. DOI: 10.1007/s10494-013-9482-8.

[75] J. Kim, P. Moin, and R. Moser. "Turbulence statistics in fully developed channel flow at low Reynolds number". In: *J Fluid Mech* 177, 133–166 (1987). DOI: https://doi.org/10.1017/S0022112087000892.

[76] K. C. Kim and R. J. Adrian. "Very large-scale motion in the outer layer". In: *Phys Fluids* 11.2 (1999), p. 417. ISSN: 10706631. DOI: 10.1063/1.869889.

[77] J. C. Klewicki and R. E. Falco. "On accurately measuring statistics associated with small-scale structure in turbulent boundary layers using hot-wire probes". In: *J Fluid Mech* 219.-1 (1990), p. 119. ISSN: 0022-1120. DOI: 10.1017/S0022112090002889.

[78] A. Kolmogorov. "The local structure of turbulence in incompressible viscous fluid for very large Reynolds numbers". In: *Doklady Akademiia Nauk SSSR* 30.1890 (1941), pp. 301–305. DOI: 10.1098/rspa.1991.0075.

[79] J. R. Koseff and R. L. Street. "The lid-driven cavity flow: A synthesis of qualitative and quantitative observations". In: *J. Fluids Eng.* 106 (1984), pp. 390–398. DOI: https://doi.org/10.1115/1.3243136.

[80] B. Kosovic. "Subgrid-scale modelling for the large-eddy simulation of high-reynolds-number boundary layers". In: *J Fluid Mech* 336.1 (1997), pp. 151–182.

[81] M. Kozuka, Y. Seki, and H. Kawamura. "DNS of turbulent heat transfer in a channel flow with a high spatial resolution". In: *Int J Heat Fluid Flow* 30 (2009), pp. 514–524. DOI: 10.1016/j.ijheatfluidflow.2009.02.023.

[82] R. H. Kraichnan. "Helical turbulence and absolute equilibrium". In: *J Fluid Mech* 59 (1973), pp. 745–752. DOI: https://doi.org/10.1017/S0022112073001837.

[83] A. G. Kravchenko and P. Moin. "On the Effect of Numerical Errors in Large Eddy Simulations of Turbulent Flows". In: *J Comput Phys* 131.2 (1997), pp. 310–322. ISSN: 00219991. DOI: 10.1006/jcph.1996.5597.

[84] H-P. Kreplin and H. Eckelmann. *Behavior of the three fluctuating velocity components in the wall region of a turbulent channel flow*. Ed. by G Comte-Bellot and J Mathieu. Vol. 22. ERCOFTAC pp 229-236 7. Lille, France: Springer, 1979, pp. 1233–1239. ISBN: 9788578110796. DOI: 10.1063/1.862737.

[85] E. Labourasse et al. "Towards large eddy simulation of isothermal two-phase flows: Governing equations and a priori tests". In: *Int J Multiphase Flow* 33.1 (2007), pp. 1–39. ISSN: 03019322. DOI: 10.1016/j.ijmultiphaseflow.2006.05.010.

[86] M. C. Lai, Y. H. Tseng, and H. Huang. "An immersed boundary method for interfacial flows with insoluble surfactant." In: *J Comput Phys* v. 227, n. (2008).

[87] J. Laufer. "Investigation of turbulent flow in a two-dimensional channel". In: *NACA Tech. Note* TN2123 (1950).

[88] M. Lee and R. D. Moser. "Direct numerical simulation of turbulent channel flow up to $Re_\tau = 5200$". In: *J Fluid Mech* 774:395–4 (2015). DOI: https://doi.org/10.1016/j.compfluid.2008.10.003.

[89] S. K. Lele. "Compact Finite Difference Schemes with spectral like resolution". In: *J Comput Phys* 103 (1992), pp. 16–42. DOI: https://doi.org/10.1016/0021-9991(92)90324-R.

[90] A. Leonard. "On the energy cascade in Large-Eddy Simulations of turbulent flows." In: *Adv in Geophys* A18 (1973).

[91] E. Leriche and S. Gavrilakis. "Direct numerical simulation of the flow in the lid-driven cubical cavity." In: *Phys Fluids* 12 (2000), pp. 1363–1376. DOI: https://doi.org/10.1017/jfm.2015.268.

[92] M. Lesieur, O. Métais, and P. Comte. *Large-Eddy Simulations of Turbulence*. Cambridge University Press, 2005.

[93] D. Lilly. "A proposed modification of the Germano subgrid-scale closure method." In: *Phys Fluids* v. 4, p. 6 (1992).

[94] S. Liu, C. Meneveau, and J. Katz. "Experimental study of similarity subgrid-scale models of turbulence in the far field of a jet. In Direct and Large Eddy Simulation I." In: pp. 3748 (1994).

[95] S. Liu, C. Meneveau, and J. Katz. "On the properties of similarity subgrid-scale models as deduced from measurements in a turbulent jet". In: *J Fluid Mech* 215 (1994), pp. 82–119. DOI: https://doi.org/10.1017/S0022112094002296.

[96] A. Lozano-Durán and J. Jiménez. "Effect of the computation domain on direct simulations of turbulent channels up to $Re_\tau = 4200$". In: *Phys Fluids* 26:011702 (2014). DOI: https://doi.org/10.1063/1.4862918.

[97] H. Lu, C. J. Rutland, and L. M. Smith. "A posteriori tests of one-equation LES modeling of rotating turbulence". In: *Int J Mod Phys C* 19.12 (2008), pp. 1949–1964. ISSN: 1468-5248. DOI: 10.1080/14685240701493947.

[98] J. L. Lumley. "Toward a turbulent constitutive relation". In: *J Fluid Mech* 41 (1970), pp. 413–434. DOI: https://doi.org/10.1017/S0022112070000678.

[99] T. S. Lund and E. A. Novikov. "Parametrization of subgrid-scale stress by the velocity gradient tensor". In: Center of Turbulence Research - Annual Research Briefs. 1992.

[100] P. Majander and T. Siikonen. "Evaluation of Smagorinsky-based subgrid-scale models in a finite-volume computation". In: *Int J Numer Meth Fluids* 00:1–36 (2002). DOI: https://doi.org/10.1002/fld.374.

[101] N. N. Mansour, J. Kim, and P. Moin. "Reynolds-stress and dissipation-rate budgets in a turbulent channel flow". In: *J Fluid Mech* 194 (1998), pp. 15–44. DOI: https://doi.org/10.1017/S0022112088002885.

[102] N. Marati, C. Casciola, and R. Piva. "Energy cascade and spatial fluxes in wall turbulence." In: *J Fluid Mech* 521:191–215 (2004). DOI: https://doi.org/10.1017/S0022112004001818.

[103] L. Marstorp et al. "Explicit algebraic subgrid stress models with application to rotating channel". In: *J Fluid Mech* 639 (2009), pp. 403–432. DOI: https://doi.org/10.1017/S0022112009991054.

[104] B. J. McKeon et al. "Further observations on the mean velocity distribution in fully developed pipe flow". In: *J Fluid Mech* 501 (2004), pp. 135–147. DOI: https://doi.org/10.1017/S0022112003007304.

[105] C. Meneveau. "Germano identity-based subgrid-scale modeling: A brief survey of variations on a fertile theme". In: *Phys Fluids* 24.12 (2012). ISSN: 10706631. DOI: 10.1063/1.4772062.

[106] C. Meneveau. "Statistics of turbulence subgrid-scale stresses: Necessary conditions and experimental tests." In: *Phys Fluids* 6, 815 (1994). DOI: https://doi.org/10.1063/1.868320.

[107] C. Meneveau and J. Katz. "Scale-invariance and turbulence models for large-eddy simulation". In: *Annu Rev Fluid Mech* 32 (2000), pp. 1–32. ISSN: 0066-4189. DOI: 10.1146/annurev.fluid.32.1.1.

[108] J. Meyers and P. Sagaut. "On the model coefficients for the standard and the variational multi-scale Smagorinsky model". In: *J Fluid Mech* 569 (2006), pp. 287–319. DOI: https://doi.org/10.1017/S0022112006002850.

[109] R. J. Moffat. "Describing the uncertainties in experimental results". In: *Exp Therm Fluid Sci* 1.1 (1988), pp. 3–17. ISSN: 0894-1777. DOI: http://dx.doi.org/10.1016/0894-1777(88)90043-X.

[110] P. Moin and J. Kim. "Numerical investigation of turbulent channel flow". In: *J Fluid Mech* 118 (1982), p. 341. ISSN: 0022-1120. DOI: 10.1017/S0022112082001116.

[111] P. Moin and K. Mahesh. "Direct Numerical Simulation: a tool in turbulent research". In: *Annu Rv of Earth and Planet Sci* 30:539–78 (1998). DOI: https://doi.org/10.1146/annurev.fluid.30.1.539.

[112] Parviz Moin. "Advances in large eddy simulation methodology for complex flows". In: *Int J Heat Fluid Flow* 23.5 (2002), pp. 710–720. ISSN: 0142727X. DOI: 10.1016/S0142-727X(02)00167-4.

[113] J-P. Mollicone et al. "Effect of geometry and Reynolds number on the turbulent separated flow behind a bulge in a channel". In: *J Fluid Mech* 823 (2017), pp. 100–133. DOI: https://doi.org/10.1017/jfm.2017.255.

[114] J-P. Mollicone et al. "Turbulence dynamics in separated flows: the generalised Kolmogorov equation for inhomogeneous anisotropic conditions". In: *J Fluid Mech* 841 (2018), pp. 1012–1039. DOI: https://doi.org/10.1017/jfm.2018.114.

[115] A. S. Monin and A. N. Yaglom. *Statistical Fluid Mechanics*. MIT Press, 1975.

[116] J. P. Monty. "Developments in smooth wall turbulent duct flows". PhD thesis. University of Melbourne, 2005, p. 272.

[117] R. D. Moser, J. Kim, and N. N. Mansour. "Direct numerical simulation of turbulent channel flow up to $Re_\tau = 590$". In: *Phys Fluids* 11 (1999), pp. 943–945. DOI: 10.1063/1.869966.

[118] T. A. Oliver et al. "Estimating uncertainties in statistical category computed from direct numerical simulation". In: *Phys Fluids* 26 (2014), p. 035101. ISSN: 1070-6631. DOI: 10.1063/1.4866813.

[119] R. Örlü and P. Schlatter. "Comparison of experiments and simulations for zero pressure gradient turbulent boundary layers at moderate Reynolds numbers". In: *Exp Fluids* 54.6 (2013). ISSN: 07234864. DOI: 10.1007/s00348-013-1547-x.

[120] J. M. Osterlund. "Experimental studies of zero pressure-gradient turbulent boundary layer flow". PhD thesis. Royal Institute of Technology (KTH), 1999.

[121] U. Piomelli. "Large-eddy and direct simulation of turbulent flows". In: CFD Odyssey - 9e conférence annuelle de la Société canadienne de CFD. 2001.

[122] U. Piomelli, P. Moin, and J. H. Ferziger. "Model consistency in large eddy simulation of turbulent channel flows." In: *Physics Fluids* 31(7):1884 (1988). DOI: https://doi.org/10.1063/1.866635.

[123] U. Piomelli, Y. Yu, and R. J. Adrian. "Subgrid-scale energy transfer and near-wall turbulence structure". In: *Phys Fluids* 8 (1996), p. 215. DOI: https://doi.org/10.1063/1.868829.

[124] U. Piomelli et al. "Subgrid-scale backscatter in turbulent and transitional flows." In: *Phys Fluids A* 3 (7), 176 (1991). DOI: https://doi.org/10.1063/1.857956.

[125] H. Pitsch. "Large-eddy simulation of turbulent combustion". In: *Annu Rv of Earth and Planet Sci* 38.1 (2006), pp. 453–482. ISSN: 0066-4189. DOI: 10.1146/annurev.fluid.38.050304.092133.

[126] S. B. Pope. "A more general effective-viscosity hypothesis". In: *J Fluid Mech* 72, 331-34 (1975). DOI: https://doi.org/10.1017/S0022112075003382.

[127] S. B. Pope. *Turbulent Flows*. Cambridge University Press, 2000, pp. 213–214. DOI: https://doi.org/10.1017/CBO9780511840531.

[128] A. K. Prasad and J. R. Koseff. "Reynolds Number and End-Wall Effects on a Lid-Driven Cavity Flow". In: *Phys Fluids A* 1 (1989), pp. 208–218. DOI: https://doi.org/10.1063/1.857491.

[129] A. Rasam et al. "Large eddy simulation of channel flow with and without periodic constrictions using the explicit algebraic subgrid-scale model". In: *J Turbul* 15.11 (2014), pp. 752–775. ISSN: 1468-5248. DOI: 10.1080/14685248.2014.929292.

[130] O. Reynolds. "On the dynamical theory of incompressible viscous fluids and the determination of the criterion". In: *Philos Trans R Soc Lond* 186 (1895), pp. 123–164. ISSN: 1364-503X. DOI: 10.1098/rsta.1979.0079.

[131] Lewis Fry Richardson. *Weather Prediction by Numerical Process*. 1922, p. 236. ISBN: 9780521680448. DOI: 10.2136/sssaj1966.03615995003000010006x. eprint: arXiv:1011.1669v3.

[132] R. S. Rivlin. "The relation between the flow of non-Newtonian fluids and turbulent Newtonian fluids". In: *Q Appl Math* 15 (1957), p. 212. DOI: https://doi.org/10.1090/qam/91736.

[133] P. Sagaut. *Large Eddy Simulation for Incompressible Flows: An Introduction (Scientific Computation)*. 2005, p. 558.

[134] M. V. Salvetti and S. Banerjee. "A priori tests of a new dynamic subgrid-scale model for finite-difference large-eddy simulations." In: *Physics Fluids* 7(11):2831 (1995). DOI: https://doi.org/10.1063/1.868779.

[135] M. V. Salvetti and F. Beux. "The effect of the numerical scheme on the subgrid scale term in large-eddy simulation." In: *Physics Fluids* 10(11):302 (1998). DOI: https://doi.org/10.1063/1.869827.

[136] L. A. C. A. Schiavo, W. R. Wolf, and J. L. F. Azevedo. "Turbulent kinetic energy budgets in wall bounded flows with pressure gradients and separation." In: *Phys Fluids* 29.115108 (2017), pp. 29–43. DOI: https://doi.org/10.1063/1.4992793.

[137] M. P. Schultz and K. A. Flack. "Reynolds-number scaling of turbulent channel flow". In: *Phys Fluids* 25.2 (2013). ISSN: 10706631. DOI: 10.1063/1.4791606.

[138] P. N. Shankar and M. D. Desphande. "Fluid mechanics in the driven cavity." In: *Annu Rev Fluid Mech* 32 (2000), pp. 93–136. DOI: https://doi.org/10.1146/annurev.fluid.32.1.93.

[139] A. Silveira-Neto et al. "A numerical investigation of the coherent vortices in turbulence behind a backward-facing step." In: *J Fluid Mech* v. 256, p. (1993).

[140] L Skrbek and S R Stalp. "On the decay of homogeneous isotropic turbulence". In: *Phys Fluids* 12 (2000), p. 1997. DOI: https://doi.org/10.1063/1.870447.

[141] J. Smagorinsky. "General circulation experiments with the primitive equations. I. The basic experiment." In: *Mon Weather Rev* 91, 99-164 (1963). DOI: https://doi.org/10.1175/1520-0493(1963)091.

[142] C. G. Speziale. "On non-linear k-l and k-ω models of turbulence". In: *J Fluid Mech* 178 (1987), pp. 459–475.

[143] C. S. Subramanian, B. S. Kandola, and P. Bradshaw. *No Title*. Vol. 85-01. Imperial College of Science and Technology Department of Aeronautics, 1985.

[144] B. Tao, J. Katz, and C. Meneveau. "Statistical geometry of subgrid-scale stresses determined from holographic particle image velocimetry measurements". In: *J Fluid Mech* 457 (2002), pp. 35–78. ISSN: 0022-1120. DOI: 10.1017/S0022112001007443.

[145] H. Tennekes and J. L. Lumley. *A First Course in Turbulence*. Cambridge, Massachusetts, and London England: The MIT press, 1972, p. 300. ISBN: 0262200198. DOI: 10.1017/S002211207321251X.

[146] L. Thais, T. B. Gatski, and G. Mompean. "Some dynamical features of the turbulent flow of a viscoelastic fluid for reduced drag." In: *J Turbul* 13(19):1– (2012). DOI: https://doi.org/10.1080/14685248.2012.685522.

[147] L Thais, G Mompean, and T B Gatski. "Spectral analysis of turbulent viscoelastic and Newtonian channel flows." In: *J Non-Newton Fluid Mech* 200:165–176 (2013). DOI: https://doi.org/10.1016/j.jnnfm.2013.04.006.

[148] L. Thais et al. "A massively parallel hybrid scheme for direct numerical simulation of turbulent viscoelastic channel flow". In: *Computers & Fluids* 43.1 (2011), pp. 134–142. ISSN: 00457930. DOI: 10.1016/j.compfluid.2010.09.025.

[149] R. L. Thompson. "Some perspectives on the dynamic history of a material element". In: *Int j Eng Sci Technol* 46 (2008), pp. 224–249.

[150] R. L. Thompson and P. R. de Souza Mendes. "Considerations on kinematic flow classification criteria". In: *J Non-Newton Fluid Mech* 128.2-3 (2005), pp. 109–115. ISSN: 03770257. DOI: 10.1016/j.jnnfm.2005.04.002.

[151] R. L. Thompson and P. R. de Souza Mendes. "Further remarks on persistence of straining and flow classification". In: *Int j Eng Sci Technol* 45.2-8 (2007), pp. 504–508. ISSN: 00207225. DOI: 10.1016/j.ijengsci.2007.03.008.

[152] R. L. Thompson, G. Mompean, and L. Thais. "A methodology to quantify the nonlinearity of the Reynolds stress tensor". In: *J Turbul* 11 (2010). DOI: https://doi.org/10.1080/14685248.2010.501799.

[153] R. L. Thompson et al. "A methodology to evaluate statistical errors in DNS data of plane channel flows". In: *Computers & Fluids* 130 (2016), pp. 1–7. ISSN: 00457930. DOI: 10.1016/j.compfluid.2016.01.014.

[154] G. Toshiyuki, F. Daigen, and N. Tohru. "Velocity field statistics in homogeneous steady turbulence obtained using a high-resolution direct numerical simulation". In: *Phys Fluids* 14, 1065 (2002). DOI: https://doi.org/10.1063/1.1448296.

[155] A. Trofimova et al. "Direct numerical simulation of turbulent channel flows using a stabilized finite element method." In: *Computers & Fluids* 38(4):924–38 (2009).

[156] M. Uhlmann. "An immersed boundary method with direct forcing for the simulation of particulate flows." In: *J Comput Phys* 209.1994 (2005), pp. 448–476. DOI: https://doi.org/10.1016/j.jcp.2008.04.014.

[157] R. Vinuesa, R. D. Duncan, and H. M. Nagib. "Alternative interpretation of the Superpipe data and motivation for CICLoPE: The effect of a decreasing viscous length scale". In: *Eur J Mech B/Fluids* 58 (2016), pp. 109–116. ISSN: 09977546. DOI: 10.1016/j.euromechflu.2016.03.010.

[158] R. Vinuesa and H. M. Nagib. "Enhancing the accuracy of measurement techniques in high Reynolds number turbulent boundary layers for more representative comparison to their canonical representations". In: *Eur J Mech B/Fluids* 55 (2016), pp. 300–312. ISSN: 09977546. DOI: 10.1016/j.euromechflu.2015.09.004.

[159] R. Vinuesa et al. "Convergence of numerical simulations of turbulent wall-bounded flows and mean cross-flow structure of rectangular ducts". In: *Meccanica* 51.12 (2016), pp. 3025–3042. ISSN: 0025-6455. DOI: 10.1007/s11012-016-0558-0.

[160] R. Vinuesa et al. "Direct numerical simulation of the flow around a wall-mounted square cylinder under various inflow conditions". In: *J Turbul* 16.6 (2015), pp. 555–587. ISSN: 1468-5248. DOI: 10.1080/14685248.2014.989232.

[161] A. W. Vreman and J. G. M. Kuerten. "A third-order multistep time discretization for a Chebyshev tau spectral method". In: *J Comput Phys* 304 (2016), pp. 162–169. DOI: 10.1016/j.jcp.2015.10.022.

[162] A. W. Vreman and J. G. M. Kuerten. "Comparison of direct numerical simulation databases of turbulent channel flow at $Re_\tau = 180$". In: *Phys Fluids* 26.1 (2014), pp. 1–21. ISSN: 10897666. DOI: 10.1063/1.4861064.

[163] A. W. Vreman and J. G. M. Kuerten. "Statistics of spatial derivatives of velocity and pressure in turbulent channel flow". In: *Phys Fluids* 26.8 (2014). ISSN: 10897666. DOI: 10.1063/1.4891624.

[164] B. Vreman, B. Geurts, and H. Kuerten. "A priori tests of large eddy simulation of the compressible plane mixing layer". In: *J Eng Math* 29 (1995), pp. 299–327. DOI: 10.1007/BF00042759.

[165] B. Vreman, B. Geurts, and H. Kuerten. "On the formulation of the dynamic mixed subgrid- scale model." In: *Phys Fluids* 6(12):4057 (1994). DOI: https://doi.org/10.1063/1.868333.

[166] B. Vreman, B. J. Geurts, and H. Kuerten. "Comparison of numerical schemes in large-eddy simulation of the temporal mixing layer". In: *Int J Numer Meth Fluids* 22.December 1994 (1996), pp. 297–311. ISSN: 02712091.

[167] B. Wang and D. J Bergstrom. "A dynamic nonlinear subgrid-scale stress model". In: *Phys Fluids* 17.035109 (2005), pp. 1–15. DOI: https://doi.org/10.1063/1.1858511.

[168] T. Wei and W. Willmarth. "Reynolds-number effects on the structure of a turbulent channel flow". In: *J Fluid Mech* 204 (1989), pp. 57–95. ISSN: 0022-1120. DOI: 10.1017/S0022112089001667.

[169] G. S. Winckelmans et al. "A priori testing of subgrid-scale models for the velocity-pressure and vorticity-velocity formulations". In: *J Fluid Mech* 336, 151-1 (1996).

[170] V. Wong. "A proposed statistical-dynamic closure method for the linear or nonlinear subgrid-scale stresses." In: *Phys Fluids A* 4 (1992), p. 1080. DOI: https://doi.org/10.1063/1.858261.

[171] X. Wu, J. R. Baltzer, and R. J. Adrian. "Direct numerical simulation of a 30R long turbulent pipe flow at $R^+ = 685$: large- and very large-scale motions". In: *J Fluid Mech* 698, pp. 2 (2012).

[172] X. Wu and P. Moin. "A direct numerical simulation study on the mean velocity characteristics in turbulent pipe flow". In: *J Fluid Mech* 608 (2008), pp. 81–112. ISSN: 0022-1120. DOI: 10.1017/S0022112008002085.

[173] M. V. Zagarola and A. J. Smith. "Mean Flow Scaling of Turbulent Pipe Flow". In: *J Fluid Mech* 373 (1998), pp. 33–79.

[174] M. V. Zagarola and A. J. Smits. "Scaling of the mean velocity profile for turbulent pipe flow". In: *Physical Review Letters* 78.5 (1997), pp. 239–242. ISSN: 0031-9007. DOI: 10.1103/PhysRevLett.78.239.

[175] Y. Zang, R. L. Street, and J. R. Koseff. "A dynamic mixed subgrid-scale model and its application to turbulent recirculating flows". In: *Phys Fluids A: Fluid Dynamics (1989-1993)* 5.12 (1993), pp. 3186–3196. ISSN: 0899-8213. DOI: 10.1063/1.858675. eprint: 93/5(12)/3186/11.

[176] Y Zhou. "Degrees of locality of energy transfer in the inertial range." In: *Phys Fluids* 5(5):1092–4 (1993).

[177] Y Zhou. "Interacting scales and energy transfer in isotropic turbulence." In: *Phys Fluids* 5(10):2511–24 (1993). DOI: https://doi.org/10.1063/1.858764.

Appendix A

Overview of publicly accessible DNS databases

Tables A.2–A.6 present the main database parameters of the numerical simulations for different Reynolds numbers. The parameters and results relative to other groups were obtained from the databases publicly available in the websites or based on the corresponding publications. The on-line address of the data can be found in Table A.1.

AKC [1]	http://www.rs.tus.ac.jp/~t2lab/db/index.html
BPO [13]	http://newton.dma.uniroma1.it/channel/
AJ [36], AJZM [37], HJ [62]	
LDJ [96]	http://torroja.dmt.upm.es/ftp/channels/data/
EUWWAFN [45], TN [38]	http://torroja.dmt.upm.es/turbdata/
FK [47], ISK [65]	http://www.thtlab.jp/
KSNFBJ [74]	ftp://ftp.mech.kth.se/pub/pschlatt/DATA/PIPE/
LM [88], MKM [117]	http://turbulence.ices.utexas.edu/
TGM [146]	http://lthais.plil.fr
VK [162, 163, 161]	http://www.vremanresearch.nl/channel.html
WBA [171], WM [172]	https://stanford.app.box.com

Table A.1 – On-line address of publicly accessible DNS databases. Accessed on 23/06/2017.

The spatial discretization methods are indicated by abbreviations that are presented as "method A–method B" where "method A" stands for the discretization method along the periodic directions (streamwise and spanwise x,z directions or streamwise and circumferential x,θ), and "method B" stands for the discretization method along the wall-normal direction y or the radial direction r; the abbreviations are given by FV2 means a second-order finite-volume approach, FG represents a Fourier-Galerkin method, SEM is a spectral element method, F represents a Fourier spectral method, C represents the Chebychev-tau method, BS7 represents a B-spline collocation method with seventh-order, FD2, FD4, and FD6 represent, respectively, second-, fourth-, and sixth-order finite-difference approximations, and CDF7 represents seven-point compact finite differences [89].

In the abbreviations S2B3 and S4B3 of Vreman and Kuerten [161], S2 and S4 repre-

Author	Abbreviation	Method	Re_τ	Tu_τ/h	T^*
Present Study	PS	F-FD6	180	235	1544
Bernardini, Pirozzoli, and Orlandi [13]	BOP	FD2-FD2	183	-	-
Del Álamo and Jiménez [36]	AJ	F-C	186	50	1315
Eggels et al. [45]	EUWWAFN	FV2-FV2	180	28	46
Fukagata and Kasagi [47]	FK	FD2-FD2	180	11	36
Khoury et al. [74]	KSNFBJ	SEM-SEM	181	-	-
Lee and Moser [88]	LM	FG-BS7	182	32	421
Moser, Kim, and Mansour [117]	MKM	F-C	178	-	-
Vreman and Kuerten [162]	VK-FD2	FD2-FD2	180	200	585
Vreman and Kuerten [161]	VK-S2B3	F-C	180	200	585
Vreman and Kuerten [161]	VK-S4B3	F-C	180	100	146
Wu and Moin [172]	WM	FD2-FD2	181	19	47

Table A.2 – Overview of publicly accessible DNS databases at $Re_\tau \approx 180$, where T is the averaging time.

sent a coarse and a refined grid, respectively, while B3 represents a third-order time discretization scheme.

Author	Abbreviation	Method	Re_τ	Tu_τ/h	T^*
Present Study	PS	F-FD6	590	97	640
Abe, Kawamura, and Choi [1]	AKC	FD4-FD2	640	10	44
Bernardini, Pirozzoli, and Orlandi [13]	BPO	FD2-FD2	550	36	236
Del Álamo and Jiménez [36]	AJ	F-C	547	12	210
Iwamoto, Suzuki, and Kasagi [65]	ISK	F-C	642.5	40	55
Khoury et al. [74]	KSNFBJ	SEM-SEM	550	-	-
Lee and Moser [88]	LM	FG-BS7	544	14	184
Moser, Kim, and Mansour [117]	MKM	F-C	587	-	-
Thais, Gatski, and Mompean [146]	TGM	F-FD	590	20	131
Vreman and Kuerten [163]	VK	F-C	590	100	109
Wu, Baltzer, and Adrian [171]	WBA	FD2-FD2	685	14	70

Table A.3 – Overview of publicly accessible DNS databases at $Re_\tau \approx 544 - 685$.

Other details about the publicly accessible DNS databases are presented in Tables A.7–A.12. The described parameters are: domain size, number of grid points, and mesh resolution. The simulation lengths are normalized by the channel half-width (for channel flows) or the radius (for pipe flows). The grid resolution is given in wall units, employing the kinematic viscosity ν and friction velocity u_τ.

Since Khoury et al. [74] used a computational fluid dynamics solver based on the spectral element method, solving the incompressible Navier-Stokes equations by using a Legendre polynomial based SEM that involves a number of elements and grid points, their mesh information is not included in Tables A.7, A.8, or A.9. In their simulations, a circular pipe of axial length $25R$ is considered and the mesh information is given in Table A.10.

Author	Abbreviation	Method	Re_τ	Tu_τ/h	T^*
Present Study	PS	F-FD6	1000	4.2	21
Bernardini, Pirozzoli, and Orlandi [13]	BPO	FD2-FD2	999	26.9	176
Del Álamo et al. [37]	AJZM	F-C	934	8.5	111
Khoury et al. [74]	KSNFBJ	SEM-SEM	1000	-	-
Lee and Moser [88]	LM	FG-BS7	1000	12.5	164
Thais, Gatski, and Mompean [146]	TGM	F-FD	1000	7.1	35
Wu and Moin [172]	WM	FD2-FD2	1142	7.8	20

Table A.4 – Overview of publicly accessible DNS databases at $Re_\tau \approx 934 - 1142$.

Author	Abbreviation	Method	Re_τ	Tu_τ/h	T^*
Bernardini, Pirozzoli, and Orlandi [13]	BPO	FD2-FD2	2021	14.9	98
Hoyas and Jiménez [62]	HJ	F-CFD7	2003	10.3	135

Table A.5 – Overview of publicly accessible DNS databases at $Re_\tau \approx 2000$.

Author	Abbreviation	Method	Re_τ	Tu_τ/h	T^*
Bernardini, Pirozzoli, and Orlandi [13]	BPO	FD2-FD2	4079	8.5	55
Lee and Moser [88]	LM	FG-BS7	5186	7.8	68
Lozano-Durán and Jiménez [96]	LDJ	F-CDF7	4179	15.0	16

Table A.6 – Overview of publicly accessible DNS databases at $Re_\tau > 4000$.

Author	$L_1/h \times L_3/h$	$N_{x_1} \times N_{x_2} \times N_{x_3}$	$\delta {x_1}^+$	$\delta {x_2}^+_{max}$, $\delta {x_2}^+_w$	$\delta {x_3}^+$
PS	$8\pi \times 3\pi/2$	$512 \times 129 \times 128$	8.80	7.10, 0.200	6.60
BOP	-	- ×129× -	-	- , 0.063	-
AJ	$12\pi \times 4\pi$	- ×96× -	8.90	6.10, 0.010	4.50
EUWWAFN	$10 \times 2\pi$	$96 \times 128 \times 256$	7.03	1.88, -	8.44
FK	$20 \times 2\pi$	$96 \times 128 \times 512$	7.03	2.99, 0.460	–
LM	$8\pi \times 3\pi$	$1024 \times 192 \times 512$	4.50	3.40, 0.010	3.10
MKM	$4\pi \times 4\pi/3$	$128 \times 129 \times 128$	17.70	4.40, 0.054	5.90
VK-FD2	$4\pi \times 4\pi/3$	$512 \times 256 \times 256$	4.40	2.20, 0.241	2.90
VK-S2	$4\pi \times 4\pi/3$	$384 \times 192 \times 192$	5.90	2.90, 0.241	3.90
VK-S4	$4\pi \times 2\pi/3$	$576 \times 576 \times 288$	-	0.98, 0.003	-
WM	$15 \times 2\pi$	$256 \times 512 \times 512$	5.31	1.647, 0.167	2.22

Table A.7 – Overview of publicly accessible DNS databases at $Re_\tau \approx 180$.
$L_1/h \times L_2/h \times L_3/h$ are the channel dimensions normalized by the channel half-height h, $N_{x_1} \times N_{x_2} \times N_{x_2}$ are the number of discretized cells in x, y and z directions, respectively, δx_1^+ and δx_3^+ are the grid size in wall units in x and z directions, respectively, $\delta {x_2}^+_{max}$ and $\delta {x_2}^+_w$ are the maximum and minimum grid size in wall units in y direction, respectively.

Author	$L_1/h \times L_3/h$	$N_{x_1} \times N_{x_2} \times N_{x_3}$	$\delta {x_1}^+$	$\delta {x_2}^+_{max}$, $\delta {x_2}^+_w$	$\delta {x_3}^+$
PS	$8\pi \times 3\pi/2$	$1536 \times 257 \times 512$	9.60	10.40, 0.500	5.40
AKC	$4\pi \times 2\pi$	$1024 \times 256 \times 1024$	8.00	8.02, 0.150	4.00
BPO	$6\pi \times 2\pi$	$1024 \times 256 \times 512$	10.00	6.90, 0.010	6.70
AJ	$8\pi \times 4\pi$	$1536 \times 257 \times 1536$	8.90	6.70, 0.041	4.50
ISK	$5\pi/2 \times \pi$	$288 \times 257 \times 384$	17.7	7.98, 0.049	5.32
LM	$8\pi \times 3\pi$	$1536 \times 384 \times 1024$	8.90	4.50, 0.019	5.00
MKM	$2\pi \times \pi$	$384 \times 257 \times 384$	9.70	7.20, 0.044	4.80
TGM	$8\pi \times 3\pi/2$	$1536 \times 257 \times 512$	9.60	10.40, 0.500	5.40
VK	$2\pi \times \pi$	$768 \times 385 \times 768$	4.80	4.80, 0.020	2.40
WBA	$30 \times 2\pi$	$256 \times 1024 \times 2048$	10.03	11.30, 0.144	4.20

Table A.8 – Overview of publicly accessible DNS databases at $Re_\tau \approx 544 - 685$. $L_1/h \times L_2/h \times L_3/h$ are the channel dimensions normalized by the channel half-height h, $N_{x_1} \times N_{x_2} \times N_{x_2}$ are the number of discretized cells in x, y and z directions, respectively, δx_1^+ and δx_3^+ are the grid size in wall units in x and z directions, respectively, $\delta {x_2}^+_{max}$ and $\delta {x_2}^+_w$ are the maximum and minimum grid size in wall units in y direction, respectively.

Author	$L_1/h \times L_3/h$	$N_{x_1} \times N_{x_2} \times N_{x_3}$	$\delta {x_1}^+$	$\delta {x_2}^+_{max}$, $\delta {x_2}^+_w$	$\delta {x_3}^+$
PS	$6\pi \times 3\pi/2$	$1536 \times 513 \times 768$	12.30	8.40, 0.500	6.10
BPO	$6\pi \times 2\pi$	$2048 \times 384 \times 1024$	9.20	6.90, 0.010	6.10
AJZM	$8\pi \times 3\pi$	$3072 \times 2304 \times 385$	9.20	7.60, 0.030	3.80
LM	$8\pi \times 3\pi$	$2304 \times 512 \times 2048$	10.90	6.20, 0.019	4.60
TGM	$6\pi \times 3\pi/2$	$1536 \times 513 \times 768$	12.30	8.40, 0.500	6.10
WM	$15 \times 2\pi$	$300 \times 1024 \times 2048$	8.37	11.30, 0.410	7.01

Table A.9 – Overview of publicly accessible DNS databases at $Re_\tau \approx 934 - 1142$. $L_1/h \times L_2/h \times L_3/h$ are the channel dimensions normalized by the channel half-height h, $N_{x_1} \times N_{x_2} \times N_{x_2}$ are the number of discretized cells in x, y and z directions, respectively, δx_1^+ and δx_3^+ are the grid size in wall units in x and z directions, respectively, $\delta {x_2}^+_{max}$ and $\delta {x_2}^+_w$ are the maximum and minimum grid size in wall units in y direction, respectively.

R^+	# of elements	# grid points	$\delta {x_1}^+$	$\delta {x_2}^+$	$\delta {x_3}^+$
180	36,480	1.867×10^7	(0.14, 4.44)	(1.51, 4.93)	(3.03, 9.91)
550	853 632	4.370×10^8	(0.15, 4.49)	(1.45, 4.75)	(3.06, 9.99)
1000	1 264 032	2.184×10^9	(0.15, 5.12)	(0.98, 4.87)	(2.01, 9.98)

Table A.10 – Overview of the mesh employed by Khoury et al. [74] in turbulent pipe flow simulations. $\delta {x_1}^+$, $\delta {x_2}^+$ and $\delta {x_3}^+$ are the minimum and maximum grid size in wall units in x, y and z directions, respectively.

Author	$L_1/h \times L_3/h$	$N_{x_1} \times N_{x_2} \times N_{x_3}$	$\delta {x_1}^+$	$\delta {x_2}^+_{max}$, $\delta {x_2}^+_w$	$\delta {x_3}^+$
BPO	$6\pi \times 2\pi$	$4096 \times 768 \times 2048$	9.30	- , 0.01	6.2
HJ	$8\pi \times 3\pi$	$6144 \times 633 \times 4608$	8.20	8.90, -	4.1

Table A.11 – Overview of publicly accessible DNS databases at $Re_\tau \approx 2000$. $L_1/h \times L_2/h \times L_3/h$ are the channel dimensions normalized by the channel half-height h, $N_{x_1} \times N_{x_2} \times N_{x_2}$ are the number of discretized cells in x, y and z directions, respectively, δx_1^+ and δx_3^+ are the grid size in wall units in x and z directions, respectively, $\delta {x_2}^+_{max}$ and $\delta {x_2}^+_w$ are the maximum and minimum grid size in wall units in y direction, respectively.

Author	$L_1/h \times L_3/h$	$N_{x_1} \times N_{x_2} \times N_{x_3}$	$\delta {x_1}^+$	$\delta {x_2}^+_{max}$, $\delta {x_2}^+_w$	$\delta {x_3}^+$
BPO	$6\pi \times 2\pi$	$8192 \times 1024 \times 4096$	9.40	6.90, 0.010	6.2
LM	$8\pi \times 3\pi$	$10,240 \times 1536 \times 7680$	12.70	10.30, 0.498	6.4
LDJ	$2\pi \times \pi$	- $\times 1081 \times$ -	12.80	10.70, -	6.4

Table A.12 – Overview of publicly accessible DNS databases at $Re_\tau > 4000$. $L_1/h \times L_2/h \times L_3/h$ are the channel dimensions normalized by the channel half-height h, $N_{x_1} \times N_{x_2} \times N_{x_2}$ are the number of discretized cells in x, y and z directions, respectively, δx_1^+ and δx_3^+ are the grid size in wall units in x and z directions, respectively, $\delta {x_2}^+_{max}$ and $\delta {x_2}^+_w$ are the maximum and minimum grid size in wall units in y direction, respectively.

Appendix B

Validation of the spatial/spectral distribution of the TKE equation terms

We present here a validation of the results at $Re_\tau = 180$ by comparison with the work of Bolotnov et al. [17].

A sketch of the bin distribution of the present work and the one of Bolotnov et al. [17] one is given in Fig. B.1. The bin structure in the present study seeks to be similar with the one presented by Bolotnov et al. [17]. In this way, the impact of differences for quantities representing the dynamics dominated by high-wave-number events is minimized.

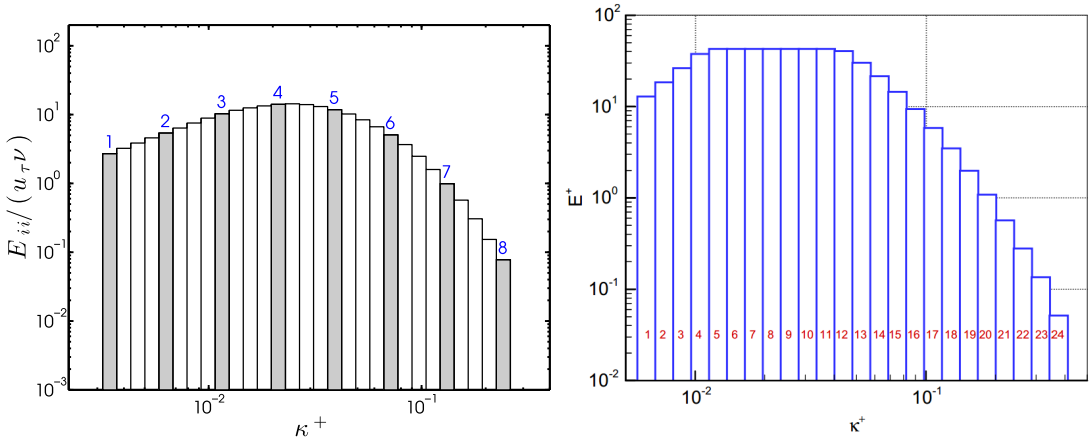

(a) Present work (b) Bolotnov et al. [17]

Figure B.1 – Comparison of the wave number bin distribution and numeration between the present work and the one by Bolotnov et al. [17].

We now compare (Figs. B.2 to B.5) the contours of some important source terms in Eq. 2.25 at the plane κ^+–y^+ obtained in the present work with those presented by Bolotnov et al. [17].

The turbulent kinetic energy contour is displayed in Fig. B.2. A peak is observed in the same area ($0.05 \leq \kappa^+ \leq 0.08$ and $10 \leq y^+ \leq 20$) in both cases and the decreasing rate in other regions is very similar.

In Fig. B.3, the turbulent production is shown. Again, our results are in accordance

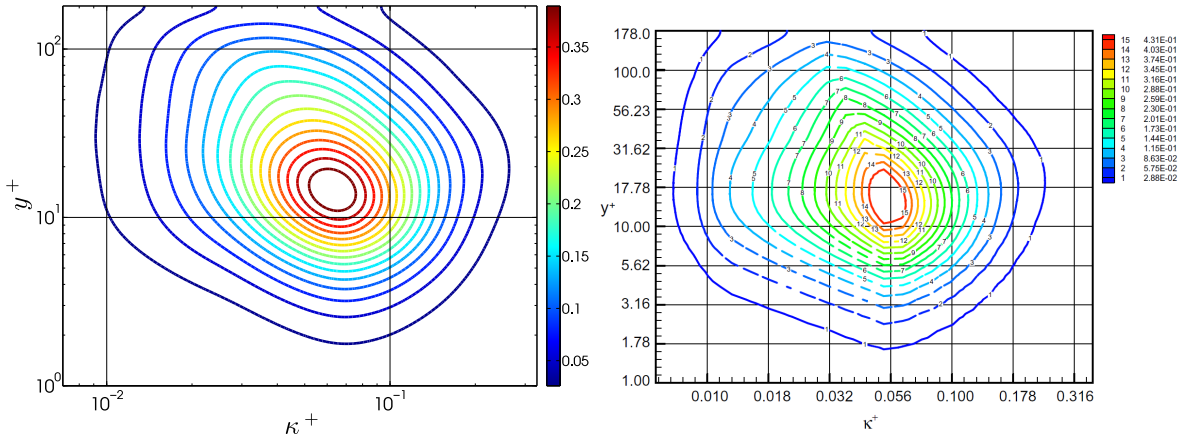

(a) Present work. (b) Bolotnov et al. [17]

Figure B.2 – Comparison of turbulent kinetic energy contour levels at $Re_\tau = 180$.

with those found by Bolotnov et al. [17]. The highest production is centered at $\kappa^+ \approx 0.085$ and $y^+ \approx 12$, and the decreasing rate is in very good agreement with the reference by Bolotnov et al. [17].

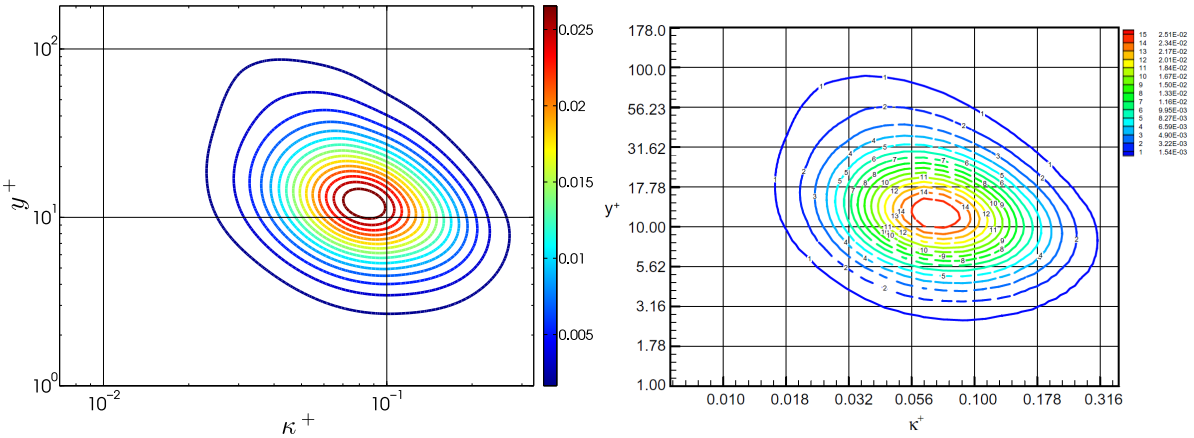

(a) Present work. (b) Bolotnov et al. [17]

Figure B.3 – Comparison of turbulent production contour levels at $Re_\tau = 180$.

The in-plane turbulent dissipation, shown in Fig. B.4, presents a major peak at $\kappa^+ \approx 0.12$ and $y^+ \approx 12$, and, again, recovers very well the results of Bolotnov et al. [17].

The inter-plane turbulent dissipation contour shown in Fig. B.5 presents the same peak location, found at $\kappa^+ \approx 0.07$ and $y^+ \approx 1$. Moreover, the decay rate in $\kappa+$ and in $y+$ is also very similar to the reference behavior.

Figures B.6 to B.12 show the comparison of the various source terms from Eq. 2.25 integrated in bin regions as function of the wall distance y^+ at several wave number bin. The normalization employed is given by Eq. 2.42.

Figures B.13 to B.19 show the comparison of the various source terms from Eq. 2.25 integrated in bin regions as function of the wall distance y^+ at several wave number bin. The normalization employed is given by Eq. 2.42.

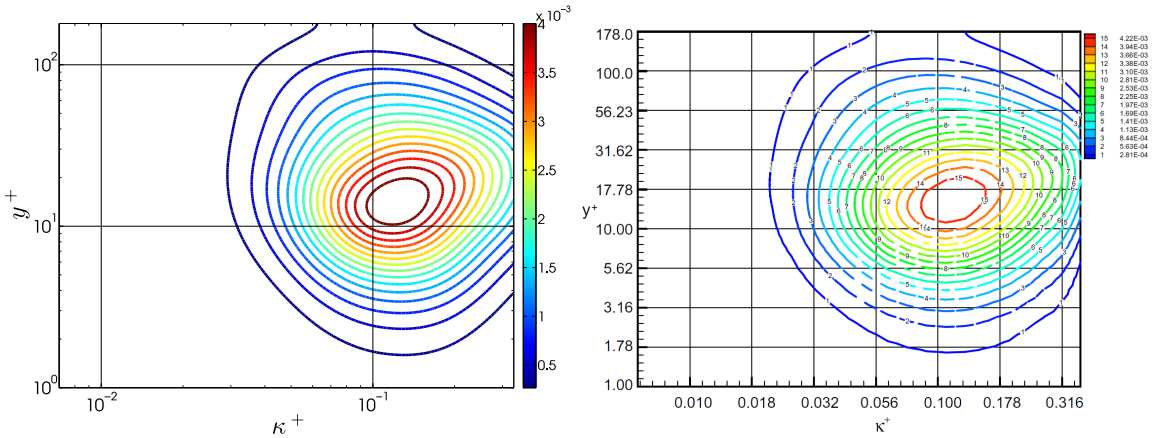

(a) Present work. (b) Bolotnov et al. [17]

Figure B.4 – Comparison of in-plane turbulent dissipation contour levels at $Re_\tau = 180$.

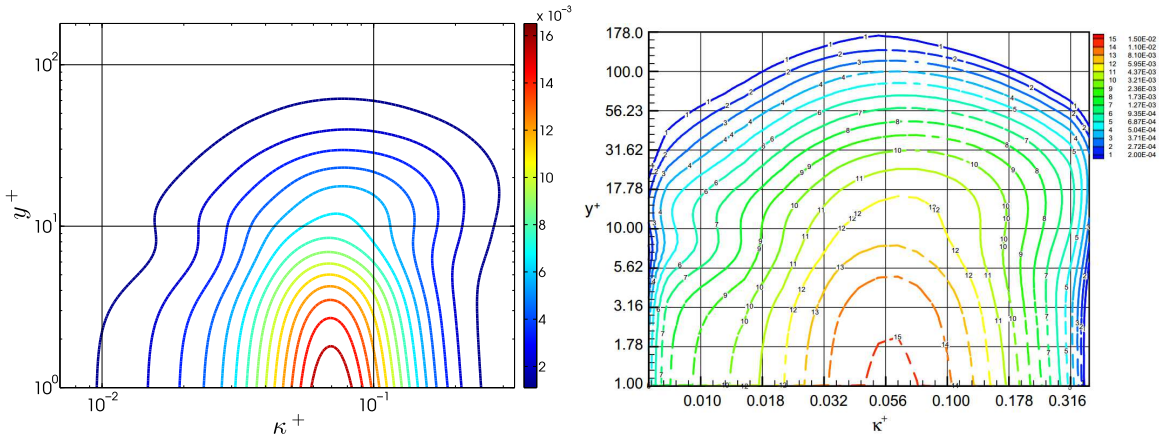

(a) Present work. (b) Bolotnov et al. [17]

Figure B.5 – Comparison of inter-plane turbulent dissipation contour levels at $Re_\tau = 180$.

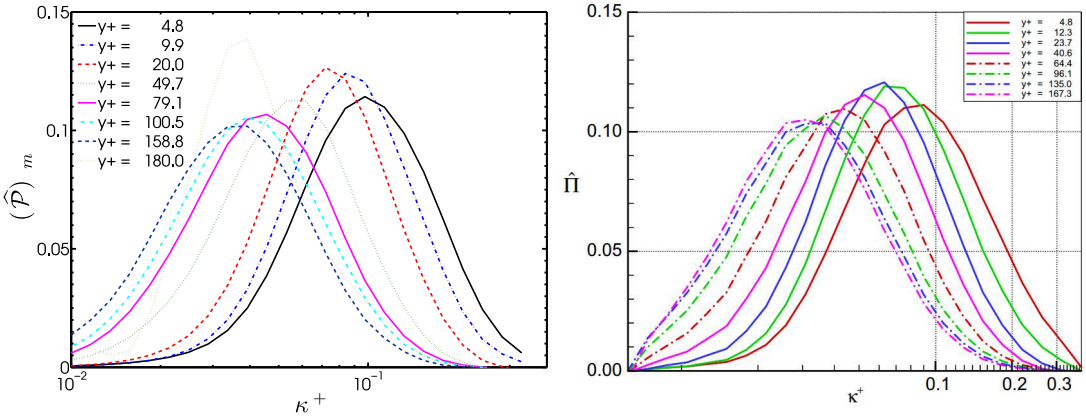

(a) Present work (b) Bolotnov et al. [17]

Figure B.6 – Turbulent production spectra at various y^+ locations.

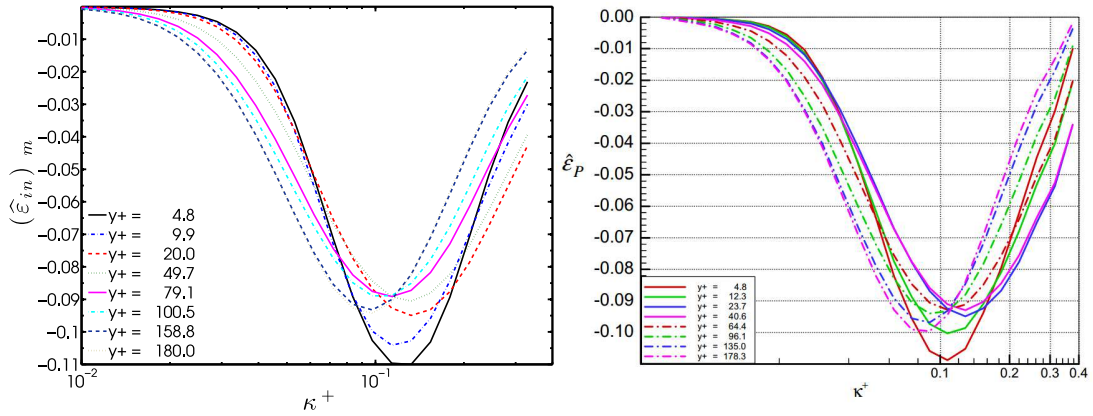

(a) $Re_\tau = 180$ (b) Bolotnov et al. [17]

Figure B.7 – In-plane dissipation spectra ε^+_{in} at various y^+ locations.

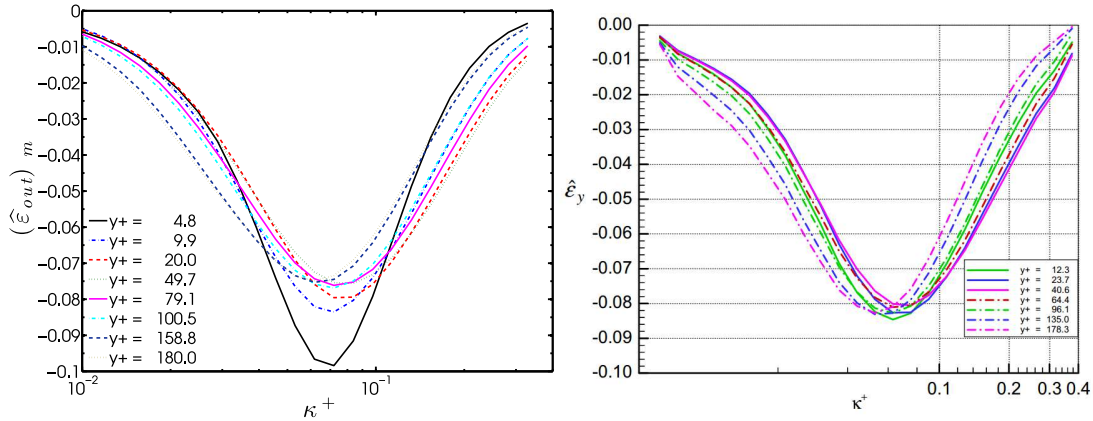

(a) Present work (b) Bolotnov et al. [17]

Figure B.8 – Inter-plane dissipation spectra ε^+_{in} at various y^+ locations.

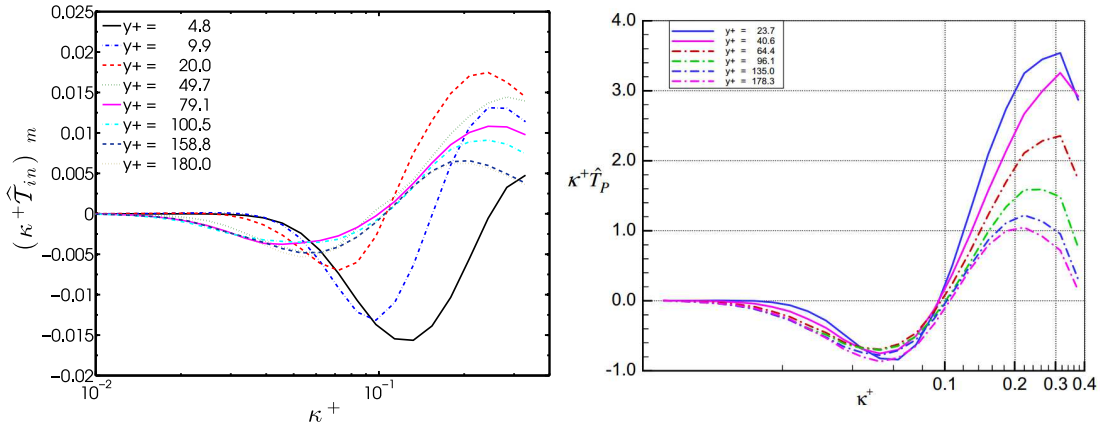

(a) Present work (b) Bolotnov et al. [17]

Figure B.9 – Product of the in-plane nonlinear term spectra at various y^+ locations.

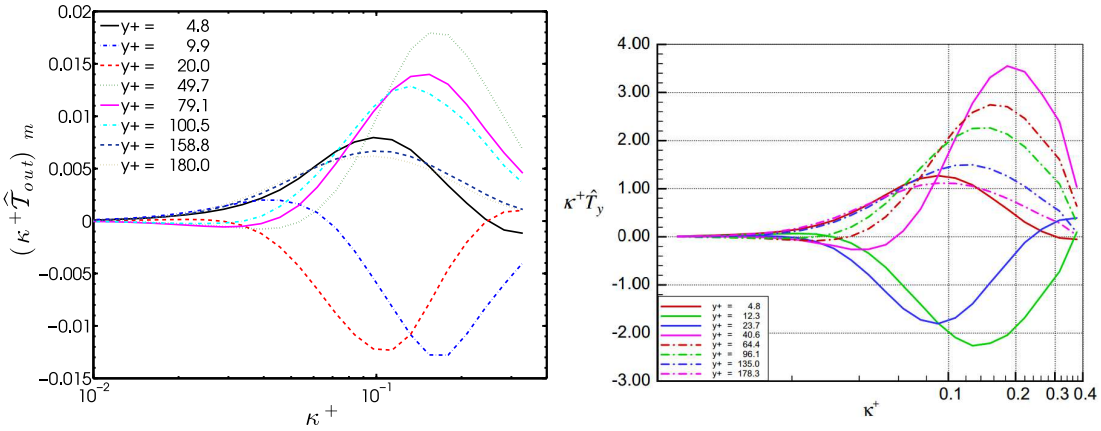

(a) Present work (b) Bolotnov et al. [17]

Figure B.10 – Inter-plane nonlinear term spectra at various y^+ locations.

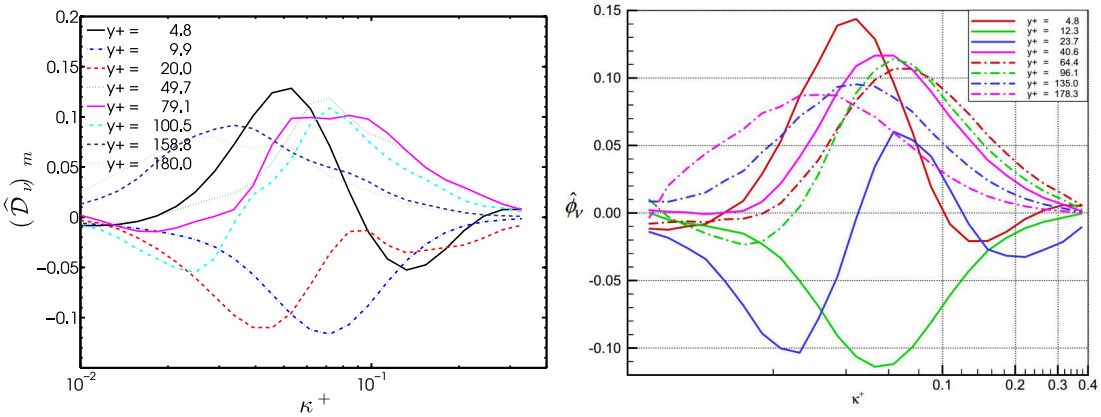

(a) Present work (b) Bolotnov et al. [17]

Figure B.11 – Viscous diffusion term at various y^+ locations.

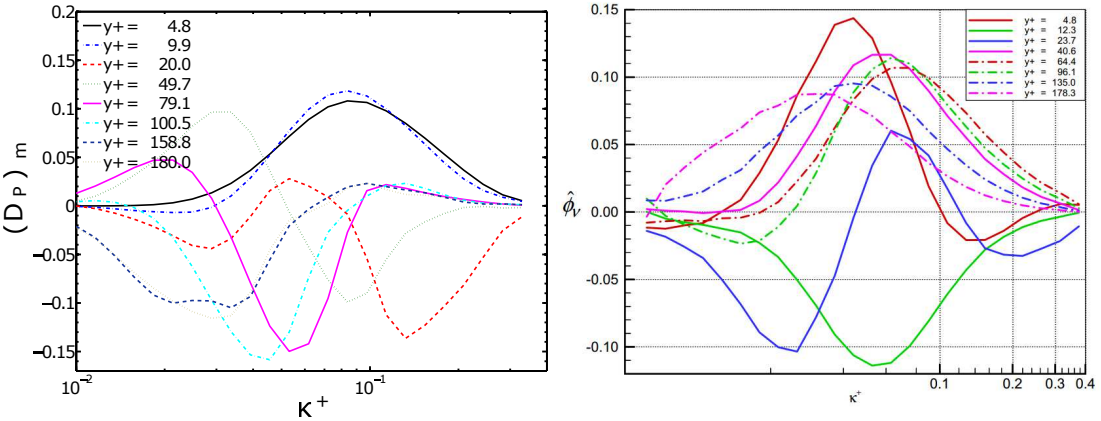

(a) Present work (b) Bolotnov et al. [17]

Figure B.12 – Pressure correlation spectra at various y^+ locations.

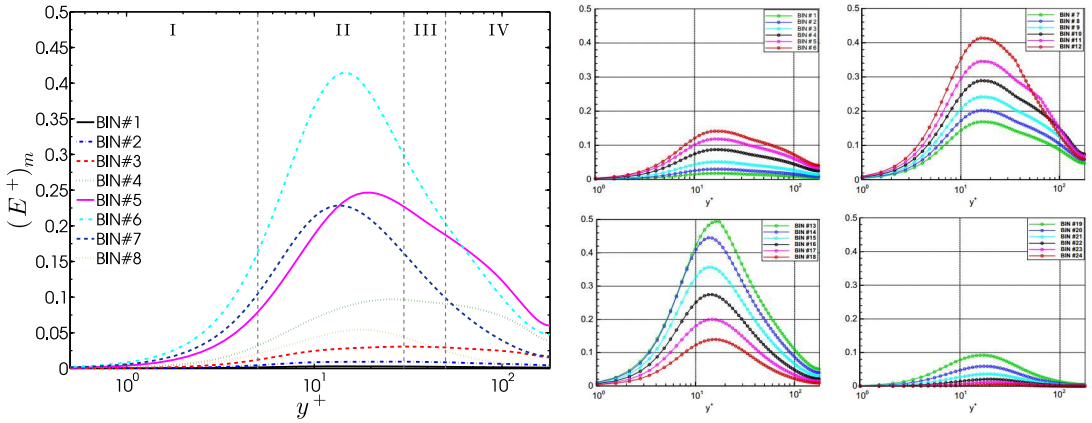

(a) Present work (b) Bolotnov et al. [17]

Figure B.13 – The distribution of turbulent kinetic energy k^+ of various wave number bins vs. distance to the wall.

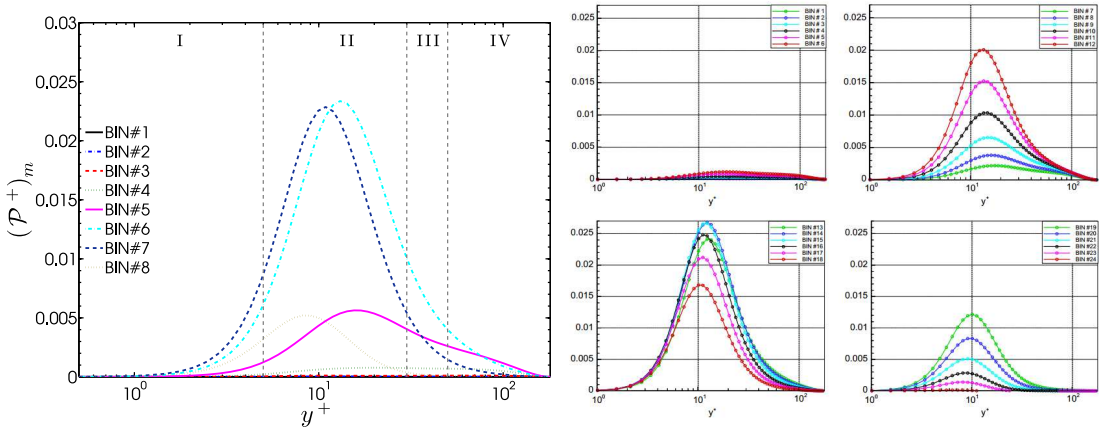

(a) Present work (b) Bolotnov et al. [17]

Figure B.14 – Turbulent production $\mathcal{P}^+$ – spectral distribution vs. distance to the wall.

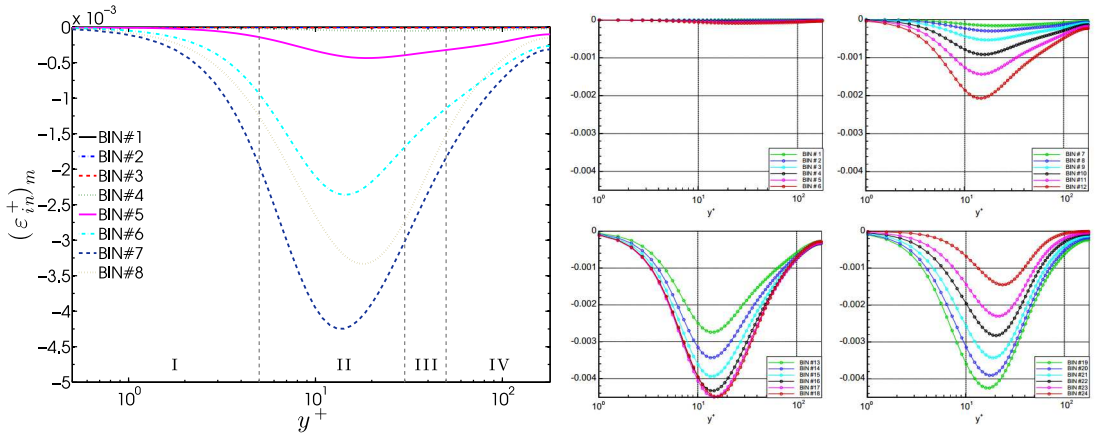

(a) Present work (b) Bolotnov et al. [17]

Figure B.15 – In-plane turbulent dissipation ε^+_{in} – spectral distribution vs. distance to the wall.

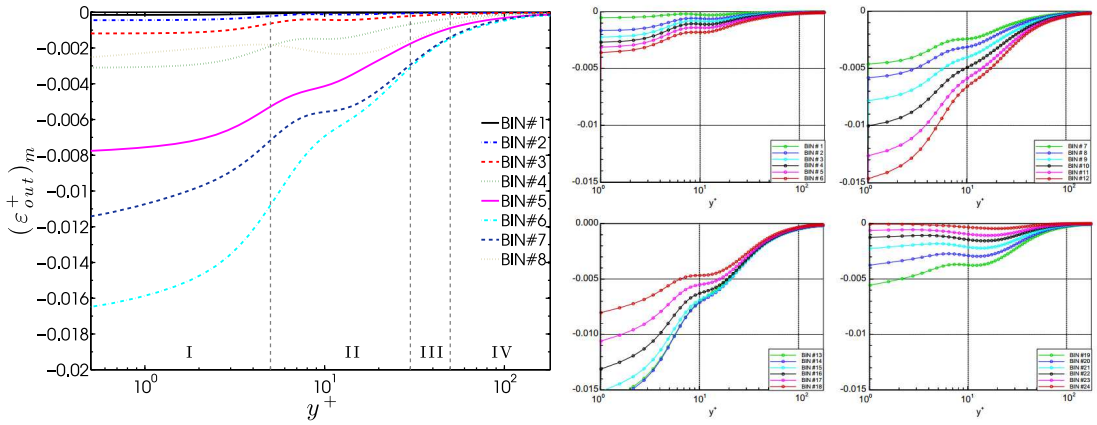

(a) Present work (b) Bolotnov et al. [17]

Figure B.16 – Inter-plane turbulent dissipation ε^+_{out} – spectral distribution vs. distance to the wall.

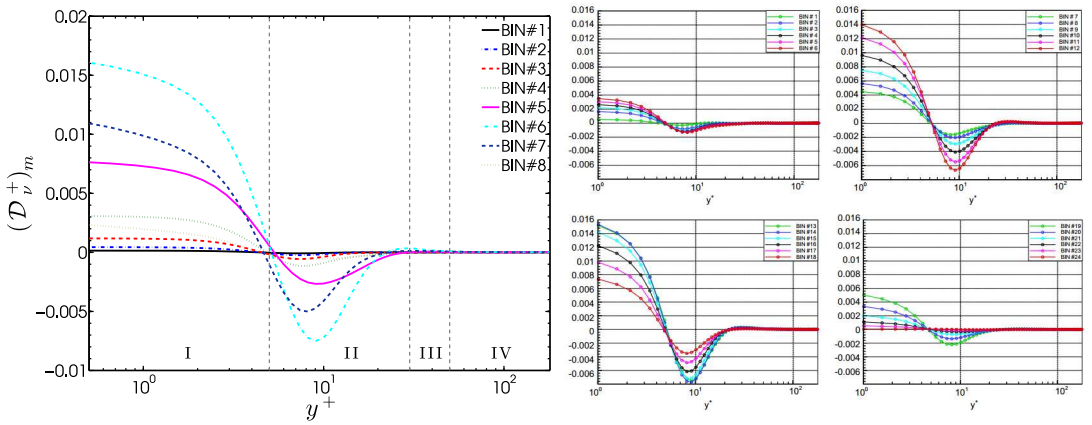

(a) Present work (b) Bolotnov et al. [17]

Figure B.17 – Turbulent viscous diffusion $\mathcal{D}_\nu^+$ – spectral distribution vs. distance to the wall.

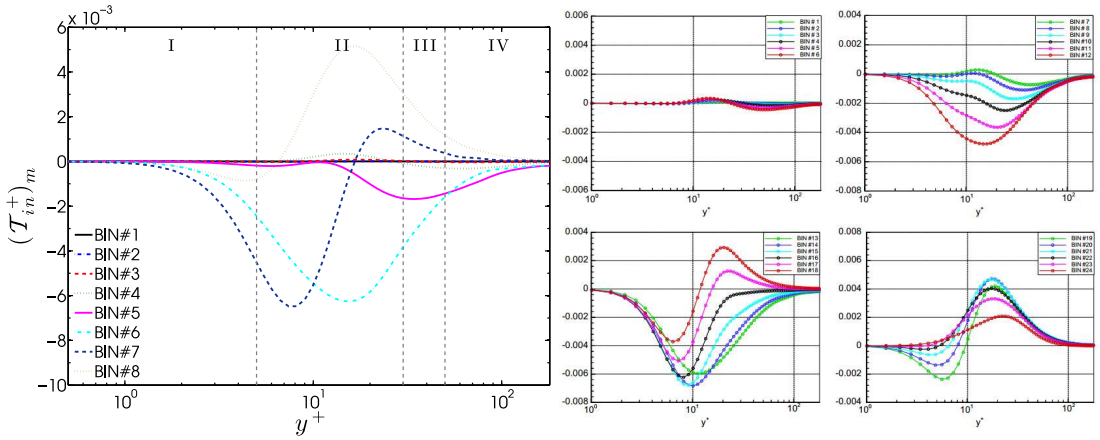

(a) Present work (b) Bolotnov et al. [17]

Figure B.18 – In-plane nonlinear transfer term $\mathcal{T}_{in}^+$ – spectral distribution vs. distance to the wall.

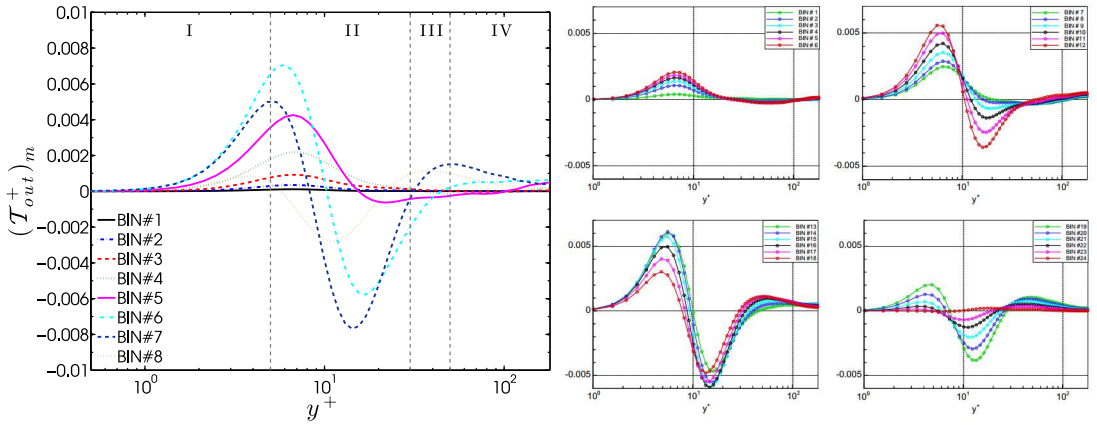

(a) Present work (b) Bolotnov et al. [17]

Figure B.19 – Inter-plane nonlinear transfer term $\mathcal{T}^+_{out}$ – spectral distribution vs. distance to the wall.

Contents

Spectral analysis of the turbulent energy cascade and the development of a novel nonlinear subgrid-scale model for large eddy simulation

Abstract

The purpose of the present work is to analyze and to provide an enhancement of the knowledge about the subgrid-scale behavior and to propose novel nonlinear subgrid-scale models for large eddy simulations of turbulent fluid flows. In this way, the present thesis is subdivided into three main parts. The first topic is an analysis of the statistical uncertainties associated with direct numerical simulation data for turbulent channel flow, showing a novel physically-based quantification of these errors. In this analysis, the mean velocity error is estimated by considering the Reynolds stress tensor, and using the balance of mean force equation. This analysis is performed in order to verify the quality of the statistical data coming from the direct numerical simulation applied in the present work. Secondly, seeking to understand the contained physics in the whole wavenumber spectrum of turbulent flows, an analysis of the spectral turbulent kinetic energy budget in fully developed turbulent plane channel flow is performed. The analysis is focused on the influence of the Reynolds number on the spectral cascade of energy and the corresponding energy cascade in physical space in the presence of inhomogeneity and anisotropy. Finally, a novel nonlinear subgrid-scale model for large eddy simulation based on a set of objective tensors is presented. In the proposed closure model, the modeled subgrid-scale stress tensor is a function of the resolved rate-of-strain tensor and the resolved non-persistence-of-straining tensor, where both are local and objective kinematic entities. The non-persistence-of-straining tensor represents the local ability of the fluid to avoid being persistently stretched. To check the consistency of the proposed model, *a priori* and *a posteriori* tests are performed by simulating different wall-bounded turbulent flows. Comparisons with the exact subgrid-scale stress tensor and experimental data revealed that the inclusion of nonlinear terms on the subgrid-scale model can significantly increase the accuracy of the results, showing the great potential of the proposed tensorial base.

Keywords: turbulent wall-bounded flows, energy cascade, turbulent kinetic energy budget, inhomogeneity, anisotropy, turbulent channel flow, turbulence, direct numerical simulation, large eddy simulation, subgrid-scale model, nonlinear subgrid-scale model

Laboratório de Mecânica dos Fluidos (MFLab)
Av. João Naves de Ávila, 2121 – Bairro Santa Mônica – 38400-902 Uberlândia – Brasil

Analyse spectrale de la cascade d'énergie turbulente et développement d'un nouveau modèle non-linéaire sous-maille pour la simulation de grandes échelles

Résumé

L'objectif de cette thèse est d'analyser et d'acquérir de nouvelles connaissances sur le comportement de la dynamique de petites échelles des écoulements turbulents et de proposer un nouveau modèle sous-maille non linéaire pour la simulation des grandes échelles de la turbulence. De cette façon, la présente thèse est subdivisée en trois parties principales. Le premier sujet concerne l'analyse des incertitudes statistiques associées aux données de simulation numérique directe pour des écoulements turbulents en canal plan, fournissant une nouvelle quantification physique de ces erreurs. Dans cette analyse, l'erreur de vitesse moyenne est estimée en prenant en compte le tenseur de contrainte de Reynolds et en utilisant l'équation de forces moyennes. Cette analyse est effectuée afin de vérifier la qualité des données statistiques provenant de la simulation numérique directe appliquée dans le présent travail. Deuxièmement, pour comprendre la physique contenue dans l'ensemble du spectre de nombre d'ondes des écoulements turbulents, une analyse du bilan d'énergie cinétique turbulente dans un écoulement de canal plan turbulent complètement développé est réalisée. L'analyse est centrée sur l'influence du nombre de Reynolds sur la cascade spectrale d'énergie et la cascade d'énergie correspondante dans l'espace physique en présence d'inhomogénéité et d'anisotropie. Finalement, nous présentons un nouveau modèle sous-maille non linéaire, conçu pour la simulation des grandes échelles de la turbulence, basé sur un ensemble de tenseurs objectifs. Dans le modèle de fermeture proposé, le tenseur de contrainte à l'échelle sous-maille est fonction du tenseur de la vitesse de déformation et du tenseur de non-persistance de contraintes, où les deux sont des entités cinématiques locales et objectives. Le tenseur non-persistance de contraintes représente la capacité locale du fluide à ne pas être constamment étiré. Pour vérifier la cohérence du modèle proposé, de tests *a priori* et *a posteriori* sont effectués en simulant différents écoulements turbulents délimités par de parois. Des comparaisons avec le tenseur de contrainte exact à l'échelle de sous-maille et de données expérimentales ont révélé que l'inclusion de termes non linéaires dans le modèle sous-maille peut conduire à de meilleurs résultats, montrant le potentiel important de la base tensorielle proposée.

Mots clés : écoulements turbulentes de parois, cascade d'énergie, équation différentielle de l'énergie cinétique turbulent, inhomogénéité, anisotropie, écoulement turbulent en canal plan, turbulence, simulation numérique directe, simulation des grandes échelles, modèle sous maille, modèle sous maille non linéaire